EPFL

Thèse n° 8809

Analysis of a Novel Toroidal Configuration for Hadron Therapy Gantries

Présentée le 19 février 2021

Faculté informatique et communications
Groupe SCI IC BD
Programme doctoral en génie électrique

pour l'obtention du grade de Docteur ès Sciences

par

Enrico FELCINI

Acceptée sur proposition du jury

Prof. J.-Ph. Thiran, président du jury
Dr B. Dutoit, Dr L. Bottura, directeurs de thèse
Prof. L. Rossi, rapporteur
Dr Y. Iwata, rapporteur
Prof. J. M. Schippers, rapporteur

École
polytechnique
fédérale
de Lausanne

2021

Acknowledgements

First of all, I would like to thank Dr. Luca Bottura from the bottom of my heart for his constant and tireless teachings. We met almost ten years ago, and you taught me everything I know about superconductors, magnets, Life, Universe, and Everything. In these years, you have been a master and a model both professionally and personally. Thanks for giving me the opportunity and the trust to work with you in the amazing project that is GaToroid. Grazie Luca, ti devo più di quanto immagini. Farò del mio meglio per essere all'altezza di tutto ciò che mi hai insegnato.

I am extremely grateful to Dr. Bertrand Dutoit, who provided me with infinite support and advice. Thank you, Bertrand, for your patience and your kindness. It was a pleasure to be your student and I was very lucky to have you as a supervisor. Merci Bertrand, surtout pour avoir été si gentil avec moi, même si je suis ingénieur.

I would also like to extend my deepest gratitude to the president of my oral examination Jury, Prof. Jean-Philippe Thiran, as well as to the members, Prof. Lucio Rossi, Prof. Jacobus Maarten Schippers and Dr. Yoshiyuki Iwata, for the thorough revision of this thesis and the stimulating discussions. I really hope that we will have the chance to work together soon. Merci, grazie, danke, arigatō gozaimashita.

I am grateful to Dr. Gijs de Rijk for welcoming me in the MDT section at CERN and teaching me the art of magnet design, Dutch money management and lots of embarrassing jokes. Thank you Gijs, for your patience (also in reading this thesis), spirit and wisdom.

I also wish to thank Dr. Manuela Cirilli for the teachings, the financial (and moral) supports as well as for the long coffees and talks. Grazie Manu, per il tuo aiuto, per i tuoi consigli e per la tua pazienza.

I have an eternal debt with Prof. Ugo Amaldi who made me discover the world of hadron therapy and tried to make a physicist out of me. Grazie Professore, per la sua instancabile e contagiosa voglia di fare, e di fare meglio.

Thanks to Alexander, Stefano and Vittorio for guiding me through the land of beam optics: may the torch of hadron therapy always shine!

Thanks to Giovanni and Rita for your incredible work, your enthusiasm and your amazing attitude.

Thanks to Alexandre for the extensive discussions and your fundamental help on the GaToroid project.

Thanks to the colleagues of the MDT section, old and new, young and less young, Paolo, Ezio, Glyn, Andrea, Friedrich, Daniel, Jeroen, Douglas, Thomas, Sebastian and Jose for sharing with me your knowledge, time and smile.

Thanks to Ariel for carrying on the work on GaToroid. Bon courage et bonne chance.

Thanks to Juan, Jacky, Francois-Oliver, Pietro, Remy, Sebastien, Nicolas, Lukas, Frederic, Gregory and each and every one of 927 for taking the time to teach me how to do a magnet, for real.

Thanks to Tuukka and Diego for the amazing mechanical design work and for explaining me the basis that I should have already known.

Thanks to Carlo for the technical and philosophical discussions, as well as for the coffees.

Thanks to Davide for the wise advice and the lessons on magnet design.

Thanks to Elena, Simone, Alfredo, Andrea, Marco, Peter, Mikko and everyone involved in the GaToroid carbon ion studies for teaching me what does it mean to put in the same room physicists, engineers and doctors. Thanks to Dr. Sandro Rossi and Dr. Marco Pullia that, nevertheless, welcomed me in the CNAO adventure.

Thanks to Prof. Marco Breschi for this decade of intense and fruitful collaboration.

Thanks to Laura, Giovanni and Jerome: you really taught me a lot. May your future be more and more brilliant.

Thank you to the Charly's friends, Letizia, Daniele, Eleonora, Flavio, Marco e Stefano for sharing countless beers and stories, as well as these beautiful years.

Matteo, Vittorio e Mattia. A voi soprattutto. Garzie. Enrico Felcini. D. L.

Thanks to Nicolò for your tireless support. It was a pleasure to share the doctoral student path with you.

Thanks to Dario, Marco and Fabrizio for sharing lunches, coffees and friendship.

Thanks to the friends and collegues of Hop Suisse: Alex, Max, Maelle, Catta, Al, Chris, Nora, Vera, Victor, Iole, Jaime, Gilles, Emma, and Christian.

Alla mia cara Beatrice, meravigliosa compagna ed insostituibile supporto, grazie di cuore per aver attraversato con me questa folle avventura con il tuo irriducibile coraggio ed il tuo fantastico sorriso.

Infine, un ringraziamento speciale ai miei genitori, Anna Rosa ed Oldano, che mi hanno instancabilmente supportato in ogni mia scelta. Grazie di avermi dato la forza di guardare sempre avanti ed il coraggio di puntare ogni giorno più in alto. Grazie a Pablo, mi hermano, che nonostante la distanza è sempre stato un punto di riferimento ed un sostegno; anche a te devo quello che sono oggi.

Abstract

Hadron therapy refers to a medical treatment technique that uses hadron beams (i.e. protons and ions) to deliver localized energy that suppresses cancerous cells, sparing the neighbouring healthy tissues from unwanted radiation. The major technical components of a hadron therapy centre are the particle accelerator (cyclotron, synchrotron, or linac) and the beam delivery system that controls, shapes and orients the particles towards the area to be treated. The beam delivery can consist of fixed transfer lines, or it can include a gantry, a transfer line that rotates around the patient and allows radiation from multiple directions.

The present work investigates a new toroidal gantry for hadron therapy, named *GaToroid*. This novel gantry configuration allows the dose delivery from a discrete number of angles avoiding magnets as well as patient rotation. Compared to traditional gantries that require rotating magnets, this improvement is made possible by a toroidal magnet operating in steady-state. This design constitutes the ideal conditions for the use of superconductors to generate a significantly higher magnetic field compared to normal-conducting solutions, as well as to reduce the weight and footprint of the magnets.

The study of a GaToroid system requires the integration of several aspects of physics and engineering. In this framework, the focus of this research is on the design of the superconducting coils integrated with beam optics and particle tracking analyses.

The first part of the thesis illustrates the optimization of the toroidal magnet. Coupling two-dimensional particle tracking and magnetic field calculations, an algorithm was developed to identify optimal gantry configurations that maximize the energy acceptance of the system. Two solutions composed of 16 coils, differing in high and low values of engineering current density, were investigated. In line with current clinical requirements, the beams converged at the isocenter within 1 mm over the whole treatment energy spectrum for both configurations.

The second part of the thesis describes the algorithm implemented for the two- and three-dimensional particle tracking. Building upon the results of the magnetic optimization, a linear beam optics formalism was developed to determine the focusing properties of GaToroid.

The third part of the thesis focuses on the engineering design of the low current density solution. Using two thermo-electric models, lumped and one-dimensional, the Nb-Ti and ReBCO cable geometries were validated, together with the quench protection

system. Furthermore, analytical and numerical studies on mechanics made it possible to estimate the overall footprint and weight of the system. Results show that, compared with the state-of-the-art gantries, the proposed GaToroid solution has the potential to be more compact and lighter by at least a factor two.

Finally, the last part of the thesis describes the design of a scaled-down demonstrator wound with ReBCO tapes. Studies on quench protection, mechanics and experimental implementation aimed at testing the use of ReBCO technology for GaToroid coils are discussed.

In conclusion, this work presents the first overall description of a GaToroid system, ranging from the analytical definition, magnetic optimization, particle tracking and magnet engineering. The investigation of this new toroidal paradigm for gantries represents a quantum step toward more compact and less expensive solutions for hadron therapy centres.

Keywords: Hadron therapy; Gantry; Toroidal magnet; Superconducting magnet; Beam optics; High temperature superconductors

Sintesi

Il termine *adroterapia* si riferisce ad un tipo di trattamento medico oncologico che utilizza raggi di adroni (protoni e ioni) per sopprimere le cellule cancerogene, risparmiando i vicini tessuti sani da radiazioni indesiderate. Le principali componenti tecnologiche di un centro di adronterapia sono l'acceleratore di particelle (ciclotrone, sincrotrone o linac) e le linee di trasferimento, che controllano, modellano e orientano il fascio di particelle verso l'area da trattare. Quest'ultime possono essere fisse, oppure possono includere una gantry, cioè una linea di trasferimento che ruota intorno al paziente consentendo l' irraggiamento da più direzioni.

Il lavoro presentato in questa tesi si pone l'obiettivo di indagare un nuovo concetto di gantry, chiamato *GaToroid*. A differenza delle gantries tradizionali, Gatoroid consente l'irraggiamento del tumore da un numero discreto di angoli, evitando sia la rotazione dei magneti, che quella del paziente. Questo tipo di miglioramento è reso possible dalla presenza di un magnete toroidale che, operando in stato stazionario, crea le condizioni ideali per l'uso di superconduttori. Questi ultimi, infatti, sono in grado di generare un campo magnetico significativamente più elevato rispetto ai materiali normal conduttori, consentendo di ridurre sia peso che ingombro dei magneti.

L'analisi e lo sviluppo di GaToroid richiedono l'integrazione di diversi principi di fisica ed ingegneria. In questo contesto, gli studi descritti nella tesi integrano aspetti di ingegnerizzazione dei magneti superconduttori insieme ad aspetti di fisica dei fasci di particelle.

La prima parte della tesi illustra il processo di ottimizzazione magnetica. Accoppiando le simulazioni di tracciamento di particelle assieme a quelle per il calcolo dei campi magnetici, è stato possibile massimizzare l'accettanza in energia della gantry. Due soluzioni sono state analizzate nel dettaglio: entrambe composte da 16 bobine, si differenziano per densità di corrente e per tecnologia dei superconduttori.

La seconda parte della tesi descrive l'algoritmo implementato per il tracciamento di particelle, sia nel caso bidimensionale che tridimensionale. Sulla base dei risultati dell'ottimizzazione magnetica, è stato sviluppato un formalismo per studiare l'ottica del fascio all'interno di GaToroid.

La terza parte della tesi si concentra sulla progettazione ingegneristica della configurazione a bassa densità di corrente. Utilizzando circuiti elettrici a parametri concentrati e modelli monodimensionali, le geoemtrie dei cavi in Nb-Ti e ReBCO sono state validate. In aggiunta, analisi meccaniche del sistema hanno permesso di stimare

l'ingombro ed il peso complessivi della macchina. I risultati mostrano che GaToroid potrebbe risultare più compatto e leggero di almeno un fattore due rispetto ai gantries tradizionali.

Infine, l'ultima parte della tesi descrive la prototipizzazione di un magnete in scala ridotta realizzato in HTS, concentrandosi sulla protezione da quench, la meccanica e l'implementazione sperimentale.

In conclusione, questa tesi fornisce per la prima volta una descrizione completa del sistema GaToroid, passando dalla definizione analitica, all'ottimizzazione magnetica, fino all'ottica delle particelle e all'ingegneria dei magneti. Lo studio passato, presente e futuro di questa nuova configurazione toroidale per gantries rappresenta un progresso sostanziale e concreto verso soluzioni più compatte e meno costose per i centri di adroterapia.

Keywords: Adroterapia; Gantry; Magneti toroidali; Magneti superconduttivi; Ottica di fascio; Superconduttori ad alta temperatura

Contents

List of Figures

List of Tables

Acronyms

AG-CCT Alternating Gradient Canted Cosine Theta

BNL Brookhaven National Laboratory (US)

BSCCO Bismuth Strontium Calcium Copper Oxide

CCT Canted Cosine Theta

CERN European Council for Nuclear Research

CNAO Centre for Oncological Hadrontherapy (IT)

CTD101 A Type of Impregnation Resin

CTE Coefficient of Thermal Expansion

EuCARD European Coordination for Accelerator Research and Development

FEA Finite Element Analysis

GFR Good Field Region

HiLumi High Luminosity LHC

HIMAC Heavy Ion Medic al Accelerator in Chiba (JP)

HIT Heidelberg Ion-beam Therapy centre (DE)

HTS High Temperature Superconductors

IMPT Intensity Modulated Proton Therapy

LBNL Lawrence Berkeley National Laboratory (US)

LHC Large Hadron Collider

LTS Low Temperature Superconductors

MB Main Dipole

MCBX Inner Triplet Orbit Corrector

MIT Massachusetts Institute of Technology (US)

MLI Multilayer Insulation

MMF MagnetoMotive Force

MQE Minimum Quench Energy

MQE Minimum Quench Energy

MRI Magnetic Resonance Imaging

MY750 A Type of Impregnation Resin

NI Non Insulated

NIRS National Institute of Radiological Science (JP)

NMR Nuclear Magnetic Resonance

FFAG Fixed Field Alternating Gradient

PCB Printed Circuit Board

PIMMS Proton Ion Medical Machine Study

PSI Paul Scherrer Institute (CH)

PTCOG Particle Therapy Co-Operative Group

RBE Relative Biological Effectiveness

ReBCO Rare-earth Barium Copper Oxide

RMC Racetrack Model Coil

RRR Residual Resistance Ratio

SAD Source-to-Axe Distance

SHI Sumitomo Heavy Industries (JP)

SS Stainless Steel

TERA Therapy with Hadronic Radiations

TuLiP Turning Linac for Protontherapy

List of Symbols

A	$[m^2]$	Cross-section
B	$[T]$	Magnetic Flux Density
$(B\rho)$	$[Tm]$	Beam Rigidity
$B_{\theta min}$	$[T]$	Minimum Toroidal Magnetic Flux Density
$B_{\theta p}$	$[T]$	Peak Toroidal Magnetic Flux Density
B_p	$[T]$	Peak Magnetic Flux Density
B_0	$[T]$	Ideal and Uniform Toroidal Magnetic Flux Density
BdL	$[Tm]$	Integral of Magnetic Flux Density along the Particle Trajectory
c	$[m/s]$	Speed of Light
Cp_{eq}	$[J/KgK]$	Equivalent Heat Capacity
D_{eq}	$[Kg/m^3]$	Equivalent Volumetric Density
E_{tot}	$[MeV]$	Particle Total Energy
E_0	$[V/m]$	Threshold Electric Field
E_0	$[MeV]$	Particle Rest Energy
f	$[N/m^3]$	Force Density
F_θ	$[N]$	Fault Force
F_c	$[N]$	Centring Force
H	$[A/m]$	Magnetic Field
I	$[A]$	Current
I_{nc}	$[A]$	Current in the Normal-Conducting part of the cable
I_{sc}	$[A]$	Current in the Superconducting part of the cable
J	$[A/m^2]$	Current Density
J_{en}	$[A/m^2]$	Engineering Current Density
J_{op}	$[A/m^2]$	Operating Current Density
J_c	$[A/m^2]$	Critical Current Density
K	$[MeV]$	Particle Kinetic Energy
k	$[T/m]$	Quadrupole Gradient
L	$[H]$	Inductance
l_c	$[m]$	Length of the Bucking Cylinder
l_i	$[m]$	Length of the Inter-Coil Structure
m	$[g]$	Particle Mass
$\mathbf{M}$		Linear Transfer Matrix

N		Number of Coils
$N_{particles}$		Number of Simulated Particles
NI	$[At]$	Magnetomotive Force
P	$[MPa]$	Contact Pressure
p	$[MeV]$	Particle Momentum
P_c	$[m]$	Zero-Torque F_c application point
q	$[C]$	Particle Charge
Q_J	$[W]$	Power generated due ot the Joule Effect
R_{in}	$[m]$	Internal Radius of the Torus
R_{nc}	$[\Omega]$	Resistance of the Normal-Conducting part of the cable
R_{sc}	$[\Omega]$	Resistance of the Superconducting part of the cable
R_d	$[\Omega]$	Dump Resistance
s	$[m]$	Beam Orbit
T	$[Nm]$	Torque
T_{op}	$[K]$	Operating Temperature
t_c	$[m]$	Thickness of the Bucking Cylinder
t_i	$[m]$	Thickness of the Inter-Coil Structure
v	$[m/s]$	Particle Velocity
V_{max}	$[V]$	Maximum Voltage on the Dump Resistor
$\mathbf{X}$		Vector of beam position (x, y) and derivatives (x', y')
z_v	$[m]$	Vector Magnet Position on the Torus Axis
(z, y, x)	$[(m, m, m)]$	Co-Moving Beam Reference System
$(\mathbb{Z}, \mathbb{R}, \mathbb{X})$	$[(m, m, m)]$	GlobalReferenceSystem
α		Gradient of Beta Function
α_E	$[rad.]$	Vector Angle
β	$[m]$	Beta Function
$\Delta p/p$		Momentum Spread
γ	$[1/m]$	Optical Function of the Beam
γ_L		Lorentz Factor
λ		Relative error between tracked and matrix calculated particles
μ_0	$[H/m]$	Vacuum Permeability
ρ_{eq}	$[\Omega m]$	Equivalent Electrical Resistivity
ρ_E	$[m]$	Particle Radius of Curvature
σ_θ	$[MPa]$	Inter-coil Stress
σ_{VM}	$[MPa]$	Von-Mises Equivalent Stress
σ_c	$[MPa]$	Cylindrical Hoop Stress

σ_c	$[MPa]$	Cylindrical Hoop Stress
τ	$[MPa]$	Shear Stress
τ_c	$[s]$	Characteristic discharge time
θ	$[rad.]$	Azimuthal Angle
ε	$[mm\ mrad\ ]$	Beam Emittance

Introduction 1

"The ideal subject of radiotherapy for an engineer
is a homogeneous, perfectly rigid and immobile patient...
alas, this is not a very interesting subject for a practising physician"

Luca Bottura, KT Seminar on Medical Applications, CERN, 2018

In this first chapter, an overview of the general concepts of hadron therapy is provided, underlining the main challenges and the current situation in terms of clinical centre features. Furthermore, a description of the state of the art of operational gantries for both protons and carbon ions is presented, comparing the different solutions developed over the years. Finally, an analysis of gantry concepts under development is presented.

1.1 Hadron Therapy

Hadron therapy refers to a medical technique that uses hadron* beams, *i.e.* protons and ions, for cancer treatment. This kind of therapy benefits from the localised energy deposition of hadrons, the Bragg peak, to suppresses cancerous cells, sparing the neighbouring healthy tissues from unwanted radiation.

This is possible because tumour cells are generally more sensitive to ionizing radiations if compared to healthy cells, phenomenon that can be attributed to the more rapid proliferation of the tumour cells.

To quantify the biological effects of ionizing radiations on living cells, the Relative Biological Effectiveness (RBE) is commonly used. The RBE is the ratio between the absorbed dose of a reference photon (Co60 2 MeV) and the absorbed dose of the particle of interest, used to generate the same biological effect. Higher RBE correspond to higher effectiveness of the radiation. Protons have similar a RBE as x-rays but, thanks of the Bragg peak, can sensibly reduce side effects. Carbon ions have instead a RBE 3-4 times larger than photons, and therefore can be used to treat *radioresistant* tumours [1] [2].

The medical use of protons was firstly prosed by Robert R. Wilson in 1946 [3], and implemented already in 1954 at the Lawrence Berkeley National Laboratory (LBNL,

*hadron (from Greek hadroś, "stout, thick, strong") is a subatomic particle composed by quarks

US). After four decades, in 1991, the first clinical proton therapy facility became operational in Loma Linda (US)[4]. Following the success of treatments with protons, LBNL proceeded with studies on ions and, in 1977, the first patient was treated with a carbon beam [5]. After almost twenty years and two thousand patients, Berkeley passed the *baton* to the National Institute of Radiological Science (NIRS, JP) where the first heavy-ions accelerator in the world, HIMAC (Heavy Ion Medic al Accelerator in Chiba), started clinical applications in 1994 [6][7].

Nowadays, hadron therapy is a solid reality and a concrete treatment possibility for thousands of patients all over the world. The scientific effort and the continuous collaboration between physicists, engineers and physicians* allowed the establishment and the continuous improvement of this type of radiation therapy. It was estimated that at the end of 2018 more than two hundred fifty thousand patients (cumulative) were treated with protons and heavy ions [8]. The trend is shown in *Fig.1.1* and provides a clear view of the continuous growth of this therapy in terms of clinical applications and technology development.

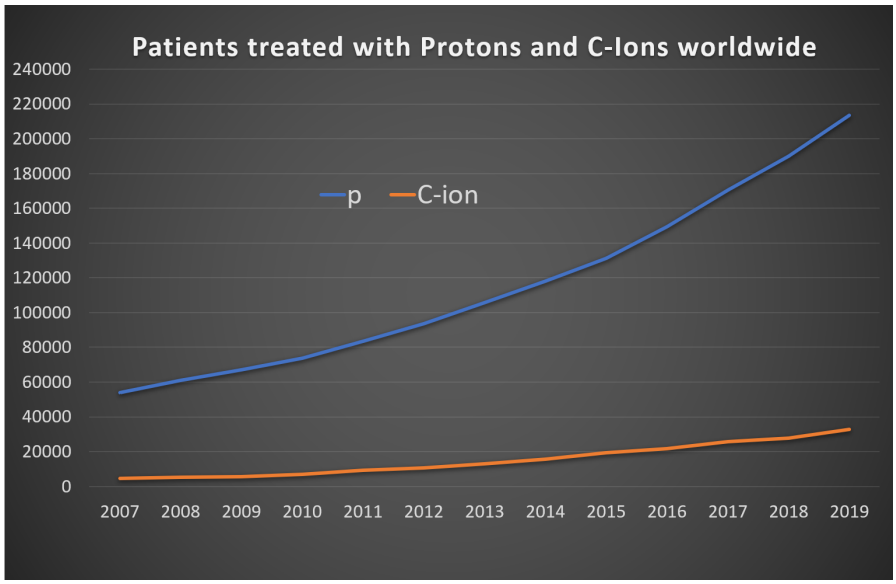

Figure 1.1 *Patients treated with protons and carbon ions worldwide by the end of 2018. [8]*

The major technical components of a hadron therapy centre are the particle accelerator and the beam delivery system. The accelerator is used to produce beams in a suitable range of kinetic energies, *i.e.* from 70 MeV to 250 MeV for protons and from 120 MeV/u to 430 MeV/u† for carbon ions. Different energies are required to modify the depth of the Bragg peak (*range*), therefore to deposit the energy in a shallower or deeper location inside the human body.

*as well as technicians, nurses and all the clinical operators!

†Kinetic energy per nucleon

The beam delivery system is used to control, shape and orient the particles towards the area to be treated. It consists either of fixed or rotating transfer lines; rotating transfer lines are named *gantries*. A gantry is usually mounted on a large mechanical structure that rotates around the patient and allows irradiation from multiple directions. For this reason, a gantry is considered a superior mean of beam delivery, because of the higher treatment flexibility and the related reduction of unwanted parasitic dose to healthy tissues, derived from ability to select appropriate treatment angles.

Because of these structures, hadron therapy centres, especially those based on ion beams, tend to be relatively large, complex and costly installations. This is why, in spite of the potential benefits [9] [1], the diffusion of this medical technology is still limited. To give a good scale of the unexploited potential, it has been estimated that the optimal number of treatment rooms over the coming ten years for a population of ten million people would be as much as seven for treatments based on protons, and one for treatments based on ions [10]. Considering the European population, this would sum to hundreds of installations: around five hundred rooms for protons and seventy rooms for carbon ions. Yet, only 28 hadron therapy centres, of which 4 using ions, are currently operating and treating patients in Europe [8].

As reported by the Particle Therapy Co-Operative Group (PTCOG), in 2020 it is possible to count 98 hadron therapy centres worldwide, while other 37 new facilities are under construction [8]. *Fig.1.2* presents the distribution of the centres in terms of particles and beam transfer technology. The great majority (90%) operates only with protons, due to the simpler and cheaper required technology. The remaining part of this facility can either use C-ions in conjunction with protons (half-blue half-red in *Fig.1.2*) or just carbon. The proportion is similar for the centres under development, where the possibility of carbon ions treatments is still limited in the order of 10%. This proportion is coherent with the aforementioned estimation, where the ideal ratio is considered one C-ions every seven proton treatment rooms [10].

Regarding the transfer lines, 85% of the operating centrers has opted for the use of gantries, either in combination with fixed beam lines (half-blue half-red in *Fig.1.2*) or as the only solution. This percentage underlines how the gantries are considered by the community a relevant assets for the treatment quality. However, the complexity of the technology, as well as the high capital cost, prevents the spreading of gantries for carbon ions, limited to just two installations without other implementation foreseen in the near future (five years).

Given the overall numbers, it is clear that finding solutions to reduce size, complexity and cost of accelerators and beam delivery systems would result in significant social and economic impact. In this context, several initiatives, past, present and future, have been dedicated to reducing the size and cost of accelerators and beam delivery systems [11][12], key elements and cost drivers of a hadron therapy centre [13]. This thesis

is part of this framework, focusing on the development of a novel concept of toroidal gantry.

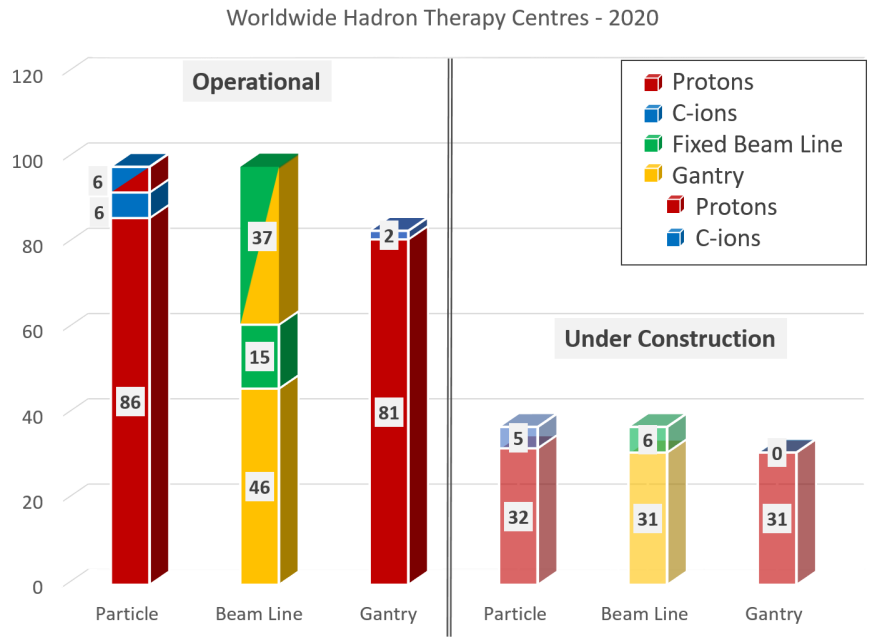

Figure 1.2 *Number and distribution of worldwide hadron therapy centres. Elaboration from PTCOG (Particle Therapy Co-Operative Group) data updated in May 2020 [8]*

1.2 Hadron Therapy Gantries

The last three decades have seen the development of several gantry concepts that, as depicted in *Fig.1.3*, can be classified on the basis of the delivery system topology and its relative movement with respect to the patient [14] [15].

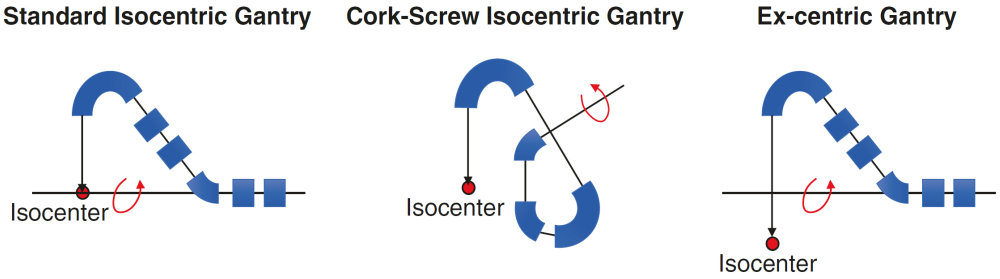

Figure 1.3 *Schematic representation of gantry layout types [15]*

The great majority of the gantries currently in operation are *isocentric* machines: the beam delivery system rotates around the isocenter, where the tumour is located, and the patient generally is fixed in space. A subset of isocentric configurations is represented by

Cork-Screw gantries, where the price to pay to reduce the length is a total bending angle exceeding 360°. Aiming to a further footprint reduction, in *ex-centric* configurations the gantry rotation axis is not coincident with the patient location. Up to these days, only one ex-centric gantry has been built, and it was operational until 2018 at the Paul Scherrer Institute (PSI, CH). It is worth pointing out that also in isocentric gantries, the patient can be shifted from the nominal axis to perform non-isocentric treatments. As illustrated by Pedroni [16], in the history of hadron therapy gantries, among the extraordinary technological challenges and the engineering feats, it is possible to identify a few milestones:

- 1991 - Loma Linda University, California (US): the first hospital-based proton therapy facility and first known use of gantries (Corkscrew)
- 1992 - Paul Scherrer Institute, Villigen (CH): the first pencil beam scanning gantry (Ex-centric). First patient treated 1996
- 1998 - National Cancer Centre, Kashiwa (JP): the first commercial gantry (Isocentric) developed by SHI (Sumitomo Heavy Industries) in collaboration with IBA [17]
- 2008 - M. D. Anderson Hospital, Texas (US): first commercial scanning system delivered by Hitachi
- 2008 - Heidelberg Ion-Beam Therapy, Heidelberg (DE): first gantry for carbon ions therapy (Isocentric). First patient treated 2012
- 2015 - Heavy-Ions Medical Accelerator in Chiba, Chiba (JP): first superconducting gantry for carbon ions therapy (Isocentric). First patient treated 2017 *

On the one hand, to these days the technology related to proton therapy gantries can be considered mature, counting dozens of installations worldwide and several companies able to commercialise specific solutions. The main examples of this proton gantries are described in *Sec.1.2.1*, providing a comparison in terms of features, footprint and weight. On the other hand, the development of carbon ions gantries is still in its early phase and the only two machines in operation are the magnificent result of specialised research centres, as illustrated in *Sec.1.2.2*. However, several new configurations were proposed and are actually under study. The scientific community is pushing toward size, weight and cost reduction, aiming for a widespread diffusion of heavy ions gantries in the next decades. Examples of novel gantry concepts under investigation are reported in *Sec.1.2.3* and *Sec.1.2.4*.

*this point was added by the author since happened after the Pedroni's presentation of 2010 [16]

1.2.1 Operating Gantries for Proton

The information regarding commercial proton therapy systems was collected from scientific papers, public presentations, commercial brochures and companies' websites. However, the details concerning accelerator and gantries are very sensitive data and are often not publicly available. For a comprehensive comparison between the gantries, when it was reasonably possible, some of these values were estimated by the author through technical drawings or simple calculations. These estimations are explicitly reported in the text.

ProBeam (Varian, US)

The Varian ProBeam system uses a Nb-Ti superconducting isochronous cyclotron able to accelerate the particles up to 250MeV [18]. The footprint of a single room facility is approximately 420 square metres [19]. The proton beam is guided from the accelerator into the treatment room with a transfer line, where a degrader system able to modulate the energy from $70 - 230$ MeV is located. At the end of the transfer line, the gantry and the scanning system are placed as exhibited in *Fig.1.4*. The Varian ProBeam system installed at PSI (Gantry3) is characterised by a diameter of 10.5 metres, a length of about 10 metres, a total weight 270 tons, and rotates by $\pm 190°$[20].

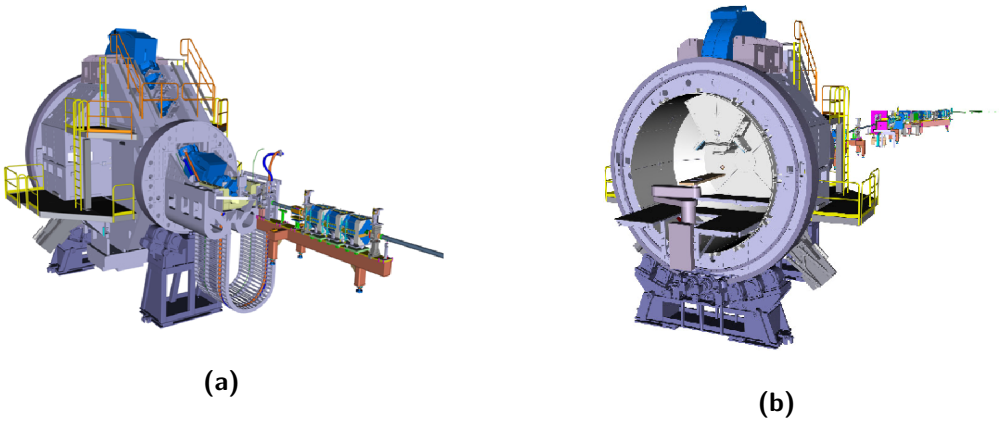

(a) **(b)**

Figure 1.4 *Rear* ***(a)*** *and front* ***(b)*** *view of Varian ProBeam gantry installed at PSI [20]*

ProteusOne (IBA, BE)

The IBA ProteusOne is based on a Nb-Ti superconducting synchrocyclotron: S2C2 [21]. With a yoke radius of 1.25 m, 50 tons of weight and 5.7 T of peak magnetic flux density, the synchrocyclotron can accelerate the particles up to 230 MeV. The system has a footprint of 140 (7.3 m x 19 m) square metres and, including the shielding of the structure, it occupies an area of more than 360 square metres [22]. As shown in *Fig.1.5*, the gantry is composed of 7 quadrupoles (2 standard, 2 reduced and 1 long) and 3 dipole magnets (of 40°, 70°and 60°), for a total length of 9.5 metres and 110 tons of weight [23]. Two separate scanning magnets are placed upstream of the last dipole, in order to guarantee a proper value of SAD (source to axis distance) with the reduced radius. This implies a larger gap value of the last dipole, that must be able to handle the beam, deflected at different angles by the scanning system. The gantry proposed by IBA can rotate by 220°, with a radius of 3.6 m [24]: 30% smaller than the IBA 360 degree gantry.

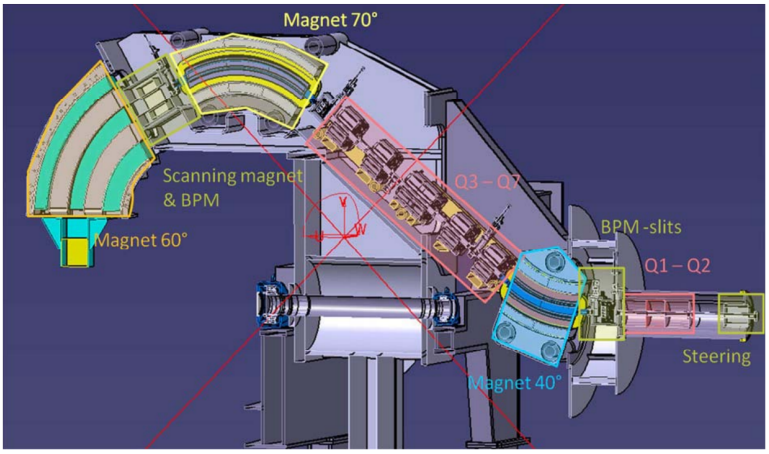

Figure 1.5 *The IBA's ProteusOne Gantry [21]*

Radiance 330 (ProTom, US)

Radiance 330 uses a synchrotron of 5 metres of diameter to accelerate the particles up to 330 MeV [25] [26]. The choice of synchrotron allows to select the desired energy without the introduction of a degrader, reducing the residual radioactivity and the required shielding. ProTom uses the concept of *half-gantry* that covers only 180°* of treatment range. The single-room facility is compact and the footprint is claimed to be similar to the one of the conventional radiation therapy. Precise values of the system dimensions, as well as for the radius of the gantry are not available for the public. Based on the diameter of the synchrotron, the footprint of the single-room facility and the gantry were estimated as presented in *Fig.1.6*. The total footprint, including the shielding is around 380 square metres, while the radius of the gantry is about 4 metres.

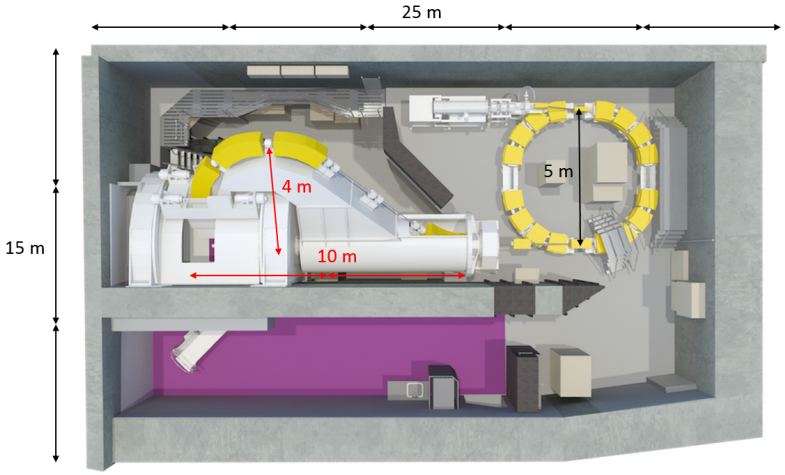

Figure 1.6 *Footprint ProTom Radiance 330. The dimensions of the room are estimated by the diameter of the synchrotron (16 feet ≃ 5 metres) [25]*

*Given the proton low entrance dose, some experts consider the use of many different angles (IMRT-like) not necessary

S250i (Mevion, US)

The Mevion S250i is the only operating system with a particle accelerator mounted directly on a rotating structure [27][28]. It is based on a superconducting synchrocyclotron installed on an isocentric gantry, that can rotate by 190°. From the accelerator, the proton beam goes through the nozzle directly to the patient without using quadrupoles or bending magnets. This solution greatly reduces costs and footprint, but complicates the spot scanning technique and may give unwanted neutron doses to the patient. The 17 tons synchrocyclotron, developed in collaboration with the Massachusetts Institute of Technology (MIT, US), is composed of Nb_3Sn coils maintained at 4 K during the operation, with a maximum magnetic flux density of 8.5 T, able to reach 250 MeV of proton kinetic energy. The absence of transfer line from the accelerator to the patient results in a small footprint of 140-180 m^2 (11.3 m x 9.8 m x 8.5 m), as depicted in *Fig.1.7* [29]. From this figure, the radius of the gantry was estimated as 4.2 metres. Mevion has also introduced the Intensity Modulated Proton Therapy (IMPT) with the HyperScan system, where the energy modulation occurs just before the nozzle. However this approach is characterized by a limited distance between the devices and patient, who can be exposed to the secondary dose of neutrons (and disagreeable noise due to the energy modulation).

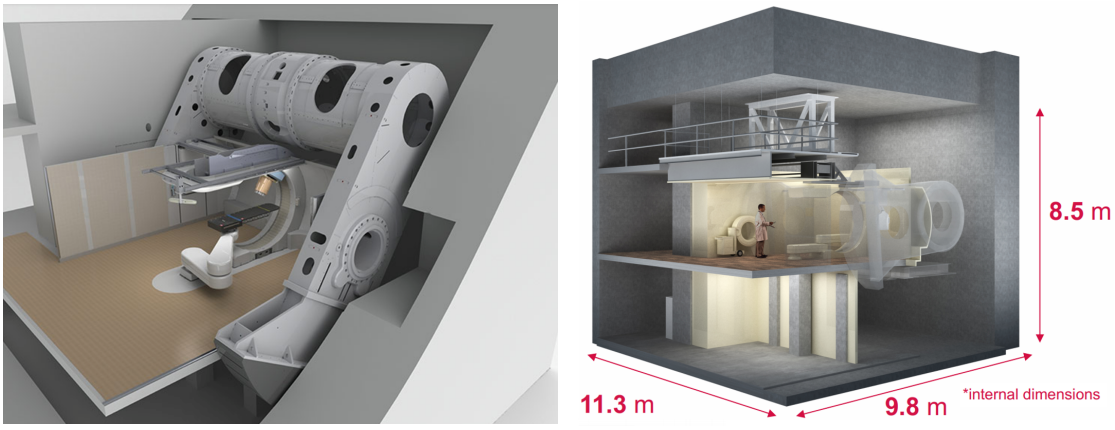

Figure 1.7 *Mevion S250 proton therapy system* ***(a)*** *and a view with the single room facility dimensions* ***(b)*** *[28][29]*

SC360 Gantry (ProNova, US)

ProNova proposes the SC360 two-room solution with a superconducting cyclotron and two superconducting 360°gantries. The footprint, including the shielding, is 30 m x 19 m, equivalent to 570 square metres [30]. The gantry is composed of superconducting magnets capable of ramping from 2 T (at 70 MeV) to 4 T (at 230 MeV) in about 1 min. As described in *Fig.1.8*, it is made of two bending sections of 60°and 150°, each one containing two superconducting dipoles with a superconducting quadrupole triplet in between. The bending sections have been designed in order to be locally achromatic. The gantry height is 4 metres and its length is almost 5 metres, for a total weight of about 25 tons. A combined function scanning magnet at a distance of about 2 metres from isocentre is used to deflect the proton and create a scanning area of 25 cm x 25 cm.

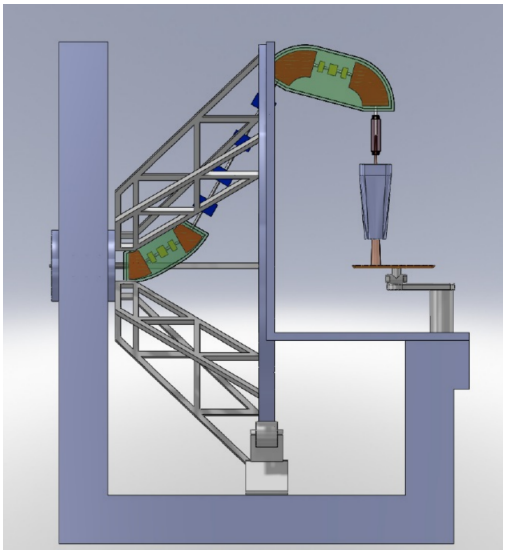

Figure 1.8 *ProNova SC360 gantry [30]*

Hitachi Gantries (JP)

Building upon the experience of the hadron therapy centres of Tskukuba and Nagoya, Hitachi has developed a 360°gantry with 4 metres of radius, 8 metres of (estimated) length and 125 tons of weight, as illustrated in *Fig.1.9* [31]. The footprint of the accelerator and gantry complex can be estimated around 330 square metres, without the shielding. The particles are accelerated up to 220 MeV with a synchrotron of about 5 metres, preceded by an injector linac and a microwave ion source. Hitachi proposes a wide range of transfer line possibilities, including a half-gantry design, with a rotation of 180°. This configuration implies a reduction of the footprint and, combined with robotics couch, high degrees of freedom for patient positioning.

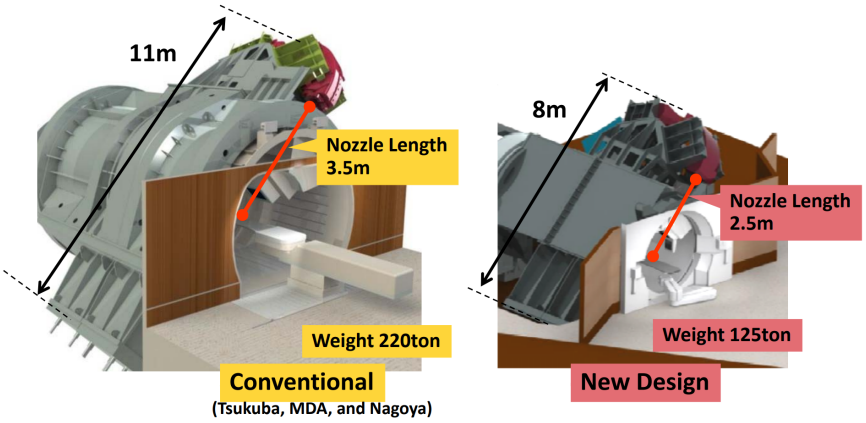

Figure 1.9 *Design of the conventional and the new Hitachi gantries [31]*

SHI Gantries (JP)

Sumitomo Heavy Industries (SHI) continues its research and development programme proposing a 360°gantry in Corkscrew configuration and an associated vertical single room facility based on a cyclotron [15][32] . The geometry of the gantry results in a compact length of 4.6 m and an estimated radius of 4.5 m. The single room facility has a footprint of 16 m x 20 m.

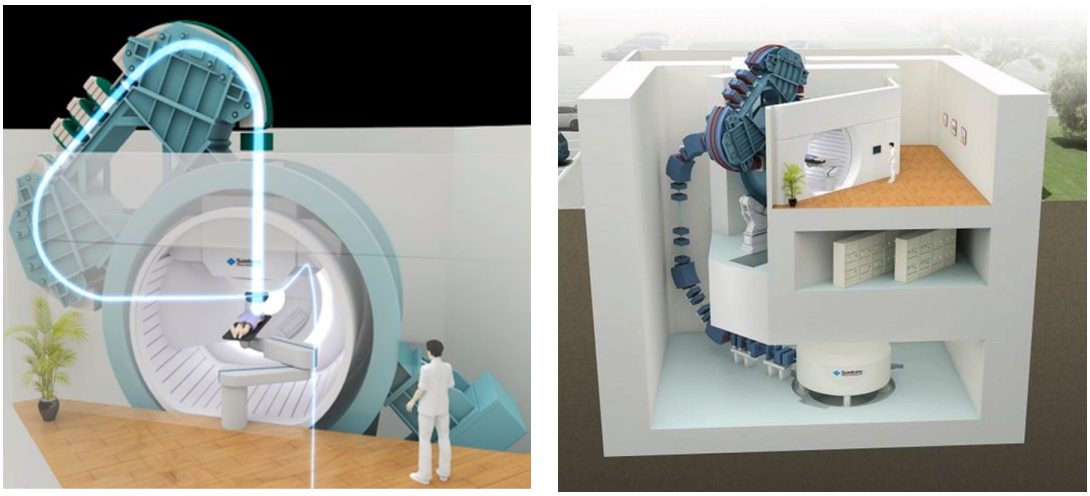

(a) **(b)**

Figure 1.10 *Representation of the Sumitomo gantry with the beam path* ***(a)*** *and in the associated vertical single room facility* ***(b)*** *[32]*

PSI Gantries (CH)

Paul Scherrer Institute (PSI) has a long history in the field of hadron therapy. Patients with eye tumours have been treated by the OPTIS facility since 1984, while the Gantry 1 is in operation since 1996. Furthermore, in the 1990s the *spot-scanning* technique was developed at PSI [33] and used for the first time in the Gantry 1. Nowadays, PSI can count the COMET superconducting compact cyclotron, 2 gantries and special facility dedicated for treatment of ocular tumours, OPTIS 2.

Gantry 1, shown in *Fig.1.11*, is a system designed in 1991 for protons, based on the experience gained with pion therapy in the 1980s [34]. This gantry was an incredible innovation in the field of hadron therapy, and from 1996 until 2008 it was the only scanning gantry in the world. The ex-centric mounting of the patient table on the gantry front wheel reduces the radius of the system down to 2 metres. After more than 20 years of service and 1300 treated patients, Gantry 1 was eventually shut down in 2018.

Gantry 2, exhibited in *Fig.1.12*, has a total length of 11.6 m and an overall radius of 4.2 m, for a total weight of 200 tons [35] [36]. It is composed of two dipoles of 58°and a third larger dipole of 90°, able to handle the upstream scanning system. Two separate magnets are used for this purpose, able to offer a parallel scanning over a treatment area of 20 cm x 12 cm. 7 quadrupoles are placed along the line to focus the beam, together with several devices for diagnostics and correction. The system is achromatic and the optics is realised in order to have a 1:1 imaging from the coupling point to the isocentre. Differently from Gantry 1, the Gantry 2 is isocentric and the rotation is limited to one-side, from -30°to +180°. The same hardware design of the PSI Gantry 2 was adopted by MedAustron (AT) that adapted the optics to their specific constraints and accelerators [37].

Finally, Gantry 3 is an implementation of the Varian ProBeam Gantry in the existing facilities of the PSI. It became operational in July 2018 with the same treatment capabilities of the Gantry 2 and an enlarged irradiation field of 30 x 40 cm^2. More detailed characteristics are reported in the Varian ProBeam Gantry section and depicted in *Fig.1.4*.

Figure 1.11 *PSI Gantry 1 [34]*

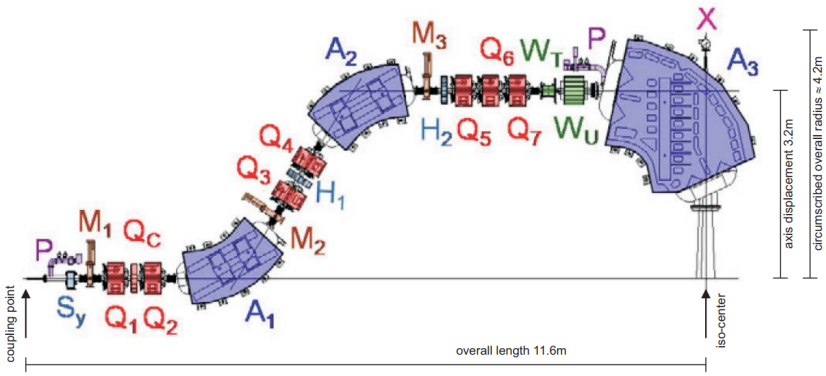

Figure 1.12 *Beam line of the PSI Gantry 2[35]*

1.2.2 Operating Gantries for Carbon Ions

HIT Gantry (DE)

The Heidelberg Ion-Beam Therapy centre (HIT, DE) is the world's first heavy ion treatment facility with a 360°gantry [39]. The centre has three treatment rooms, one of which is dedicated to the carbon ion gantry, used to treat the first patient in 2012. The energy range is between 50 and 430 MeV/u, corresponding to the capability of the synchrotron. The HIT gantry is an impressive device of 25 metres of length, 13 metres of diameter and 670 tons of total weight, of which about 600 tons are rotating parts; *Fig.1.13* allows to better understand the meaning of these values. The layout of the gantry is shown in *Fig.1.14*: two 45°and one 90°dipoles are installed along the gantry structure, while the transverse focusing of the beam is provided by eight quadrupoles. The scanning magnets, placed upstream of the last dipole magnet, allow to irradiate a field of 20 cm x 20 cm and sensibly increase size and weight of the last dipole. The total weight of the described normal-conducting magnets is 145 tons [40]. The rotating structure is installed on two large rings at both ends (so-called *barrel* type structure), that allows a rotation of ±180°.

Figure 1.13 *Picture of the HIT carbon Gantry [38]*

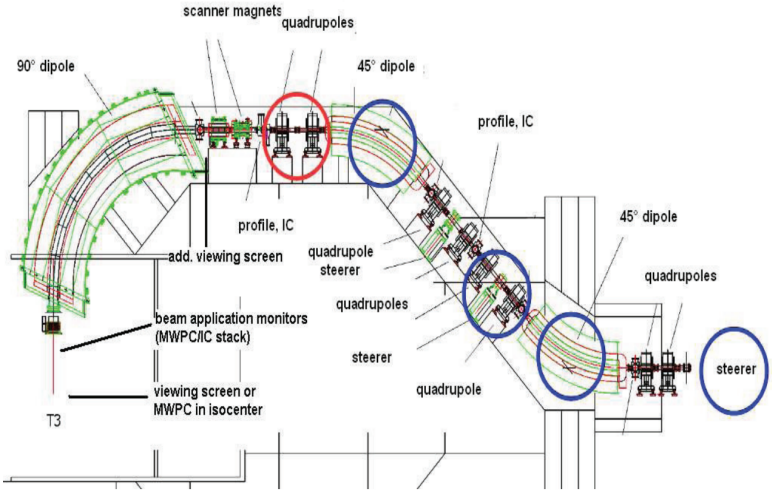

Figure 1.14 *Gantry beam line with beam diagnostic devices. Red circle: final focus setting quadrupoles. Blue circles: final position setting dipoles/steerer [41]*

NIRS Gantry (JP)

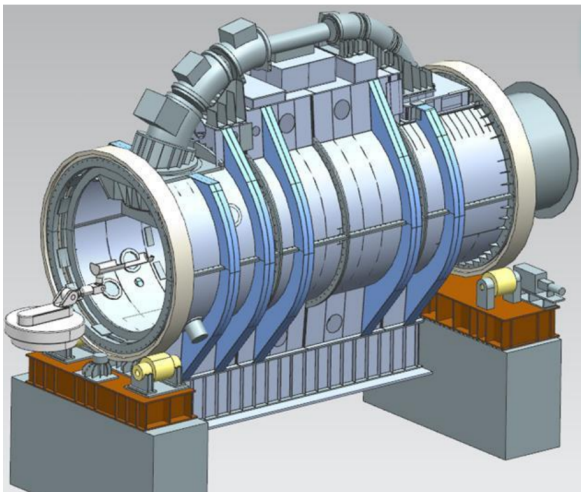

Figure 1.15 *NIRS superconducting gantry [42]*

The National Institute of Radiological Science (NIRS, JP) is the basis of the Heavy Ion Medic al Accelerator in Chiba (HIMAC), which since 1994 treats patients with carbon ions, using fixed beam lines [6][7]. Up to 2016, more than 10 thousand patients have been treated with successful clinical results. In 2015 the construction and the commissioning of the NIRS superconducting rotating gantry were completed. The gantry has a beam orbit radius of 5.5 metres, a length of 13 metres, and it is designed to deliver carbon ions up of energy to 430 MeV/u, accelerated by a synchrotron ring. Thanks to superconducting magnets, the dimensions of the machine are considerably reduced and the total weight is in the order

of 300 tons. The gantry is installed on a barrel structure and can fully rotate within a range of ±180°, as exhibited *Fig.1.15*. The gantry, shown in detail in *Fig.1.16*(a), consists of ten combined functions superconducting magnets (BM1-10) and a pair of scanning magnets (SCM-X and SCM-Y)[43]. The use of combined function superconducting magnets, with a peak magnetic flux density of 2.88 T and a maximum gradient of 9.3 T/m, allows a relevant footprint reduction. These peculiar magnets, shown in *Fig.1.17*, provide both dipole and quadrupole fields and allow to avoid the use of standard quadrupoles along the line. The scan size at the isocentre is approximately 200 mm^2.

A more compact design of the gantry is now under study [44]. As presented in *Fig.1.16*(b), the novel layout is composed by three 90°combined functions magnets with a maximum flux density of 5 T and gradient 15 T/m. The increase of the magnetic field leads a sensible reduction of the machine size that with a 4 meters radius (beam line) and 5 metres in length can be considered comparable to proton therapy gantries.

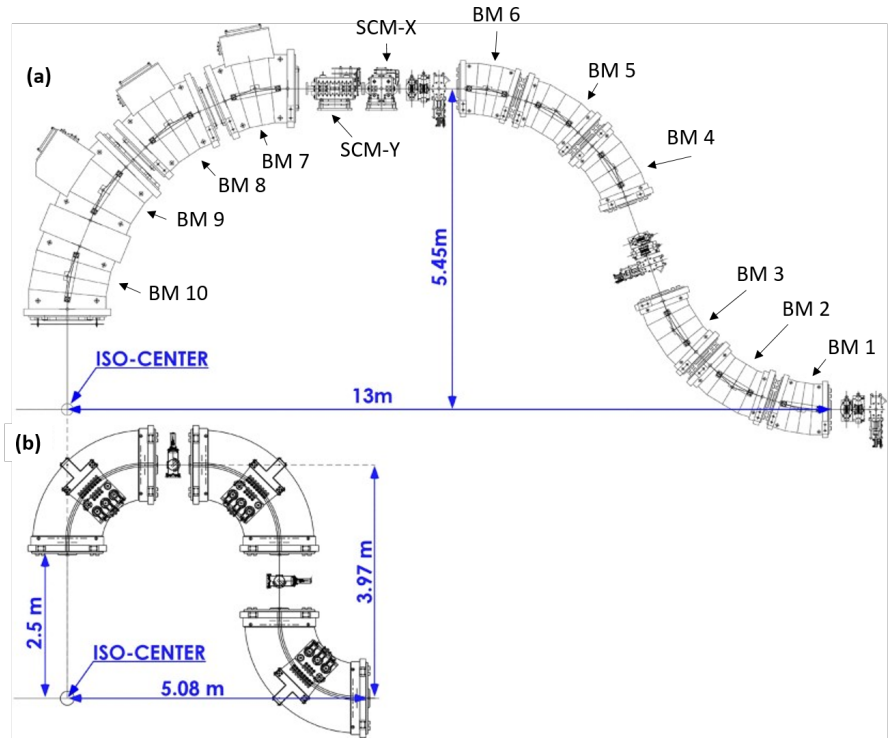

Figure 1.16 *Comparison of gantry layout between* ***(a)*** *the present superconducting gantry, as installed in NIRS, and* ***(b)*** *the new compact superconducting gantry [43][45]*

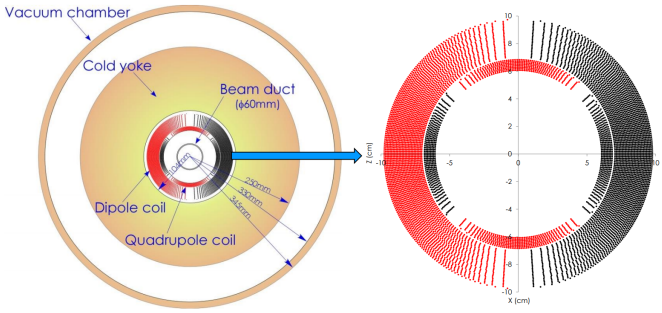

Figure 1.17 *Cross section of NIRS superconducting combined-function magnet [42]*

1.2.3 Gantry Concepts Under Development

TERA Gantries

Several gantry designs have been proposed by the TERA Foundation (TErapia Radiazioni Adroniche, Italian acronym for therapy with hadronic radiations) in the last decades, such as the FASST [46] or the complete AG-CCT based gantry [47]. In this paragraph, the concept of the Turning Linac for Protontherapy (TuLiP) [48] [49] [50], depicted in *Fig.1.18*, is briefly described. The basic idea is somehow similar to the one proposed by Mevion, where the accelerator is part of the gantry and rotates around the patient. In this case, the accelerating structure is a linac (linear accelerator): the low energy part (up to 70 MeV) is fixed the ground, while the high-energy part (up to 250 MeV) rotates. Among the peculiarities of this concept, there is the use of $FeCo$ normal-conducting magnets that allow to reach a field of 1.8 T [51]. This gantry solution results in a radius of 4.6 metres and a length of 12.2 metres from the coupling point. Considering the extra room for the accelerator and the shielding, it results in a single room facility of 22 m x 9 m, with an estimated weight of 70 tons.

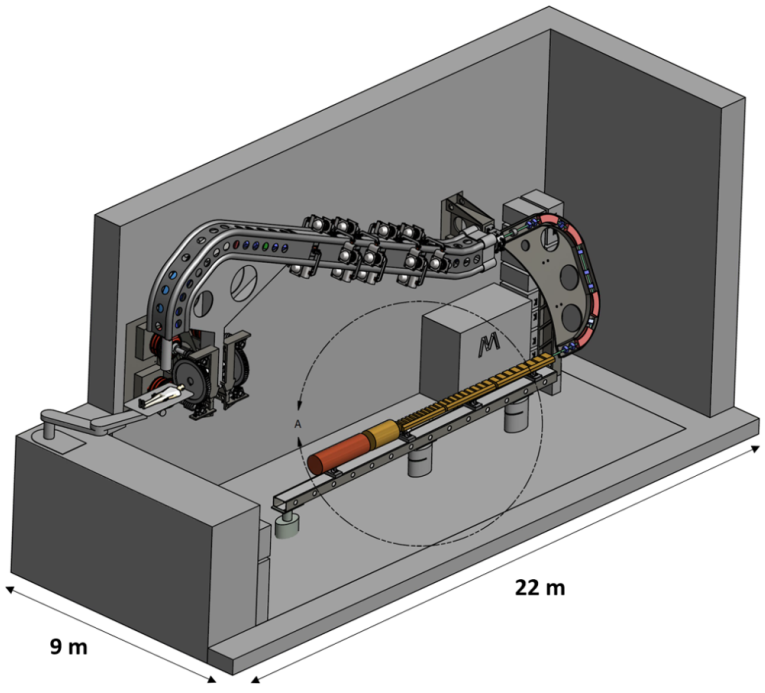

Figure 1.18 *Sketch of TULIP all-linac solution (courtesy of Mohammad Vaziri—TERA Foundation) [49]*

FFAG Gantry

The Brookhaven National Laboratory (BNL, US) proposes the use Fixed Field Alternating Gradient (FFAG) magnets to create a gantry with high momentum acceptance [52]. The dimensions and weight of the structure could be dramatically reduced and the operations would be highly simplified thanks to the large momentum acceptance. With a fixed magnetic field setting, the gantry can operate covering a large momentum acceptance (either 200-400 MeV/u or 100-200 MeV/u), as shown in *Fig.1.19*. The gantry for carbon ions measures 8 m in length and 8.4 m in diameter for a total estimated weight of 1.7 tons (considering just the magnets and not the mechanical structure). A basic *"cell"* is composed of a central magnet that produces major bending and has a linear horizontal defocusing gradient. Two smaller identical but opposite bending magnets are placed on both sides of the central one.

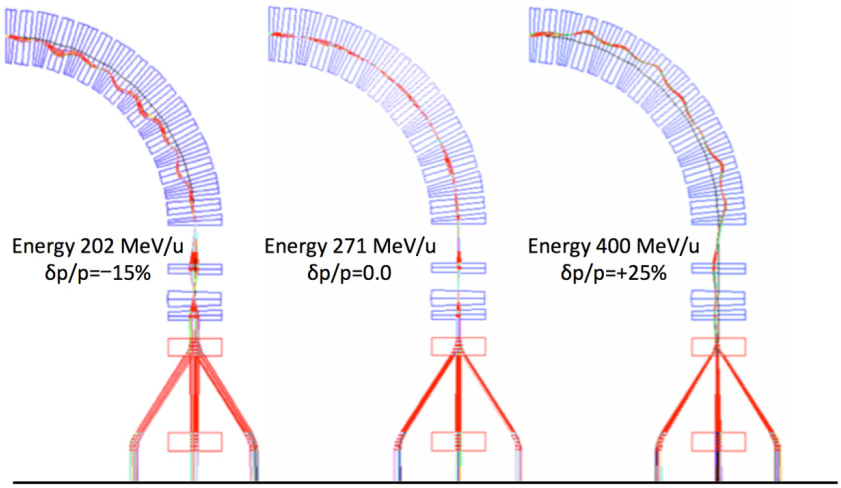

Figure 1.19 *FFAG superconducting gantry shown with carbon ions passing with three energies 202, 271, and 400 MeV/u under the fixed magnetic field, with scanning magnets [53]*

Riesenrad Gantry

A *Riesenrad* gantry was proposed in the framework of the Proton Ion Medical Machine Study (PIMMS) in 1993. More recently, CNAO (Italian Hadrontherapy National Centre) led a design study on this kind of gantry, under the auspices of the ULICE project of the European Union [54][55]. In this design, the treatment room is mounted on a rotating mechanical structure, which turns around the beam line. This highly simplifies the optics of the gantry that in this case is managed by just one 90°bending magnet and three quadrupoles. Differently from the gantries presented above, the isocentre moves around the beamline and this configuration is known as *mobile isocentre*. *Fig.1.20* exhibits the concept and the operating principle of the Riesenrad Gantry for the ULICE project. The Riesenrad structure, designed for carbon ions, measures 16 metres in length and 8.5 metres of radius, with a mass of 350 tons. The total footprint of the structure is 19 x 11.5 square metres and considering the shielding, it reaches the order of 350 square metres. Only the last section of the beamline (including the 90° bending magnet) rotates, allowing to reduce to its minimum the weight of the structure and the size of the room. One possible drawback of the system is considered the non-trivial accessibility to the patient during the treatment.

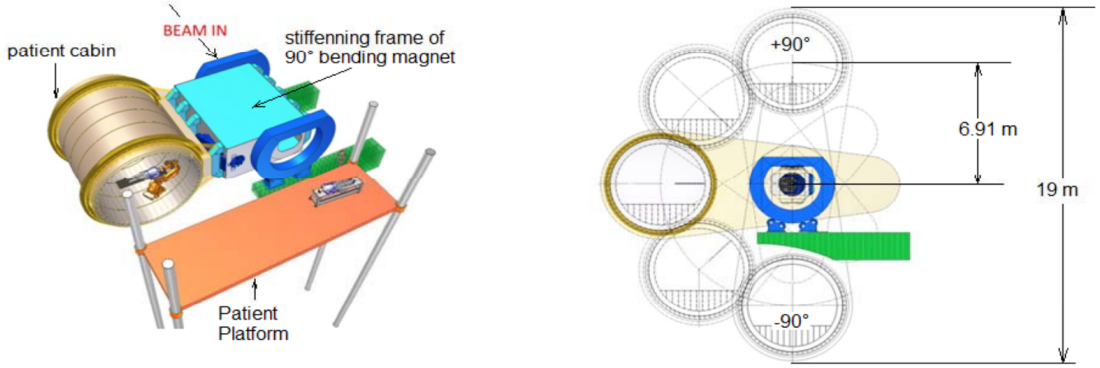

Figure 1.20 *Riesenrad gantry for the ULICE project [54]*

PSI New Concepts

In presence of an upstream scanning system, the last bending section of a gantry is usually the largest and heaviest magnetic part of the machine*.

To reduce weight and size of the last bending section, PSI is investigating the implementation of a superconducting combined functions magnet with high energy acceptance [56] [57]. The basic idea is to use the final magnet to achieve a local achromaticity and strongly enhance the momentum acceptance up to ±15% (equivalent to ±30% in energy). Due to this feature, it was estimated that more than 70% of treatments could be performed without variation of the magnetic field and current in the magnets. This is clearly in favour of using superconducting technology and in this specific context Nb_3Sn was selected to operate at 4.2 T at 4.2 K, resulting in a magnetic flux density of 3 T in the Good Field Region (GFR), and total magnet weight below 10 tons [58]. A schematic view of the gantry for protons is presented in *Fig.1.21* together with a model of the magnets. It measure 3.8 metres in radius and 5.5 metres in length.

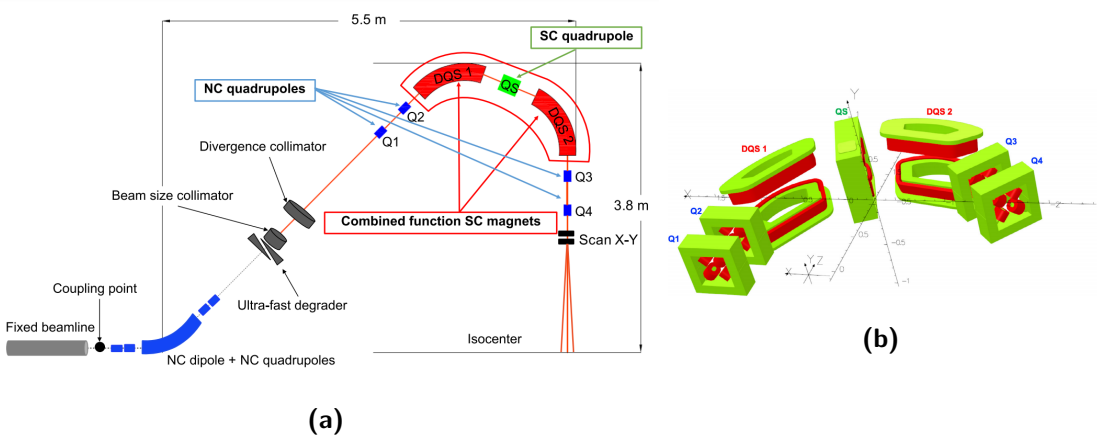

Figure 1.21 *Scheme of the superconducting gantry concept at PSI* ***(a)*** *and a closer look to the combined functions magnets model* ***(b)*** *[57]*

Furthermore, PSI is also studying the new concept of *Fast Proton-Arc Scanning*, where thanks to a solenoidal field the beam is bent down to the patient from different directions without the need of rotation of massive magnetic structures [59]. The concept is presented in *Fig.1.22*: the outermost solenoids produce the field used to bend and focus the particles, the innermost solenoid cancel the field at the patient location, and the arc-scan magnet group is used to select the incident angle of the beam at the patient. The system could provide a fast variation of treatment direction, as well as

*The 90°magnet of Gantry 2 weights 34 tons (over the 200 tons of overall weight) [35] and the 90°magnet of HIT gantry weights 90 tons (over 145 tons of magnets) [39]

implement arc and flash therapy. Still in the early phase of study, this design share some features with the non-rotating toroidal gantry discussed in this thesis.

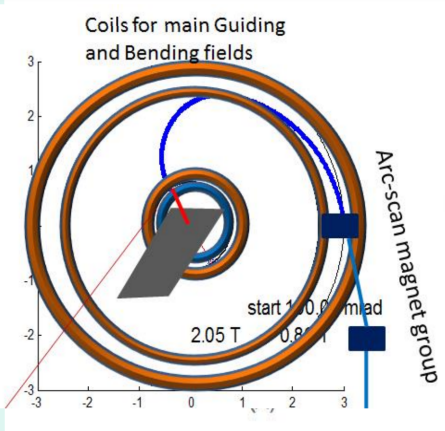

Figure 1.22 *Schematic representation of the Fast Proton-Arc Scanning concept [59]*

1.2.4 Gantry Related Technologies

CCT Magnet

To reduce footprint and weight of gantry magnets, Lawrence Berkeley National Laboratory (LBNL, US) proposes the use of superconducting Canted Cosine Theta (CCT) magnets. Shaping the path of the conductor in the support structure, this technology allows the generation of tailored field harmonics and can be used to design combined functions magnet with alternating gradients (AG-CCT) and specific focusing-defocusing sequences, as presented in *Fig.1.23* [60]. In this way, it is possible to create an achromatic bending region that increases the momentum acceptance up to 25%. Similarly to the new PSI combined function concept, this approach reduces the need of field and current variations during the treatments and favourably suits the use of superconducting technology. Different configurations are under study; the opting with Nb-Ti conductors operating at $5-6\ T$ at $4.2\ K$ results in a magnet weight of about $500-750\ Kg$. Including cryogenics and vacuum, it sums up to $2-3$ tons: a factor 10 lower than the actual PSI Gantry 2 final magnet.

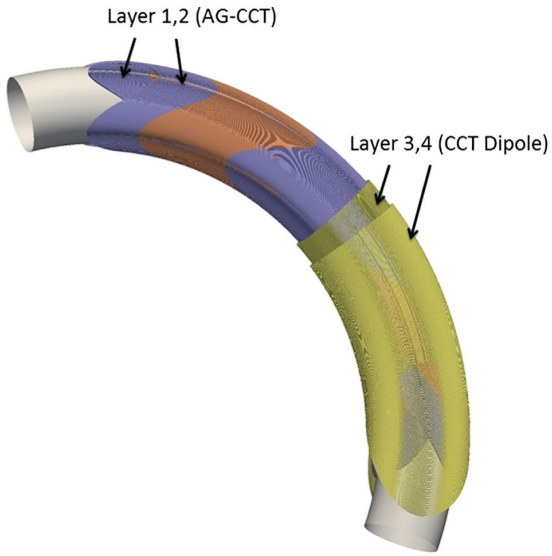

Figure 1.23 *Scheme of the toroidal bending magnet [60]*

Toroidal Bending Magnet

To overcome the problem of the large and heavy last bending section of a gantry, the Massachusetts Institute of Technology (MIT, US) suggests exploiting toroidal magnets for magnetic flux return instead of classical iron yoke solutions [61]. This self-shielded toroidal magnet is mounted on a rotating transfer line and the space between a single pair of coils is used for the beam transfer as a dipole (or combined with quadrupolar components). Only the space between a pair of coils is used for the beam transfer, while the rest of the coils are used to close the magnetic flux avoid heavy iron structures. A schematic representation of the toroidal bending magnet is provided by *Fig.1.24*. The current distribution inside the coil geometry can be modified to shape the field in desired profile, for bending and focusing the beam. Combining two toroidal magnets in series and profiting of their symmetry, a local achromatic bending region can be obtained with a consequent increase of the momentum acceptance. The magnetic field variation on the magnet can be therefore limited to 25% and a superconducting solution is proposed. Making use of Nb-Ti operating at 4.2 K with a peak magnetic flux density of 3 T (2 T in the good field region), the weight of a 60°bending magnet for protons is estimated to be around 300 Kg.

Similarly, the toroidal gantry studied in this thesis uses the free space between the coils for the beam transfer. However the toroidal gantry is not mounted on a rotating transfer line with other magnets, but it is a gantry itself, able to irradiate from different directions the patient placed on the torus axis.

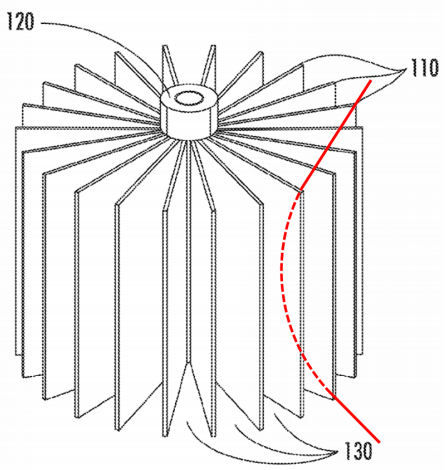

Figure 1.24 *Scheme of the toroidal bending magnet, with the trajectory of a particle in red [61]*

Piotron

Even if not strictly related to hadron therapy, it is important to mention that tori of superconducting coils were used in the *Piotron* at PSI, to produce a large acceptance channel that focused pions cancer treatment [62] [63] [64]. The system, put in operation in 1980, consisted of two tori built with 60 coils each, shaped and positioned so to collect the pions produced by a proton beam on a target, select a suitable momentum range, and focus them onto the patient location. This concept does not provide control of the beam direction, nor the possibility to paint the area of interest.

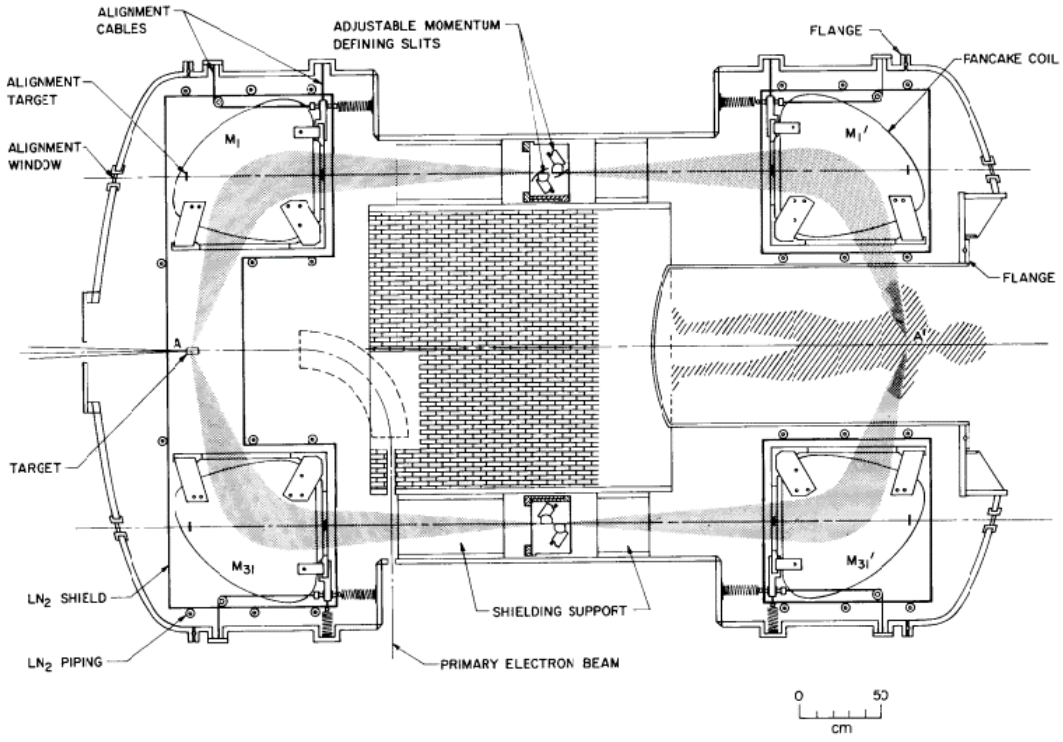

Figure 1.25 *Cross section view of the Piotron [64]*

1.2.5 Summary

The main parameters of the operating proton and carbon ion gantries discussed in the previous sections are summarized in *Tab.1.1*. As crucial features of commercial machines were not always accessible, some parameters included in the table were estimated from drawings or derived from other information. They are indicated in the table with the symbol (*). The gantry concepts that are still under development are not included in the table.

Main Parameters of Operating Proton and Carbon Ion Gantries					
Gantry	Radius [m]	Length [m]	Weight [tons]	Magnets	Rotation
Varian *ProBeam*	5.2	10	270	NC	360°
IBA *ProteusOne*	3.6	9.5	110	NC	220°
ProTom *Radiance330*	4*	10*		NC	180°
Mevion *S250i*	4.2	/	17 (just accel.)	/	190°
ProNova *SC360*	4	5	25	SC	360°
Hitachi	4	8*	125	NC	360°
Sumitomo	4.5	4.6		NC	360°
PSI *Gantry2*	4.2	11.6	200	NC	220°
HIT (C-ions)	6.5	25	670	NC	360°
NIRS (C-ions)	5.5	13	300	CF-SC	360°

Table 1.1 *Geometrical and operative parameters of carbon ion gantries. (*) indicates estimated values from drawings and calculations. NC: normal-conducting, SC: superconducting, CF: combined-function*

As extensively discussed in this chapter, in the last decades numerous efforts have been dedicated to the development of novel gantry concepts. The research in this field is rich and thriving, as several aspects of physics and engineering still need to be further investigated. Along with the stimulating scientific challenges, the ultimate goal should be the development of systems that bring the cost of hadron therapy down to the cost of traditional radiotherapy [11]. The present thesis is rooted in this framework: by

investigating a novel concept of toroidal gantry for hadron therapy, *GaToroid*, it aims to develop a solution that significantly reduces footprint and cost of hadron therapy gantries.

GaToroid

2

J.R.R. Tolkien, *The Lords of the Rings*, 1954

GaToroid: a toroidal gantry for hadron therapy. In this chapter, the concept and the main features of GaToroid are presented and discussed. This part of the thesis is intended as a prelude of the particle physics and engineering work discussed in the next chapters. Under ideal assumptions of a uniform magnetic field generated by a hard edge magnet, the properties of this toroidal gantry are investigated. Analytical and geometrical expressions are introduced and used as a solid base for numerical calculations.

The work presented in this chapter is also reported in:
L. Bottura, E. Felcini, G. De Rijk, and B. Dutoit, *GaToroid: A Novel Toroidal Gantry for Hadron Therapy*, Nuclear Inst. and Methods in Physics Research, A 983 (2020) 164588

GaToroid (a portmanteau word coined by the union of Gantry and Toroid) is a novel configuration of hadron therapy gantry under study at CERN since 2017. The concept is based on the use of toroidal magnets and aims at reducing footprint, weight and cost of traditional systems [65] [66]. The basic principle consists in the use the axial-symmetric toroidal magnetic field to bend and focus the particle beam down to the isocentre, providing multiple direction of radiation without the rotation of neither the magnet nor the patient. The GaToroid concept is composed by two main elements:

- the *vector magnet*, connected to the accelerator with a traditional transfer line, that provides an appropriate kick to the beam, depending on its energy and the desired direction of treatment;

*Inscription on the One Ring: "One ring to rule them all, One ring to find them, One ring to bring them all and in the darkness bind them"

- the *toroidal gantry*, that consists of one or more co-axial toroidal magnets, that bend and focus the beam by using the free space between the coils. The combination of magnet geometry and field profile allows directing the beam down to the tumour location with a very high energy acceptance.

Fig.2.1 illustrates the GaToroid working principle, showing a set of N coils with a beam tracked from the vector magnet through the toroidal magnetic field down to the patient location.

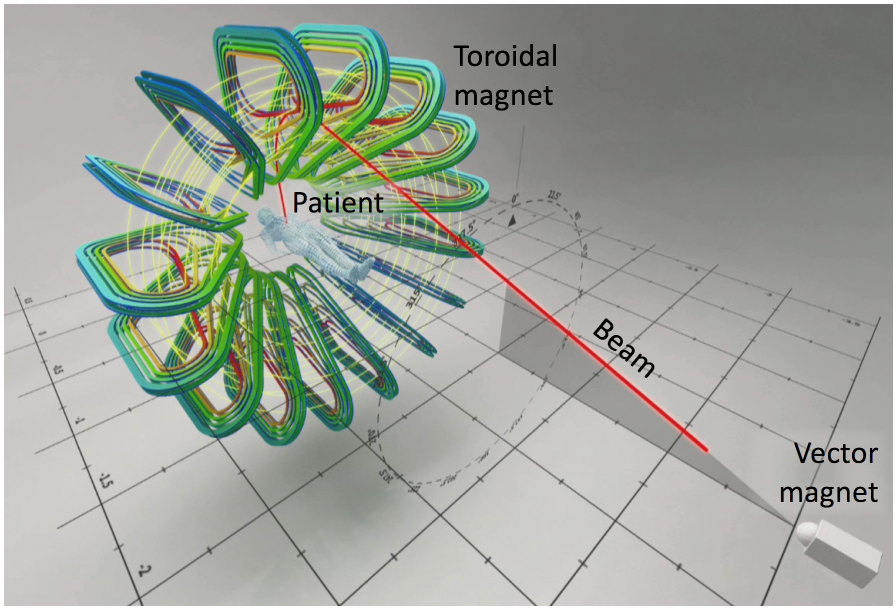

Figure 2.1 *Schematic representation of the GaToroid components. The patient is located in the (field-)free bore of the toroidal magnet. (Courtesy of Daniel Dominguez, CERN Design and Visual Identity Service).*

In the context of this thesis, the investigation of the GaToroid system is limited to a single toroidal magnet, with the simplified assumption of considering the vector magnet as a point.

2.1 Vector Magnet

The function of the vector magnet is to bend the extracted beam in any direction by an angle that depends on the beam energy and the required direction of treatment.

To achieve this function, the vector magnet can consist of a single dipole rotating around its axis with the ability to sweep the field strength. Depending on the magnet design, the change in field strength required to steer beams of different energy can be relatively fast. A rotation, on the other hand, corresponding to a change in irradiation

direction, will be much slower. An alternative to achieve fast response in both functions is to consider a two-axis vector magnet, producing a combination of horizontal and vertical dipole with arbitrary direction. In this case the two dipoles should change setting frequently, providing the ability for rapid energy and direction changes, and eliminating the need for a heavy rotating machinery. This feature makes the two-axis option more elegant and interesting.

Furthermore, the vector magnet can act with deviations from the nominal angles to achieve the beam spot scanning that is requested in hadron therapy. This is similar to the ability to direct the beam in an arbitrary direction described above, albeit by a much smaller amount. This concept is investigate in *Sec.4.5*

The vector magnet poses by itself a significant technology challenge. An ideal vector magnet should be short, to keep the aperture at the exit small, but sufficiently strong to avoid a large distance from the toroidal gantry. This would result in relatively large fields and a consequent superconducting solution. In this case, the inductance of the magnet and AC losses would limit the ramping speed, going against the idea of a fast switching. The accuracy of the angles imposed by the vector magnet is of uppermost importance to direct particles at the isocenter with sufficient precision. This is true both for the large steps that cover the desired range of momentum and direction of treatment, as well as the small deviations used for the spot scanning.

Without entering in the details of the vector magnet design, the functions described above suggest the use of a sequence of magnets with specific features. A fast combined-function resistive magnet followed by a superconducting bend with a large aperture could result in the most practical configuration. Regarding the large superconducting magnet, an interesting solution could be the use of a *forward* toroid, operating in steady-state, that amplifies the angle of the beam received from the resistive magnet.

2.2 Toroidal Gantry

The description of the working principle of a GaToroid system composed by a single torus is provided by *Fig.2.2*, where cylindrical coordinates (R,z,θ) are used as reference. Considering the symmetry plane between two coils, the coordinate system is reduced to (R,z).

Although in classical toroidal magnets the magnetic flux density decrease with the radius, R, it is possible to arbitrarily modify this dependence by spacing the conductors in the winding and distributing the current density inside the coil profile (*coil grading*). This mechanism is discussed in detail in *Sec.3.1.*

To explain the basic principle of a GaToroid gantry, the simplified case of an ideal magnetic flux density $B = B_0$ is hereafter assumed.

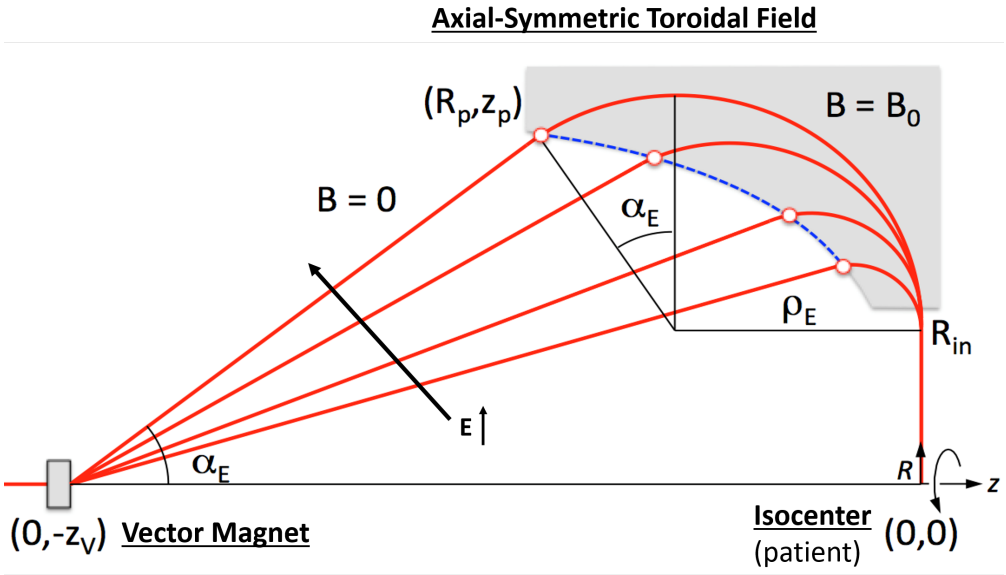

Figure 2.2 *Construction of the ideal profile of a toroidal magnetic flux density B_0 (grey area) that directs particles of different momentum to charge ratio p/q on a single focal point by making use of different kick angles at the location of the vector magnet. The toroidal field area is shaded in the picture. The dashed boundary can be computed using Eq.(2.4)*

Particle beams with different rigidities $(B\rho)_E$, *i.e.* 1.2 to 2.4 Tm for protons and 3.3 to 6.6 Tm for carbon ions, are deviated by a vector angle α_E through the vector magnet placed in $(0, -z_V)$. Small α_E are imposed to low energy beams, while larger α_E are imposed to higher energy beams. Considering the uniform axial-symmetric magnetic flux density B_0 and the hard edge approximation (grey area), the principle shown in *Fig.2.2* is quite intuitive: high rigidity beams interact with the magnetic field for a longer length, while low-energy beams are bent by the field for a shorter path. By adjusting the vector angle α_E and shaping the field profile, it is possible to direct beams of different energies at the same point, the isocentre. For the sake of simplicity, only the case limited to a perpendicular incident angle at the patient is investigated in the thesis. The magnetic field can be shaped to have an arbitrary incident angle at the patient [66].

Considering the uniform magnetic flux density B_0, the particle momentum, p, and its charge, q, for each energy E,the radius of curvature ρ_E is calculated as:

$$\rho_E = \frac{p}{q}\frac{1}{B_0} = \frac{(B\rho)_E}{B_0} \tag{2.1}$$

where $(B\rho)_E$ is the beam rigidity. The vector angle α_E is then calculated as follows:

$$\alpha_E = asin\left(\frac{\rho_E(z_v - \rho_E) + R_{in}\sqrt{R_{in}^2 + z_v^2 - 2z_v\rho_E}}{(z_v - \rho_E)^2 + R_{in}^2}\right) \tag{2.2}$$

The integral of the magnetic flux density along the trajectory described for each energy is:

$$(\int B\, dL)_E = B_0\rho_E\left(\frac{\pi}{2} + \alpha_E\right) \tag{2.3}$$

Using simple trigonometric equations, it is possible to design the field profile, highlighted with dashed blue line in *Fig.2.2*:

$$\begin{aligned} z_E &= -\rho_E + \rho_E cos\left(\frac{\pi}{2} + \alpha_E\right) \\ R_E &= R_{in} + \rho_E sin\left(\frac{\pi}{2} + \alpha_E\right) \end{aligned} \tag{2.4}$$

where z_E and R_E are the coordinates of the field profile points corresponding to each energy, and the isocentre is in (0,0).

Through these formulae, peculiarly shaped coils can be designed and assembled in toroidal configuration around the z-axis. The geometry of the coil can, therefore, be fully parametrised by B_0, z_v and R_{in} for a given range of beam energies. *Fig.2.3* depicts the trends of the vector angle α_E as a function of the beam rigidity and the field profile (described by *Eq.(2.4)*) for different positions of the vector magnets on the axis, z_v. In this case, the ideal magnetic flux density, B_0, and inner bore radius, R_{in}, were set as 3 T and 0.5 m respectively. Is it clear that the closer the vector magnet to the torus, the

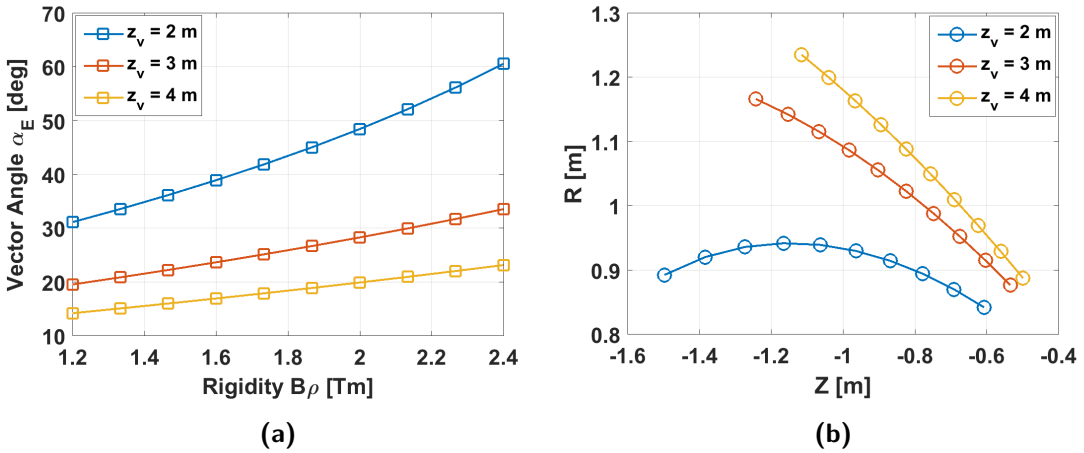

Figure 2.3 *Vector angle α_E as a function of beam rigidity in the proton treatment range* ***(a)*** *and field profile defined by Eq.(2.4)* ***(b)*** *for $B_0 = 3$ T, $R_{in} = 0.5$ m and 3 different positions of the vector magnet in the Z axis*

higher is the required vector angle to impose to the beam. While a reduced distance between the magnets can decrease the overall length of the system, on the other hand, it would induce several challenges in the design of the vector magnet. At the same time, the position of the vector magnet strongly affects the shape of the field. Small absolute values of z_v can lead to strong concavities in the shape of the coil and a consequent increase of complexity in the fabrication. The effects induced by the variation of the magnetic field and internal radius are more linear, but it is clear that the vector angle and the shape of the coils are a function of the B_0, z_v and R_{in}. These parameters were used to perform the magnetic optimisation described in section *Sec.3.1.*

Once assessed the geometry of the N coils composing the torus, the free space between each pair is used for the beam transport, providing treatment beams from N different directions to the patient.

So far the properties of GaToroid were discussed on the z-R plane described in *Fig.2.2*, without taking into account the effect of the toroidal field on the traverse beam dimensions. The effect of the field curvature on a particle entering the field region out of the z-R plane are hereafter discussed.

Firstly, the local reference system (x-y plane) of a particle travelling from the vector magnet into the toroidal gantry is considered. Each point on the x-y plane can be described by the angle θ and the radius R, as shown in *Fig.2.4.*

The curvature B_θ is perceived by the particle as a gradient on the y-component on its local reference system. This gradient can be written as:

$$B_y = B_\theta sin(\theta) = B_\theta \frac{x}{R} \tag{2.5}$$

where $x = Rsin(\theta)$. The quadrupole component of the toroidal field can then be expressed as:

$$k = \frac{\partial B_y}{\partial x} = \frac{B_\theta}{R} \tag{2.6}$$

This means that a beam entering an ideal toroidal field around z-R plane would be naturally focused. Furthermore, this effect is dependent on the radius R, even if the field is radially constant. A natural $1/R$ toroidal field would have an associated $1/R^2$ gradient dependence. This is true for every torus, but in the special case of GaToroid, the particles are not entering the field parallel to the z-axis. As a consequence, the focusing component at the entrance of the field is reduced to:

$$k_E = \frac{B_\theta}{R_E} cos(\alpha_E) = \frac{B_\theta cos(\alpha_E)}{R_{in} + \rho_E sin\left(\frac{\pi}{2} + \alpha_E\right)} \tag{2.7}$$

For instance, to give an order of magnitude of this focusing properties, considering a field $B_\theta = 3$ T at a radius of 1 m and an angle $\alpha_E = 20$ deg., the net gradient results

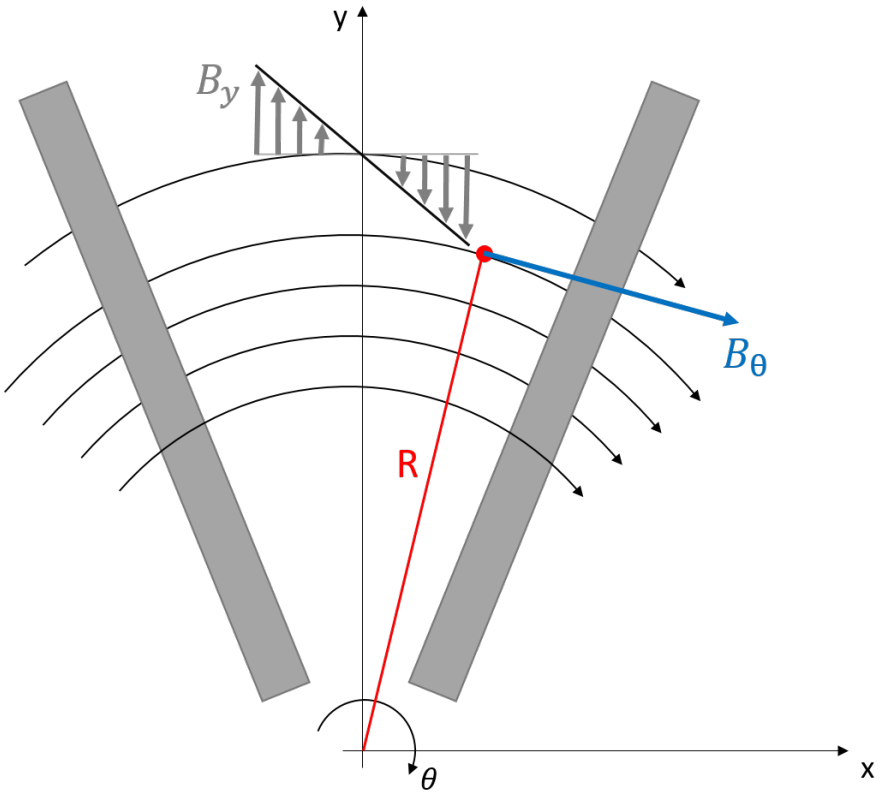

Figure 2.4 *Representation of the field gradient B_y seen by a particle entering (red point) the toroidal field B_θ at an arbitrary point (x, y). The natural curvature of the toroidal field induces a focusing on the beam. The schematics of a pair of coil is shown in grey*

in 2.8 T/m. It is important to underline that the beam trajectories change inside the field, and so does the way the particles perceive the toroidal field. For example, close to the exit of the magnet (isocentre direction), the trajectories are basically perpendicular to the z-axis (and parallel to the R-axis) and cannot appreciate the curvature of the field, *i.e.* the gradient induced by the curvature is zero. Furthermore, the deviation of the magnetic flux lines introduced by a finite number of coils can modify the gradient and the focusing features of the machine. The focusing properties of such a toroidal magnet are interesting and complex, and are investigated in detail in *Chap.4*.

Finally, it is worth to underline that because of the axis-symmetric configuration the magnetic flux density on the patient (located in the gantry bore) is below any value of concern for instrumentation or humans (order of μT). In case of lack of symmetry, due for instance to a short-circuit in one ore more coils, the magnetic flux could penetrate inside the bore. This circumstance must be strictly avoided: neither the patient nor the auxiliary devices can be subject to a magnetic field, especially if transient[†]. It is

[†]the dB/dt limits in MRI machines are in the order of $1 - 3\ T/s$ [67]

therefore important to maintain the symmetry of the system in case of faults, issue that is tackled by designing quench protection scenarios where the current discharge occurs simultaneously in all the coils. These topics are investigated in *Sec.3.1.3* and *Sec.5.1.*

Magnetic Design

3

"*Perché io sono molto attento ar design*"

Humphrey Bogart as Baiocchi, 2007

Based on the theoretical concept and analytical description of GaToroid, this chapter describes the magnetic design of the toroidal gantry. The technique of coil grading is discussed and implemented in a magnetic optimisation aiming to maximise the energy acceptance over the whole treatment range. The general features of the resulting machine are then presented for both high and low engineering current density solutions, suitable to operate with Non Insulated (NI) and traditional insulated coils respectively. Furthermore, the magnetic efficiency of a torus is presented as a function of the number of coils. Both analytical formulations and numerical simulations were used to select the appropriate number of coils, as a compromise between the complexity of the superconductor technologies and the available aperture for the beam.

The work presented in this chapter is also reported in:
E. Felcini, L. Bottura, J. van Nugteren *at al.*, *Magnetic Design of a Superconducting Toroidal Gantry for Hadron Therapy*, in IEEE Transactions on Applied Superconductivity, vol. 30, no. 4, pp. 1-5, June 2020.
L. Bottura, E. Felcini, V. Ferrero *et al.*, *Delivery, beam and range monitoring in Particle Therapy in a highly innovative integrated design*, accepted for publication in Frontiers in Physics, Medical Physics and Imaging, 2020

3.1 Magnetic Optimization

The working principle of GaToroid, explained in *Chap.2*, is based on the assumption of a ideal and uniform magnetic flux density ($B = B_0$) and hard-edge approximation ($B = 0$ outside the coils). Starting from this concept and related analytical formulation, it is possible to create a coil geometry following the ideal field profile described by *Eq.(2.4)*, as illustrated in *Fig.3.1* (dashed blue line).

Arranging a number N of these coils around the $\mathbb{Z}$-axis, the generated toroidal magnetic field is enclosed within the coil profile. A torus is characterised by an axial-symmetric magnetic flux density inversely proportional to the radius R, obeying the Biot-Savart law:

$$B_\theta = \mu_0 \frac{NI}{2\pi R} \tag{3.1}$$

where I is the current flowing in a coil. The product NI is the magnetomotive force (mmf), expressed in Ampere-turns (At) and it can be used to do the magnetic design of the toroidal gantry.

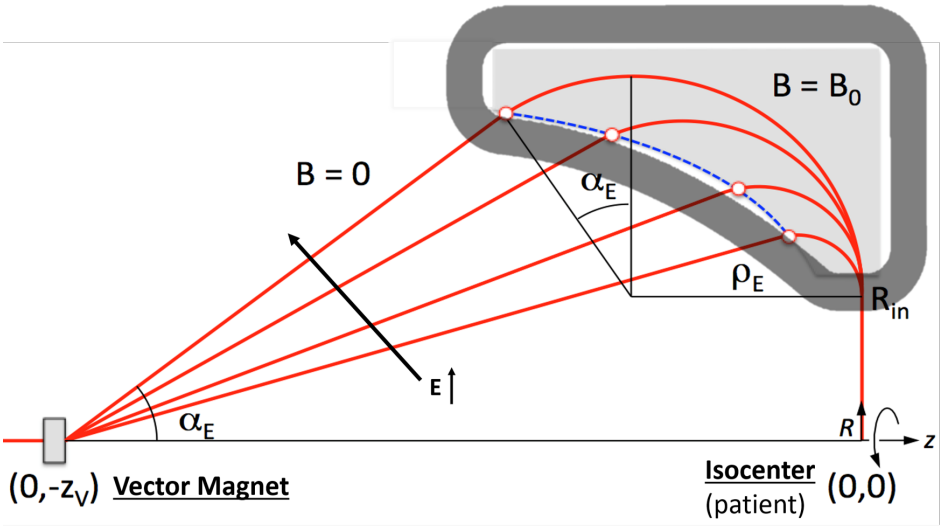

Figure 3.1 *Construction of the ideal coil profile using Eq.(2.4), around an ideal and uniform magnetic flux density $B = B_0$*

Fixing a value of magnetic flux density at a given radius R (distance from the z-axis of the torus), the magnetomotive force can be easily calculated as

$$NI = \frac{B_\theta}{\mu_0} 2\pi R \tag{3.2}$$

For instance, assuming $B_\theta = 2\ T$ at $R = 1.0\ m$, it results in $NI = 10\ MAt$ (MegaAmpere-turns). This quantity can be subdivided in an arbitrary number of coils, *e.g.* 10 coils carrying 1 MA, or 20 coils carrying 0.5 MA. As discussed in *Sec.3.2*, the choice of the number of coils impacts the peak magnetic field on the conductors and therefore the type of superconducting technology to be used. As illustrated in the next section, the magnetic design of GaToroid was done with $N = 16$. The magnetic field calculated for a torus with 16 coils and 10 MAt Ampere-turns is presented in *Fig.3.2*, together with the particle trajectories over the whole proton energy spectrum.

At $R = 1.0\ m$, the toroidal flux density B_θ is 2 T, however, it decreases with radius. For the GaToroid concept this means that the higher the beam energy, the larger the vector angle α_E and the lower the field experienced by the particles. Intuitively, this is clearly against the principle shown in *Fig.3.1* and the strong defocusing effect introduced by the 1/R field dependence becomes clear in *Fig.3.2*. A coil optimisation process is required to solve this *undesirable* feature of tori.

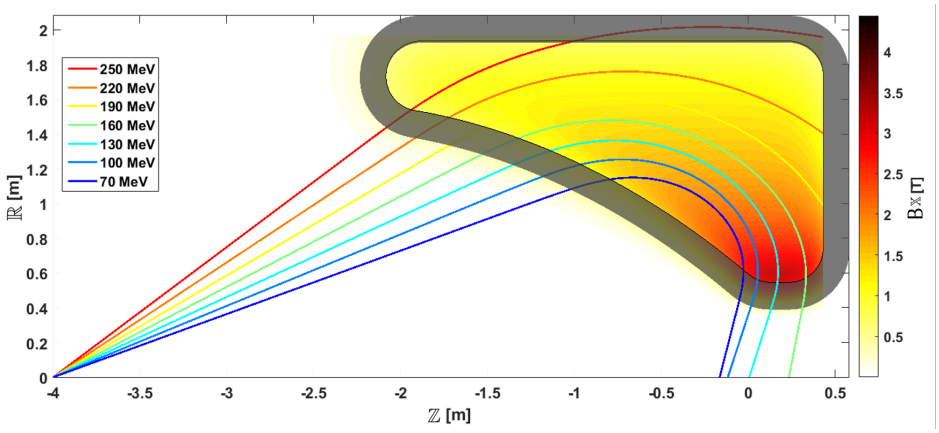

Figure 3.2 *Particle trajectories in the whole range of proton treatment energies for an analytical coil geometry described by Eq.(2.4). Blue line: 70 MeV, Red line: 250 MeV. The lines are at intervals of 30 MeV*

To create a suitable magnetic field, able to bend the particle trajectories toward the isocentre in the whole range of treatment energies, it was necessary to modify the current distribution inside the coils, *i.e.* introducing a *coil grading*. In this context, a *grade* is defined as a sub-coil composing the winding. By adjusting geometrical parameters of the coil and the conductor positions, it was possible to arbitrarily shape the field profile and its dependence with the radius. *Fig.3.3* shows how the current distribution inside the coil area can modify the field in the region of interest. The coil of *Fig.3.3*a is not graded, while the coil of*Fig.3.3*b is composed of 5 grades of equal current (the most two outer grades are at zero distance).

To find an appropriate solution, an iterative optimisation based on the minimisation of the gap between the particle orbit positions at the isocentre at different energies was implemented. As shown in *Eq.(2.4)*, the coil geometry can be described by the vector magnet position $\mathbb{Z} = z_v$, internal bore radius R_{in} and ideal magnetic flux density B_0. These three parameters, together with the current distribution inside the coil surface (grade positions and currents), were used to perform the numerical optimisation. The algorithm was designed to reduce the gap between beam positions at the isocentre over the whole range of proton treatment energies, *i.e.* 70 to 250 MeV, and the convergence criterion for the presented configurations was set equal to 1 mm. The minimisation

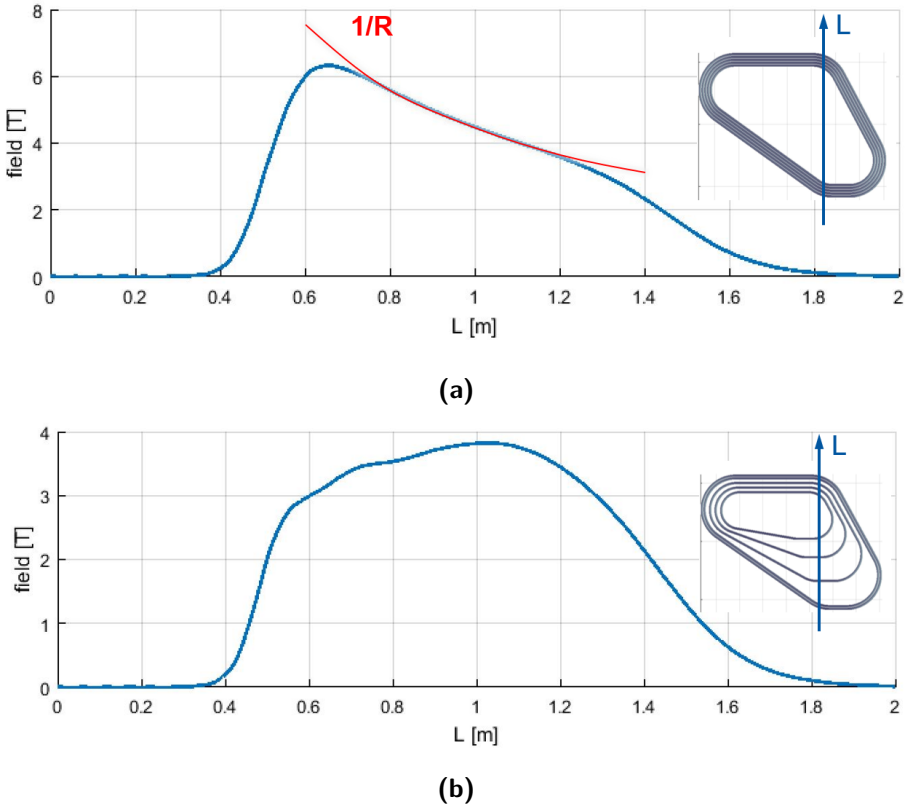

Figure 3.3 *Magnetic flux density profiles along the radius in case non-graded* ***(a)*** *and graded* ***(b)*** *coil. In the first case, the flux density exhibits a natural 1/R profile, while thanks to the grading the field profile can be arbitrarily modified*

function and the weights on position and incident angle can be tailored, depending on the beam requirements at the patient.

The electromagnetic simulations presented in the thesis were done with Field2017 [68].

3.1.1 Resulting Configurations

Hereafter, two optimised solutions for proton GaToroid are presented. These two options differ for the value of engineering current density in the cable and reflect the use of alternative superconducting technologies and quench protection systems. In this context, the engineering current density is defined as the overall current density of each grade, *i.e.* the current carried by each grade divided by its cross-section (considering superconductor and stabilizer).

The first solution was designed pushing the engineering current density to 500 A/mm^2, while the second one relies on the use of a more modest value of 100 A/mm^2. To provide a clear comparison between these configurations, the main parameters of the gantries, such as the number of coils and the overall dimensions, were kept constant. Both tori count 16 coils, each one composed of 5 grades of equal current. The number of coils has a strong effect on the peak field, driving the choice of the superconducting technology and the cost of the machine. This effect and related implications are discussed in *Sec.3.2*. The choice of 5 grades of equal current was done to maintain the number of optimisation parameters below 10, in order to reduce the optimization computation time.

The analytical coil profile described by *Eq.(2.4)* has a limb with negative curvature (concave shape of *Fig.3.1*). To simplify the winding procedure, the profile was straightened, with only little effect on the beam bending properties.

The size of the coil is considered a crucial parameter, not only for the total footprint and weight of the gantry, but also for the amount of conductor and the stored energy, indicators of the final cost of the machine [69]. For this reason, the geometry of the return current limb (located in the positive part of the $\mathbb{Z}$-axis in *Fig.3.4*) was tilted to reduce the coil area and the required length of conductors. Finally, the design of the machine was optimised limiting the peak magnetic flux density on the conductors in the order of $7 - 8\ T$, to accommodate the use of both Low (LTS) and High (HTS) Temperature Superconductors.

The high current density (500 A/mm^2) solution suits the use of Non-Insulated High Temperature Superconductors (NI HTS) [70][71]. This technology is based on the idea of avoiding insulation between tapes to promote current and heat sharing in the radial direction of the windings during a quench. At the same time, the stabilizer is used as an *insulations* during the normal operating condition, where the superconductors has (in first approximation) zero resistance. The resulting geometry is presented in *Fig.3.4*, together with the magnetic field and particle trajectories over the complete proton treatment range. The convergence at the isocentre is within 1 mm, with a maximum angle difference between the orbits of about 5 degree. The complete description of the

simulation tool used for particle tracking is provided in *Chap.4*.

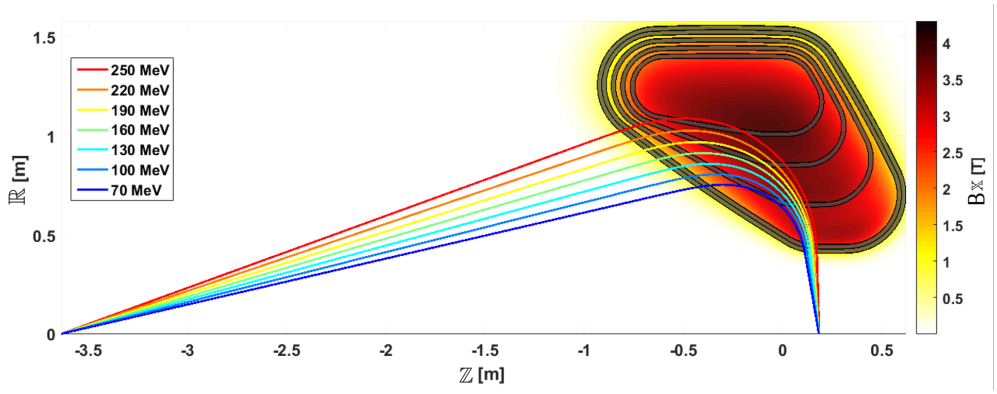

Figure 3.4 *Single particle trajectories in the whole range of proton treatment energies for the optimised coil geometry operating at* 500 A/mm^2 *(non-insulated winding)*

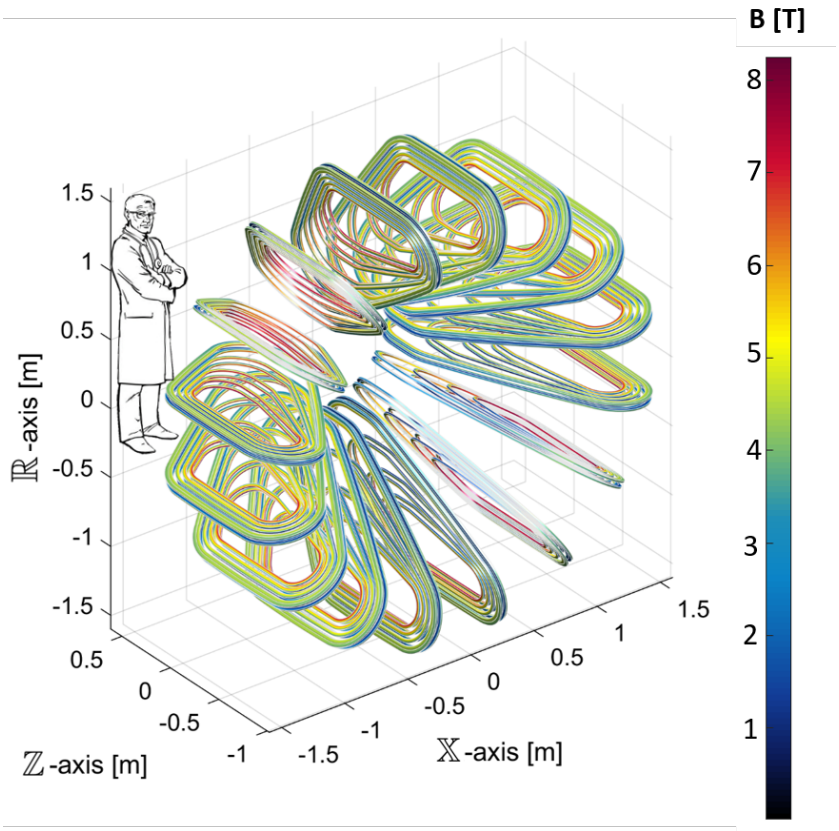

Figure 3.5 *Magnetic flux density map on the surface of the optimised GaToroid for protons for a current density of* 500 A/mm^2*. The schematic picture of a doctor is used for size comparison*

The main coil parameters of the optimised geometry are summarised in *Tab.3.1* (column

high J_{en}). Each coil is composed of 2 symmetric pancakes with 5 grades of equal current each (the two outermost grades are at zero distance). To limit the peak magnetic flux density on the conductors to approximately 8 T, gaps of the order of 2 cm were introduced between grades in the outward leg and the two layers of the pancake were separated by 3 cm.

The torus, resulting from optimisation of this first configuration and composed by 16 coils, is presented in *Fig.3.5* and the main parameters are reported in *Tab.3.2* (column high J_{en}). *Fig.3.5* shows the magnetic flux density map on the conductor surface (maximum 8.2 T) and a schematic representation of a doctor for size comparison*.

Likewise, an optimised configuration was obtained for a lower value of engineering current density. Considering a more classical solution, based on insulated and copper stabilised cables, the optimisation process was performed with $J_{en} = 100\ A/mm^2$. This kind of cable configuration, analysed in detail in *Sec.5.1*, was conceived to work with both LTS and HTS conductors. The geometry of the coil and the particle trajectories from 70 to 250 MeV are presented in *Fig.3.6*. Also in this case, the particles are converging at the isocentre within 1 mm, with a difference between the incident angles of 8 degree.

The number of grades was kept equal to 5 (the two outermost grades are at zero distance), while the layer of the pancake was increased up to 4. The current is already *diluted* inside the conductor, therefore gaps between the grades or layers were not needed to reduce the value of peak magnetic field on the conductors. In this way, it was possible to maintain limited coil dimensions, coherent with those of the high current density version. The parameters of the low J_{en} coil are listed in *Tab.3.1.*
The complete torus geometry is shown in *Fig.3.7*; as highlighted by the magnetic flux density on the conductor, the use of a limited engineering current density allows the reduction of the peak flux density below 7 T. A detailed list of geometrical and electrical features of this torus is presented in *Tab.3.2* (column low J_{en}).

Summarizing, despite the large difference in engineering current density, the two machines have a comparable design and, as expected, they share the same value of total ampere-turns (22.6 MAt). Using this value in *Eq.(3.4)*, at 1 metre radius, the ideal flux density B_θ results is 4.5 T, coherent with the flux density values reported in *Fig.3.4* and *Fig.3.6*. The main differences between the two configurations are the thickness of the grades and the available space for the mechanical structure inside the coil profile, as shown in *Fig.3.4* and *Fig.3.6*. Furthermore, the number of pancake's layer in the Low J_{en}y solution is doubled if compared with the High J_{en} one. Strictly

*The disappointment of the doctor is not related to the gantry, but it is probably due to long and stressful working hours in the hospital

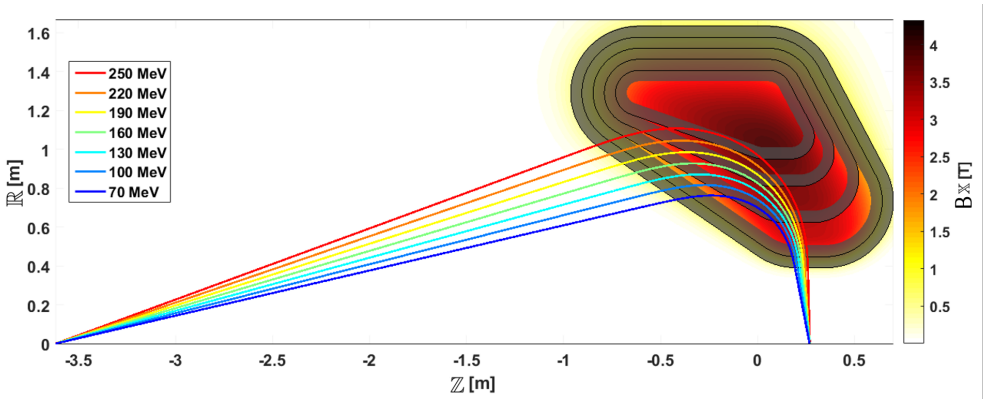

Figure 3.6 *Single particle trajectories in the whole range of proton treatment energies for the optimised coil geometry engineering at* 100 A/mm^2 *(insulated windings)*

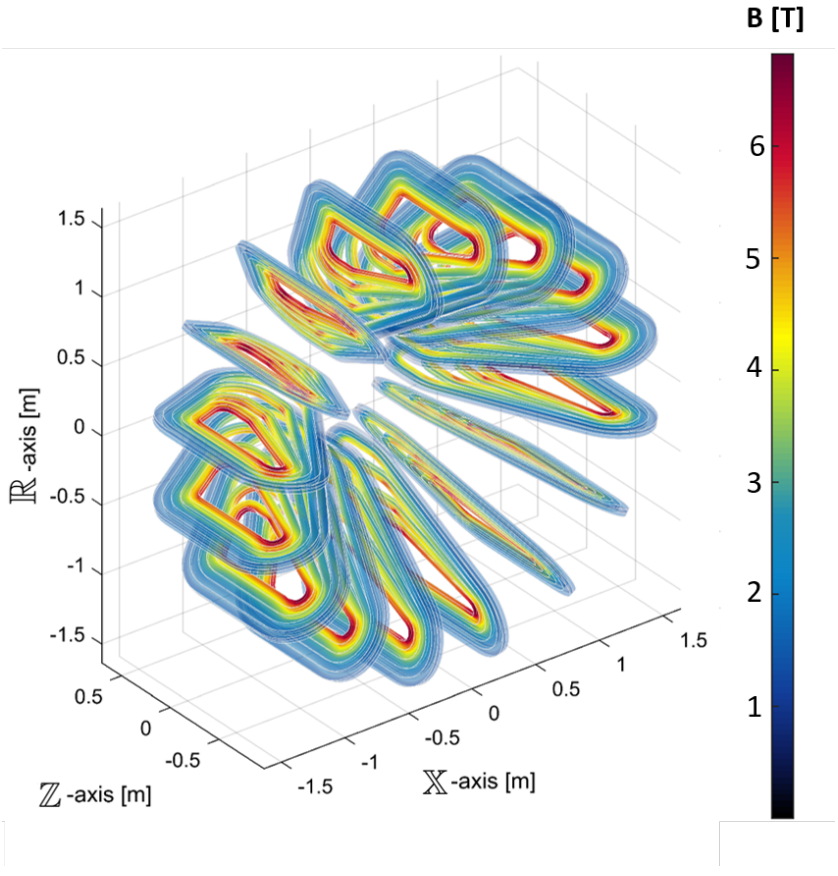

Figure 3.7 *Magnetic flux density map on the surface of the optimised GaToroid for protons for a current density of* 100 A/mm^2

speaking, the coil is thicker in the 𝕏-direction of *Fig.3.4* and *Fig.3.6*.

Nevertheless, both tori are quite compact, with an external radius of 3.3 metres and

Proton GaToroid - Main Coil Parameters			
Parameter	Unit	High J_{en}	Low J_{en}
Number of Grades/Layer		5	5
Number of Layers		2	4
Length	[m]	1.8	1.7
Height	[m]	1.2	1.3
Thickness	[m]	0.05	0.05
Engineering Current Density | J_{en}	$[A/mm^2]$	500	100
Peak Magnetic flux density | B_p	[T]	8.2	6.8
Ampere-Turn	[MAt]	1.4	1.4

Table 3.1 *Main parameters of the optimised coils for proton GaToroid*

Proton GaToroid - Main Torus Parameters			
Parameter	Unit	High J_{en}	Low J_{en}
Engineering Current Density | J_{en}	$[A/mm^2]$	500	100
Peak Magnetic Flux Density | B_p	[T]	8.2	6.8
Number of Coils | N		16	16
Bore Radius | R_{in}	[m]	0.4	0.4
External Diameter	[m]	3.3	3.3
Torus Length	[m]	1.8	1.7
Vector Magnet Position | z_v	[m]	3.5	3.6
Stored Energy	[MJ]	34	31
Total Ampere-Turn	[MAt]	22.6	22.6

Table 3.2 *Main parameters of the optimised tori for proton GaToroid*

an internal bore of 0.8 metres. The total length of the machines, considering the vector magnet location (punctual) and the coil dimensions, is about 4 metres.

To be noted that the magnet bore was chosen intentionally small, in the range of that of MRI magnets, to find the minimal possible dimension that can be achieved with such a system. The author is aware that this does not leave enough room to insert the customary beam diagnostics and controls. Indeed, adding the typical dimension of a radiation therapy nozzle would at least double the magnet bore. It is however interesting to highlight that work is in progress to examine the possibility to integrate compact solid-state beam range and position monitoring in the gantry dimension assumed here [72].

The presented configurations have the potential to substantially reduce the footprint

of the state-of-the-art gantries (*Tab.1.1*) by a factor two.

3.1.2 Load lines and Margins

Once assessed the magnetic configurations of the two gantry options (High J_{en} and Low J_{en}), the operating conditions of the superconductor were investigated in terms of current density, magnetic field and temperature. The first step toward this analysis was the selection of the appropriate superconductor.

Regarding LTS conductors, given the low price, limited magnetic field, simplicity of winding (no heat treatment) and high experience level gained in the last decades [73], Nb-Ti was chosen instead of Nb_3Sn.

Regarding HTS conductors, the choice is essentially limited between BSCCO (Bismuth Strontium Calcium Copper Oxide) and ReBCO (Rare-earth Barium Copper Oxide). The latter was selected for this application. In fact, at present, ReBCO coated conductors are widely used in the community, not only for toroidal fusion magnets [74][75], but also for a new generation of high field magnets for particle physics [76] and medical applications, such as gantries [77] and NMR-MRI [78]. ReBCO is a relative recent technical superconductor and it is still in an intense research and development phase. Several producers are working to reduce the cost of the material, as well as to overcome technical limitations on the unit length and the uniformity of the tapes. This HTS conductor does not require any heat treatment after the winding and, provided the absence of hard-way bending and small radii of curvature, can be easily wound. Finally, at the moment, ReBCO appears to have a larger margin of technological improvement [79] and represents a stimulating research challenge.

Then, the second step was the definition of the operating conditions of the superconductors, in terms of current density J_{op} and temperature T_{op}. For Nb-Ti, under the assumption of a cryogenic system based on supercritical helium at 4.5 K, the operating current density on the superconductor was set equal to 400 A/mm^2. Profiting from the much larger critical temperature, ReBCO can operate in gaseous helium at 20 K. At this temperature, the operating current density in the tape was set to 500 A/mm^2, coherently with the high engineering current density solution (non-insulated). *Tab.3.3* summarises the operating conditions of the three investigated configurations: one High J_{en} (HTS) and two Low J_{en} (LTS and HTS).

Referring to the operating of parameters *Tab.3.3*, the load line current margins of the LTS and HTS options were calculated. Concerning the former, the calculation of the critical surface was done using the largely used fit proposed by [80], where the

Proton GaToroid - LTS and HTS Cables Parameters				
Parameter	Unit	HTS	LTS	HTS
		High J_{en}	Low J_{en}	
Conductor		ReBCO	Nb-Ti	ReBCO
Cable Topology		Non-Insulated	Rutherford	Non-Twisted Stack
Operating Current Density	$[A/mm^2]$	500	400	500
Operating Temperature	$[K]$	20	4.5	20
Peak Magnetic Flux Density	$[T]$	8.2	6.8	6.8
Load Line Current Margin		31%	73%	38%
Temperature Margin	$[K]$	16	1.5	18

Table 3.3 *Main cable parameters for LTS and HTS configurations*

critical current density J_c is a function of the reduce magnetic field $b = B/B_{C2}(T)$ and normalised temperature $t = T/T_{C0}$:

$$\begin{aligned} J_c &= \frac{C_0}{B} b^{\alpha}(1-b)^{\beta}(1-t^n)^{\gamma} \\ B_{C2}(T) &= B_{C20}(1-t^n) \end{aligned} \tag{3.3}$$

with $C_0 = 7.21 \cdot 10^{10}$, $T_{C0} = 9.5\ K$, $B_{C20} = 14.5\ T$, $n = 1.7$, $\alpha = 0.6$, $\beta = 1.0$ and $\gamma = 2.0$, to recreate the properties of the conductors used for LHC magnets (2750 A/mm^2 at 4.2 K, 5 T).

With respect to HTS conductor, given the variability provided from different manufacturers and the dynamic R&D process, the critical surface of the tape from Bruker was used as reference [81] (670 A/mm^2 at 4.2 K, 20 T). The complexity of the parametrisation and the number of constants are higher than for Nb-Ti and for the sake of conciseness, it is not reported in this thesis. A full description is available in [81]. *Fig.3.8* presents the load lines and critical surfaces for both LTS and HTS conductors. The *load line fraction* is defined as the ratio between operational current density J_{op} and short sample current density (critical current density) J_c at the operating field and temperature. The load line margin, namely the complement to one of the load line fraction $(1 - J_{op}/J_c)$, is reported for the three configurations in *Tab.3.3*.

The current margin for the HTS options is in the order of $30 - 40\%$, while it is more than 70% in the Nb-Ti version. It is important to remind that the proposed design is for a medical device and, therefore, reliability and robustness are of uppermost importance during the treatments. At the operating condition of *Tab.3.3*, the Nb-Ti temperature margin (difference between current sharing temperature, T_{cs} and operating temperature, T_{op}) is 1.5 K, value considered as a good compromise between efficiency

and safety. Regarding the HTS, the temperature margin is in the order of 16-18 K, clearly much more stable in terms of heat disturbance if compared with the LTS version.

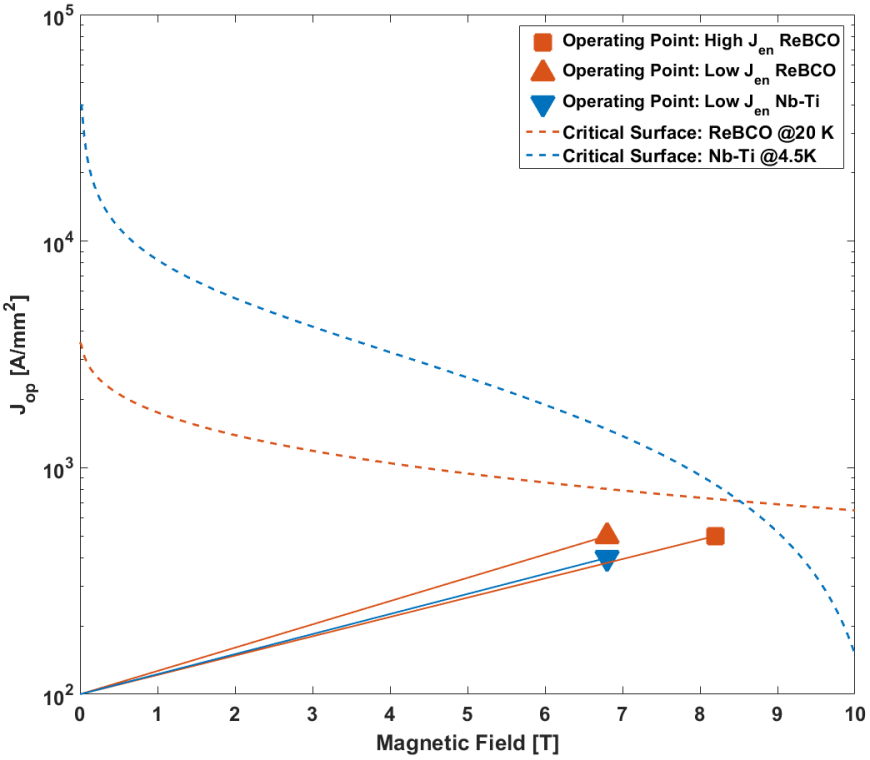

Figure 3.8 *Load lines for the high J_{en} (square) and the low J_{en} (triangles: HTS in red and LTS in blue) configurations. The critical surfaces for ReBCO (red curves) at 20 K Nb-Ti (blue curves) at 4.5 K are reported.*

A detailed description of the cables is provided in *Sec.5.1*, where the analysis on the effects of the current density and copper ratio is described in function of the proposed quench protection system.

3.1.3 Magnetic flux density in the torus bore

Due to the axisymmetric configuration, the magnetic flux density at the isocentre ($\mathbb{X} = 0$ and $\mathbb{R} = 0$), is below the critical threshold for instrumentation and humans safety (order of μT) for both high and low current density configurations, as shown in *Fig.3.9*. Similarly, the flux density rapidly decays with the radius inside the bore and at $\mathbb{R} = 30$ cm is in the order of 10 mT. In the figure, values above 10 mT are in grey.

In case of a loss of symmetry, for instance due to a short-circuit in a coil, the magnetic flux density strongly penetrates inside the bore, as presented in *Fig.3.10*, where the scale is now in 100 mT and values above 100 mT are in grey. In this configuration, the field inside the bore exceeds everywhere the 10 mT and this kind of asymmetric operation must be strictly avoided. For this reason, the quench protection system described in *Sec.5.1* considers the simultaneous discharge of all the coils on external resistors.

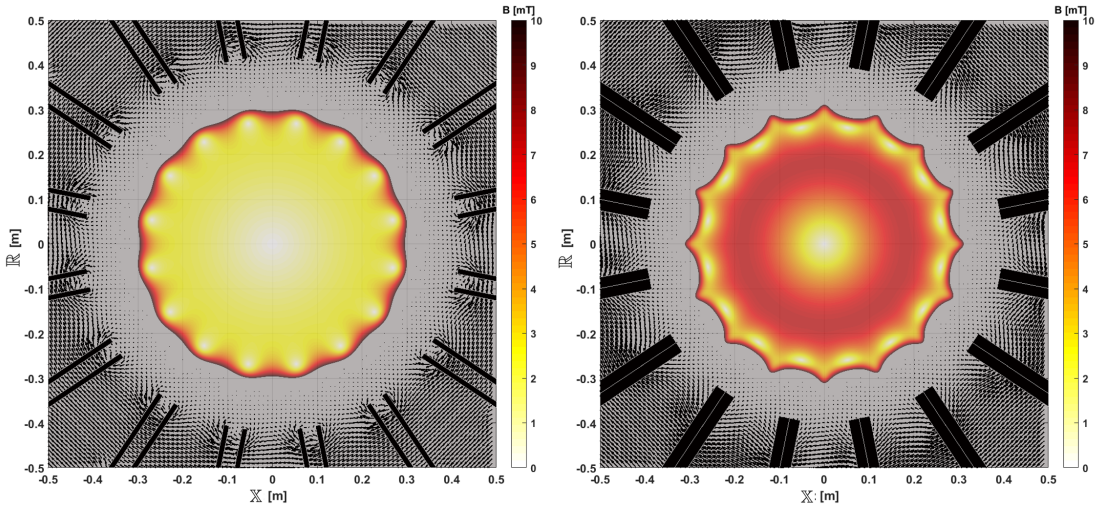

(a) **(b)**

Figure 3.9 *Magnetic flux density in the GaToroid bore region, both for the high current density ($J_{en} = 500\ A/mm^2$)* ***(a)*** *and low current density ($J_{en} = 100\ A/mm^2$)* ***(b)*** *configurations. The colour map indicates values from 1 to 10 mT; the grey area of the bore has a flux density greater than 10 mT.*

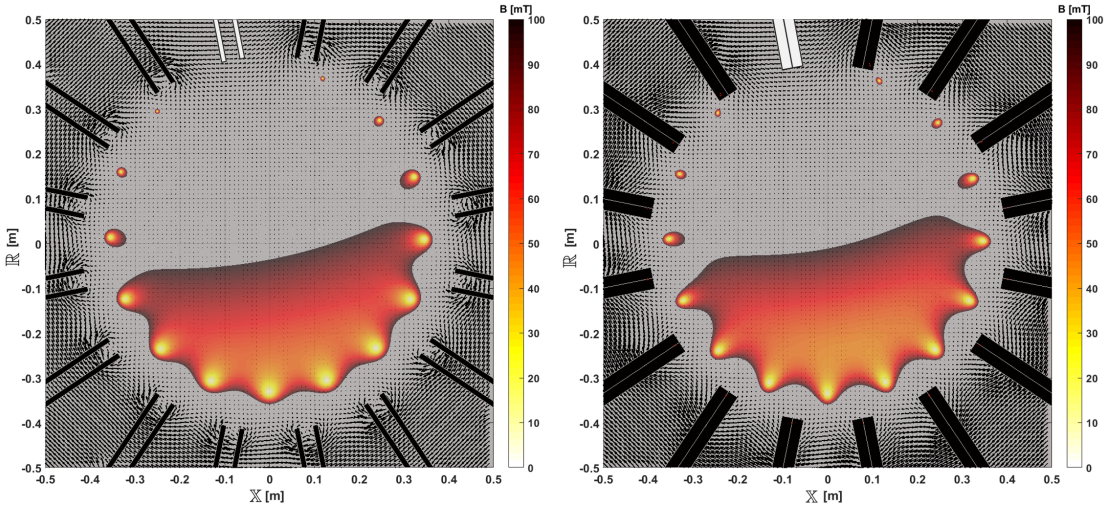

Figure 3.10 *Magnetic flux density in the GaToroid bore region in case of a single coil quench (white coil), both for the high current density ($J_{en} = 500\ A/mm^2$)* ***(a)*** *and low current density ($J_{en} = 100\ A/mm^2$)* ***(b)*** *configurations. The colour map indicates values from 1 to 100 mT; the grey area of the bore has a flux density greater than 100 mT.*

3.2 Magnetic Efficiency

Before entering in detail on the GaToroid beam physics and magnet engineering, it is interesting to investigate the ratio between the magnetic field used to bend the beams and the peak field on the coils. As already mentioned in the previous sections, in an ideal torus, where the number of coils tends to infinity, the flux density inside the coil region is azimuthally constant and equal to:

$$B_\theta = \mu_0 \frac{NI}{2\pi R} \tag{3.4}$$

where NI is the magnetomotive force and R is the radius. For a given gantry configuration, defined by the overall dimensions and the flux density integral $\int B_\theta ds$ along the beam trajectory s, the magnetomotive force can be subdivided in an arbitrary number of coils N.

In a real torus composed by a finite number of coils, the flux density is periodic along the azimuthal coordinate θ and is higher close to the coils while minimum in between [82][83]. As GaToroid uses the symmetry plane between each pair of coils to bend the particles, it is clear that the ratio between the minimum and the maximum magnetic field is fundamental for the design of the gantry. This ratio is here defined as the *magnetic efficiency* of the torus and was used to determine the optimal number of coils to use as a function of the superconducting technology as well as the relative implementation complexity. This section presents an analytical approach is presented to drive the choice of the appropriate number of coils, resulting from a compromise between the magnetic efficiency and the space available for the beam transport.

Considering a set of N infinitely long parallel straight current filaments arranged on a common circle of radius R_a, equally spaced in the azimuthal direction θ and carrying a current I, the azimuthal component of the generated magnetic flux density can be expressed as [84]:

$$B_\theta = \begin{cases} \dfrac{\mu_0 IN}{2\pi R} \dfrac{\rho^2 - \rho cos(N\theta)}{1 - 2\rho cos(N\theta) + \rho^2} & \text{for } R < R_a \\ -\dfrac{\mu_0 IN}{2\pi R} \left\{ \dfrac{\rho^{-2} - \rho^{-1} cos(N\theta)}{1 - 2\rho^{-1} cos(N\theta) + \rho^{-2}} - 1 \right\} & \text{for } R > R_a \end{cases} \tag{3.5}$$

where

$$\rho = \left(\frac{R}{a}\right)^N \tag{3.6}$$

This representation can be used to model a toroidal magnetic flux density [85]. Two sets of N current filaments can be placed at $R = R_1$ (internal radius) and $R = R_2$

(external radius), respectively. These two sets of filaments carry an equal and opposite current I: it flows into the page for $R = R_1$ and out of the page for $R = R_2$ in *Fig.3.11*. Assuming infinite length in the axial direction, these filaments represent the inner and the outer current limb of the toroidal coils, as shown in *Fig.3.12*. The highlighted annular area of *Fig.3.11* is where the toroidal magnetic flux density was calculated: $R_1 < R < R_2$.

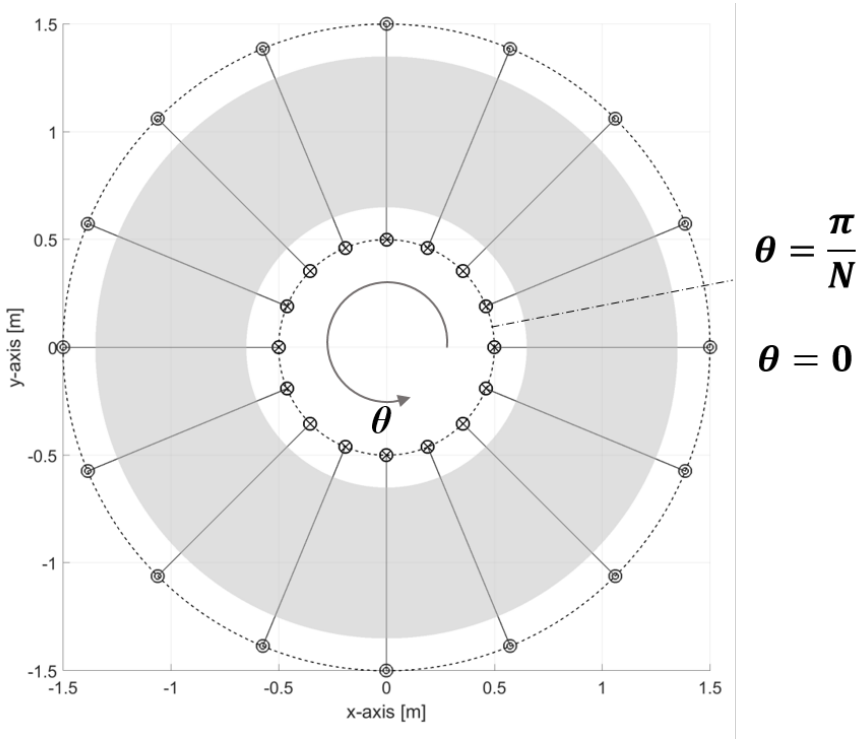

Figure 3.11 *Representation of a set of N=16 current filaments arranged in toroidal configuration. $\theta = 0$ is the peak field region (coil) and $\theta = \pi/N$ is the minimum field region (particles)*

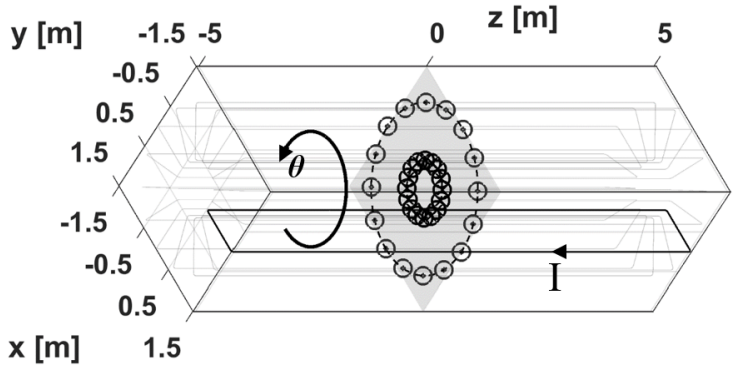

Figure 3.12 *3D representation of a set of N=16 current filaments arranged in a toroidal configuration*

Using *Eq.(3.5)*, the toroidal flux density B_θ can be calculated as superimposition of the effects of the internal radius current lines (for $R > R_1$) and the external radius current lines (for $R < R_2$):

$$B_\theta = \frac{\mu_0 IN}{2\pi R}\left\{\frac{\rho_2^2 - \rho_2 cos(N\theta)}{1 - 2\rho_2 cos(N\theta) + \rho_2^2} - \frac{\rho_1^{-2} - \rho_1^{-1} cos(N\theta)}{1 - 2\rho_1^{-1} cos(N\theta) + \rho_1^{-2}} + 1\right\} \tag{3.7}$$

where

$$\rho_1 = \left(\frac{R}{R_1}\right)^N; \qquad \rho_2 = \left(\frac{R}{R_2}\right)^N \qquad R_1 < R < R_2 \tag{3.8}$$

and N is the number of coils. Considering the filaments aligned at $\theta = 0$ (see *Fig.3.11*), the peak flux density lies on $\theta = 0, \frac{2\pi}{N}, \frac{4\pi}{N}, ...$ Using these values of θ, *Eq.(3.7)* results in:

$$B_{\theta p} = \frac{\mu_0 IN}{2\pi R}\left\{\frac{\rho_2}{\rho_2 - 1} - \frac{\rho_1^{-1}}{\rho_1^{-1} - 1} + 1\right\} \tag{3.9}$$

On the other hand, the minimum flux density, $B_{\theta min}$, is located within each pair of coils, at $\theta = \frac{\pi}{N}, \frac{3\pi}{N}, \frac{5\pi}{N}, ...$, on the ideal trajectory lines of the particle beam:

$$B_{\theta min} = \frac{\mu_0 IN}{2\pi R}\left\{\frac{\rho_2}{\rho_2 + 1} - \frac{\rho_1^{-1}}{\rho_1^{-1} + 1} + 1\right\} \tag{3.10}$$

Using *Eq.(3.9)* and *Eq.(3.10)* is, therefore, possible to evaluate the ratio between the peak field on the torus and the magnetic field used to bend the particles. At *zero-order* this ratio can be used to estimate the magnetic efficiency of the torus, and select consequently a proper number of coils.

Considering a torus with $R_1 = 0.5\ m$ and $R_2 = 1.5\ m$, the results are shown in *Fig.3.13*, as a function of the coil number N for different radii. While for small values of R, the curves easily saturate below 10 coils, at higher radii the difference between the number of coils is quite relevant: more than 20% of variation can be appreciated between the 8 and 16 coil configurations.

Furthermore, it is also interesting to compare the analytical formulae so far described with numerical computations performed with Field2017 [68]. Keeping $R_1 = 0.5\ m$ and $R_2 = 1.5\ m$, the infinitely long current filaments were modelled with a conductor of 1 cm^2 of cross-section and 10 m of length (along the torus axis direction), as shown in *Fig.3.12*. The numerical results are presented in *Fig.3.14* (dashed lines, triangles), in comparison with analytical calculation based on *Eq.(3.7)*.Numerical and analytical calculations are in good agreement, even if small discrepancies (5%) are present at a low number of coils.

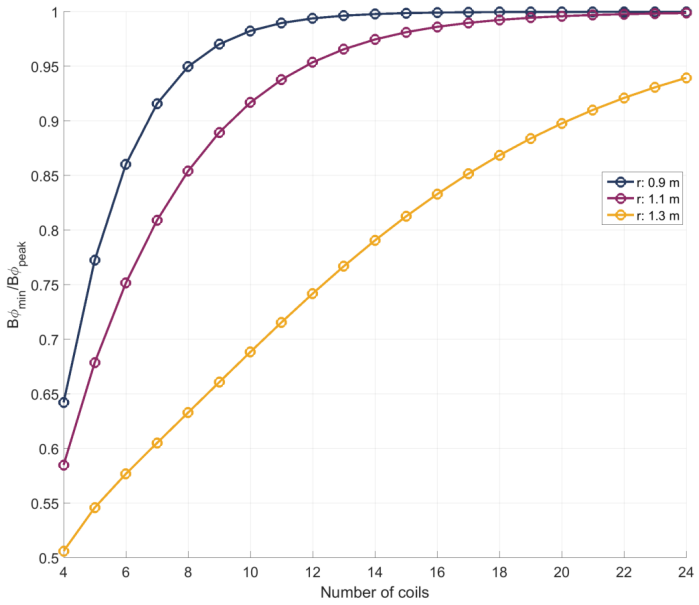

Figure 3.13 *Ratio between minimum and peak toroidal flux densities as a function of the number of coils, plotted for different radius values, in a torus with* $R_1 = 0.5\ m$ *and* $R_2 = 1.5\ m$

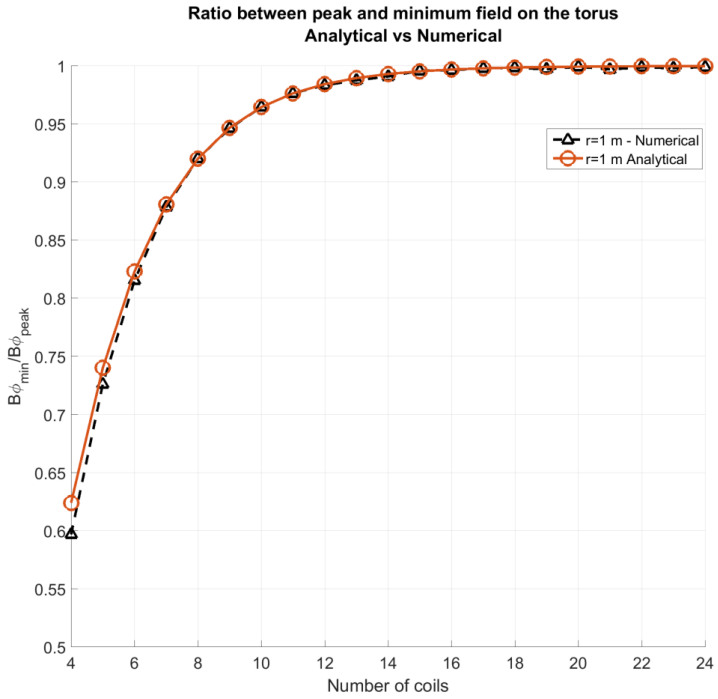

Figure 3.14 *Comparison between analytical (solid lines, circles) and numerical (dashed lines, triangles) results of the ratio between minimum and peak toroidal flux densities as a function of the number of coils, in a torus with* $R_1 = 0.5\ m$ *and* $R_2 = 1.5\ m$*. The plot shows the results for the average radius* $R = 1\ m$

What has been described so far is valid for a classical toroidal configuration, *i.e.* without any grading between the coils. In the next paragraph we analyse the case of a toroid with graded coils, superimposing the effect of each grade, using *Eq.(3.7)* with appropriate R_{1-i} and R_{2-i}, $i = 1...n_{grade}$. The schematic of the optimised GaToroid high J_{en} configuration with 5 grades (detailed described in *Sec.3.1*) is presented in *Fig.3.15*. To be consistent with the definition of equation *Eq.(3.7)*, the $B_{\theta min}/B_{\theta peak}$ ratio can be evaluated only for $R_{1-5} < R < R_{2-5}$ (grey area in *Fig.3.15*).

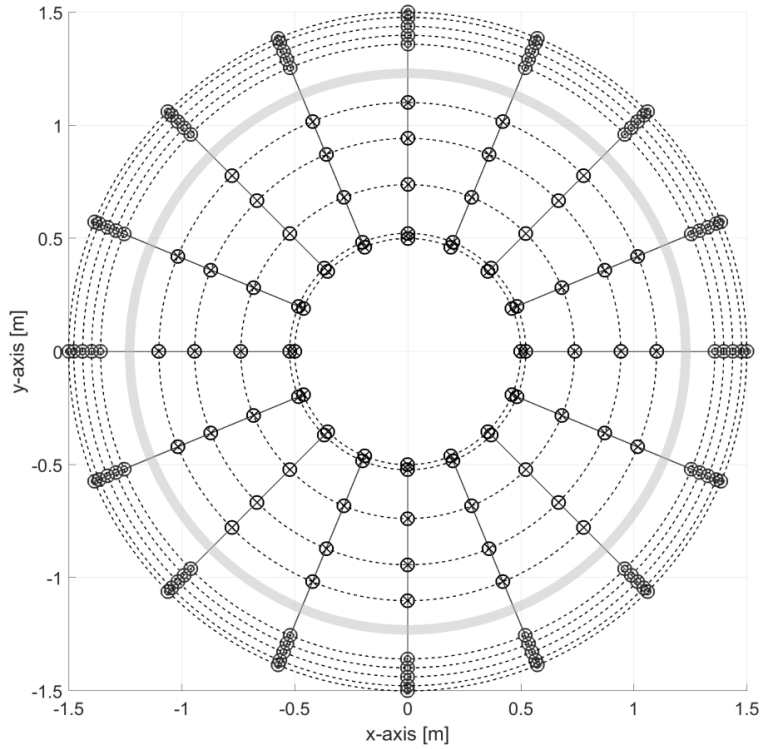

Figure 3.15 *Model of toroidal coils composed by a set of $N = 16$ current filaments, graded in proton GaToroid configuration*

In this case, as shown in *Fig.3.16*, the saturation of the curve is difficult to achieve, but around 16 coils there is a drastic change of slope. With the presented analytical approach, it was possible to the relation between the toroidal field component experienced by the particle beam and the peak field sustained by the coils. On the one side, a high number of coils is desirable to maximise the ratio $B_{\theta min}/B_{\theta peak}$. On the other side, a high number of coils would reduce the space available for the beam transport and introduce not negligible complexity in the construction of the gantry.
Nevertheless, given the complex shape of the GaToroid coils, their asymmetry, aspect ratio (finite axial dimension) and thickness, it is necessary to rely on numerical calculations to precisely evaluate the magnetic efficiency of the machine. Furthermore, the

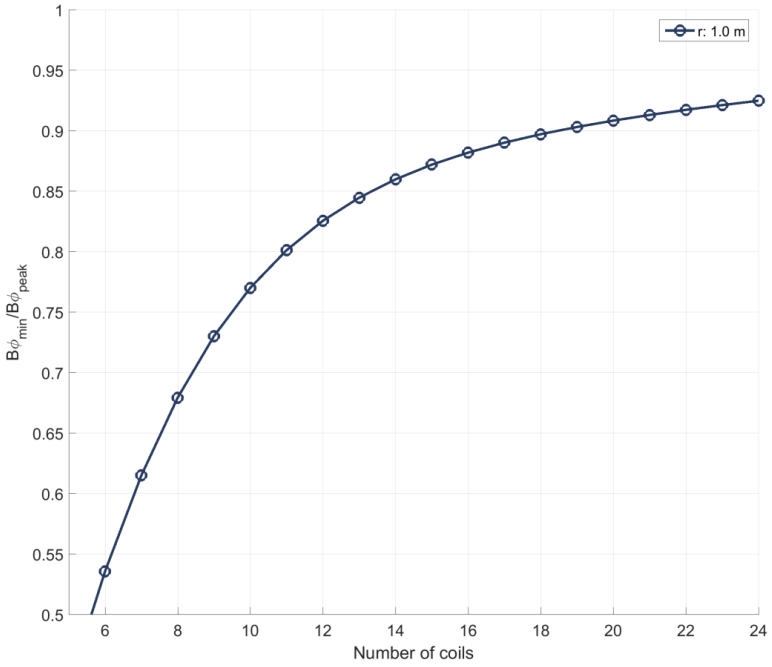

Figure 3.16 *Ratio between peak and minimum toroidal flux densities as a function of the number of coils, plotted for different normalised radii r/r_1, with proton GaToroid coil distribution*

definition of $B_{\theta min}$ and $B_{\theta peak}$ is only valid within the inner and outer radius of the innermost grade, while the particle trajectories cross the great majority of the coil and the inner radius of each grade.

Keeping a constant value of Ampere-turns ($NI = 22.6\ MAt$), the magnetic efficiency of the machine was evaluated as a function of the number of coils. As a reference, the high engineering current density configuration of *Sec.3.1-Tab.3.2* was used for the simulations. *Fig.3.17* shows the magnetic efficiency of the torus as a function of the number of coils, together with the beam aperture, *i.e.* the free space between the coil available for beam transport. The peak magnetic flux density is the maximum flux density on the conductor surface, while the minimum magnetic flux density is calculated in the symmetry plane between the coils at position $\mathbb{Z} = 0$, $\mathbb{R} = 1\ m$. Differently for the analytical solutions, a saturation of the $B_{\theta min}/B_{\theta peak}$ curve cannot be appreciated and the trend of the ratio is almost linear with the number of coils. Nevertheless, the beam aperture between the coils sensibly decreases with the number of coils and above $N = 16$, the available space for the particles is less than 100 mm. As discussed in *Sec.4.5*, this space is used for beam spot scanning in the azimuthal direction and values below 100 mm cannot be considered acceptable.

Moreover, *Fig.3.18* depicts the trends of the peak flux density on the conductor as a function of the number of coils. Although a geometry composed by a reduced number

of coils could seem appealing in terms of beam aperture, costs, and complexity, the resulting peak flux density would require a complete change of technology. More than 28 T are reached in the 4 coils configuration, while 15 T in the 8 coils one. In the first case, the only working solution could be represented by HTS magnets operating (far) beyond 20 T; this is one of the technological challenges of this decade concerning superconducting magnets. An 8-10 coils option would have to tackle similar issues and complexities of ITER Nb_3Sn magnets [86]. 14 and 16 coils configurations operate in the range of Nb-Ti magnets and both can be considered functional solutions. The 16 coil option, with 8.2 T peak flux density, was selected as a compromise between efficiency, aperture and complexity.
Finally, it is interesting to see that configurations with the magnetomotive force ($NI = 22.6\ MAt$) maintain constant values of integrated flux density $\int B_\theta ds$ (for $N > 10$) and can therefore be considered equivalent from the beam optics point of view.

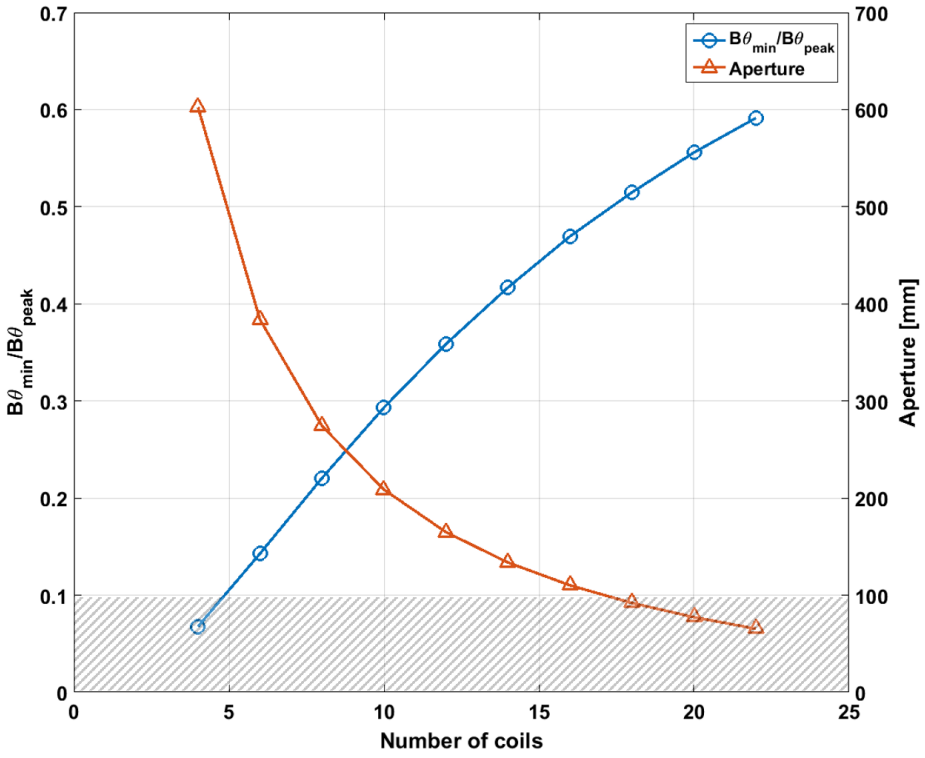

Figure 3.17 *Ratio between peak and minimum toroidal flux densities (blue circles) and beam aperture (red triangles) as a function on the number of coils for the high J_{en} GaToroid configuration. An aperture smaller than 100 mm (grey area) is considered of no interest for beam scanning*

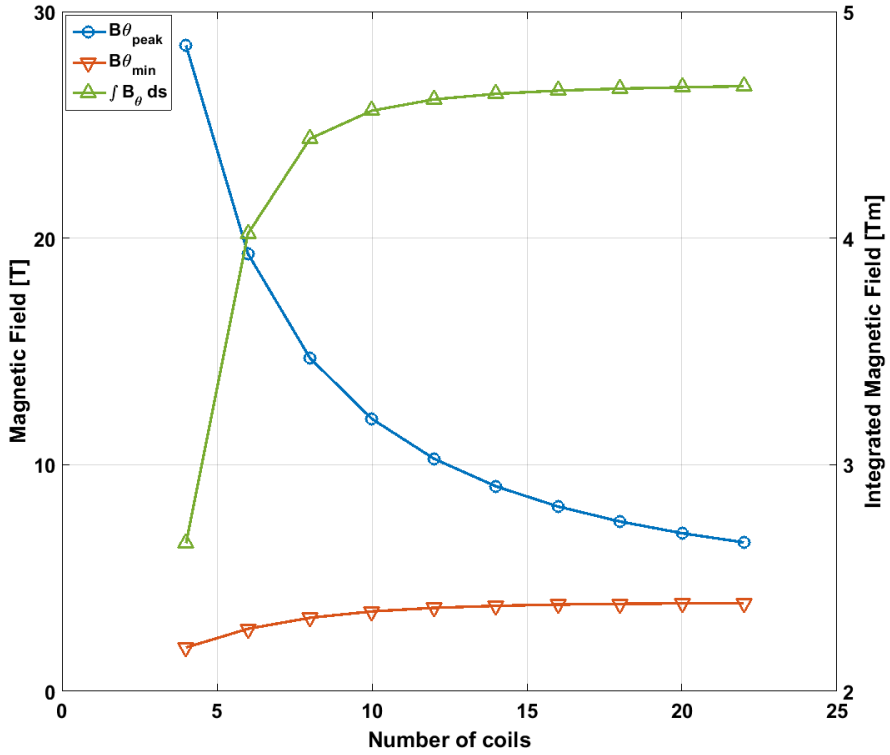

Figure 3.18 *Peak magnetic flux density on the conductor (blue circles), magnetic flux density calculated in the symmetry plane between the coils at* $\mathbb{Z} = 0$, $\mathbb{R} = 1$ *m (red downward-pointing triangle) and the integrated magnetic flux density along the 250 MeV trajectory (green upward-pointing triangle) as a function on the number of coils for the high* J_{en} *GaToroid configuration*

Linear Beam Optics

4

"Remember that all models are wrong;
the practical question is how wrong do they have to be to not be useful"

George E. P. Box, Empirical Model-Building and Response Surfaces, 1978

To analyse and optimise the optical properties of GaToroid, two- and three-dimensional particle tracking codes were developed. Firstly, the two-dimensional particle tracking, fully-coupled with magnetic field calculation, was developed and used to optimise the coil geometry and the magnetic field, to maximise the energy acceptance of the magnet. Around the calculated orbits, a linear beam optics formalism was then developed to perform three-dimensional particle tracking and it was used to determine the focusing properties of the system. These two tools, different in complexity and purpose, were used to evaluate the effect of errors induced by coils misalignment and energy spread in the beam. Finally, the concept of upstream scanning system at the vector magnet was analysed and the relative Source-to-Axis Distance (SAD) was evaluated. In this chapter, the high J_{en} configuration discussed in Sec.3.1 was used as a reference to evaluate the beam optics properties of a GaToroid system. Similar studies were done for the low J_{en} torus and summarized in Appendix II.

The work presented in this chapter is also reported in:
E. Felcini, L. Bottura, J. van Nugteren, A. Gerbershagen, and B. Dutoit *Particle Tracking and Beam Optics Analysis on Toroidal Gantry for Hadron Therapy*, submitted for publication to Focus on Early Career Researchers in Physics in Medicine & Biology, 2020

4.1 Principles of Particle Physics

Before entering in the details of beam optics of the GaToroid system, it may be useful to recall a few concepts of particle physics to clarify the terminology and the

symbols used in the chapter. The total energy of a particle is the sum of its rest energy $E_0 = mc^2$ (m particle mass and c the speed of light) and the kinetic energy K [87]:

$$E_{tot} = E_0 + K \tag{4.1}$$

The kinetic energy K, in MeV, is commonly used to described particle beams for hadron therapy. To change the Bragg peak depth (*range*) in a given material, it is necessary to modify the kinetic energy of the particles. For example, protons are usually accelerated to a range of kinetic energy of 70 MeV to 250 MeV, corresponding to about 38 cm of water range [88].
The Lorentz factor γ_L is given by:

$$\gamma_L = \frac{E_{tot}}{E_0} \tag{4.2}$$

Thus, the velocity of the particle can then be calculated with *Eq.(4.3)* and used for the particle tracking procedures described in the next sections.

$$v = c\sqrt{1 - \frac{1}{\gamma_L^2}} \tag{4.3}$$

The momentum, $p = \gamma_L mv$, can be expressed as:

$$p = \frac{1}{c}\sqrt{E_{tot}^2 - E_0^2} \tag{4.4}$$

The beam rigidity ($B\rho$) is defined as the ratio between the particle momentum and its charge q:

$$(B\rho) = \frac{p}{q} \tag{4.5}$$

This quantity indicates how the particles interact with an applied magnetic field or, in other words, how *rigid* is the beam in relation to the bending force introduced by the magnetic field. Beam rigidity is expressed in Tm and for proton therapy ranges from 1.2 Tm (70 MeV) to 2.4 Tm (250 MeV). Beams of different rigidity are used to deposit the dose at different depths.

The motion of a charged particle subject to a magnetic field is governed by the Lorentz force and is described by:

$$F_L = \gamma_L m\frac{d\mathbf{v}}{dt} = q(\mathbf{v} \times \mathbf{B}) \tag{4.6}$$

where $\mathbf{v}$ and $\mathbf{B}$ are the particle velocity and the magnetic flux density, respectively*. The solution of *Eq.(4.6)* uniquely determines the particle trajectories in vacuum, neglecting the effects of electric fields and beams *self-fields*, *i.e.* space charge and weak-

*The bold notation indicates a vector

fields [89]. Considering a circular orbit, a centripetal force can be associated to a particle:

$$F_{centr} = \frac{\gamma_L m v^2}{\rho} \tag{4.7}$$

where ρ is the radius of curvature. Simplifying *Eq.(4.6)* for a one-dimensional transverse flux density, and combining it with *Eq.(4.7)*, the definition of beam rigidity can be derived:

$$(B\rho) = \frac{\gamma_L m v}{q} = \frac{p}{q} \tag{4.8}$$

In particle accelerators, it is common practice to define the beam properties around an ideal trajectory, s, named orbit. The beam can be represented through the *Twiss parameters*, α and β [90][91]:

$$E(s) = \sqrt{\varepsilon\beta(s)} \qquad \alpha(s) \equiv -\frac{1}{2}\beta(s)' \tag{4.9}$$

where the envelope $E(s)$ indicates the particles oscillation range along the orbit s, ε is the emittance, considered as an invariant of the system and $\beta(s)'$ is the derivative of $\beta(s)$. The parameter β is related to the beam size and α to its first derivative, *i.e.* the tendency of the beam to converge or diverge.

It can be demonstrated that the general solution of the Hill's equation, describing the motion of particles* in a periodic focusing lattice, can be expressed through a parametric equation of an ellipse in the $x - x'$ plane [90]:

$$\gamma(s)x^2(s) + 2\alpha(s)x(s)x'(s) + \beta(s)x'^2(s) = \varepsilon \tag{4.10}$$

where

$$\gamma(s) \equiv \frac{1 + \alpha^2(s)}{\beta(s)} \tag{4.11}$$

The emittance ε, is, within a factor π, the area of the phase ellipse. According to Liouville's theorem, the emittance is an intrinsic beam parameter and cannot be changed by the focal properties. A general ellipse is depicted in *Fig.4.1* for the $x - x'$ plane, and provide a visual representation of the correlation between particle position x and derivative x', as a function of the Twiss parameters α and β. This kind of representation is generally used to describe an entire beam, composed by a Gaussian distribution of particles. Depending on the considered standard deviation (σ), the ellipse encloses a given fraction of the total particles: 68.3% for $\varepsilon_{1\sigma}$, 95.5% for $\varepsilon_{2\sigma}$ and 99.7% for $\varepsilon_{3\sigma}$. In the example of *Fig.4.1*, positive values of positions x are correlated to positive values of derivatives x': as a consequence, the beam is divergent.

*or planets, since George William Hill dedicated his life to the study of celestial mechanics

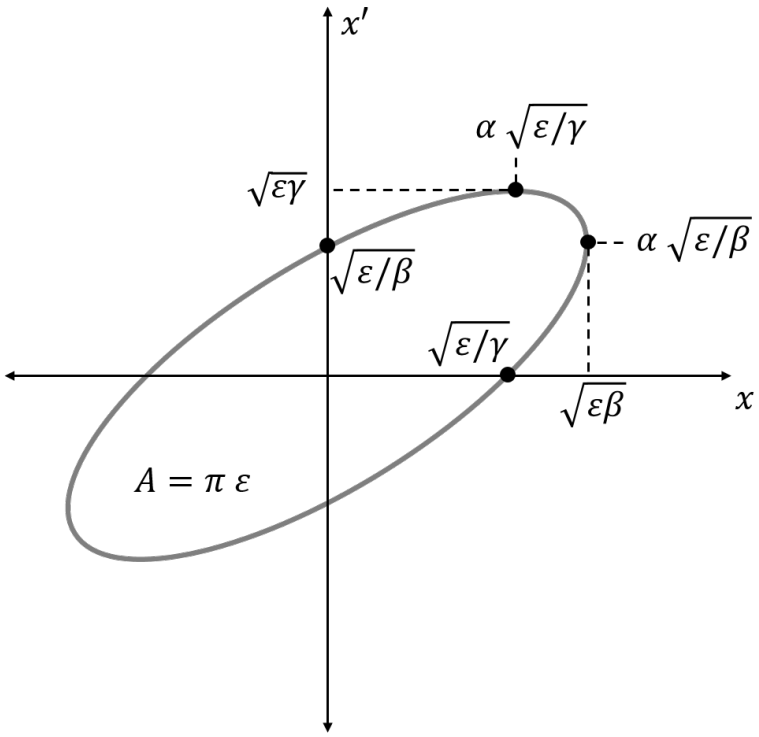

Figure 4.1 *The phase space ellipse in the $x - x'$ plane*

The Hill's equation *Eq.(4.10)* can be written as [90]:

$$\mathbf{X}^T \mathbf{\Sigma}^{-1} \mathbf{X} = \varepsilon \tag{4.12}$$

where $\mathbf{X} = [x, x']$ and $\mathbf{\Sigma}$ is the *beta matrix* define as:

$$\mathbf{\Sigma} = \begin{bmatrix} \beta & -\alpha \\ -\alpha & \gamma \end{bmatrix} \tag{4.13}$$

For a Gaussian distribution of particles, $\mathbf{\Sigma}$ can be interpreted as the covariance matrix of the particles distribution:

$$\mathbf{\Sigma} = \begin{bmatrix} \langle x^2 \rangle & \langle xx' \rangle \\ \langle xx' \rangle & \langle x'^2 \rangle \end{bmatrix} \tag{4.14}$$

For a given set of Twiss parameters, α and β, this covariance matrix can then be used to impose the required correlation between particle positions and velocities.

A more detailed description of the principles of particle physics can be found in [90].

4.2 Transverse particle tracking in 2D - Dipole component

In this section, the algorithm used for the two-dimensional particle tracking is discussed. This algorithm, conceived to be simple and computationally-light, was used for the iterative optimization of the coil geometry and magnetic field in the torus.

Considering the beam rigidity, $(B\rho)$, and a local transverse magnetic flux density at position s, $B_x(s)$, the local radius of curvature, $\rho(s)$, is defined in each point as:

$$\rho(s) = \frac{(B\rho)}{B_x(s)} \tag{4.15}$$

For a given orbit s, it is possible to associate a co-moving coordinate system (z, y), as shown in *Fig.4.2*, that rotates accordingly with the beam locally bent by the magnetic field [90]. With a change of coordinates, infinitesimal variations in the global reference

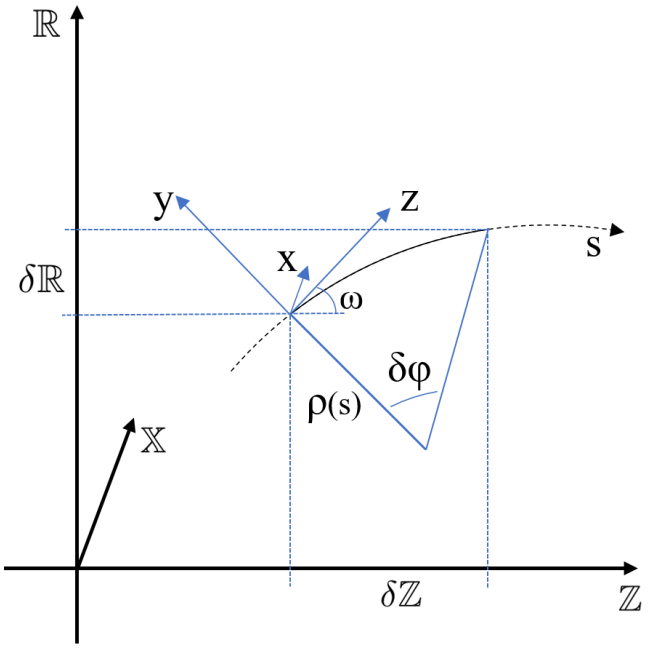

Figure 4.2 *Representation of the global reference system* $(\mathbb{Z}, \mathbb{R}, \mathbb{X})$ *and co-moving coordinate system* (z, y, x) *along the orbit* s

system $(\mathbb{Z}, \mathbb{R})$ can be expressed as:

$$\begin{aligned} \delta\mathbb{Z} &= sin(\omega)\rho(s)(1 - \cos(\delta\varphi)) + \cos(\omega)\rho(s)\sin(\delta\varphi) \\ \delta\mathbb{R} &= -cos(\omega)\rho(s)(1 - \cos(\delta\varphi)) + \sin(\omega)\rho(s)\sin(\delta\varphi) \end{aligned} \tag{4.16}$$

where ω is the angle between the co-moving and the global coordinate system (between z and $\mathbb{Z}$), and $\delta\varphi$ is the angle between two consecutive steps at distance δs, $(\delta\varphi = \delta s/\rho(s))$. The local reference system rotates around the $\mathbb{X}$ axis (cohicindent

with x); z is tangential and y is orthogonal to the orbit s. In the symmetry plane between each pair of coils the toroidal magnetic field is orthogonal to the particle velocity and the integration of *Eq.(4.16)* can be used to calculate two-dimensional trajectories at different kinetic energies, *i.e.* 70-250 MeV for protons.

This algorithm for particle tracking was used for iterative optimisation of the coil geometry [92]. By iterating on the magnet profile described by *Eq.(2.4)* and on the current distribution inside the coil (*coil grading*), it was possible to minimise the distance between the focal points of different energies at isocentre in the whole treatment spectrum*. The results of the two-dimensional particle tracking optimisation are presented in *Fig.4.3* for the complete energy range of proton treatments together with the magnetic field map produced by the whole torus in the symmetry plane.

Concerning the flux density map, it is interesting to note that the magnetic flux density value at the isocentre is in the order of μT (see *Sec.3.1.3*). As expected from a toroidal magnet, the magnetic flux lines are closed, resulting in negligible values of the magnetic field at the isocenter.

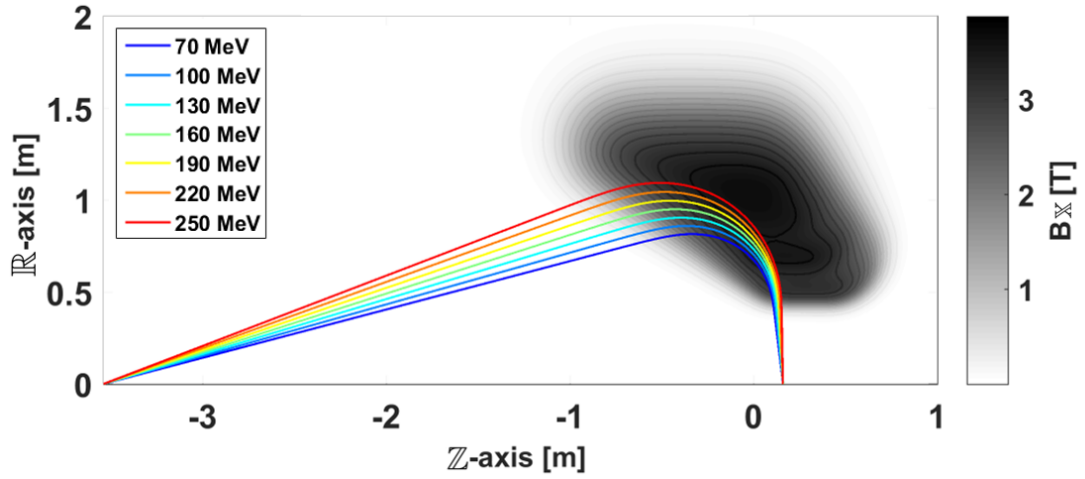

Figure 4.3 *Two-dimensional particle tracking over the whole proton treatment energy range (solid lines), together with the transversal magnetic flux density $B_{\mathbb{X}}$ (greyscale map) generated by the optimised coil*

The solutions of the simplified *Eq.(4.6)* so far described represent the ideal trajectories of the particle beams at different energies: the orbits. Given the fact that the vector magnet imposes a different steering angle for each beam rigidity, the central trajectory of the beam is different for each beam rigidity . In other words, different orbits, around which the formalism of linear beam optics described in *Sec.4.3* was developed, correspond to beams with different energies.

*The detailed description of the GaToroid magnetic optimization is presented in *Chap.5*

Building upon the light and fast algorithm for the two-dimensional tracking, a statistical misalignment error study was performed on the coil positions. More precisely, 100 different displacements following a normal random distribution were applied at each grade of the 16 coils in the 3 dimensions. The means of the applied errors were 0 and the standard deviations corresponded to the imposed values, namely, 1 mm and 0.5 mm. The deviation of the beam position at the isocentre induced by these errors are presented in *Fig.4.4* over the whole spectrum of energies. The mean standard deviation (*mean std.* in the plot) was calculated as follows: for each energy, the standard deviation of the position differences from the nominal value is computed. The mean standard deviation is then presented in the plots as a black dashed line. The mean value standard deviations were 0.7 mm and 0.4 mm, for imposed errors of 1 mm and 0.5 mm, respectively. Given the fact that the position of the isocentre must have an accuracy below 1 mm for clinical specifications, this value was used as a threshold.

The trend of standard deviations is reported in *Fig.4.5* as a function of beam energy. *Fig.4.4*a and *Fig.4.5* exhibit that with a misalignment of 1 mm the position error easily exceeded *locally* the threshold, as well as the standard deviation at 70 MeV approaches 0.9 mm. Considering a misalignment error of 0.5 mm, the resulting maximum standard deviation was below 0.5 mm and just 3% of the local peaks were above the threshold for the 70 MeV case.

Consequently, the limit of 0.5 mm was considered an appropriate misalignment constraint. It is important to note that this kind of alignment precision is not trivial to achieve due to the overall size of the machine (outer diameter of about 3 metres) , its weight (10-15 tons) and cryogenic operating conditions.* Nevertheless, the effects induced by a static (non-variable in time) coil misalignment can be partially compensated during the commissioning phase by adjusting the input angle at the vector magnet.

*the LHC main dipole extremities are aligned with a precision of ± 0.3 mm

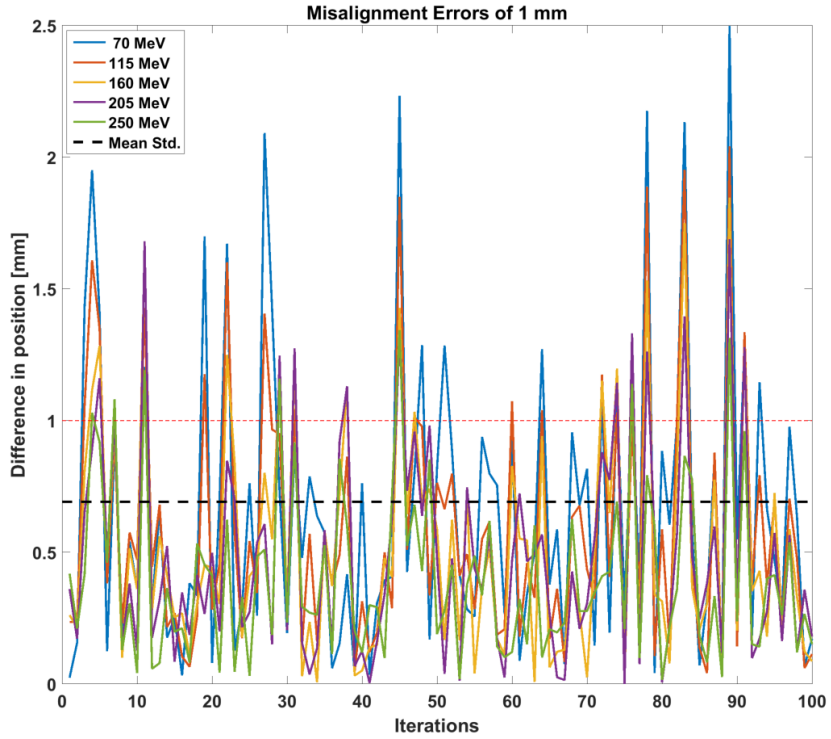

(a)

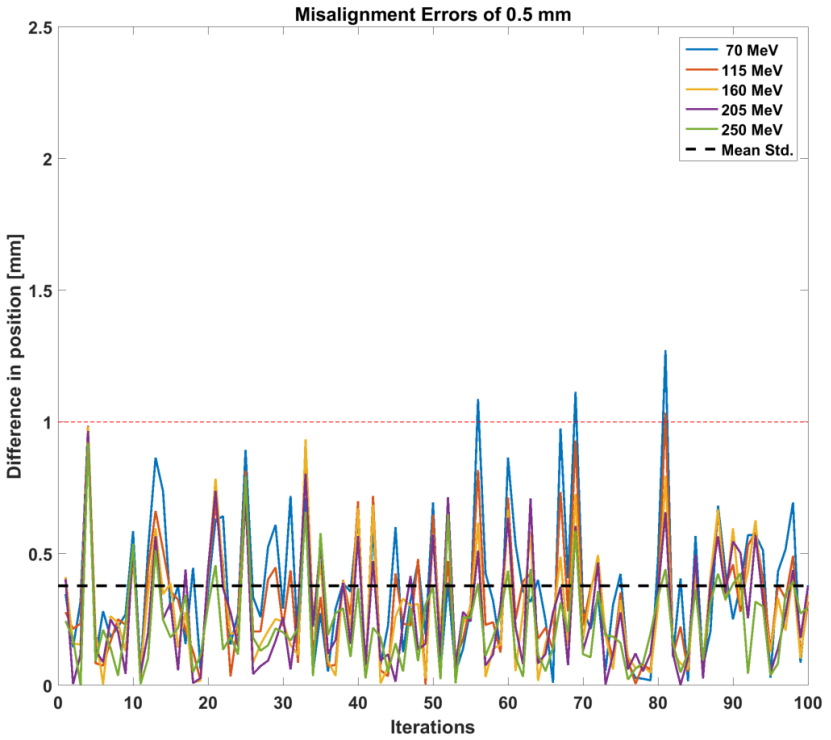

(b)

Figure 4.4 *Isocentre position error induced by a misalignment distribution with standard deviation of 1 mm* ***(a)*** *and 0.5 mm* ***(b)*** *in the whole range of treatment energy. The threshold (red dashed lined) and the average on the energies of the standard deviations (black thick dashed line) are shown.*

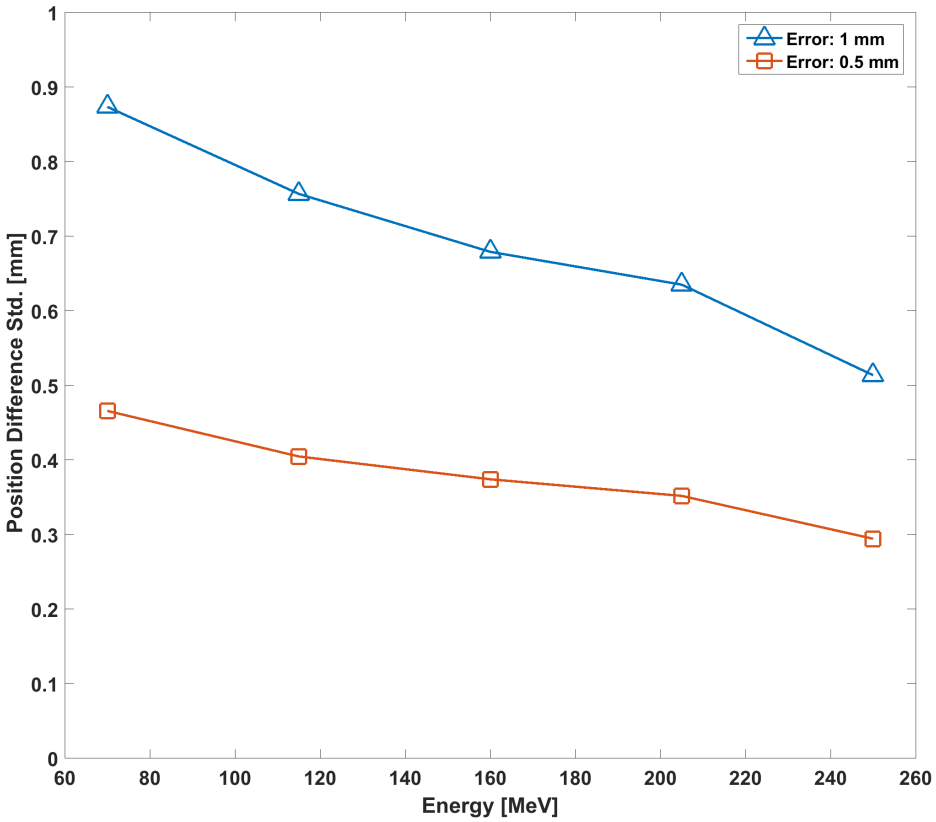

Figure 4.5 *Standard deviation of the position difference at the isocentre resulting from an applied misalignment error of 1 mm (blue triangles) and 0.5 mm (red squares) as a function of beam kinetic energy.*

4.3 Transverse particle tracking in 3D

Once assessed the possibility of directing the orbit at the isocenter in the whole range of treatment energy, it is interesting to evaluate the effects of the GaToroid magnetic field on a realistic beam. In this section, the algorithm for the three-dimensional tracking is presented and used to investigate the focusing properties of the gantry.

Considering a particle beam of finite transverse dimensions, the interaction between the particles and magnetic field can be no longer limited to the symmetry plane between coils. Therefore, a complete solution of the three-dimensional equation of motion of charged particles in a magnetic field, described by *Eq.(4.6)*, was required. As presented in *Fig.4.2*, along each orbit s, derived from the two-dimensional tracking, it is possible to define the co-moving transverse plane $(x-y)$, where classical transverse beam dynamic theory can be applied. Around each orbit s the properties of the beam, *i.e.* the Twiss parameters (α and β) were defined.

Using the Twiss parameters, it is possible to generate the corresponding particle distributions. In order to do that, it is necessary to introduce the appropriate correlation between particle positions and velocities. Starting from uncorrelated Gaussian distributions of particle positions, x_{uc}, and derivatives, x'_{uc}, the Cholesky transformation was applied to obtain the desired correlation [93] [94] [95]. The Cholesky transformation is commonly used in Monte Carlo methods for simulating systems with multiple correlated variables. The covariance matrix of *Eq.(4.13)* was decomposed, giving the lower-triangular matrix L:

$$\Sigma = LL^T \tag{4.17}$$

The application of the L matrix to a vector of uncorrelated samples resulted in a vector with the covariance properties of the system being modelled, *i.e.* the correlation between position and velocity dictated by α and β:

$$\begin{bmatrix} x \\ x' \end{bmatrix} = L \begin{bmatrix} x_{uc} \\ x'_{uc} \end{bmatrix} \tag{4.18}$$

In this way, the Twiss parameters were *translated* into particle position and velocity distributions. Naturally, the same approach was applied to the $y - y'$ phase space to model the beam parameters on the other plane. As an example, *Fig.4.6* graphically shows the effect of the Cholesky transformation on an uncorrelated particle distribution, where $\alpha = 1$ and $\beta = 5$ m were specified.

Using *Eq.(4.14)* and *Eq.(4.13)*, the α and β of the correlated particle distribution were recalculated to verify the accuracy of the Cholesky transformation. Discrepancies below 1% were observed simulating at least 10,000 particles. This kind of error was

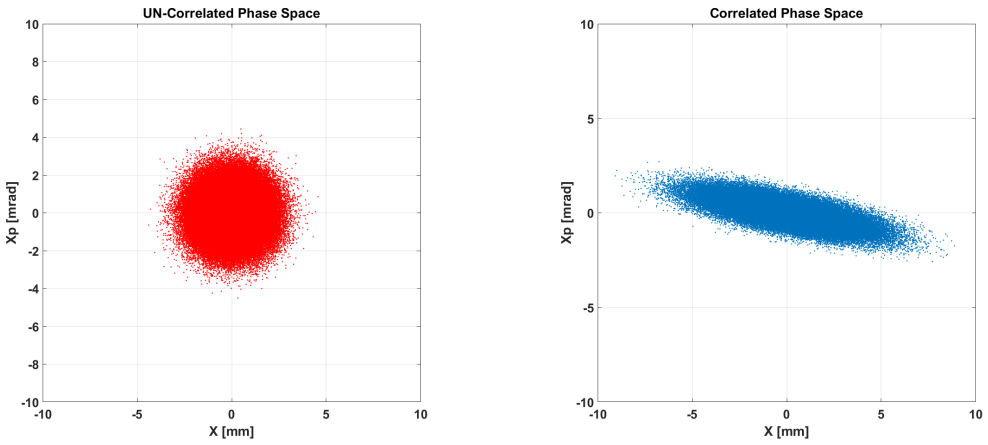

Figure 4.6 *Generic particles distribution on the x-x' phase space before* ***(a)*** *and after* ***(b)*** *the application of the Cholesky transformation with* $\alpha = 1$ *and* $\beta = 5$ *m*

considered acceptable and to save computational time during the particle tracking, the presented simulations were limited to 100,000 particles following random normal distributions of positions and velocities in both planes.

The correlated particle distributions were then imposed transversally at the orbit corresponding to a given beam energy on (x-y) plane of *Fig.4.2*. The relation between local (of the beam: x, y, z) and global ($\mathbb{X}, \mathbb{Z}, \mathbb{R}$) reference systems at the beginning of the tracking algorithm (at the vector magnet: $\mathbb{Z} = Z_v$ and $\omega = \alpha_E$) are:

$$\begin{aligned} \mathbb{X} &= x \\ \mathbb{Z} &= y\cos\alpha_E - z\sin\alpha_E \\ \mathbb{R} &= y\sin\alpha_E + z\cos\alpha_E \end{aligned} \tag{4.19}$$

$$\begin{aligned} v_{\mathbb{X}} &= v\sin x' \\ v_{\mathbb{Z}} &= v(\cos y'\cos\alpha_E - \sin y'\sin\alpha_E)\cos x' \\ v_{\mathbb{R}} &= v(\cos y'\sin\alpha_E + \sin y'\cos\alpha_E)\cos x' \end{aligned}$$

where v is the particle velocity calculated using relativistic correction expressed by *Eq.(4.3)*. Acting on the distribution of particles' kinetic energy, an arbitrary momentum spread can be introduced, dp/p, in the beam.

The solution in three-dimensions of *Eq.(4.6)* was performed through a six-stage, fifth-order, Runge-Kutta method (MATLAB ode45 [96]). The magnetic field map was calculated with Field2017 [68], using a direct Biot-Savart method on a cubic mesh with 3 mm edges in the space between a pair of coils, with a margin of 50 cm on $\mathbb{Z}$-axis

to properly consider the stray field outside the tours; it resulted in about 10 million points. During the solution of *Eq.(4.6)*, the field was then interpolated for each particle with a cubic function.
Although the proposed algorithm can, in principle, also deal with longitudinal particles distributions, the presented analyses were done considering a pure transverse beam, neglecting any longitudinal effect. Furthermore, this method does not take into account any particle interaction with matter, assuming vacuum conditions down to the patient. The multiple scattering effects on the beam travelling through ionisation chambers, air gaps and patient equivalent tissues were estimated in previous works through dedicated MonteCarlo simulations [46].

At first, the case of a parallel beam ($\alpha_x = \alpha_y = 0$) was analysed. The high J_{en} toroidal configuration presented in *Sec.3.1* was taken as a reference and the parameters listed in *Tab.4.1* were used for the particle tracking. Since a broad kind of accelerators [12][11], *i.e.* cyclotrons, synchrotron or linacs, could be used to feed the gantry, a reference value of $\varepsilon_{1\sigma} = 1$ mm mrad was selected (where $\varepsilon_{1\sigma}$ is the 1σ normalised emittance). The results from the tracking of 10^5 particles at 250 MeV with no momentum spread, $\Delta p/p = 0$, are shown in *Fig.4.7* and in the *Output* column of *Tab.4.1*. The presented results made quite clear that the beam was defocused while

Transverse beam optics parameters			
Parameter	Unit	Input	Output
K	[MeV]	250	250
$N_{particles}$		10^5	10^5
$\Delta p/p$		0%	0%
$\varepsilon_{x-1\sigma}$	[mm mrad]	1	1
$\varepsilon_{y-1\sigma}$	[mm mrad]	1	1
α_x		0	-69
β_x	[m]	10	122
α_y		0	-15
β_y	[m]	10	17

Table 4.1 *250 MeV beam input and output parameters*

crossing the magnetic field of GaToroid: the beam x-size increased by a factor 3*. This phenomenon seems to be counter-intuitive, if compared with the focusing properties of an ideal torus explained in *Chap.2*. However, the presence of a discrete number of coils deforms the fields introducing a gradient in the opposite direction. As explained

*$\beta_{x-OUT} \approx 10\beta_{x-IN}$. Let's remind that the beam envelope $E(s) = \sqrt{\varepsilon\beta(s)}$. Follows that $E_{x-OUT} \approx \sqrt{10}E_{x-IN}$

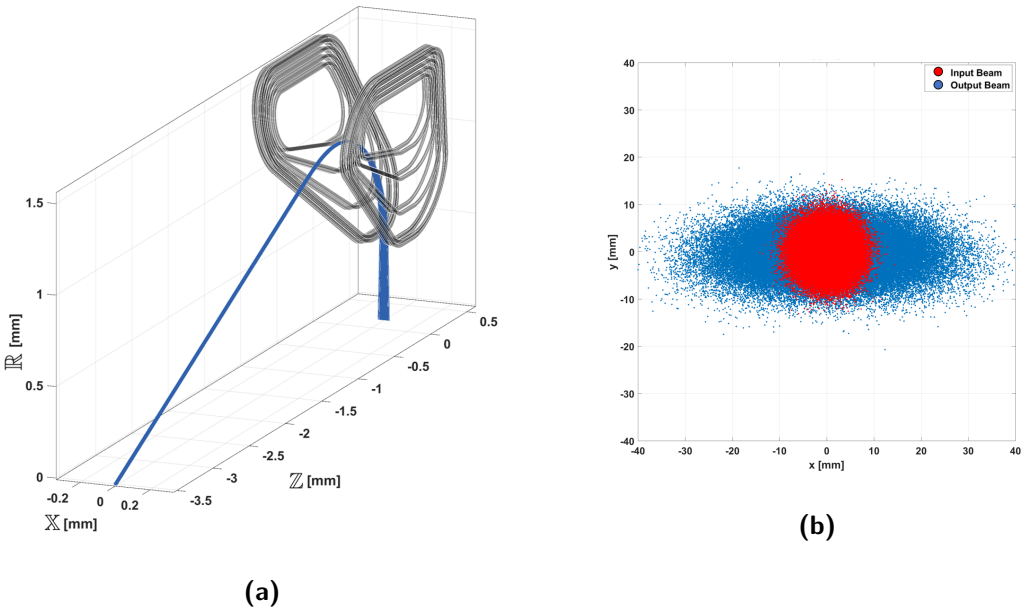

Figure 4.7 *Particle trajectories together with two coils of the torus* ***a)*** *and the particle distributions at the exit of the vector magnet (red) and the isocentre (blue) for a 250 MeV parallel beam described in Tab.4.1* ***b)***

in *Fig.4.8*, the ideal toroidal flux lines (black lines) are deviated in the proximity of the conductors. For a particle entering into the page, at the inner radius location the resulting field (blue lines) generates a defocusing gradient, while at the outer radius it generates a focusing gradient*. In the picture, the current flows into the page on the bottom part of the coil (circle-cross) and flows out of the page in the top part of the coil (circle-point). This behaviour can be observed in *Fig.4.9*, where the simulated magnetic flux lines are presented for the GaToroid system. This defocusing feature can also be analysed through the field components. Considering a line placed at the entrance of the 250 MeV beam into the torus (blue line in *Fig.4.10*), it is possible to evaluate the magnetic field and its effect on the beam. *Fig.4.11a* indicates the presence of a sextupole component (Bx) on top of the bending field (Bx_0), while By and Bz are defocusing gradients (quadrupole). Considering the backside of the torus (*Fig.4.10*, red line), a mirror picture can be observed, where the gradients are now reversed and are focusing the beam. These field snapshots can be the basics for the idea of using a series of focusing and defocusing co-axial toroidal magnets to generate an achromatic configuration [66] [61] [64].

Given the natural defocusing features of GaToroid, it was necessary to adjust the Twiss parameters at the vector magnet to obtain a beam able to fulfil clinical re-

*of course, the opposite consideration must be done for a particle coming out of the page

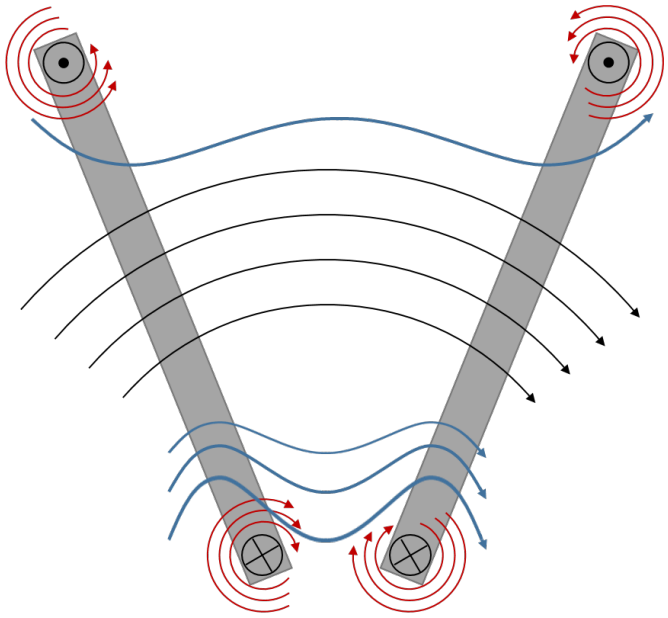

Figure 4.8 *Concept of the defocusing effect introduced by the field deviation in the coil proximity. The ideal toroidal field (black lines) is deviated by the local magnetic field around the conductor (red lines) and the resulting field (blue lines) has an opposite concavity toward the inner radius. The current flows into the page on the bottom part of the coil (circle-cross) and flows out of the page in the top part of the coil (circle-point).*

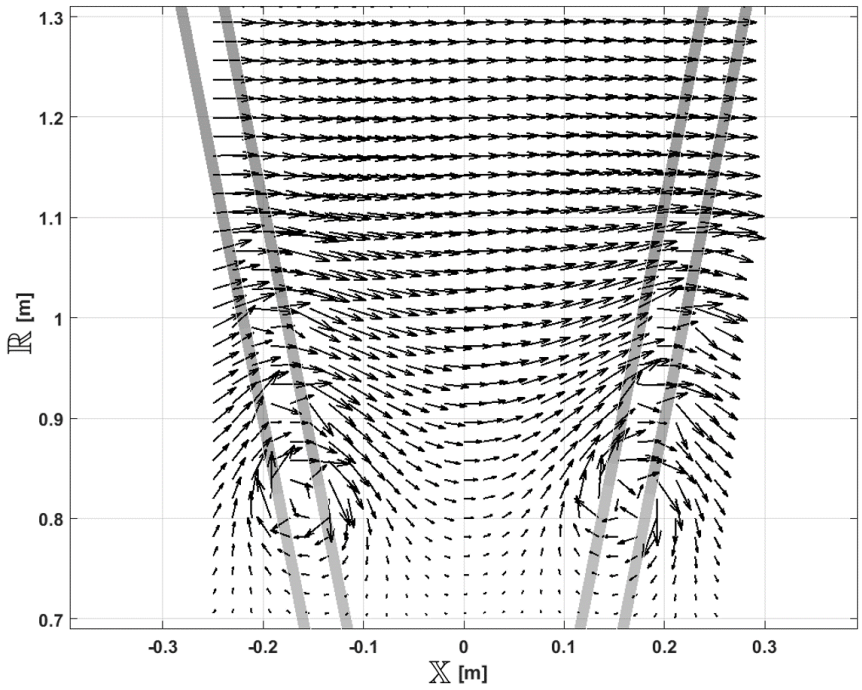

Figure 4.9 *Simulated magnetic flux lines close to the coils*

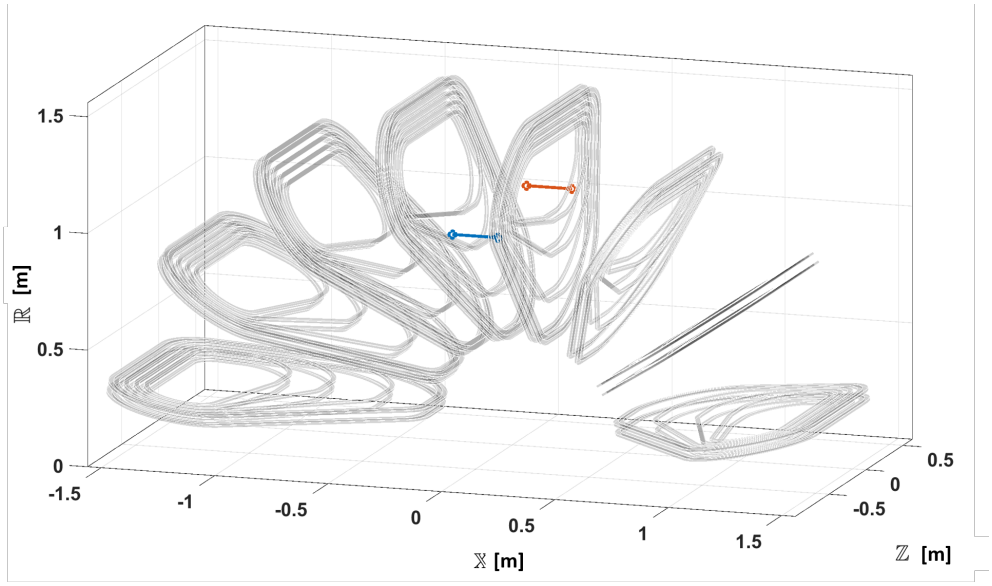

Figure 4.10 *Entrance (blue) and backside (red) lines used to evaluate the magnetic flux density components presented in Fig.4.11*

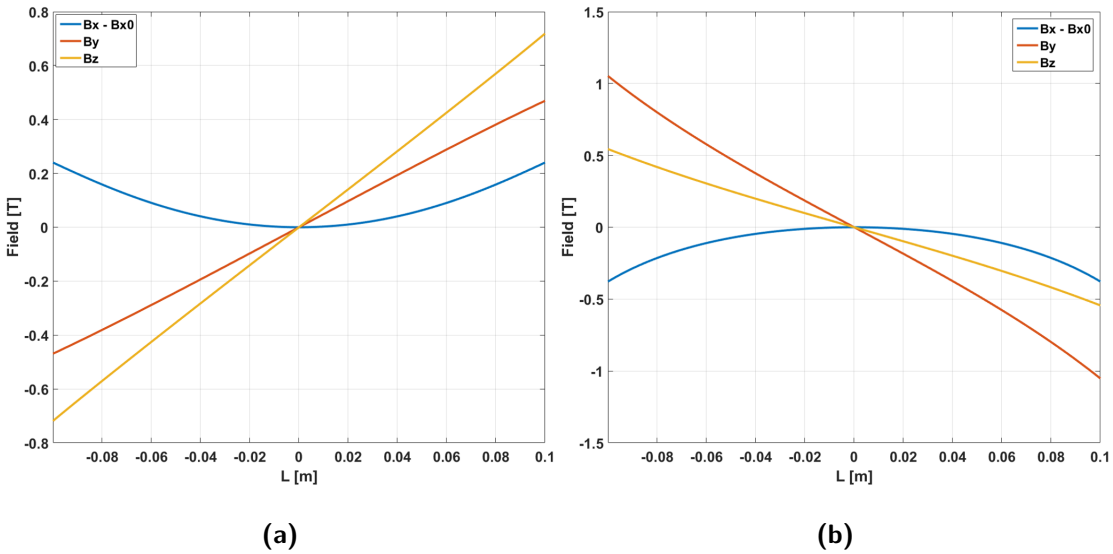

Figure 4.11 *Magnetic flux density components on the entrance* ***a)*** *and backside* ***b)*** *lines shown in Fig.4.10*

quirements. Concentrating the analysis on the high J_{en} configuration and using the parameters of a convergent beam listed in *Tab.4.2*, it was possible to obtain adequate beams at isocentre over the whole energy spectrum. For the sake of clarity, constant input Twiss parameters over the whole energy spectrum were used, but ad hoc adjustments on α and β at the vector magnet may be used to refine the output beam (classical matching procedure). The trajectories of the 10^5 particles at 250 MeV tracked inside

Transverse beam optics parameters		
Parameter	Unit	Input
$N_{particles}$		10^5
$\Delta p/p$		0%
$\varepsilon_{x-1\sigma}$	[mm mrad]	1
$\varepsilon_{y-1\sigma}$	[mm mrad]	1
α_x		9.5
β_x	[m]	35.0
α_y		4.8
β_y	[m]	20.0

Table 4.2 *Input parameters used for the particle tracking over the whole spectrum of treatment energies (70-250 MeV)*

the GaToroid magnetic field are reported in *Fig.4.12*. The figure also presents a zoom at the vector magnet location ($\mathbb{Z} = -z_v$), showing the reference orbit (red line) resulting from the two-dimensional tracking, and the reference plane (dashed line), where the input beam parameters are defined. *Fig.4.13* shows the particle distributions at the vector magnet exit (in red), imposed as input, and at the isocentre (in blue), resulting from the multi-particle tracking. Furthermore, the phase spaces in $x - x'$ and $y - y'$ are reported in *Fig.4.14*. Using the same input Twiss parameters listed in *Tab.4.2*, the three-dimensional particle tracking was done in the complete energy range and the results are summarised in *Fig.4.15*. Although for high energies the beams have round shape, the x-dimension became larger at low energies creating an asymmetric beam profile. Making use of a matching section (quadrupoles) placed upstream of the vector magnet, it should be possible to adjust the Twiss parameters at isocentre to the desired values. The matching can be practically performed through classical accelerator codes (*e.g.* MADx [97]) using the extrapolated transfer matrices (see *Sec.4.4*), avoiding the complexity of a three-dimensional particle tracking optimisation. Since the design of the vector magnet is in an early stage of design, it was not possible to perform an accurate matching procedure. The presented results are aims to demonstrate the validity of the developed three-dimensional particle tracking method between the end of the

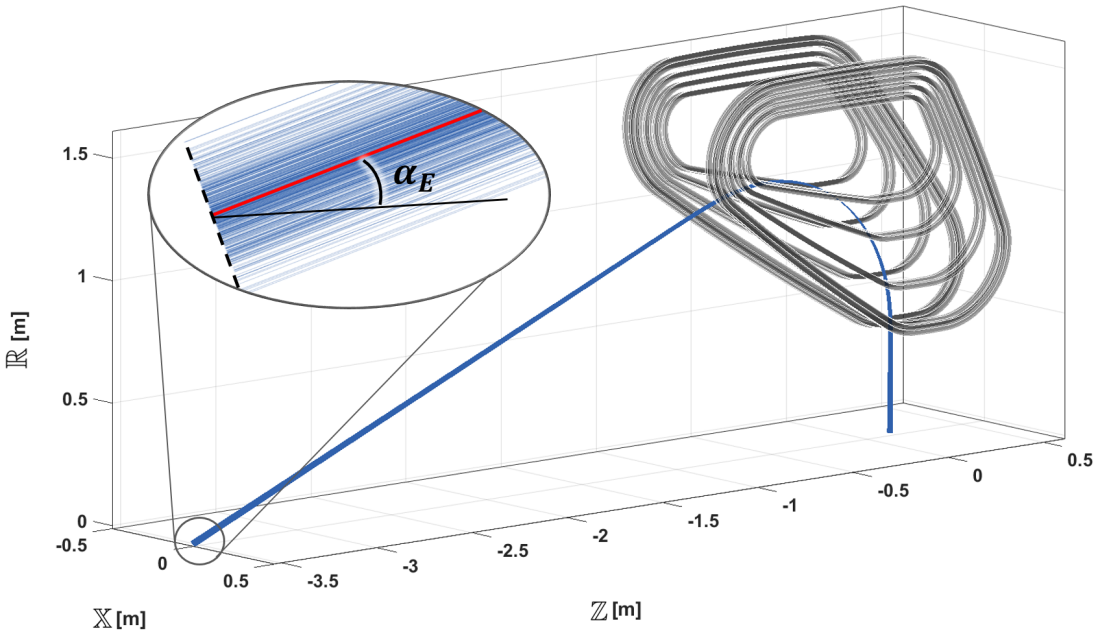

Figure 4.12 *Particle trajectories for a 250 MeV beam described in Tab.4.2 together with two coils of the torus. A zoom view at $\mathbb{Z} = -z_V$ shows the reference orbit (in red) and the reference plane (dashed line)*

vector magnet and the isocentre.

Applying the β-function definition, the beam envelope can be calculated as $E = \sqrt{\varepsilon_{1\sigma}\beta}$: it represents the beam radius at 1σ value of the Gaussian distribution. At 250 MeV, the beam envelope is 2.1 mm in both planes, while at 70 MeV is 5.5 mm and 1.5 mm in x and y respectively. This difference in size is also presented in *Fig.4.16*, where the x and y profile are shown at isocentre for 70 and 250 MeV tracking. Although the Gaussian profile is maintained for both cases, the beam asymmetry is clear in the low energy case.

However, it is worth to underline that for low beam energies the multiple scattering in air and patient tissues becomes the main factor that determines the beam spot size [46]. This phenomenon should completely overcomes the difference in beam size.

In addition, as shown in *Fig.4.15*, the negative values of α indicate divergent beams in both planes at isocentre, especially at low energies. Also in this case, the multiple scattering affects the divergence and up to $\alpha = \pm 100$ it dominates the direction of the beam [46].

Overall, the presented results indicates that the beam properties at the isocentre should be coherent with the clinical requirements, both for the beam size and divergence.

Nevertheless, given the long-bending region inside the torus, the beam dispersion

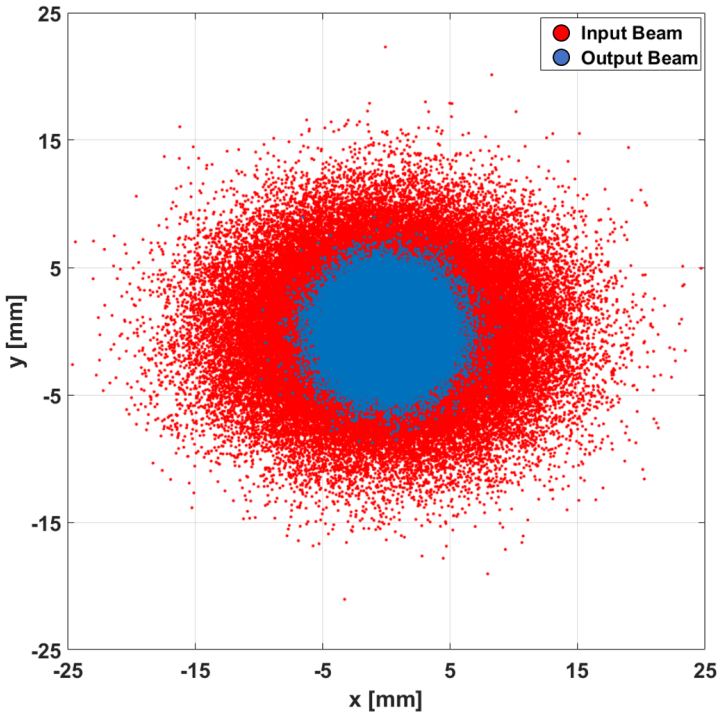

Figure 4.13 *Particle distributions at the exit of the vector magnet (red) and at the isocentre (blue), resulting from the tracking of* 10^5 *particles with Gaussian transverse distribution at 250 MeV*

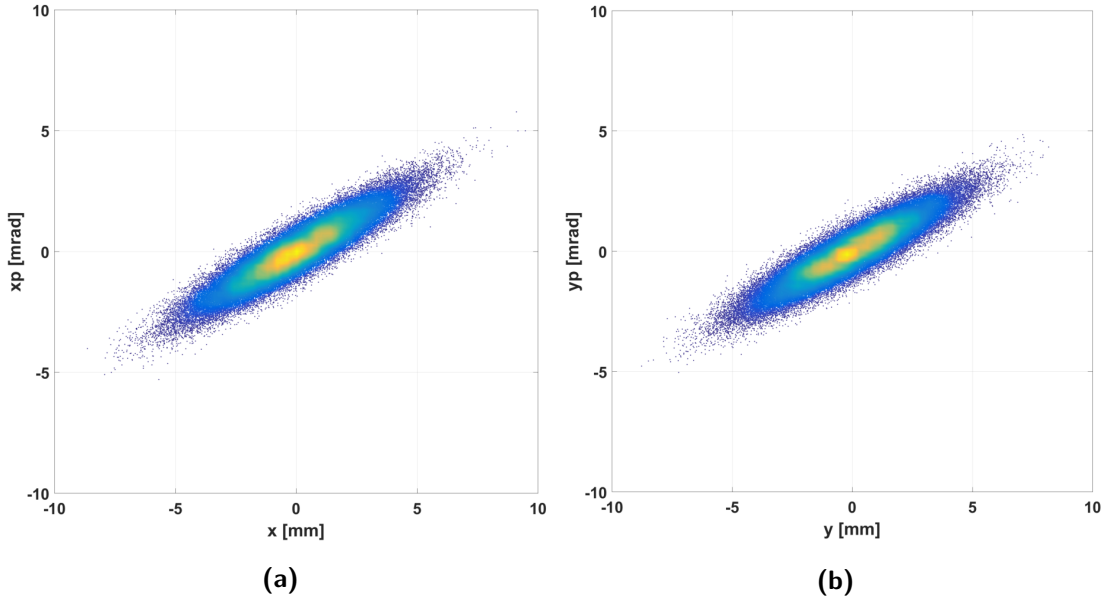

Figure 4.14 $x - x'$ ***(a)*** *and* $y - y'$ ***(b)*** *phase space at isocentre, resulting from particle tracking at 250 MeV*

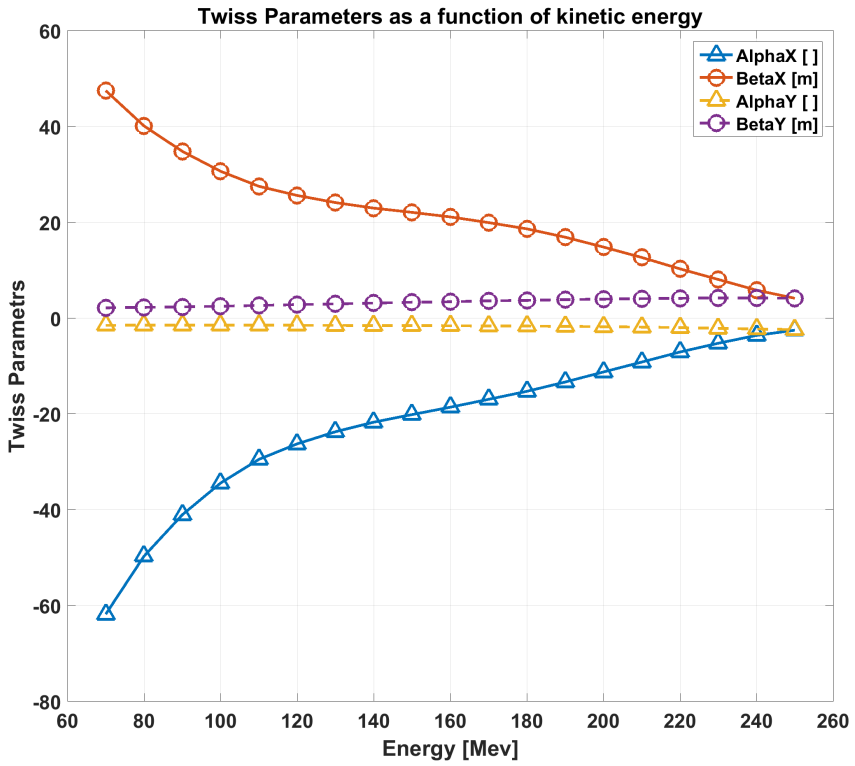

Figure 4.15 *Twiss parameters as a function of beam kinetic energy*

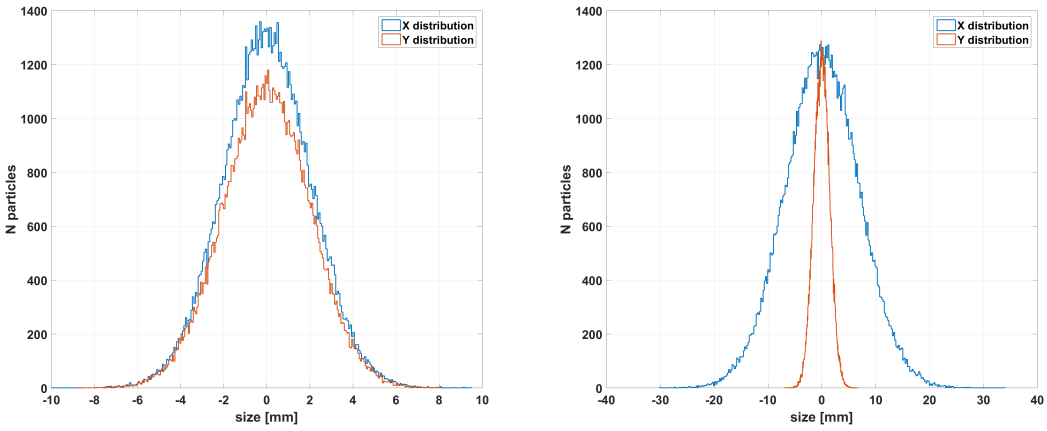

(a) **(b)**

Figure 4.16 *x (blue) and y (red) beam profile at the isocentre resulting from particle tracking at 70 MeV* ***(a)*** *and 250 MeV* ***(b)***

function D strongly opens, increasing the beam dimension on the bending plane (y) by a factor $\Delta dp/p$ [90]. *Fig.4.17* shows the effect of a Gaussian distributed momentum

spread of 0.5 % and 1% on the beam size at isocentre. In this analysis the effects of the energy spread were just considered inside the gantry, *i.e.* the dispersion was assumed to be closed at the exit of the vector magnet. Depending on the upstream magnetic design, the dispersion function can be modified along the beam trajectories in the gantry, as well as its effect on the beam size. Without simulations of a complete beam line, it is not trivial to assess the real effect of the energy spread on the beam at isocentre. As already discussed, a possible solution could imply the use of a series of co-axial tori to create an achromatic configuration; this, clearly, would significantly increase the complexity and cost of the installation. Given the large aperture required to accommodate all the beam orbits, another option could be to propagate a non-zero dispersion from the vector magnet through the gantry, designing the focussing such that the dispersion is suppressed at the isocentre.

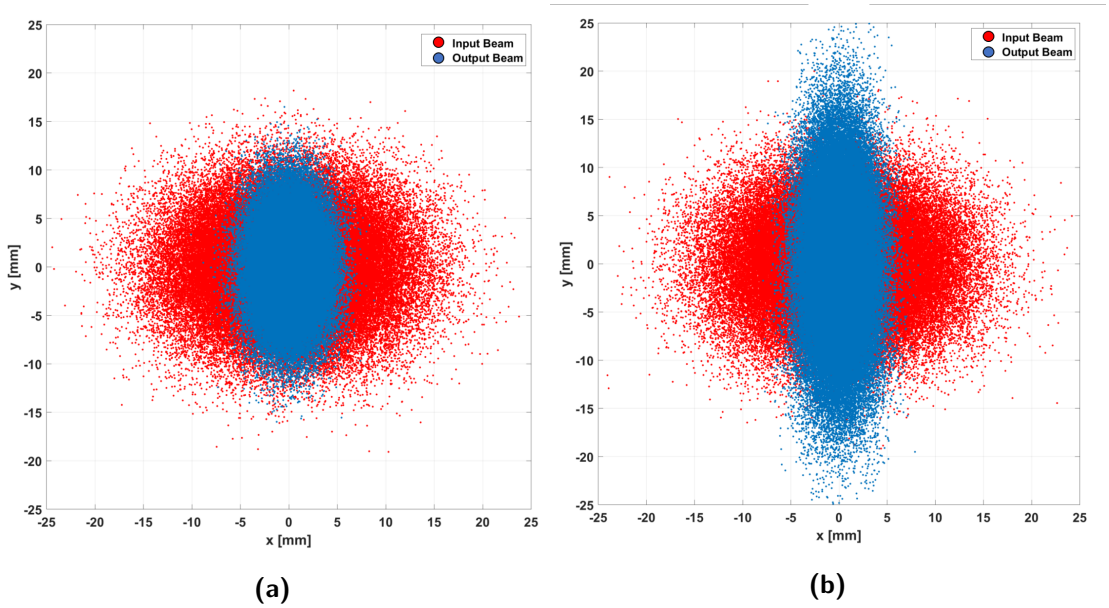

Figure 4.17 *Particle distributions at the exit of the vector magnet (red) and the isocentre (blue) for* $dp/p = 0.5\%$ ***(a)*** *and* $dp/p = 1\%$ ***(b)***

4.4 Linear Transfer Matrix

From the beam optics point of view, magnetic elements, such as dipoles and quadruples, can be represented with linear transfer matrices [90]. This simple, yet powerful, description of magnets allows to evaluate the main beam parameters, *i.e.* α and β, with sequences of matrix multiplications, avoiding more complex and time-consuming tracking simulations. Therefore, the representation of the GaToroid system through a linear transfer matrix is a fast and practical tool that can be used to match the torus to upstream magnets and accelerators. The GaToroid system can be approximately represented as $\mathbf{X_1} = \mathbf{MX_0}$, where $\mathbf{X_1}$ and $\mathbf{X_0}$ are position and angular vectors at the isocentre and the vector magnet location respectively:

$$\begin{bmatrix} x \\ x' \\ y \\ y' \end{bmatrix}_1 = \begin{bmatrix} m_{11} & m_{12} & m_{13} & m_{14} \\ m_{21} & m_{22} & m_{23} & m_{24} \\ m_{31} & m_{32} & m_{33} & m_{34} \\ m_{41} & m_{42} & m_{43} & m_{44} \end{bmatrix} \begin{bmatrix} x \\ x' \\ y \\ y' \end{bmatrix}_0 \tag{4.20}$$

$\mathbf{X_0}$ was imposed as input, while $\mathbf{X_1}$ is the result of the three-dimensional particle tracking. The transfer matrix can be calculated as:

$$M = \mathbf{X_1}\mathbf{X_0}^T(\mathbf{X_0}^T\mathbf{X_0})^{-1} \tag{4.21}$$

Each beam energy defines its own orbit and, therefore, at each beam energy corresponds a particular transfer matrix. To verify the accuracy of the solution, the tracked particles at isocentre, expressed as $\mathbf{X_1}$, were compared with the particles calculated through the transfer matrix, $\mathbf{X_{1M}} = \mathbf{MX_0}$. The relative error is defined as:

$$\lambda_x = \frac{\sigma(x_{1M}) - \sigma(x_1)}{\sigma(x_1)} \tag{4.22}$$

where σ represents the standard deviation of the particle distributions. In the same way, the relative error can be calculated for x',y and y'. λ provides an estimation of the beam parameters accuracy calculated with the transfer matrices in respect with the particle tracking. It has to be intended as a global error of the beam and does not provide specific information about single particle deviations, considered, at this stage, not relevant.

Performing the three-dimensional multi-particle tracking and solving *Eq.(4.21)* between 70 and 250 MeV, the linear transfer matrices associated with each energy were evaluated. For the sake of clarity, the transfer matrix elements are summarised in *Fig.4.18* and *Fig.4.19* as a function of beam energy. Even if the values of the elements are not trivial to interpret, the trends provide useful insights to comprehend the physics of the system. First of all, the coupling terms $m_{31}, m_{41}, m_{32}, m_{42} mm_{13}, m_{23}, m_{14}, m_{24}$

are constantly nearly zero for all energies as shown in *Fig.4.18*. It means that the coupling between x- and y-planes is negligible, and they can be treated separately. Furthermore, in *Fig.4.19* it is possible to observe a monotonic reduction in the modulus of the other elements, more evident on the x-plane, *i.e.* $m_{11}, m_{12}, m_{21}, m_{22}$. This reduction is coherent with the Twiss parameters plotted in *Fig.4.15*.

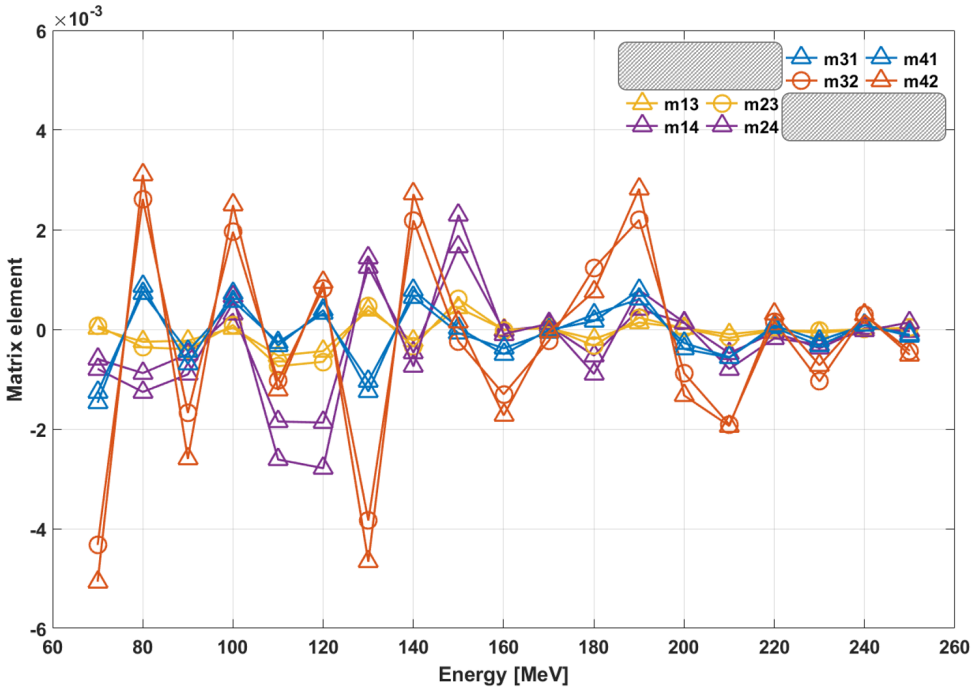

Figure 4.18 *Coupling transfer matrix elements as a function of beam energy*

In *Fig.4.20*, the relative errors λ, defined by *Eq.(4.22)*, are shown for x and y, and respective derivatives. The errors decrease with the kinetic energy and are significantly higher on the bending plane, λ_y and $\lambda_{y'}$. The red dashed line indicates the sum of the four λ errors, maximised at 0.5%.

Finally, to prove the physical consistency of the calculated matrices, the values of determinant were verified. As a consequence of the Liouville's Theorem, the determinant must be equal to 1 [90]. Coherently with the λ errors, the determinant deviates from the unity at lower energies, with a maximum error of less than 2%.

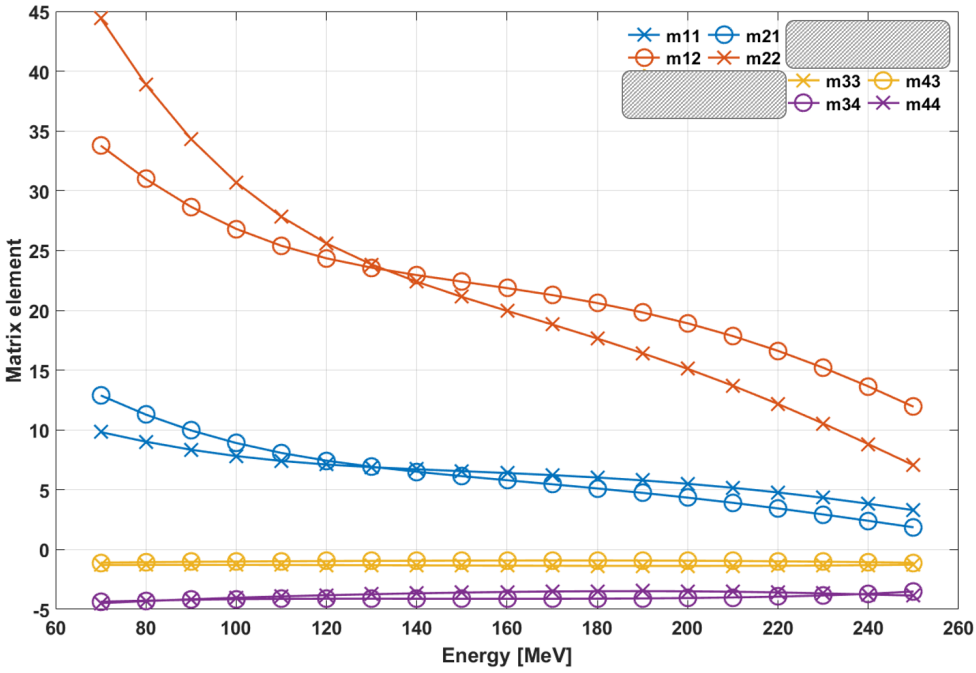

Figure 4.19 *x- and y-planes transfer matrix element as a function of beam energy*

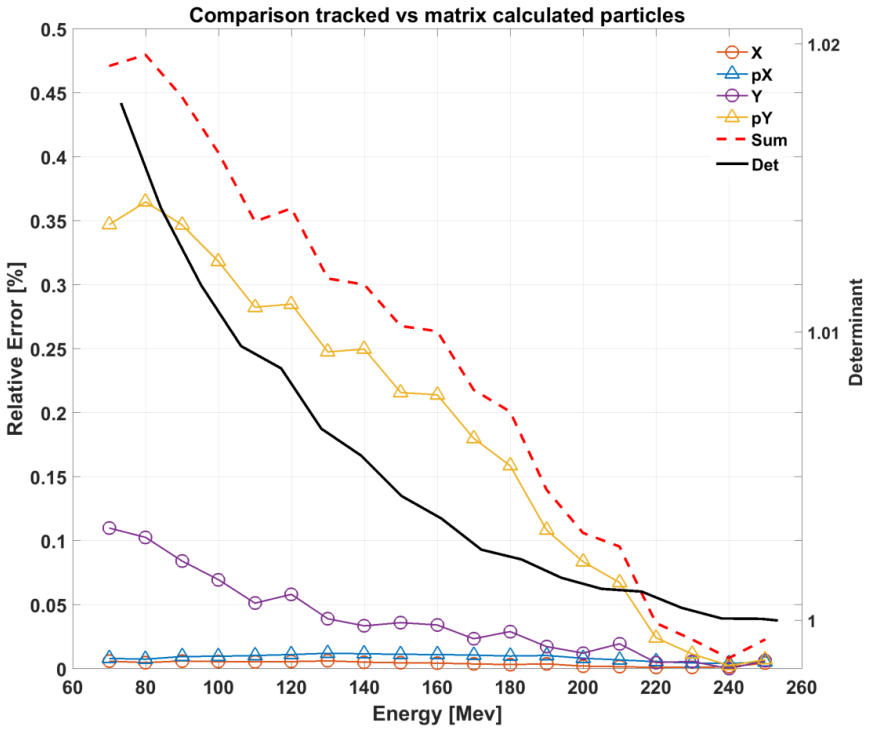

Figure 4.20 *Relative errors λ as a function of beam energy. The sum of the errors is indicated in red dashed line, while the matrix determinant in black solid line (right axis)*

4.5 Scanning System Concept

The vector magnet defines the two angles of the input beam. The discrete directions of the treatment are determined by the azimuthal angle θ, that is a discrete function of the number of coils N: $\theta_i = i2\pi/N$, where $i = 1...N$. The vector angle α_E is instead function of the beam rigidity, as expressed by *Eq.(2.2)*.

The tracking performed in nominal conditions, *i.e.* θ_i and α_E, allows the evaluation of the beam parameters at the isocentre. The deviation from the nominal angles, θ_i and α_E, can be used to perform pencil beam scanning [98], moving the beam into a defined scanning area around the isocentre. The vector magnet can, therefore, be intended as an upstream scanning system and the concept is exhibited in *Fig.4.21*.

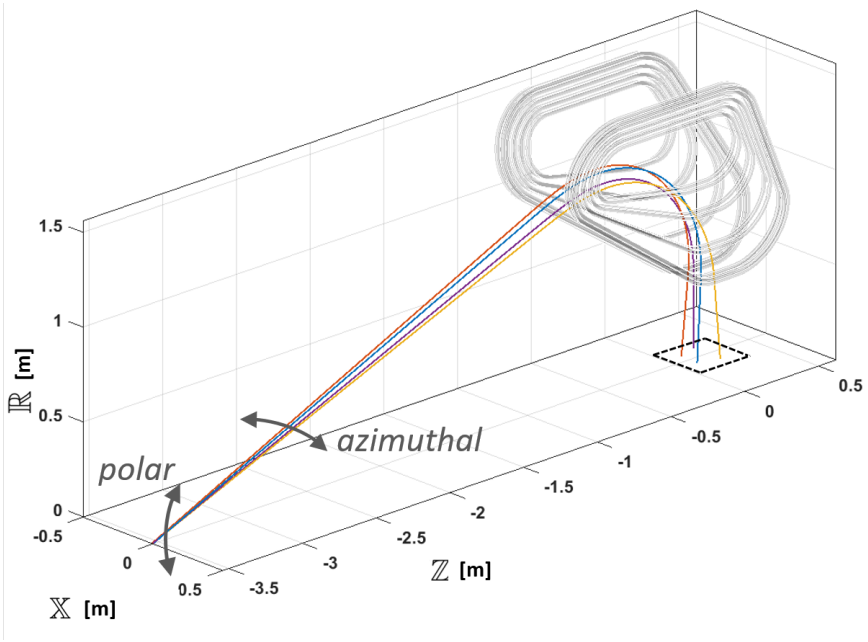

Figure 4.21 *Principle of the pencil beam scanning at the vector magnet*

A polar variation of $\alpha_E = \pm 1$ deg was translated into ± 60 mm along the axial direction of the torus. An azimuthal deviation of $\theta_i = \pm 0.4$ deg corresponded to the scanning of ± 50 mm in the gantry azimuthal direction. It is important to underline that these results indicate also the accuracy required at the vector magnet to obtain the precise beam positioning at the isocenter. To maintain the beam position at the isocenter within 1 mm, the precision required at the vector magnet is in the order of 0.01 deg (few $mrad$).

Fig.4.22 exhibits the natural response map of the beam scanning in an area of about 20 cm x 15 cm for the 250 MeV case, resulting from a linear angle deviation of $\alpha_E = \pm 1$ deg and $\theta_i = \pm 0.4$ deg. The shape of the scanning area can be adjusted acting on the

angle of the vector magnet, to contour the treatment region. The area is azimuthally limited by the geometrical aperture available between the coils, that for this 16 coils proton GaToroid is about 10 *cm*. A minimal treatment field size of about 20 *cm* x 20 *cm* is commonly required, driven by the intention of improving the treatment quality and reduce the field overlaps [99]. The shown results are intended to be a proof of principle for the system scanning feature: to provide wider scanning field size, especially in the azimuthal direction, topological modifications are required in the gantry, *i.e.* larger bore, reduced number of coils or modified angular periodicity of the coils [66].

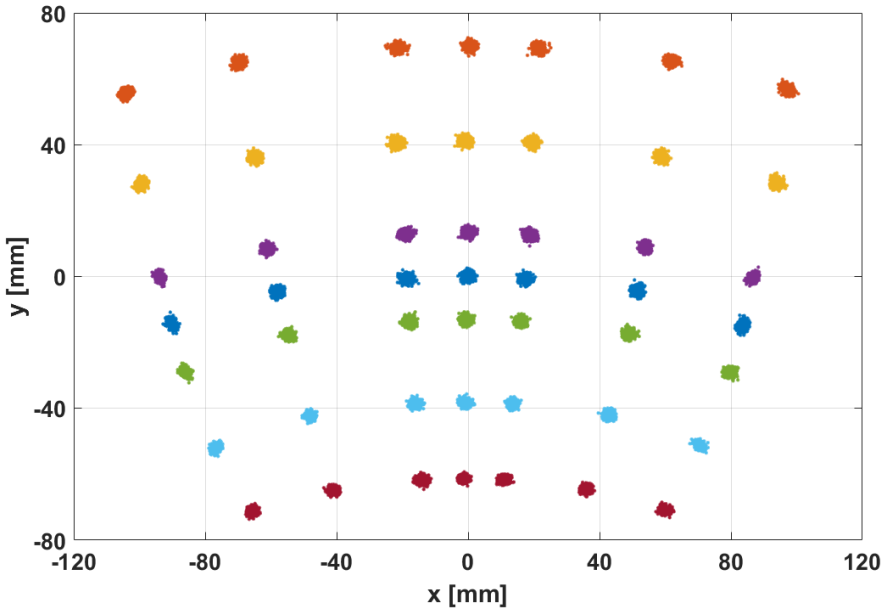

Figure 4.22 *Natural response map of the beam scanning around the isocentre, for a linear variation of* $\theta_i = \pm 0.4\,\mathrm{deg}$ *and* $\alpha_E = \pm 1\,\mathrm{deg}$

Moreover, it is also interesting to evaluate the effective Source-to-Axis Distance (SAD), namely the distance between the virtual point source and the local position of the Bragg pick at the isocentre [99]. Although the beam scattering source is the vector magnet, the virtual source point was identified through the intersection of the lines generated by the beam positions on the torus axis and relative incident angles at isocentre, as illustrated in *Fig.4.23*. *Fig.4.24* exhibits the effective SAD distance as a function of the beam kinetic energy, both an polar scanning (acting on α_E) and azimuthal scanning (acting on θ_i). The average SADs for polar and azimuthal scanning are in the order of 1 m. The azimuthal scanning is monotonically increasing with the energy, due to the fact that beams with higher momentum are entering the torus in larger radial position.

Differently, the trend of the polar SAD is flatter and determined by the field profile.

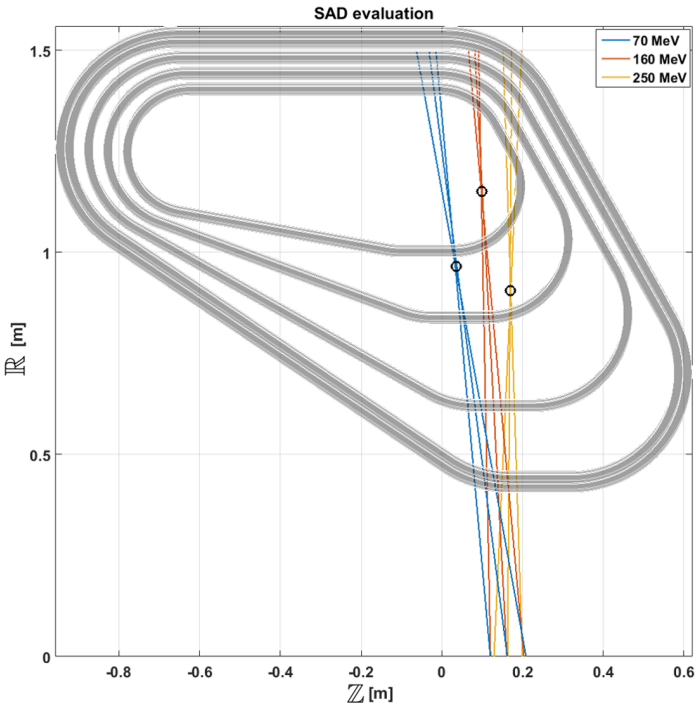

Figure 4.23 *Examples of SAD calculation for the polar scanning (around the nominal angle α_E)*

The actual value of SAD is similar to the one of the downstream scanning gantries, typical in the order of 1-2 m, and does not provide a parallel scanning. It was estimated that, to prevent exceeding the 20% threshold of superficial dose increase, a SAD of 4 m is required [99]. Furthermore, the commercial treatment planning systems (TPS) nowadays available usually work with a constant SAD in the complete energy range. It is therefore necessary to modify the coil profile at the exit of the magnet to increase the SAD. A further geometrical optimisation could be performed on the coil exit region, aiming for parallel beams during the scanning and a SAD larger than 4 m. Similarly to what is currently done in CNAO (IT)[100] and MedAustron (AT)[37] with the final dipole of the vertical line and proton gantry respectively, the edge angle at the coil exit region can be optimised to maximize the SAD. However, this study is beyond the scope of the thesis.

In any case, assuming the possibility of generating a scanning system with 4 metres of SAD, the volume reachable by the N_{coils} directions was evaluated. With 1 metres of SAD, *i.e.* a beam with larger divergence during the scanning, the reachable volume would be bigger. In this sense, the assumption of SAD = 4 m is conservative.

Fig.4.25 shows the number of beam entrance windows from which any given point in a sphere of 20 cm diameter (red circle) can be reached with the proposed configu-

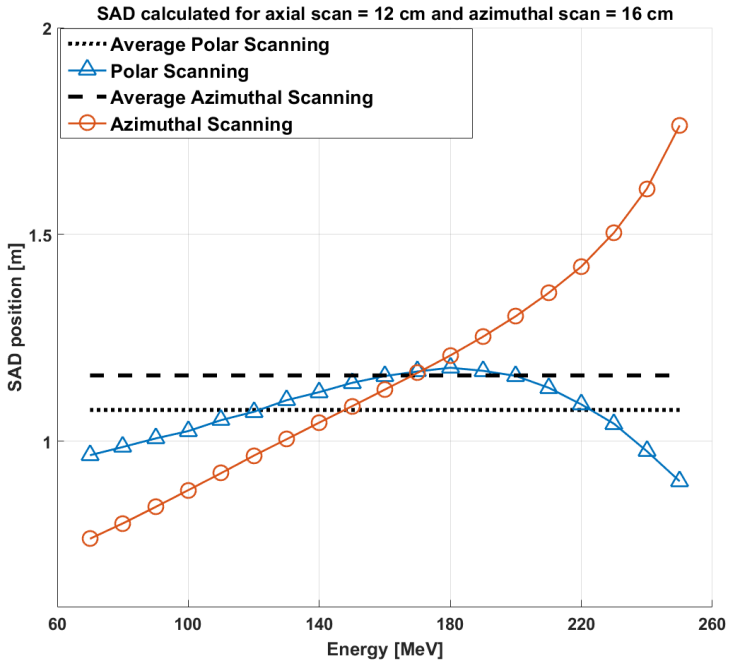

Figure 4.24 *SAD distance for polar (blue triangles) and azimuthal (red circles) scanning as a function of beam kinetic energy. Polar (dotted) and azimuthal (dashed) average are reported as lines.*

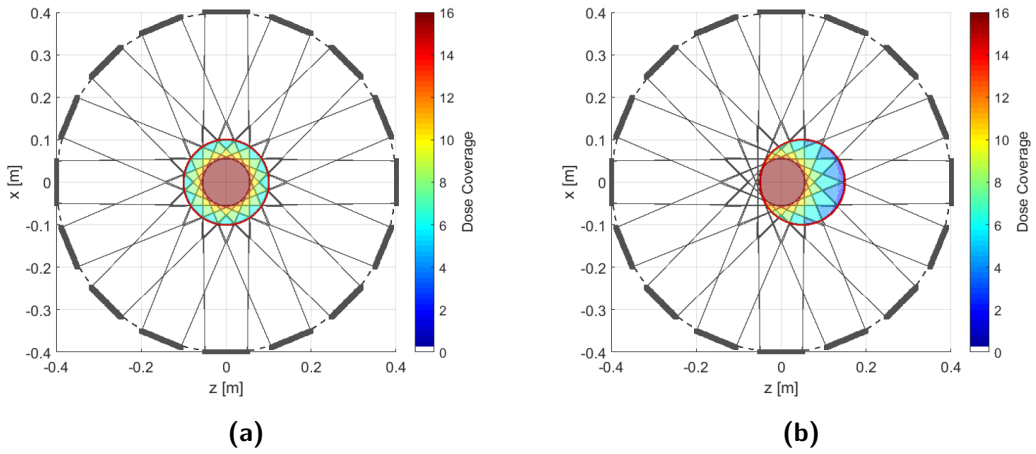

Figure 4.25 ***(a)*** *Visualisation of the map with the number of beam windows from which any point can be reached (i.e., the dose coverage), obtained with 4 m of SAD and 10 cm of beam windows length. The outer red line represents the maximum tumour volume (20 cm diameter), while the colour map indicates the number of angles that can be used to reach the target location.* ***(b)*** *By properly positioning the patient couch, different dose coverage volumes can be reached thanks to the* 16 *beam windows.*

ration. Due to the topology of the system, the beam windows (grey thick lines) have an azimuthal dimension of about 10 *cm* and with the assumption of 4 metres of SAD, the maximum divergence of the beam during the scanning is 0.7 degrees. With these geometric specifications the innermost disk of 11 *cm* diameter can be reached from 16 directions. The outermost disk, enclosed by a red line, shows a possible coverage of 20 *cm* diameter, which could be reached from 6 beam windows. If non-isocentric treatments are considered, a movement of the patient would allow to break the symmetry of irradiation and increasing the available angle at the target up to 16 in any point, as illustrated in *Fig.4.25*(b).

Magnet Engineering

5

"The science (or the art ...) of superconducting magnets is a exciting, fancy and dirty mixture of physics, engineering, and chemistry."

Ezio Todesco, Masterclass - Superconducting Accelerator Magnets, 2020

This chapter describes quench protection, mechanics and cryogenics studies performed on the GaToroid gantry. Building upon the magnetic optimisation presented in Sec.3.1, the geometries for the insulated LTS and HTS cable were defined. Two different quench protection studies were performed. The first is based on a thermo-electric lumped model and was used to validate the design of both Nb-Ti and ReBCO cables. The second, and more complex, model takes into account the longitudinal quench propagation along the cable and was specifically used to analyse the behaviour of the HTS cable. Furthermore, the presence of high magnetic fields and currents induces intense Lorentz forces acting on the conductors. Preliminary mechanical studies are presented, evaluating stresses and deformations in nominal electro-magnetic conditions and in a fault scenario. Finally, the heat loads introduced inside the cryostat were estimated and a first concept of cooling system is presented.

The work presented in this chapter is also reported in:
E. Felcini, L. Bottura, J. van Nugteren *at al.*, *Magnetic Design of a Superconducting Toroidal Gantry for Hadron Therapy*, in IEEE Transactions on Applied Superconductivity, vol. 30, no. 4, pp. 1-5, June 2020.

In *Sec.3.1* two possible optimisation solutions of GaToroid were presented: high and low engineering current density. The first configuration foresees the use of non or partial insulated coils. Although the use of non-insulated windings is a very elegant and attractive solution for a magnet such as GaToroid, operating in steady-state, it would require dedicated and extensive studies to provide a reliable and predictable behaviour of the coils in case of quench. The absence of insulation between the tapes promotes an efficient redistribution of current and heat in the radial direction of the windings.

The radial current exchange between the tapes allows the bypass of local quench zones and facilitate the recovery of the magnet: for this reason, the magnet is considered *self-protected* [101] [71].

However, the modelisation and the understanding of the non-insulated coil behaviour are still matter of discussion in the community, and the value of the contact resistance between the tapes strongly affects the process of current redistribution during a quench. The non perfect control of the current behaviour may lead to field penetration inside the torus bore, with severe consequences for the patent and the instrumentation. Furthermore, the use of NI coils in nested configurations (such as the graded coils of GaToroid) and in a background field (generated by the $N-1$ non-quenching coils) can introduce strong mechanical instabilities [102].

In conclusion, in the framework of the thesis, the low current density configuration was selected for more detailed studies on cable geometry, quench protection and mechanical analyses. This option lends itself well to the use of *conventional* insulated cables, both in LTS and HTS conductors.

5.1 Cable Design and Quench Protection

The transition from the superconducting to the normal state, defined as *quench*, is one of the most crucial aspect of superconducting magnets. A small energy perturbation could be sufficient to locally bring the superconducting material above the current sharing temperature (T_{cs}). In this regime, further energy is generated due to the Joule effect, with a consequent increase of the temperature and propagation of normal conducting zone. If not controlled, this process may lead to irreversible and violent thermal runaway in the whole magnet.

For this reason, it is of uppermost importance to design a cable configuration and a quench protection system to limit the increase of temperature in the system in case of quench.

5.1.1 Cables Geometry

Based on the magnetic optimisation of the low engineering current density configuration presented in *Sec.3.1*, the design of the LTS and HTS cable were defined. Firstly, an appropriate operating current must be selected. To reduce the heat losses introduced by the current leads in cryogenic environment, as well as to limit the complexity (and cost) of the power supplies in a clinical facility, the operating current I_{op} was set equal to 1800 A.

The modest operating current and the size of the coil well suit the choice of a small Nb-Ti Rutherford cable, as the LHC Type 4 [103], composed by strands of 0.5 mm diameter. Although Rutherford cables are usually keystoned (trapezoidal shape), in this thesis a simplified rectangular shape was considered.

For the ReBCO, due to the easiness of winding and high current density, a configuration of Non-Twisted Stack composed by 3 tapes (12 mm x 0.1 mm) was selected, similar to the concept proposed for the EuCARD insert cable [104].

Finally, *Fig.5.1* presents a schematic of both cable configurations and the main parameters are listed in *Tab.5.1.*

Proton GaToroid - LTS and HTS Cables Parameters			
Parameter	Unit	LTS	HTS
Conductor		Nb-Ti	ReBCO
Cable Topology		Rutherford	Non-Twisted Stack
N strand or tape		36	3
Cable Width	[mm]	12.2	12.2
Cable Thickness	[mm]	1.5	1.5
Stabilizer		Cu Profile	Co-Wound Cu tapes
Cu: Non-Cu ratio		3	7.3
Cable Length	[km]	2.5	2.5
Operating Current | I_{op}	[kA]	1.8	1.8
Operating Temperature | T_{op}	[K]	4.5	20
Peak Magnetic Flux Density | B_p	[T]	6.8	6.8
Engineering Current Density | ρ_{en}	$[A/mm^2]$	100	100

Table 5.1 *Main cable parameters for LTS and HTS configurations*

5.1.2 Quench protection: Thermo-Electric Lumped Model

A simple, yet effective, method to protect the magnet in case of quench is the energy extraction through an external dump resistor. A computational light lumped thermal-electrical model was used to perform the first quench studies and to validate the cable topologies in terms of maximum hot spot temperature during a quench.

The protection scheme based on an external resistor is represented through the electrical circuit shown in *Fig.5.2*, where L is the inductance of the system and R_d is the resistance of the external dump.

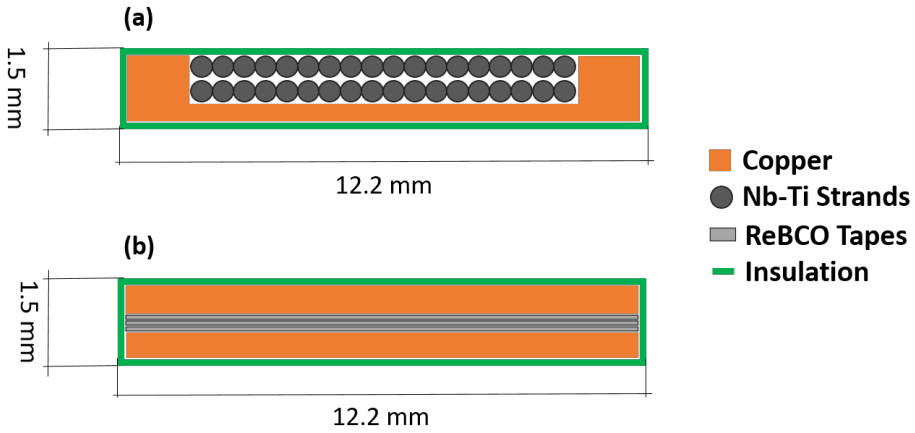

Figure 5.1 *Sketch of the LTS* ***(a)*** *and HTS* ***(b)*** *cables described in Tab.5.1*

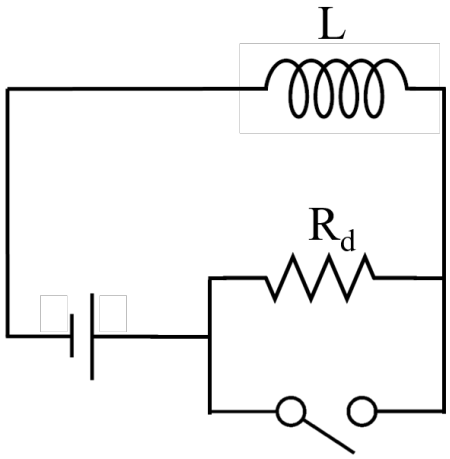

Figure 5.2 *Circuit of lumped external dump resistor*

The discharge of the inductor into the resistor is described by a simple exponential decay with time, t:

$$I(t) = I_{op} e^{-\frac{t}{\tau_c}} \tag{5.1}$$

where, I_{op} is the current at $t = 0$ and τ_c is the characteristic discharge time of the circuit:

$$\tau_c = \frac{L}{R_d} = \frac{\frac{2E}{I_{op}^2}}{\frac{V_{max}}{I_{op}}} = \frac{2E}{V_{max} I_{op}} \tag{5.2}$$

where E is the stored energy of the system and V_{max} is the maximum voltage on the dump resistor. The voltage on the external resistor must be limited to few kV to avoid potential issues at the switch or in the magnets [105]: $V_{max} = \pm 1\ kV$ was taken

as reference. The magnetomotive force of a coil is fixed by the design (*Tab.3.1*) and can be simply expressed as a function of the operating current and the total number of turns in the coil:

$$mmf = I_{op} N_{turn} \tag{5.3}$$

Comparing *Eq.(5.2)* and *Eq.(5.3)* and fixing E (related to torus design) and V_{max} (limited to avoid technological issues), the remaining free parameter is the balance between I_{op} and N_{turn}.

Low values of N_{turn} imply reduced inductances and a faster discharge on the dump resistor. In other words, the higher the operating current, the lower the time constant of the system τ_c. I_{op} was selected equal to 1800 A. The limited value of current allows to reduce the complexity of mechanics, circuitry and powering, beside limiting the cryogenic load in the system due to the current leads.

If the temperature exceeds the current sharing temperature, T_{cs}, the current flows in the normal conducting part of the cable generating heat due to the Joule effect:

$$Q_J = R_{eq}(T) I^2(t) = \rho_{eq}(T) J_{en}^2(t) A \delta x \tag{5.4}$$

where ρ_{eq} is the equivalent resistivity of the cable after the quench, function of the temperature, J_{en} the engineering current density, A is the cross-section of the cable and δx a reference unit length. The resistance of the cable does not take into account a *smooth* power law transition, but it is considered as a sharp transition to a normal-conducting state. In this lumped thermal circuit, the heat equation in adiabatic condition (no cooling term) can be written as:

$$\frac{dT}{dt} = \frac{Q_J}{m C p_{eq}(T)} = \frac{\rho_{eq}(T)\delta x}{D_{eq} C p_{eq}(T) \delta x} \frac{I^2(t)}{A^2} = \frac{\rho_{eq}(T)}{D_{eq} C p_{eq}(T)} J_{en}^2(t) \tag{5.5}$$

where m is the mass, Cp_{eq} and D_{eq} are the equivalent heat capacity and volumetric density of the cable. Depending on the discharging time profile and the value of the current density, the temperature profile can be modified to reduce the hot spot temperature in the magnet below a given threshold, here selected equal to 200 K to limit the difference in thermal expansion between the elements of the coils as well as potential damage to the conductors.

Using the described adiabatic approximation and lumped circuit elements, the cable configurations of *Tab.5.1* were validate on the basis of the hot-spot temperature. As already discussed in *Sec.3.1.3*, it is necessary to maintain a symmetric magnetic configuration during a quench to avoid strong field penetration inside the bore. The electrical circuit of the torus was split in 2 symmetric parts of 8 coils each, as shown by *Fig.5.3*. In this way, keeping a maximum voltage of $\pm$ 1 kV on each dump resistor,

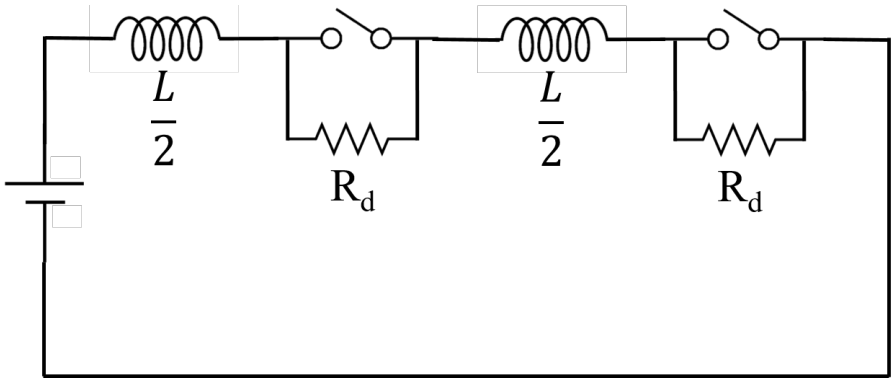

Figure 5.3 *Circuit of lumped external dump resistor considered for GaToroid quench protection*

it was possible to reduce the time constant of the system by a factor 2, resulting in $\tau_c = 8.3\ s$. A reference value of 2 seconds for quench detection and validation was selected: this value was considered a quite representative compromise for both LTS and HTS configurations. This detection time is conservative for the Nb-Ti cable (usually hundreds of milliseconds), while dedicated studied for the ReBCO are presented in *Sec.5.1.3*.

During the current discharge, the hotspot temperature rise was evaluated both for LTS and HTS cables, and the results are shown in *Fig.5.4*. The maximum temperature in the adiabatic conditions is in the order of 150 K and, therefore, in the presented approximation, the cable topologies were considered suitable for the magnet protection with an external dump.

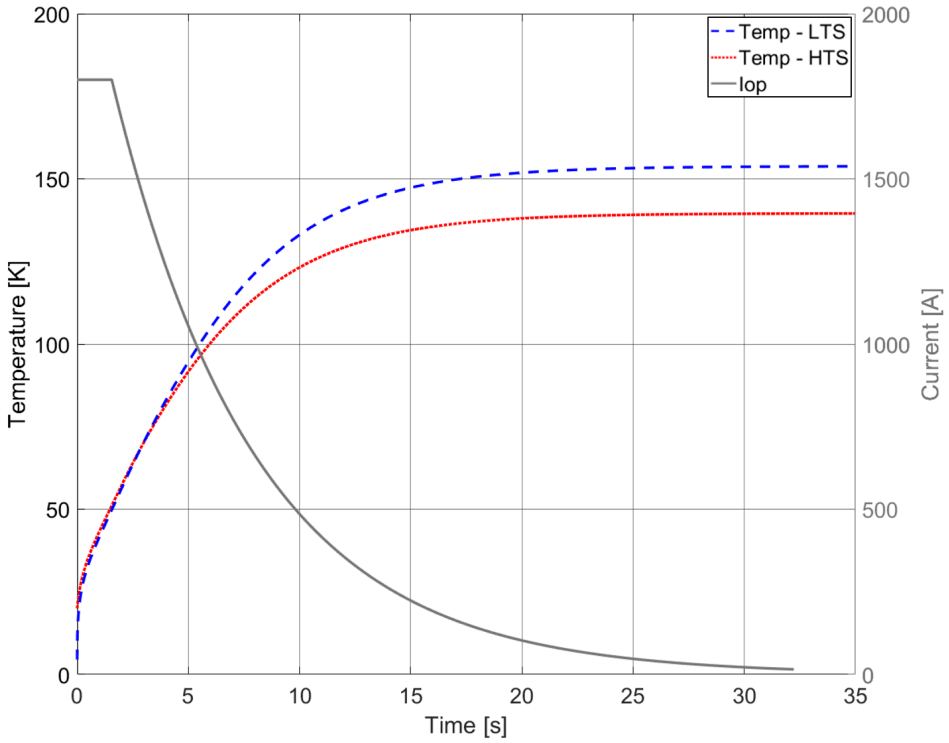

Figure 5.4 *Temperature of LTS (red dotted) and HTS (blue dashed) cables as a function of time, in case of external dump during the quench. Iop (gray solid) is the operating current in the magnet*

5.1.3 Quench Protection: One Dimensional Thermo-Electric Model on HTS Cable

Building upon the lumped model reported in the previous section, hereafter a more detailed study on the longitudinal quench propagation on the HTS cable is discussed. The electrical circuit representing the model is shown in *Fig.5.5*, where L is the inductance of the system and R_{sc} is the superconductor resistance and R_{nc} is normal-conductor resistance of a unit length δx.

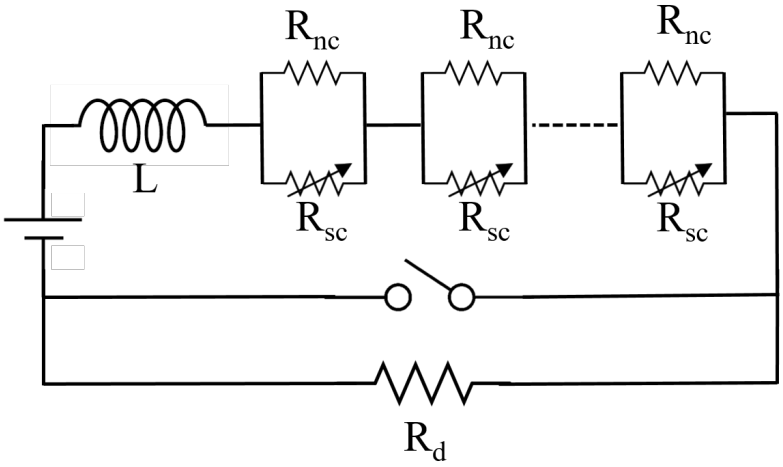

Figure 5.5 *Circuital representation of the longitudinal propagation quench model*

The governing equations of the system are presented in *Eq.(5.6)*. The former is the exponential current decay in the external dump, while the latter is 1-D heat equation that considers a longitudinal heat propagation along x and adiabatic conditions:

$$\begin{aligned} I(t) &= I_{op} e^{-\frac{t}{\tau_c}} \\ \frac{\partial T}{\partial t} &= \frac{k_{eq}(T)}{D_{eq} C p_{eq}(T)} \frac{\partial^2 T}{\partial x^2} + \frac{\rho_{nc}(T)}{D_{eq} C p_{eq}(T)} J_{nc}^2(t) \end{aligned} \tag{5.6}$$

where k_{eq} is the equivalent thermal conductivity, and J_{nc} is the current density flowing in the normal conducting part of the cable with a resistivity ρ_{nc}. The redistribution between normal and superconducting currents was calculated using a power-law expression:

$$\begin{aligned} I(t) &= I_{sc}(t) + I_{nc}(t) \\ I_{nc}(t) &= \frac{A}{\rho_{eq}} E_0 \left(\frac{I_{sc}(t)}{I_c} \right)^n \end{aligned} \tag{5.7}$$

where A is the cross-section of the cable, E_0 is electric field threshold taken as 10 $\mu V/m$ and, the n-value $n = 30$, considered to be a representative value for ReBCO tapes [106]. The proposed model is based on the following assumptions:

- adiabatic conditions: no cooling term is considered
- longitudinal quench propagation: no transversal heat propagation to neighbour cables structures
- constant characteristic time of the circuit: quench back effect neglected

While the first two assumptions are conservative, *i.e.* a pessimistic scenario was analysed, the third could be considered a strong simplification. Rigorously, the time constant of the system is calculated as:

$$\tau_c = \frac{L}{R_{dump} + \sum R_{nc}} \tag{5.8}$$

Therefore, τ_c is function of time and quench propagation. However, as shown in *Fig.5.6*, the internal resistance of the cable is 4 orders of magnitude smaller than the dump resistor and was neglected.

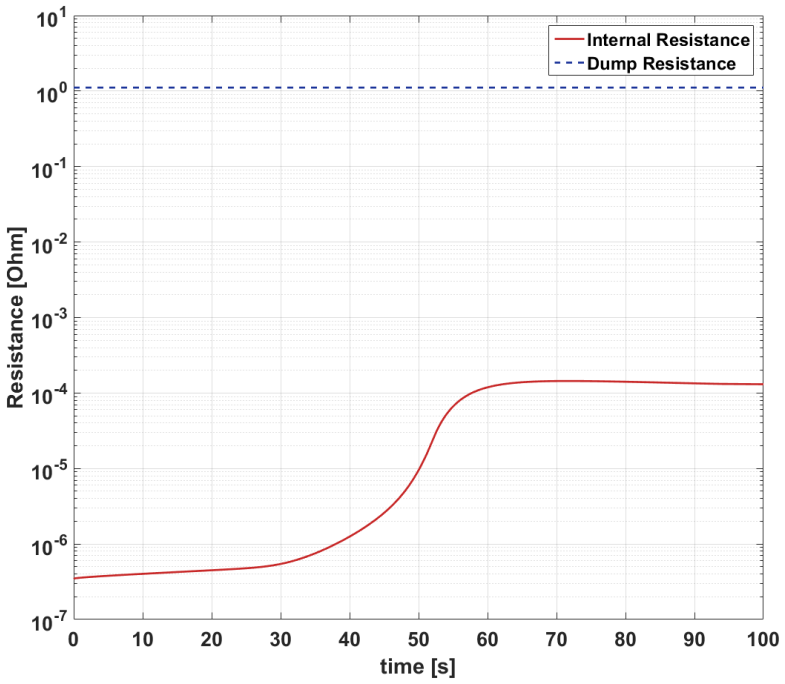

Figure 5.6 *Comparison between dump resistor (R_{dump}) and the total normal-conducting resistance R_{nc} in the coil*

The 1-D quench analysis presented in this section is based on the introduction of a local defect in the cable. For the considered HTS conductor [81] with the operating parameters listed in *Tab.3.1*, the temperature margin, ($\Delta T = T_{cs} - T_{op}$), is about 16 K. Assuming adiabatic conditions, 1 cm of heated length in 1 ms, the tape Minimum Quench Energy (MQE) was estimated to be 16 J/cm^3, without any additional stabiliser. For comparison, Nb-Ti cables of the LHC MB (Main Dipole) magnets, including interstitial superfluid helium between the strands, current-heat redistribution among strands and cooling through helium reservoir, at operating conditions of 7.0 TeV (11850 A, 8.2 T and 1.9 K) can withstand an energy deposition of 15-20 mJ/cm^3 in 1 ms due to a particle shower [107][108]. Similarly, impregnated Nb_3Sn cables of HiLumi 11T dipole at 1 ms have a MQE of about 20 mJ/cm^3 [109].

The amount of energy required to quench the GaToroid coil made in HTS is at least 3 orders of magnitude higher than LHC and HiLumi LHC magnets. This value was not considered representative by the author and, instead, the presence of a local defect on the cable was assumed. A given length of the cable was therefore considered normal conductive with a consequent energy generation due to the Joule effect. If the defect is extended to the total cable length, the one-dimensional model is equivalent to the lumped element circuit of *Sec.5.1.2*: no longitudinal distribution of heat can occur along the cable. The model was built upon the numerical tools developed in [110] and the quench simulation was performed as follows:

- introduction of defect in the cable a $t = t_0$ and consequent heat generation by the Joule effect
- quench propagation and temperature increase along the cable length, with consequent increase of normal-zone length and voltage
- quench detection threshold set at 50 mV
- after the detection, a validation and reaction time of 20 ms were considered, and the current discharges on the dump resistor with the relative time constant
- the amount of stabiliser limits the temperature increase on the cable in time between the introduction of the defect and the complete current discharge

The values of voltage threshold validation time were selected of the basis of the tests done at CERN on the *Feather* magnets [111][112].

Fig.5.7 shows the time evolution of the currents flowing in the normal and superconducting part of the cable, I_{nc} and I_{sc} respectively. As described in *Eq.(5.7)*, at each time step $I_{nc}(t) + I_{sc}(t) = I(t)$.

At time $t = t_0$ a defect is introduced in 1 centimetre at the centre of the cable of 2 metres length. In this zone, I_{sc} is forced to zero and the whole current flows in the

normal conducting part, generating heat. When the switch is closed, the total current I decays on the dump resistor, and I_{nc} and I_{sc} follow the same trend.

The results of the proposed quench protection system are summarised in *Fig.5.8*. The

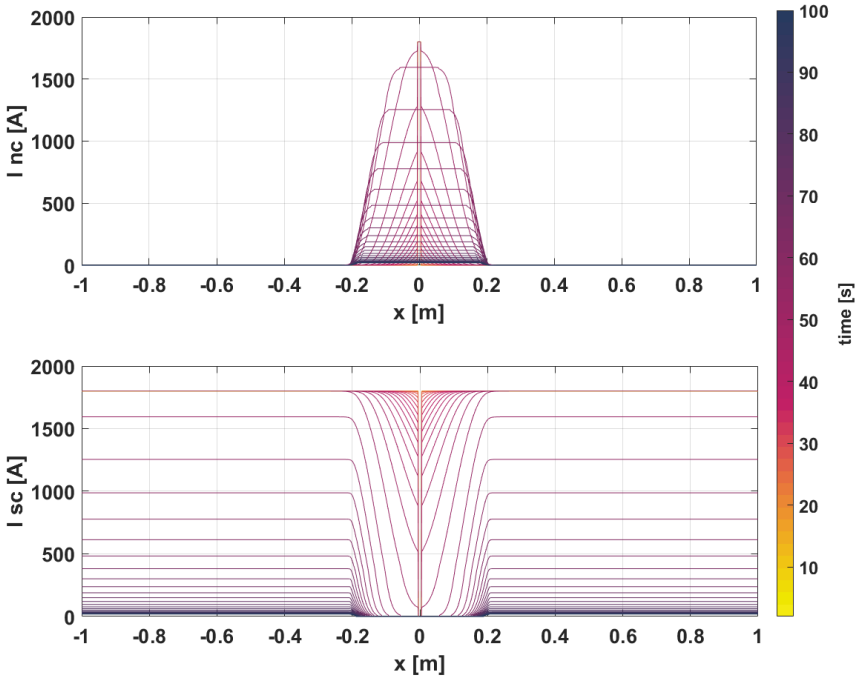

Figure 5.7 *Current on normal (Inc) and super (Isc) conductors as a function of the longitudinal cable position at different time steps*

voltage induced by quench propagation raised up to 50 mV and, after a validation time of 20 ms, triggered the current discharge on the dump resistor, with a time constant of about 8 s. The amount of stabiliser and the decay of the current limited the hot-spot temperature at the centre of the cable to about 200 K. A detailed description of the temperature profile in time and space is presented in *Fig.5.9*, where the maximum temperature is reached at $x = 0$ meters (where the defect is located). The temperature profiles shows the importance of the longitudinal heat diffusion, responsible for the temperature reduction after the complete current discharge.

In conclusion, it is possible to state that the presented HTS cable configuration is appropriate for the proposed quench protection system and boundary conditions, confirming the studies performed with the lump-circuit model.

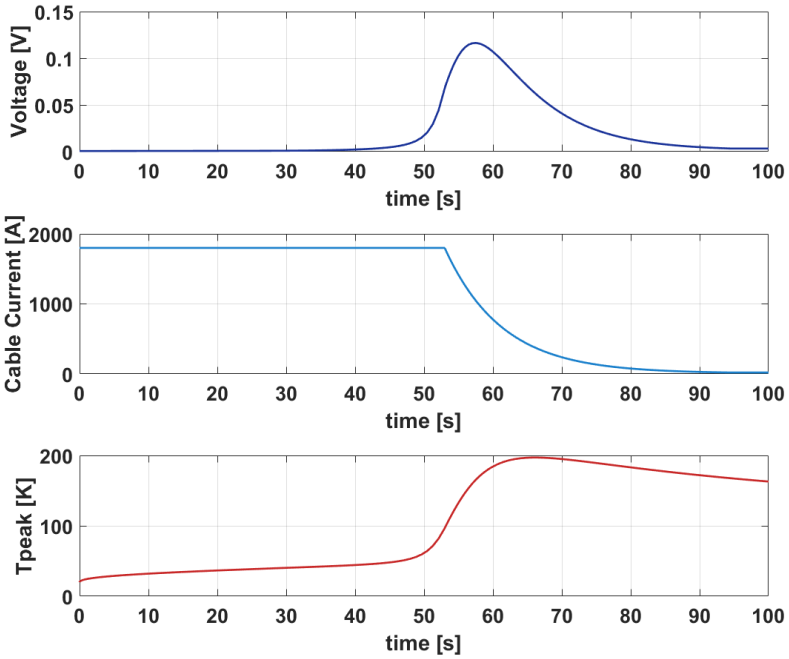

Figure 5.8 *Voltage, Cable Current and Peak Temperature as a function of time*

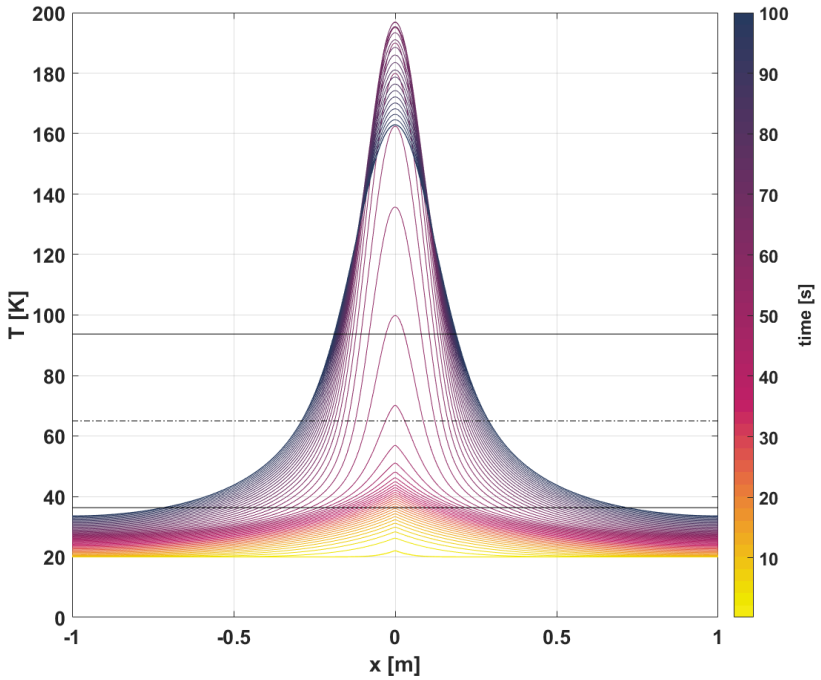

Figure 5.9 *Temperature distribution along the cable length at different time steps*

5.2 Mechanics

Given the magnetic flux density on the conductor volume, B, and the current density, J_{en}, the force density (per unit volume) distribution on the conductor was calculated as:

$$f = J_{en} \times B \tag{5.9}$$

Although considering the magnetic flux density generated by the whole torus, the description of the forces presented in this section is focused on one of the 16 coils. The choice is arbitrary and all the 16 coils are equivalent in nominal operating conditions. The distribution of the force density f is presented in *Fig.5.10*, on top of the coil geometry. The total electromagnetic force generated by each coil, F_c, was calculated

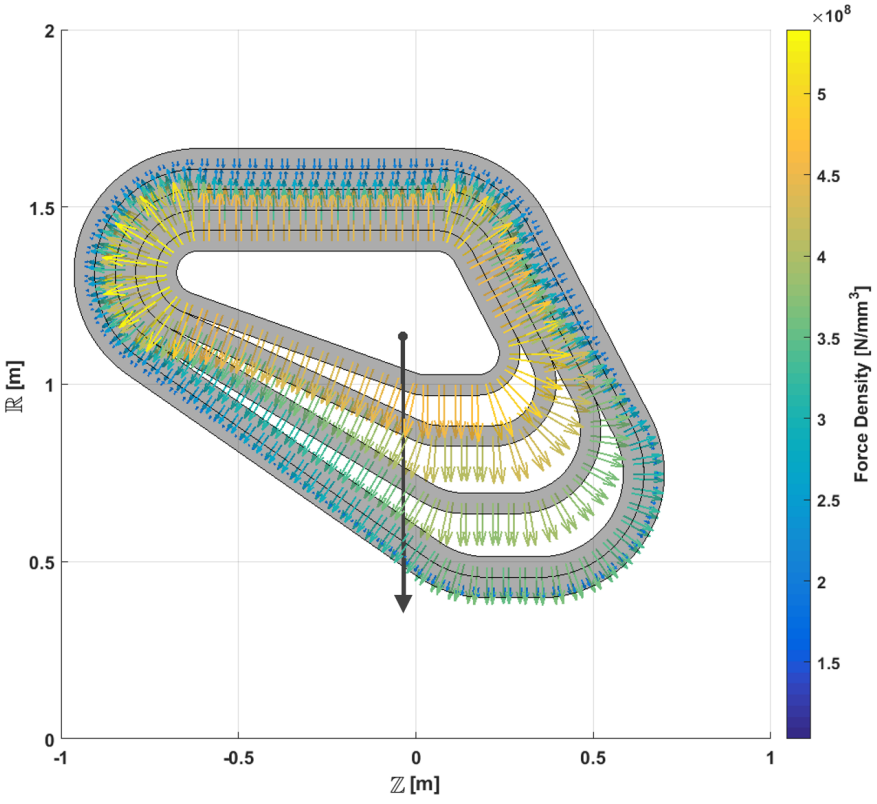

Figure 5.10 *Distribution of force density f on top of the coil geometry and the resulting force F_c*

integrating the force densities on the conductor volume:

$$F_c = \iiint f \, dV = \iiint J_{en} \times B \, dV \tag{5.10}$$

As expected from a toroidal magnet, F_c is a centring force, acting on the radial direction of the torus [85]. Selecting a general point of application P, the total torque T associated to the force densities f applied in p was computed:

$$T = \iiint (p - P) \times f \, dV \tag{5.11}$$

The point of application P_c such that the torque associated to the force F_c is zero was calculated as:

$$P_c \times F_c = \iiint p \times f \, dV \tag{5.12}$$

Eq.(5.12) has a solution only if the sum of the torques on the right-hand side is orthogonal to R_c, *i.e.* the calculation is performed on the $\mathbb{Z} - \mathbb{R}$ plane, neglecting the component of the force transverse to the coil plane. This assumption is justified by the fact that the magnetic field is mainly directed in the azimuthal direction, and therefore the force component along this direction is negligible. The forces are symmetric and periodically distributed along the azimuthal direction θ.

A first estimation of the supporting cylindrical structure was done, considering the hoop stress σ_c created by a uniform pressure on a thin-walled cylindrical surface:

$$\sigma_c = \frac{NF_c}{2\pi l_c t_c} \tag{5.13}$$

where $N = 16$ is the number of coils, and l_c and t_c are respectively the length and the thickness of the bucking cylinder. *Fig.5.11* shows a schematic representation of the cylinder.

As already discussed in *Sec.3.1.3*, to avoid significant field penetration inside the bore it is of uppermost importance to maintain the magnetic symmetry of the torus in case of a quench.

However, the mechanical structure was designed considering the fault-case scenario where the azimuthal symmetry is broken. Therefore, in the presented analyses, the current of the k-th coil was set equal to zero. Neither transient nor thermal phenomena were taken into account. Considering the coils plotted in *Fig.5.12*, the analysis was focussed on the force acting on the $(k + 1)$-th coil and the zero current condition was set on the k-th coil. This overturning force F_θ pushed the $(k + 1)$-th coil toward the $(k+2)$-th in the azimuthal direction θ, *i.e.* out of the coil plane. In general, the $(k+1)$-th coil experienced the maximum overturning force when the k-th coil had zero current [113]. Symmetrically, $(k - 1)$-th coil was subject to an equal and opposite overturning force toward the $(k - 2)$-th one. The structure foreseen to support the coils in case of quench was based on flat plates connecting the coils along the azimuthal direction. For a given length, l_i and thickness,t_i, the stress on this simplified geometrical structure can be evaluated:

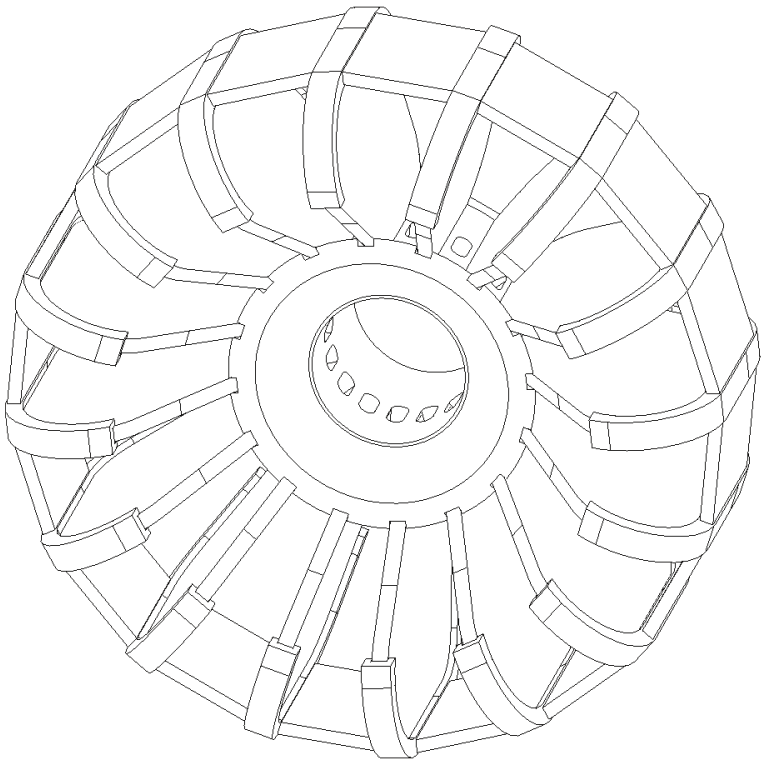

Figure 5.11 *Schematic representation of the preliminary GaToroid mechanical structure*

$$\sigma_\theta = \frac{F_\theta}{t_i l_i} \tag{5.14}$$

where l_i and t_i are respectively the length and the thickness of the inter-coil structure. The N inter-coil structures are shown in *Fig.5.11*.
The dimensions of the mechanical components and the stresses are listed in *Tab.5.2*, both for the cylinder and the inter-coils plates. A schematic representation of the mechanical structure derived from the aforementioned calculations is presented in *Fig.5.11*. It is worth to observe that the supporting cylinder requires N apertures for the beam transfer and must be coherent with the requirements of the scanning-field size (see *Chap.4*). The coil case was considered a single body in steel, realised by filling the outer perimeter (plus margins) of the conductor geometry.

Finally, this preliminary mechanical design allowed estimating the mass of the system, comprising the coil case, bucking cylinder and inter-coil structures. Assuming the use of stainless steel, the total weight of the assembly results in about 12 tons, *i.e.* one order of magnitude lighter than the nowadays available commercial gantries for proton therapy (see *Chap.1.2*).

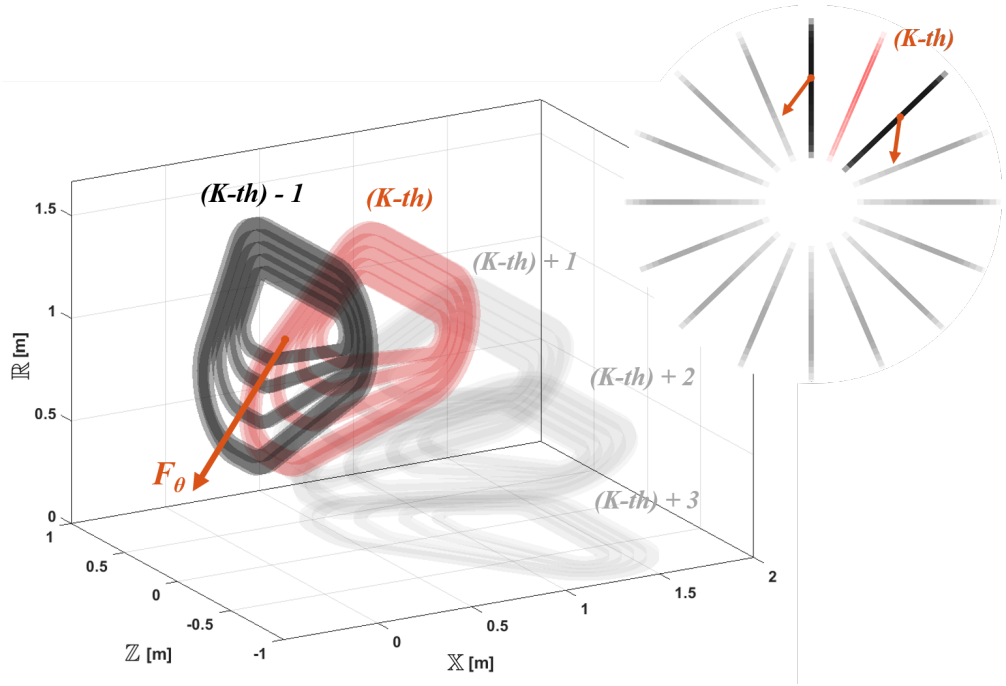

Figure 5.12 *Schematic representation the force acting in case of a coil quench. The maximum overturning forces F_φ (red arrows), in case of the k-th coil quench, are experience by the neighbours coils $(k \pm 1)$-th.*

Electromagnetic Forces and Mechanical Structure		
Parameter	Unit	Value
Centring Force $\lvert F_c \rvert$	[MN]	1.34
Fault Force $\lvert F_\theta \rvert$	[MN]	1.77
Cylinder thickness	[m]	0.06
Cylinder length	[m]	0.5
Inter-coil thickness	[m]	0.06
Inter-coil length	[m]	0.5
Cylinder hoop stress σ_c	[MPa]	113
Inter-coil stress σ_θ	[MPa]	59

Table 5.2 *Main parameters of GaToroid electromagnetic stresses and mechanical structure*

5.2.1 Finite Element Analysis

The analytical calculations performed with *Eq.(5.13)* and *Eq.(5.14)* are strongly approximated, but they are a first tool to grasp the global mechanical behaviour of the machine. Dedicated and detailed Finite Element Analysis FEA simulations are certainly required to define a proper and solid mechanical design. However, the level of detail of simulations is beyond the scope of this thesis. Nevertheless, the geometry proposed in *Fig.5.11* was used for a FEA in Ansys-Workbench. Once again, the following simulations are not intended to provide accurate and specific results, but can be used to have a global overview of the mechanical behaviour of GaToroid. The mechanical calculations presented in this section are done under the following assumptions:

- $1/N$ was analysed and azimuthal symmetry was imposed (see *Fig.5.13*): asymmetry in the forces (quench scenario) or in boundary conditions (gravity and ground supports) were not considered
- the inner surface of the bucking cylinder is considered fixed, but with no added stiffness
- all the bodies's connections are bonded: the mechanical parts cannot slide or separate
- the coil is considered as a single body, including the coil case, and the resultant force is applied to the zero-torque point of *Eq.(5.12)*
- the simulation do not consider transient phenomena nor thermal boundary conditions
- all the mechanical components are in structural steel

The analysed geometry is presented in *Fig.5.13*, where the azimuthal symmetry condition is imposed in the surfaces highlighted in green. The three components of the structure, namely the coils case, the bucking cylinder and the inter-coil structure are bonded together and no sliding or separation can occur between the bodies. This is a strong and simplistic assumption, but can already provide a first figure of the general behaviour of the structure. As shown in *Fig.5.14*, the coils tend to bend toward the torus axis due to the resultant force and its point of application. For this reason, the bucking cylinder and the inter-coil structures were elongated along the coil geometry, carefully avoiding the area where the particle beams are directed (in nominal and scanning conditions). As shown in *Fig.5.14*, the proposed configuration introduces stress concentration in the coil case at the extremity of the cylindrical support of the order of 80 MPa.

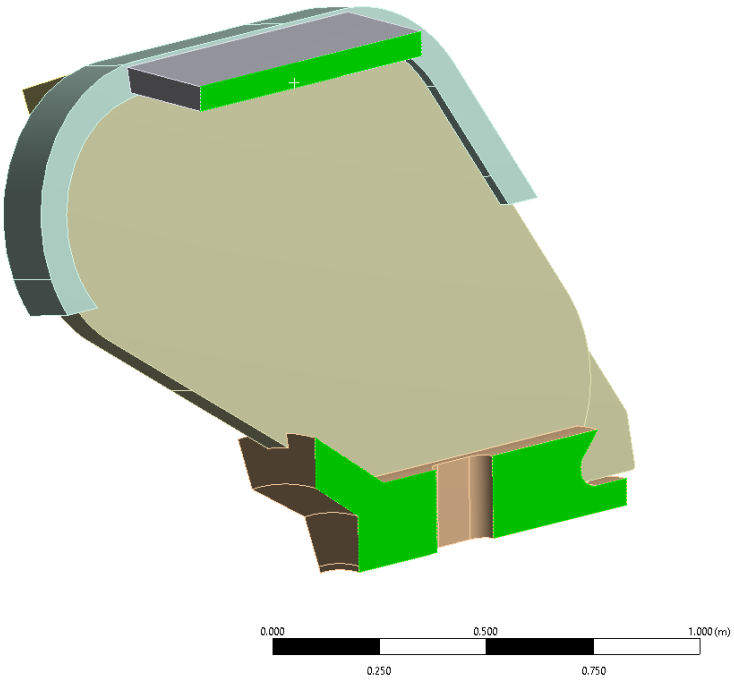

Figure 5.13 *$1/N_{coil}$ geometry of the whole structure with the surface used for the azimuthal symmetry (in green)*

Thanks to the selected geometry, the displacement of the coils is below the 0.5 *mm* threshold of the misalignment studies discussed in *Sec.4.2*.

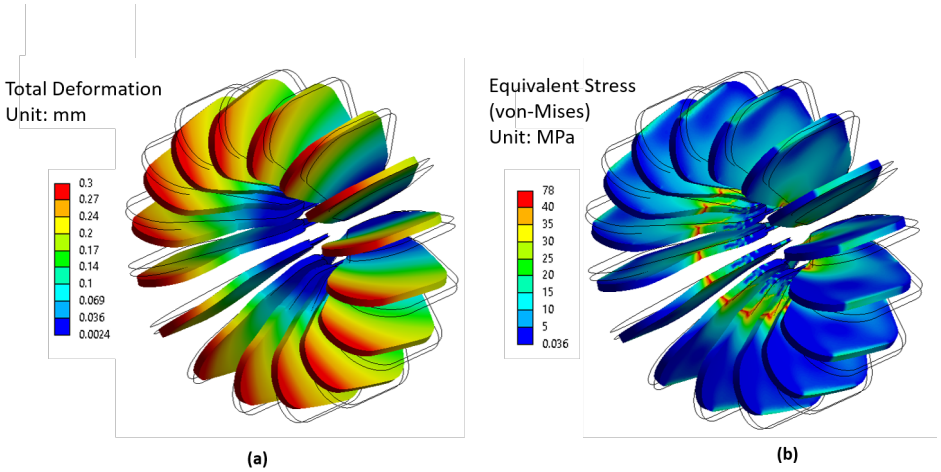

Figure 5.14 *Deformation* ***(a)*** *and equivalent von-Mises stress* ***(b)*** *on the coil casing. The undeformed model is shown with black lines*

The presence of an inter-coil structure that acts as an arc in compression in nominal conditions reduces the stress on the cylinder below the 100 MPa as shown in *Fig.5.15*.

Once again, the interconnection between the cylinder and the coils case is a delicate point and the stress need to be minimised, with geometrical optimisation and detailed mechanical analyses.

For completeness, *Fig.5.16* reports the stresses and formations in whole structures.

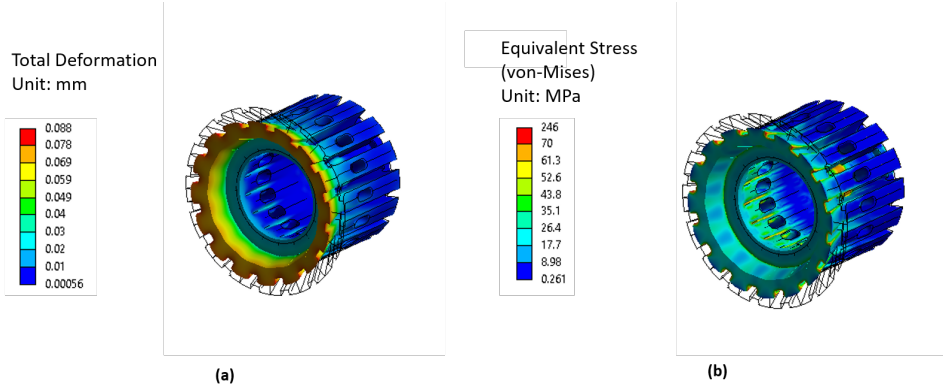

Figure 5.15 *Deformation* ***(a)*** *and equivalent von-Mises stress* ***(b)*** *on the bucking cylinder. The undeformed model is shown with black lines*

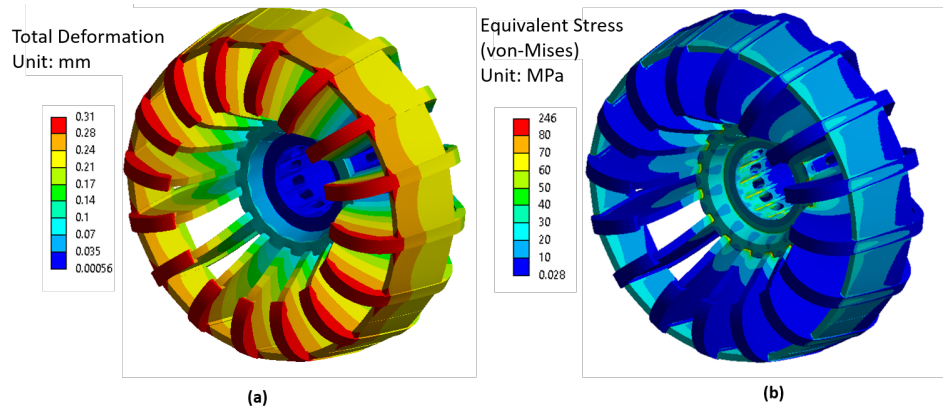

Figure 5.16 *Deformation* ***(a)*** *and equivalent von-Mises stress* ***(b)*** *on the complete mechanical structure of GaToroid*

5.3 Cryogenics

This section presents a general overview of the principal heat loads introduced inside the cryogenic environment of the Gantry. Given the high number of coils composing the investigated gantry configuration, it is practical to consider a single cryostat enclosing the whole torus. In this context, the following cryogenics analysis is focused on the LTS configuration, operating at 4.5 K. The stable operation at this temperature is crucial to maintain the 1.5 K of temperature margin, defined by the operating conditions of Nb-Ti cable listed in *Tab.5.1*. This scenario provides the upper limit for the installed power required for the maintenance of the gantry at cryogenics conditions.

5.3.1 Heat Loads

Current Leads

The superconducting magnets of the gantry need to be connected to power supplies at room temperature. This connection is done through current leads that are subjected to the temperature variation between the room and operating temperatures of the superconductors. Current leads are usually one of the most important heat loads in the cryogenics system and have a strong impact on the running cost of a superconducting system [105].

Considering a system based on liquid helium, the heat generated by the leads produces helium gas that can be used to cool-down the leads themselves. This kind of gas-cooled leads is named *self-cooled*. Traditional self-cooled current leads, operating between the room and liquid helium temperatures, are characterised by a minimum heat inleak per unit current of about 1.1 W/kA. This value can be considered roughly independent of the material due to the correlation between thermal and electrical resistivity (Wiedemann–Franz–Lorenz law) in metals and alloys. It represents the optimum operating point.

As already discussed in *Sec.5.1*, the electrical circuit of GaToroid considers all the coils connected in series. Thus, only two current leads are required (one input and one output) and given the operating current of 1.8 kA, the heat leak results in 4.0 W.

The use of HTS current leads (using self-cooling with a nitrogen bath or forced flow cooling by helium gas) could reduce the total cooling power by 30% [114][115], but given the modest heat leak and number of leads it may not represent the most practical solution.

Conduction

Similarly to the current leads, also the mechanical support of the gantry structure ranges from the cryogenic environment at 4.5 K to room temperature. This variation of temperature generates an heat flux Q_c:

$$Q_c = \frac{A}{L} \int_{4.5K}^{300K} k(T)\, dT \tag{5.15}$$

where $k(T)$ is the thermal conductivity, while A and L are the cross-section and the length of the support to the ground. This mechanical structure was dimensioned considering the total weight of the gantry, 12 tons (see *Sec.5.2*), supported by a single element in stainless steel with a maximum stress of 100 MPa. Furthermore, it is common practice to subdivide the cryogenic system in stages, introducing an intermediate thermal shielding cooled at 50 K to reduce the installed power consumption [116]. Under the aforementioned assumptions, the values of the calculated heat flux due to the mechanical support are 0.32 W at 4.5 K and 6.9 W at 50 K.

Another heat load is generated by the interconnection with the coils with the dump resistors. In the first-order estimation presented in this section, this source of heat is neglected.

Radiation

Due to the temperature difference between the surfaces of the cryostat and the gantry, another source of heat is introduced by radiation. Assuming the presence of the intermediate thermal shielding at 50 K and the use of Multilayer Insulation (MLI), the power introduced in the system by radiation can be estimated as 1 W/m^2 between 300 K and 50 K (using 30 layers of MLI) and as 50 mW/m^2 between 50 K and 4.5 K (using 10 layers of MLI) [116].

The area of one coil measures 1.3 m^2 for each side. Taking into account the 16 coils composing the torus, the radiation heat loads on the surface of the magnets at 4.5 K is 2.1 W.

The intermediate thermal shield at 50 K can be considered as two cylindrical structures around the torus at the inner and outer radius. With this assumption, the power at 50 K results in 26.6 W.

Adding up the contribution of the current leads, conduction and radiation, the total required installed power was estimated to be 6.4 W at 4.5 K and 36.5 W 50 K. Given

the large overall dimension of the gantry, the heat loads for radiation dominates the others.

Heat Loads		
Parameter	4.5 K	50 K
Current Leads [W]	4.0	
Conduction - Support [W]	0.32	6.9
Radiation [W]	2.1	29.6
Total Power [kW]	6.4	36.5

Table 5.3 *Heat flux inside the cryostat due to current leads, conduction through the ground support and and radiation.*

Finally, given the steady-state operation of GaToroid and assuming a sufficiently slow charging of the magnets, the AC losses on the superconductors are neglected in this stage of the study

5.3.2 Cooling System

On the lines of the work done for the KEK [117] and CLAS12 [118] [119] spectrometers, the coils can be conductively cooled by supercritical helium at 4.5 K flowing inside a copper tube. This copper tube follows the inner perimeter of each coil, surrounding the inner most grade that subjected to the highest magnetic field and the lowest temperature margin (1.5 K). High purity aluminium plates (or stripes) can then be added on top of each coil to create a more uniform cooling on all the grades. A sketch of this concept used on the CLAS12 coils is presented in *Fig.5.17*.

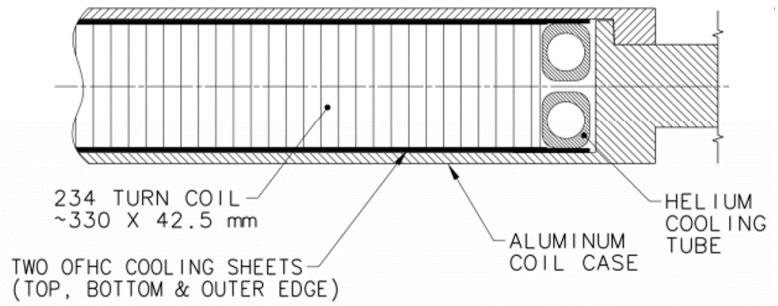

Figure 5.17 *Detail of the CLAS12 coil cross-section showing the conduction cooling mechanism [119]*

Design of GaToroid HTS Demonstrator

6

"*I can't do what ten people tell me to do*
So I guess I'll remain the same"

Otis Ray Redding Jr., *(Sittin' on) the Dock of the Bay*, 1968

This chapter presents the design of a single coil scaled-down demonstrator made with High Temperature Superconductors (HTS). A general description of the demonstrator provides the main geometrical and operating parameters of the magnet, explaining the several design choices. The HTS cable topology was modified from the full-scale GaToroid to enhance the operating current and magnetic field. Quench protection studies were then performed to validate the cable and the operating conditions using a one-dimensional thermal-electric model. The mechanical concept of the magnet was validated through finite element analysis, both with 2D and 3D models. Finally, a first demonstrator wound in stainless steel tapes and 3D printed support structure was done to develop appropriate winding tooling and to validate the peculiar geometry of the coil.

The work presented in this chapter is also reported in:
E. Felcini, L. Bottura, J. Harray, T. Lehtinen, D. Perini, and B. Dutoit, *Design of the First HTS Demonstrator of GaToroid Toroidal Gantry for Hadron Therapy* submitted for publication to IEEE Transactions on Applied Superconductivity, vol. 31, no 5, 2021

Nowadays, the use of HTS technology is a stimulating and thrilling research challenge and the use of HTS in medical applications is considered of great interest by the scientific community. As in the case of Nb-Ti for MRI and NMR in the last decades, realizing a GaToroid system in HTS could have a disruptive impact on the spread of this technology. The demand for superconducting magnets for medical applications could result in a significant reduction of production costs, together with the strengthening of this market sector.

Furthermore, the CERN TE-MSC-MDT* section is currently investing important resources on the research and development of HTS magnets, ranging from high-field accelerator magnets to spectrometers for space applications. In this framework, the GaToroid project and the design of the related HTS demonstrator are aligned with the interest of the worldwide scientific community as well as the with CERN magnet research program.

The design of a scaled-down demonstrator was undertaken as the first step toward the construction of a GaToroid machine realised in High Temperature Superconductors (HTS). The demonstrator was scaled by a factor 3 in comparison with the high engineering current density (high J_{en}) full-scale coil described in *Sec.3.1.* This size allows testing in already existing facilities and cryostats at CERN, namely the *diode cryostat* [120], capable to operate both in gaseous and liquid helium (from 50 K to 4.2 K). The design of the demonstrator was done maintaining the same coil geometry, number of pancakes and grades of the full-scale magnet, tackling similar challenges during the windings. The high engineering current density geometry was selected to push as much as possible the peak magnetic field in the demonstrator.

The basic coil geometry used for the magnetic optimisation of *Sec.3.1* was enhanced at the level of the conductor position, taking into account the grades and layer jumps, as well as part of the current leads. The demonstrator geometry is presented in *Fig.6.1*, while the main parameters are summarised in *Tab.6.1.*

Demonstrator Parameters		
Parameter	Unit	Value
Number of Layers		2
Number of Grades/Layer		5
Number of Turns/Grade		4
Size	[m x m]	0.6 x 0.4
Scale		1:3
Cable Length	[m]	50
Inductance	[mH]	0.64

Table 6.1 *Main parameters of the GaToroid demonstrator in HTS*

Fig.6.2 depicts a cross-section of the demonstrator, listing the name of the elements composing the magnet structure. The coil is composed of two symmetric pancakes made of 5 grades each, separated by the intermediate plate of 1 cm thickens.

Each grade is mechanically supported by a spacer and each layer is enclosed with

*Technology department, Magnets, Superconductors and Cryostats group, Magnet Design and Technology section

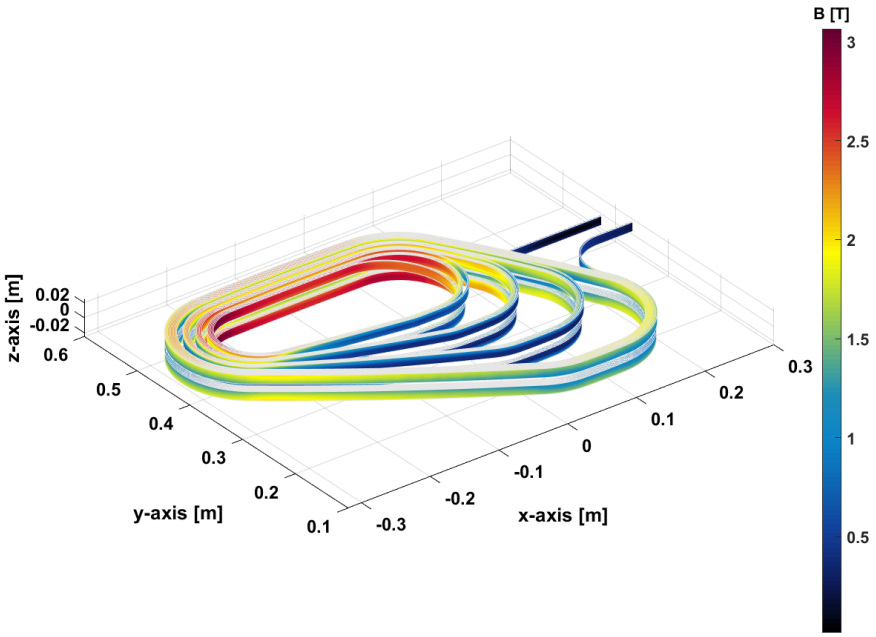

Figure 6.1 *Magnetic flux density on the conductors of the demonstrator operating at 7.1 kA and 4.2 K*

an outer rim. The pole (or a part of it) is used as support for the jump between the innermost grade of each layer.

The coil pack is then conceived to undergo a selective impregnation procedure (see *Sec.6.2.2*) to create a monolithic structure avoiding degradation of the conductors.

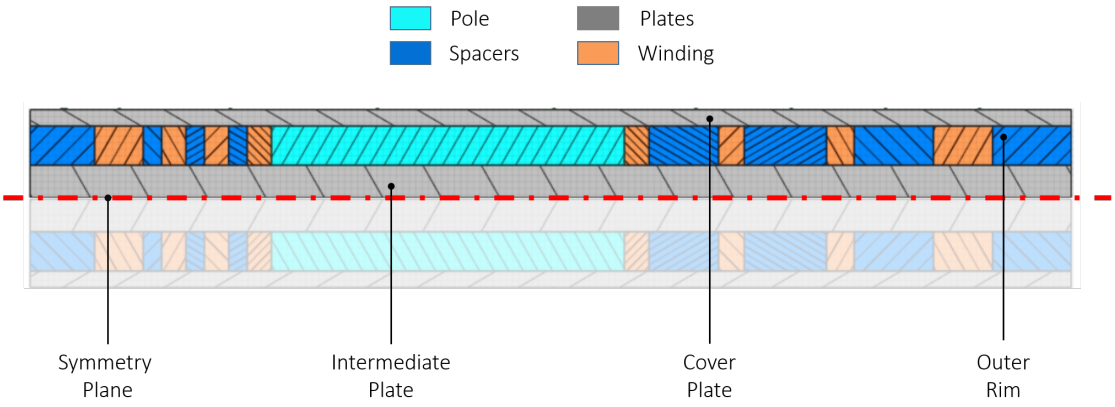

Figure 6.2 *Cross-section of the GaToroid demonstrator, with the terminology used to specify the different components*

Because it is not possible to exactly reproduce the full-scale coil conditions, two

working regimes were chosen for the demonstrator, *high temperature – low current* and *low temperature – high current*, summarised in *Tab.6.2*. The magnetic flux density map on top of the conductor surface is shown in *Fig.6.1* for the second case (7.1 kA at 4.2 K). The first configuration is representative of the GaToroid thermal operating conditions, while the second can be used to test the demonstrator at higher values of magnetic field and current density. *Tab.6.2* also reports the operating conditions of the two full-scale torus configuration, high J_{en} and low J_{en}.

Demonstrator - Operating Conditions			
Parameter	Unit	High T | Low I	Low T | High I
Operating Temperature - T_{op}	$[K]$	20	4.2
Operating Current - I_{op}	$[kA]$	5.0	7.1
Peak Magnetic Flux Density - B_p	$[T]$	2.16	3.06
Op. Current Density (Tape) - J_{op}	$[A/mm^2]$	1042	1479
Eng. Current Density (Cable) - J_{en}	$[A/mm^2]$	241	342
Peak Force Density $J \times B$	$[N/mm^3]$	0.5	1.0
Complete Torus - Operating Conditions			
Parameter	Unit	High J_{en}	Low J_{en}
Operating Temperature - T_{op}	[K]	20	20
Operating Current - I_{op}	[kA]	0.6	1.8
Peak Magnetic Flux Density - B_p	[T]	8.2	6.8
Op. Current Density (Tape) - J_{op}	$[A/mm^2]$	500	500
Eng. Current Density (Cable) - J_{en}	$[A/mm^2]$	500	100
Peak Force Density $J \times B$	$[N/mm^3]$	2.7	0.54

Table 6.2 *Description of the operating conditions of the demonstrator (High T | Low I) and (Low T | High I) in comparison with the two full-scale torus solution High J_{en} and Low J_{en}*

Fig.6.3 presents the working points for the two regimes, in comparison with the operating conditions of the GaToroid torus and a full-scale stand-alone coil, both for high and low engineering current density solutions. *Fig.6.3* reports as well the critical curves at 4.2 K and 20 K of a ReBCO tape, calculated with the parametrisation proposed by [81]. With the presented scaled-down demonstrator it is not possible to reach a magnetic field similar to the full-scale machine. The operating points were selected to work at the same current margin of the full-scale coils, but at different values of magnetic field. The complete torus operates at 73% of the critical current (27% of loadline current margin), and the demonstrator was designed to reach the same ratio in both regimes. In this operating conditions of field and current, the peak force density in the demonstrator can reach and go beyond the value of peak force density

of the low J_{en} full torus. In the high current regime, the demonstrator can reach more than one third of the peak force density of the high J_{en} torus.

To operate the demonstrator on the same load line of the torus it would have been necessary to insert it in background field. This scenario requires to use a superconducting magnet with an aperture of about 50 cm, generating approximately 5 T. Due to the complexity of the implementation, this option was not further considered.

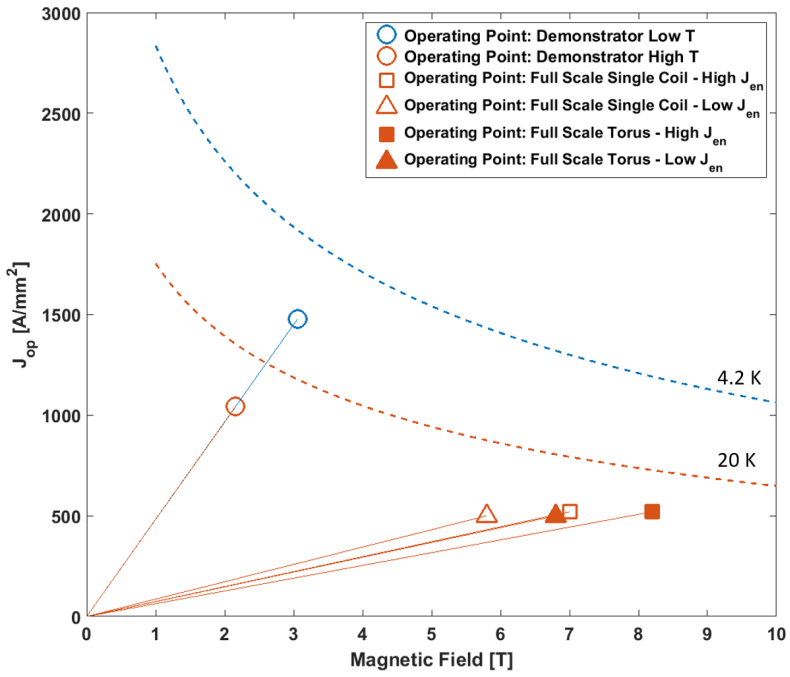

Figure 6.3 *Operating conditions, in terms of engineering current density and magnetic field, of the demonstrator in low (blue circle) and high (red circle) temperature regime. The plot reports also the operating points of the high current density configuration full-scale coil (empty square) and torus (filled square), and the operating points of the low current density configuration full-scale coil (empty triangle) and torus (filled triangle). Critical curves at 4.2 K (dashed blue line) and 20 K (dashed red line) are reported too.*

6.1 Cable Design and Quench Protection

Given the limited dimension of the demonstrator, as well as the low peak field on the conductors, the cable parameters presented in *Chap.5.1* (*Tab.3.3*) were modified to create more representative operating conditions for the HTS, *i.e.* working point at 73% of critical current, pushing the flux density up to 3 T. For this reason, a stack of 4 ReBCO non-transposed tapes*, 12 *mm* x 0.1 *mm*, was selected as a cable configuration. 2 copper tapes, 12 *mm* x 0.55 *mm*, were added for stabilisation, resulting in a ratio Cu:Non-Cu ratio of 5.3. The parameters of the demonstrator's cable are listed in *Tab.6.3*, while *Fig.6.4* reports a conceptual sketch of the cable topology.

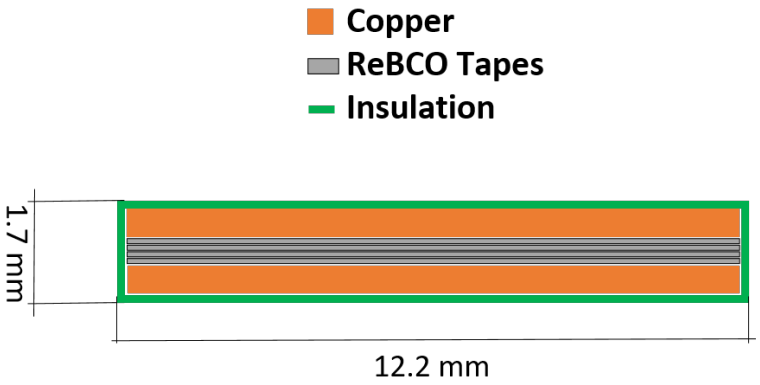

Figure 6.4 *Sketch of the HTS cable designed for the GaToroid demonstrator*

HTS Demonstrator - Cables Parameters		
Parameter	Unit	Value
Superconductor		ReBCO
Cable Topology		Non-Twisted Stack
N of HTS tape		4
N of Cu tape		2
Cable Width	[mm]	12.2
Cable Thickness	[mm]	1.7
Cu: Non-Cu ratio		5.3

Table 6.3 *Main cable parameters of HTS demonstrator*

Approximately fifty metres of the resulting cable, characterised by a cross-section of 12.2 *mm* x 1.7 *mm*, are required to wind the demonstrator. Fifty metres of unit length

*the HTS cable studied for the full-size Gatoroid is composed by 3 HTS tapes

is a *reasonable* value for ReBCO tapes and for this reason it is possible to avoid joints inside the coil.

6.1.1 Quench Protection Analysis

The amount of selected stabiliser was validated through a series of simulations based on the one-dimensional quench propagation model described in *Sec.5.1.3*, guaranteeing a controlled increase of temperature in case of failure. The approach and the assumptions are here listed for the sake of clarity:

- introduction of 1 cm defect in the centre of the cable
- adiabatic conditions
- one dimensional quench propagation (along the cable length)
- quench detection threshold set at 50 mV
- validation and reaction time of 20 ms
- current discharge with a constant characteristic time $\tau = L/R$
- voltage limit on dump resistor $\pm 1kV$
- power law (*Eq.(5.7)*) with n-value = 30
- copper with RRR = 100

The values of 50 mV of voltage threshold and 20 ms for validation time were selected based on the experience gained during the *Feather* magnets test at CERN [111][112]. The validation of the cable configuration was done in terms of maximum hot-stop temperature for both the operating regimes: *High Temperature - Low Current* and *Low Temperature - High Current*.

High Temperature - Low Current Regime

As shown in *Fig.6.5*, in this regime the increase of the voltage was slow (order of seconds) due to the limited amount of current and the high RRR of copper, reaching the threshold value of 50 mV in more than 4.5 s. For the same reason, the heat generated for Joule effect is modest and the longitudinal heat distribution along the cable is such that it is possible to maintain the peak temperature below the 100 K. Given the low inductance of the coil (0.64 mH), the current can be rapidly discharged with a time

constant of about 2 ms. The voltage, current and hot-spot temperature as a function of time are displayed on *Fig.6.5*. *Fig.6.6* exhibits the temperature profile along the cable. The temperature is higher at the centre of the cable, where the defect is placed. The generated heat slowly propagates along the conductor length, mitigating the hot-spot temperature increase. Finally, the current evolution between the normal and superconducting part of the cable is reported in *Fig.6.7*. To simulate the presence of the defect, in the central part of the cable the current on the superconductor is imposed equal to zero: $I_{sc} = 0$ and $I_{nc} = I_{op}(t)$.

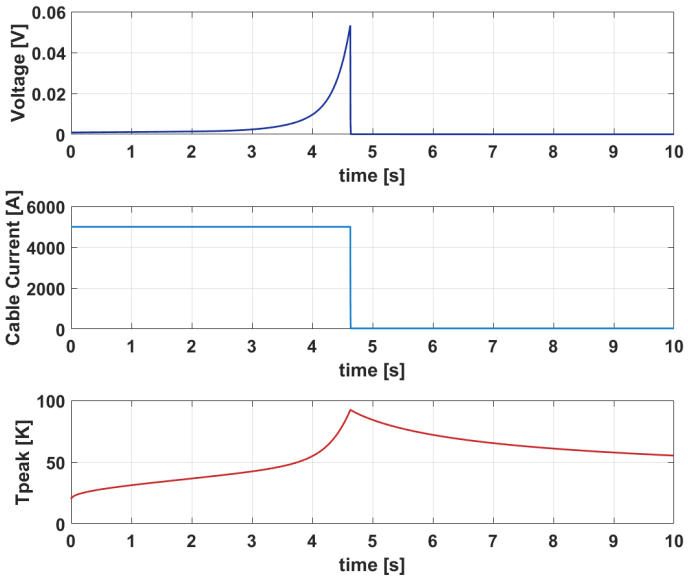

Figure 6.5 *Voltage, Cable Current and Peak Temperature as a function of time for the demonstrator operating in High Temperature - Low Current regime*

Low Temperature - High Current Regime

As illustrated in *Fig.6.8*, the increase of the operating current considerably reduced the time to reach the voltage threshold down to 1.1 s. Although the more severe conditions in terms of current, also in this case, the peak temperature is limited to less than 100 K. In this regime, the longitudinal heat distribution can be less relevant and the temperature profile along the cable of *Fig.6.9* is more *steep* if compared with the low current case. Given the shorter detection time, the time available for the heat distribution along the cable length is substantially reduced. For completeness, the profiles of the superconducting and normal currents in the proximity of the defect are shown *Fig.6.10* for the *low temperature* regime.

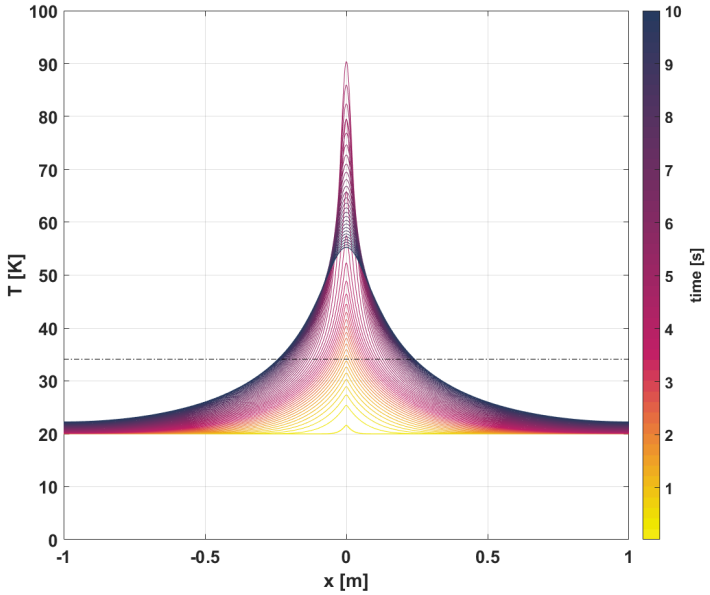

Figure 6.6 *Temperature distribution along the cable length at different time steps for the demonstrator operating in High Temperature - Low Current regime*

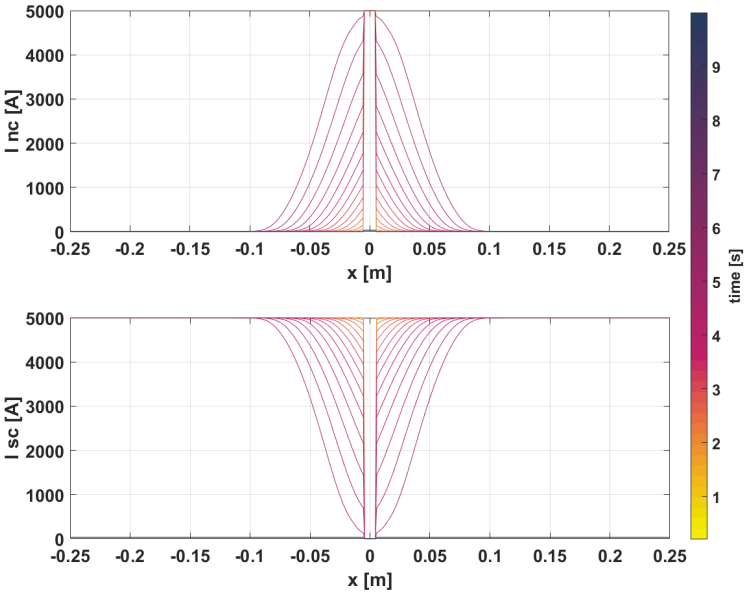

Figure 6.7 *Current on normal (Inc) and super (Isc) conductor as a function of the longitudinal cable position at different time steps for the demonstrator operating in High Temperature - Low Current regime*

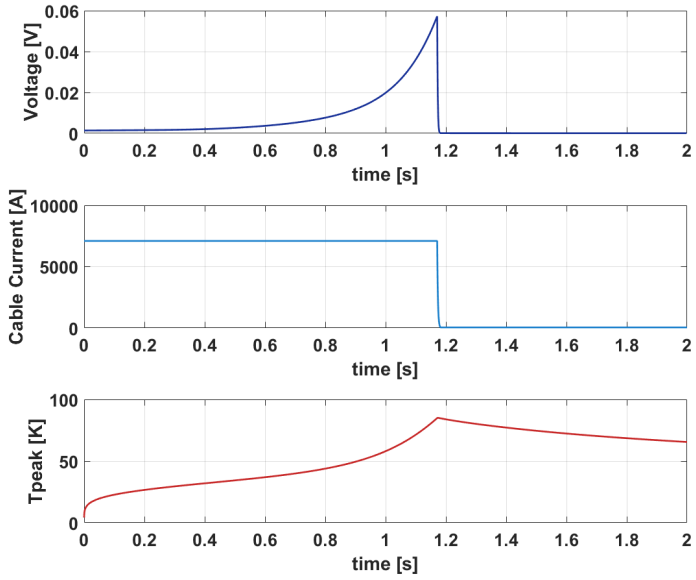

Figure 6.8 *Voltage, Cable Current and Peak Temperature as a function of time for the demonstrator operating in Low Temperature - High Current regime*

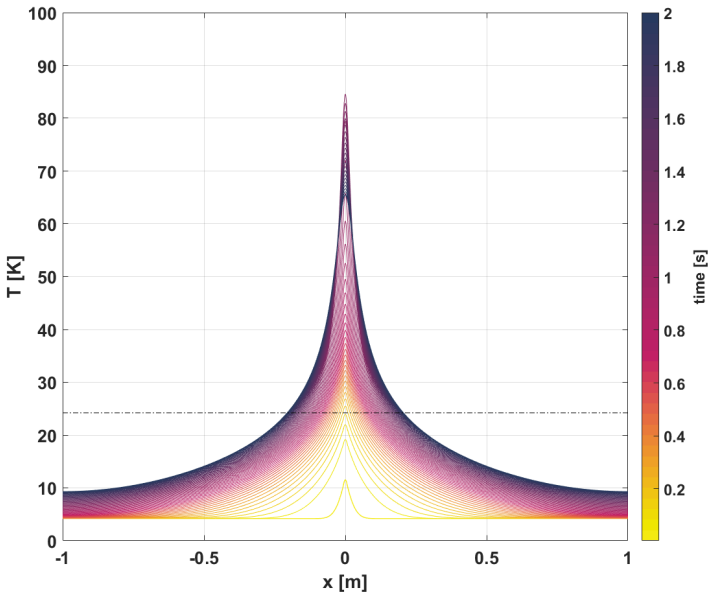

Figure 6.9 *Temperature distribution along the cable length at different time steps for the demonstrator operating in Low Temperature - High Current regime*

With the presented studies, the validity of the selected cable configuration was demonstrated in both the foreseen operating regimes.

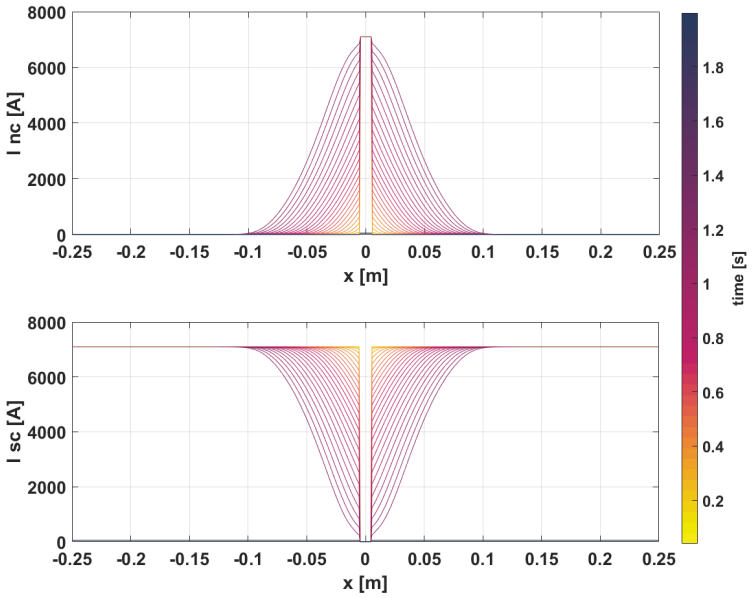

Figure 6.10 *Current on normal (Inc) and super (Isc) conductors as a function of the longitudinal cable position at different time steps for the demonstrator operating in Low Temperature - High Current regime*

6.2 Mechanical Analysis

Differently from classical low temperature superconductors [105], the energy released by mechanical disturbances is not sufficient to lead a quench in HTS due to the substantially larger energy margin*. Nonetheless, the layered composition of an HTS tape makes it particularly sensitive to specific stress states that can induce strong degradation and, ultimately, the breakage of the tape [121]. The mechanical strength of ReBCO tapes is strongly anisotropic, and this concept is well depicted by *Fig.6.11*. It is therefore important to operate HTS tapes mostly under tensile stress, reducing at minimum shear stresses, as well as peeling phenomena.

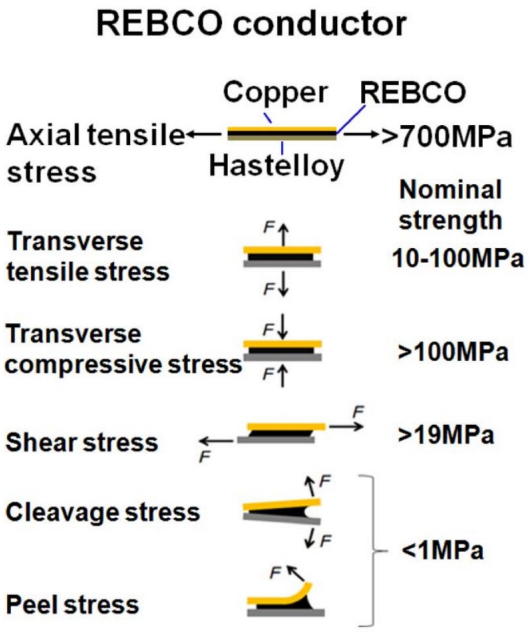

Figure 6.11 *Stress limits for a coated conductor under various mechanical constraints [121]*

Furthermore, different manufacturers propose different HTS tape, in terms of superconducting features (J_c, B_c, T_{cs}), and mechanical properties, where Young's modulus and yield strength can range in order of 30% [106]. On top of that, the assembly of the cable in stacks, the tension during the winding, the insulation and the impregnation pile up the number of unknowns. To face the complexity of the problem, yet keeping agile and flexible computations for the design process, it was necessary to make some assumptions and simplifications. The first strong assumption was to consider the tape and the cable as an isotropic mixture. The second simplification was to assume the mechanical properties of this mixture as an average between stainless steel (SS) and

*ReBCO energy margin ($10 - 20\ J/cm^3$) is 2-3 orders of magnitude larger than LHC Nb-Ti (15-20 mJ/cm^3 [107]) or HiLumi LHC Nb_3Sn (20 mJ/cm^3 [109])

copper: [70% SS, 30% Cu] for the tape, translated to [19% SS, 81% Cu] for the cable of *Fig.6.4*. The presence of insulation and impregnation was not considered.

Furthermore, the calculation of the Lorentz forces, $J \times B$, were based on a non-insulated coil scenario, where the current density J_{en} was set to 500 A/mm^2 and peak flux density resulted in 4.5 T. The calculated peak force density was $f_{max} = 2.0$ N/mm^3. The electro-magnetic forces used for in the two and three-dimensional models described in the next sections are two times higher than the forces generated in the *low temperature – high current* operating mode. On the one hand, the design of a mechanical structure able to withstand two times the nominal forces was considered a conservative assumption and used to counterbalance the aforementioned simplifications of the winding materials. On the other hands, the presented design validates, in terms of mechanics, the possibility of winding the demonstrator as a non-insulated coil.

6.2.1 2D model

Given the planar geometry of the coil, at first, the mechanical behaviour of the GaToroid demonstrator was studied with a 2D model, composed by the following bodies, shown in *Fig.6.12*:

- 4 independent coils composed by 4,4,4 and 8 turns of the HTS cable (in orange) described in *Tab.6.3*
- pole (light blue), spacers and outer rim (dark blue) acting as mechanical support

The intermediate and the cover plates were not taken into account in this model, and will be taken into account in the 3D studies. The spacers and the pole were considered to be in Stainless Steel (SS), while the material of the coils was averaged between stainless steel (19%) and copper (81%). In this approach, all the bodies were considered to have bonded connections: neither sliding nor separation can occur between the components. This strong assumption was based on an ideal behaviour of the impregnation, not subjected to cracks or breakages, that create perfect contact between the bodies. A more detailed discussion on the mechanical role of the resin is presented in *Sec.6.2.2*.

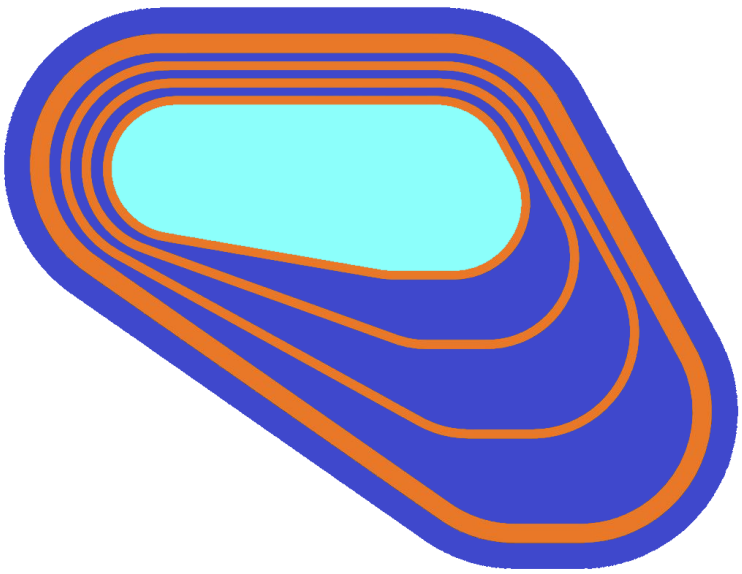

Figure 6.12 *Demonstrator geometry, composed by the graded coil (orange), the central pole (light blue) and the spacer (dark blue)*

Lorentz forces were applied on the conductors, taking into account the local distribution of the magnetic field and a constant current density. *Fig.6.13* shows the body

force densities applied on the windings, transversal to the conductor path. In the presented 2D study, the force component perpendicular to the coil plane (x-y) was not considered. Each layer of the pancake was subjected an attraction force toward each other, resulting in a null total force on the whole coil.

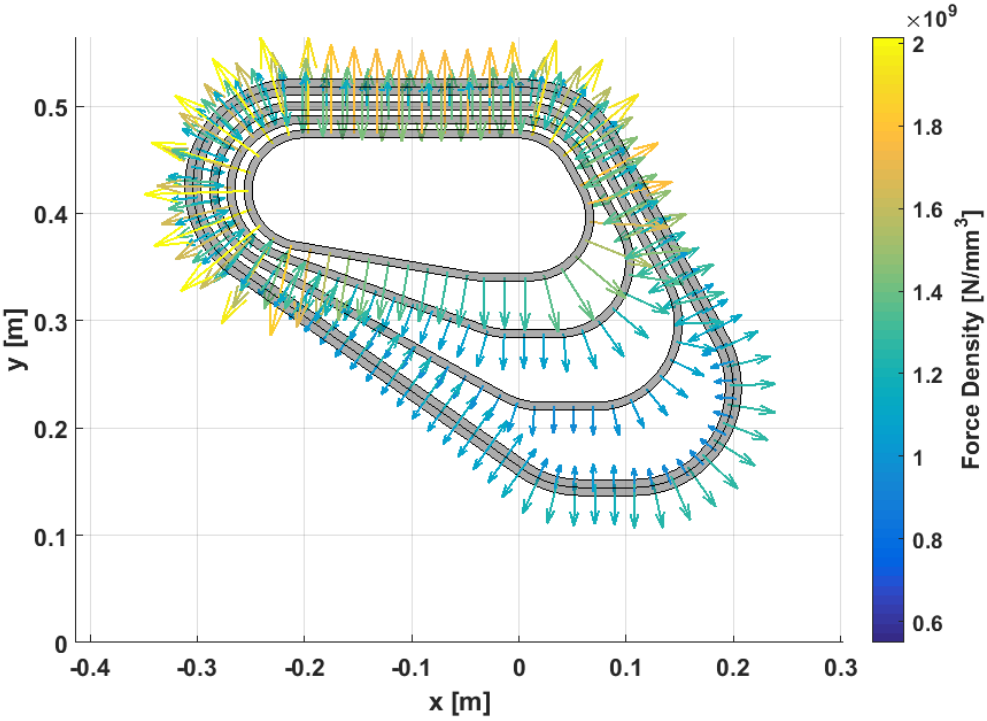

Figure 6.13 *Body force density acting on the conductor due to the Lorentz forces*

Concerning the boundary conditions of the simulations, the upper surface of the pole was connected to a virtual point to fix the body in the space without adding extra stiffness to the structure. The convergence of the simulations was guaranteed by the bonded contacts between the parts.
The stress state on the coil resulting from the described mechanical simulation is presented in *Fig.6.14*, where the maximum stress, occurring in the peak field region is 21 MPa. As shown in the zoom of *Fig.6.14*, the Lorentz forces were translated to hoop stresses, along the longitudinal winding direction: the conductor was mainly subjected to axial tensile tress. However, given the strong bond between the innermost coil and the layer jump, transversal stresses were also present; this may represent a relevant threat concerning HTS tape delamination.

The results shown in *Fig.6.14* were evaluated at room temperature, but another important source of stress for the magnet is due to the different coefficient of thermal expansion (CTE) of the of stainless steel and the equivalent HTS cable composite. With the selected materials, there was a difference of about 5% in the CTE: the coils shirked

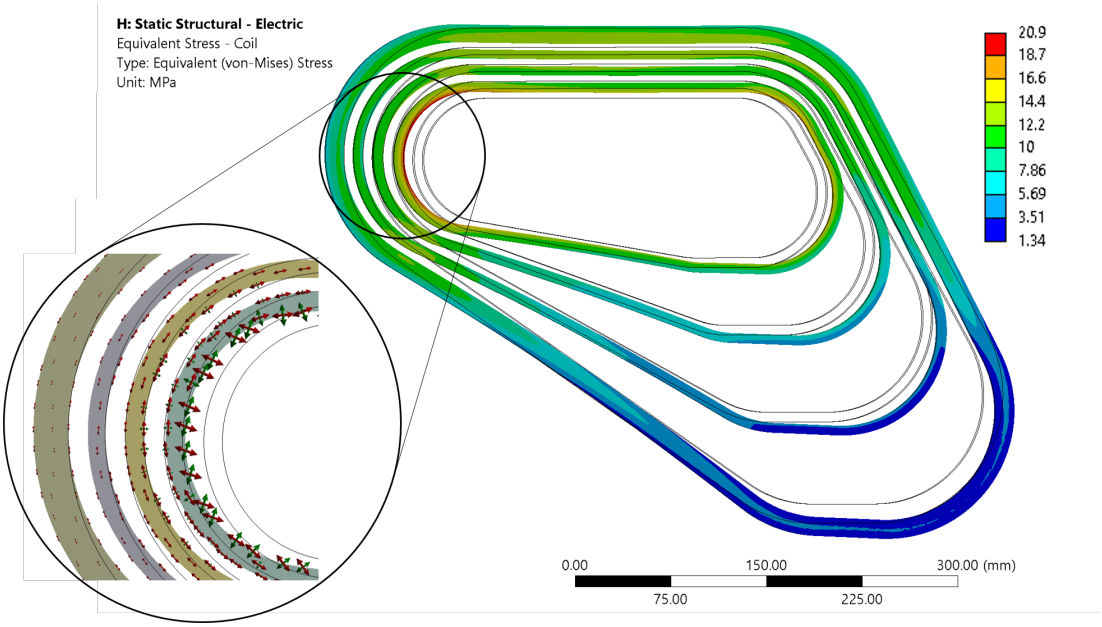

Figure 6.14 *Equivalent stress on the coil, due to the application of Lorentz forces*

5% more than the spacers. The components were bonded together and no separation can occur, and the temperature variation (from 300 K to 4.2 K) induced stresses on the conductor, that must be carefully evaluated. The contraction tended to deform the structure in the opposite direct if compared to the Lorentz forces, and this mechanism could be used to apply a specific pre-tension to the coil adjusting the CTE difference between windings and mechanical structure. This subject is described in more detail in *Sec.6.2.2*. The proposed model is linear and the effects of thermal contraction can be superimposed to the studies done on electro magnetic forces, resulting in the stress distribution presented in *Fig.6.15*. The peak stress is 40 MPa, still located in the innermost grade of the demonstrator. It is worth noting that the application of the cool-down reduced the transversal tresses between the pole and the innermost grade, strongly reducing the risk of resin debonding and tape delamination.

It is clear that the 2D model described in this section is a first approximation of the mechanical behaviour of the GaToroid demonstrator. The assumptions considered in this model neglect relevant aspects of the interaction between the coil and the structure, as the frictional behaviour with the base and top plate and the possible separation between bodies. For this reason, a complete 3D model was developed to better understand the mechanical behaviour of the demonstrator operating in cryogenic and electro-magnetic conditions.

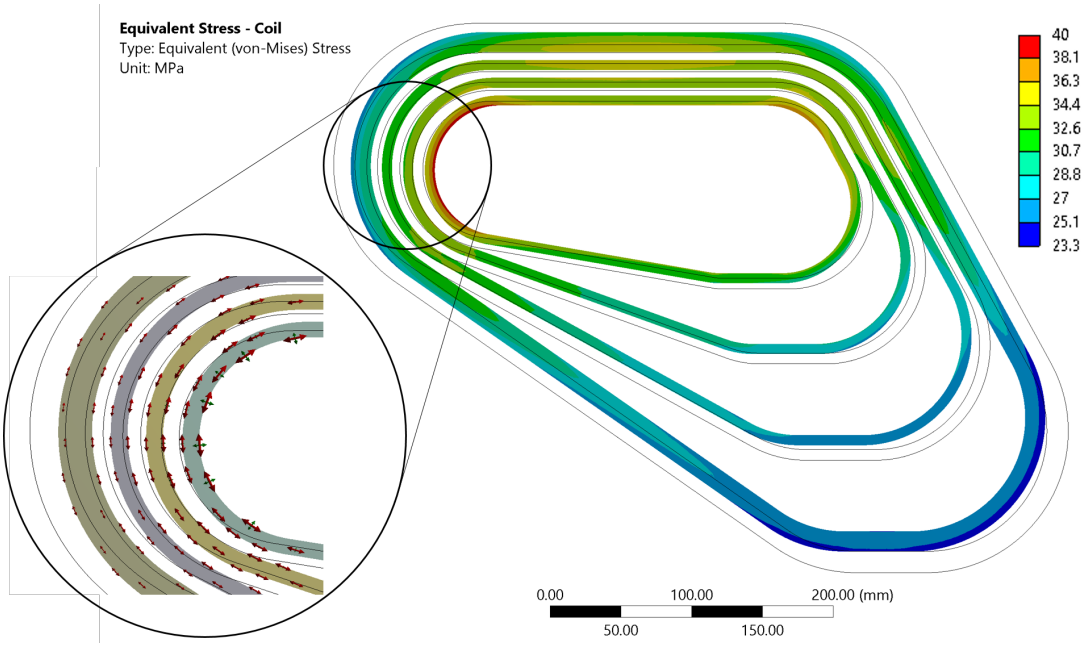

Figure 6.15 *Equivalent stress on the coil, due to the combination of cool-down at 4.2 K and the application of Lorentz forces*

6.2.2 3D model*

The next step of the mechanical analysis was to move away from the 2D approximation to grasp fundamental details of the demonstrator mechanical behaviour. The analysis was performed including all the bodies, *i.e.* coils, pole, spacers, intermediate and cover plates. One single layer was simulated, imposing a symmetry condition at half-thickness of the intermediate plate, as shown in *Fig.6.16*. The simulated geometry is presented in *Fig.6.17*, where the cover plate is omitted for a better view. The pole, plates and spacers were simulated as stainless steel, while the cable material was averaged between stainless steel (19%) and copper (81%).

The nature of contacts between these bodies is one of the discussion topic of this section. A high friction coefficient between the bodies represents the strong bonding of the resin. A low value of friction is instead used to facilitate the separation of the bodies.

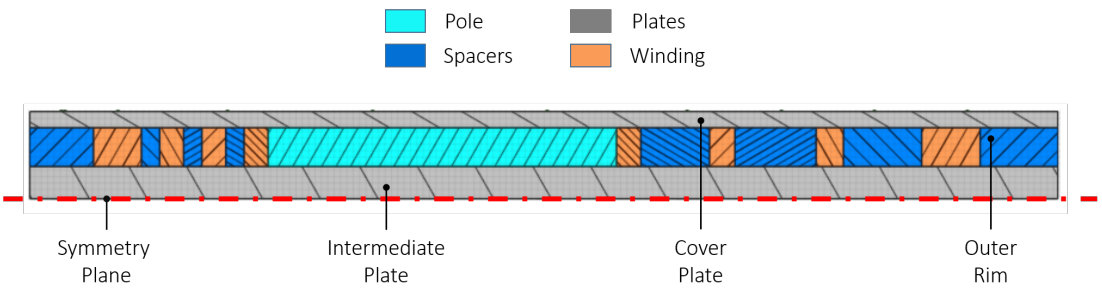

Figure 6.16 *Demonstrator cross-section used for the three-dimensional mechanical simulations*

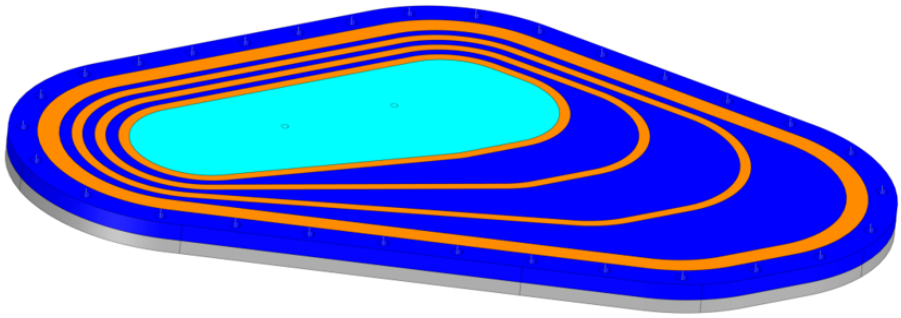

Figure 6.17 *Demonstrator geometry, composed by the graded coil (orange), the central pole (light blue), the spacers (dark blue) and the base plate (grey)*

*the 3D model was developed by Jerome Harray, under the supervision of Tuukka Lehtinen and myself

Three subsequent simulation steps were implemented:

- bolt pre-tension applied on the outer rim
- cool-down from 300 K to 4.2 K, considering the different CTEs of the components
- powering of the magnet and consequent application of Lorentz forces on the conductor

Firstly, it was important to evaluate the effectiveness of the impregnation in the demonstrator. For this reason a parametric study of the friction coefficient applied at the contacts between the bodies was done. A high value of the frictional coefficient represents an impregnated coil scenario, where the mechanical parts cannot slide nor separate. Lower values of the frictional coefficient allowed the separation of the bodies, simulating the absence of impregnation. The results are presented in *Fig.6.18*, where a clear increase of stresses on all the components is observed for low values of the frictional coefficient. In other words, the impregnation may effectively reduce the stresses on the superconducting cables.

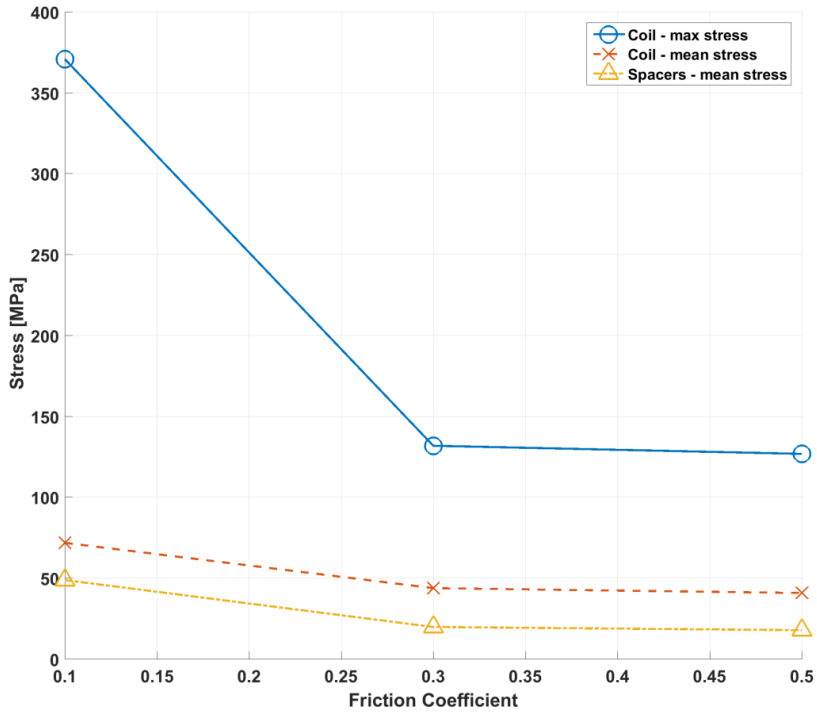

Figure 6.18 *Maximum (blue circle) and mean (red cross) stress on the coils, and mean stress on the spacers (yellow triangle) as a function of the friction coefficient applied between the demonstrator contact surfaces*

The impregnation strategy was then investigated. Considering all the bodies bonded together, the trend of contact pressure is presented in *Fig.6.19* for the different simulation steps. Negative pressure could be responsible for the pealing of the tapes and must be carefully avoided; at the same time, negative pressure could lead to a resin detachment from the surfaces with a consequent cable deterioration. Based on the experience of Feather magnets [111], a debonding limit of $-20\ MPa$ was considered a *reasonable* assumption. A fully bonded solution, strongly exceed this value and was therefore abandoned. Similarly, the positive pressure reached very high values that may bring to resin cracks and breakages. As a first thing, the impregnation between the separation and covers plates with the winding and the spacers must be avoided.

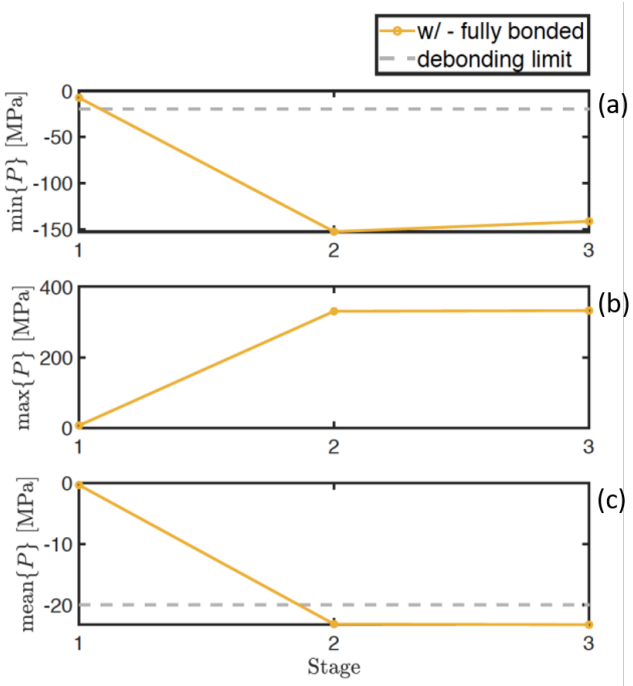

Figure 6.19 *Minimum* ***(a)****, maximum* ***(b)*** *and mean* ***(c)*** *contact pressure for the different simulation steps, considering all the bodies bonded together*

Furthermore, to evaluate the different fault scenarios of ReBCO tapes, as peeling and shear stress, the nature of the contacts between the components was investigated. During the cool-down, the coils shrink more than the stainless steel spacers, while during the powering the coils push radially outwards due to the Lorentz forces. In other words, during the cool-down, the outermost cable tended to detach from the outer rim, while during the powering, the innermost cable tended to detach from the pole. For this reason, different scenarios were analysed, where the necessity of the central pole as a mechanical support and the nature of the contacts between the bodies were questioned. The results are summarised in *Fig.6.20* and the different configurations are here listed:

- *w/o - bonded*: without pole - bonded contact between all the spacers and the windings
- *w/o - frictional rim*: without pole - bonded contact between all the spacers and the windings, except for contact between the outermost cable and the outer rim
- *w/ - bonded*: with pole - bonded contact between all the spacers (and pole) and the windings
- *w/ - frictional rim*: with pole - bonded contact between all the spacers (and pole) and the windings, except for contact between the outermost cable and the outer rim
- *w/ - frictional rim & pole*: with pole - bonded contact between all the spacers and the windings, except for contact between the outermost cable and the outer rim and the contact between the innermost cable and the pole

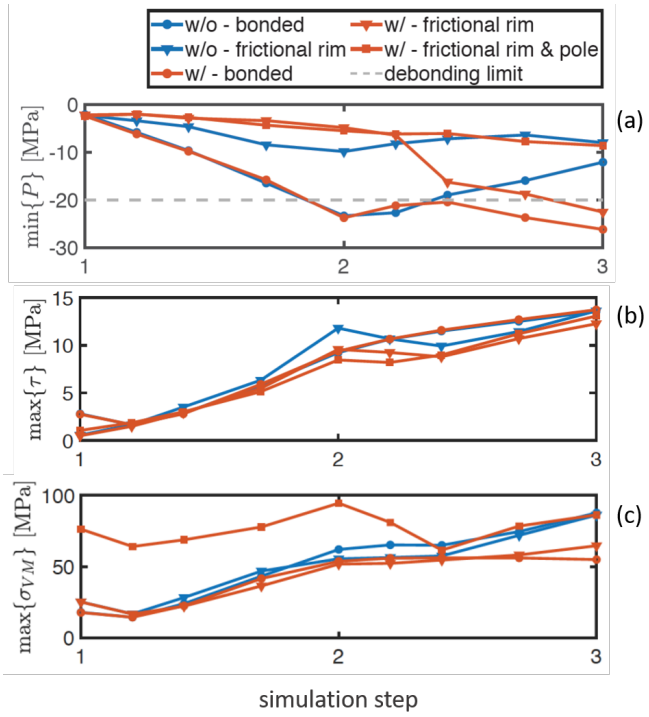

Figure 6.20 *Minimum contact pressure* ***(a)*** *and maximum shear stress* ***(b)*** *at the interfaces between windings and spacers, and maximum equivalent stress in the winding* ***(c)*** *for different configurations.*

As shown in *Fig.6.20*(a), there were two configurations where the minimum pressure was in the order of -10 MPa in both simulation steps, namely the case without the pole and frictional contact on the outer rim (*w/o - frictional rim*) and the case with the pole

and frictional contacts at the outer rim and at the pole (*w/ - frictional rim & pole*). As expected, a frictional contact at the outer rim avoided debonding during the cool-down, while a frictional contact with the pole, or its removal, prevented excessive negative pressure value during the powering. Therefore, during the impregnation procedure, the cohesion of the resin on the surfaces of the pole and the outer rim must be avoided.

Moreover, *Fig.6.20*(b) presents the trend of the shear stresses at the interfaces between windings and spacers for the different configurations. Regarding the shear, even if no major differences can be identified, the maximum value is below 15 MPa and it should be sufficiently small to avoid breakage and cracks in the resin.

Finally, *Fig.6.20*(c) reports the maximum Von-Mises stress state on the coils that for the *w/o - frictional rim* and *w/ - frictional rim & pole* configurations is maximized at about 80 MPa. This stress distribution allows the cable to work mostly in tension and within the limits described in *Fig.6.11*. This behaviour is shown in *Fig.6.21* for the scenario with the highest peak stress.

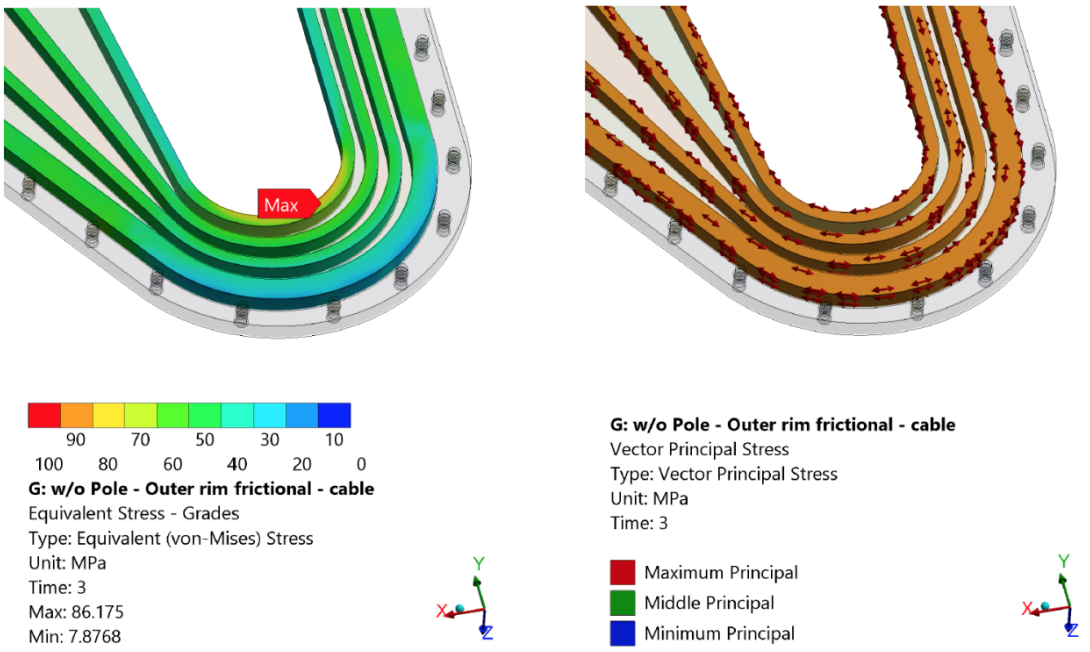

Figure 6.21 *Equivalent stress on the coil, due to the combination of cool-down at 4.2 K and the application of Lorentz forces: the conductors work mostly in tension*

Following this impregnation procedure, the possibility of using different materials with different coefficients of thermal contraction was investigated. Aluminium components, with an higher CTE value than SS , could be used to apply pre-stress during the cool-down, balancing the Lorentz forces and reducing the final stress on the conductor. In the same and opposite way, the introduction of a Titanium pole with lower CTE value than SS, can further accentuate this concept preventing the shrinkage from the

centre of the coil. *Fig.6.22* presents the results of this analysis, including cool-down (step 2) and powering (step 3) of the magnet, for three reference cases:

- (A): all the mechanical components in stainless steel
- (B): all the mechanical components in aluminium, except for the pole in stainless steel
- (C): all the mechanical components in aluminium, except for the pole in titanium

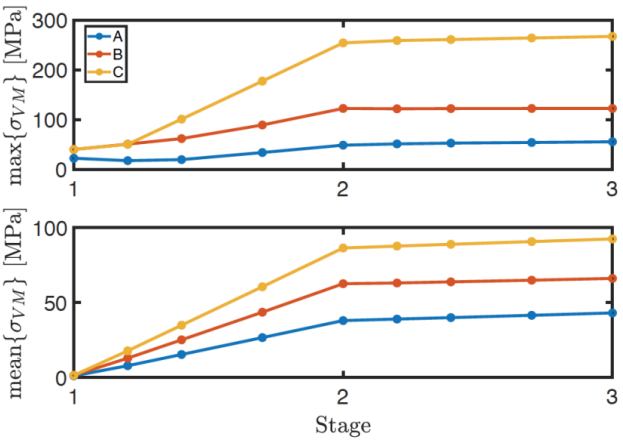

Figure 6.22 *Maximum and mean stress on the coil in case of three different material configuration.*

As expected, the use of materials with different CTE had relevant effects on the stress state of the coil. However, the stresses generated in the configurations (B) and (C), were substantially higher than the case (A) and dominated over the Lorentz forces. For this reason, the configuration (A), with only stainless steel components, was maintained. A more detailed description of the three-dimensional mechanical model presented in this section can be found in [122] [123].

6.3 Experimental Implementation

The work presented in this section is the result of intense and continuous interactions with the technicians and engineers of TE-MSC-MDT section of CERN

6.3.1 Cable Winding, Insulation and Impregnation

The cable configuration described in *Sec.6.1* requires the simultaneous winding of the 6 tapes (4 HTS and 2 Cu) with numerically adjusted tension from 6 different spools. As a matter of fact, the tape in the outermost position is wound on a longer path than the innermost one. This creates an unbalance that must be compensated in real-time during the winding. For this reason, the TE-MSC-MDT section at CERN installed and validated a new multi-spool winding table, that allows dedicated tension control in 7 spools*. A picture of the winding table is presented in *Fig.6.23* together with 3 copper tapes used for the machine validation.

If particular attention must be dedicated to the tapes' tension during the winding, it is also important to implement an appropriate insulation scheme. In this case, it is not possible to assemble and insulate the cable before the winding: these two procedures must be done *in-situ*. Once the tapes are stacked to form the cable, they must be wrapped with an insulating layer capable of allowing the necessary sliding between them.

The insulation has a dual effect: not only it must maintain electrical insulation between the windings, but it must also create a suitable surface for the impregnation resin to adhere, avoiding an excessive penetration of the resin into the cable. In fact, low thermal and electric contact resistances between the tapes constituting the cable must be maintained to facilitate heat and current sharing in case of a quench. In a scenario where the impregnation completely isolates the tapes from the stabiliser, the cable would not withstand the heat generated during the quench, damaging irreversibly the magnet; this scenario must be carefully avoided.

A glass fibre sleeve was selected as reference insulation scheme and an example of an insulated short sample is shown in *Fig.6.24*(a)*. The glass fibre can efficiently absorb the resin, but powders and residual could be blocked by the texture creating an

*the design and the assembly of the table were done by: J. Mazet, and J.C. Perez

*the development of the insulation schemes was carried out by Jacky Mazet

Figure 6.23 *View of the multi-spool winding table assembled in the TE-MSC-MDT laboratory*

inhomogeneous impregnation. At the same time, the good affinity between the resin and the fibre can create a strong adhesion between the cables and the spacers, but it can lead to a relevant resin penetration and consequent loss of electrical conductivity between the tapes. The behaviour of the resin in between the cables also depends on the winding tension and the consequent contact pressure between the windings. The proposed insulation configuration and its affinity with specific resins must be validated with impregnation tests.

A backup option is represented by the use of C-shape layer of Polymide (*e.g.* Kapton tape), as illustrated in *Fig.6.24* (b). This configuration can create a more fluid distribution of the resin but the adhesion could be less effective. The geometrical opening of the C-shape, that allows the sliding of the tapes, could be also used by the resin to enter inside the cable and compromise the sharing of heat and current.

Furthermore, the resin choice, as well as the amount and type of filler, can determine substantial differences in the results, in terms contact resistance between the tapes and adhesion to the external cable surfaces. Several kinds of resins are available for impregnation, ranging from classical epoxy used for LTS magnets, *e.g.* CTD-101, to weak bonding strength materials as paraffin or bee wax [124]. On the one hand, the use of impregnation allows creating a monolithic structure with reduced conductor movements and enhanced thermal conductivity [105]. On the other hand, the difference of coefficients of thermal expansion (CTE) between the conductor and impregnation

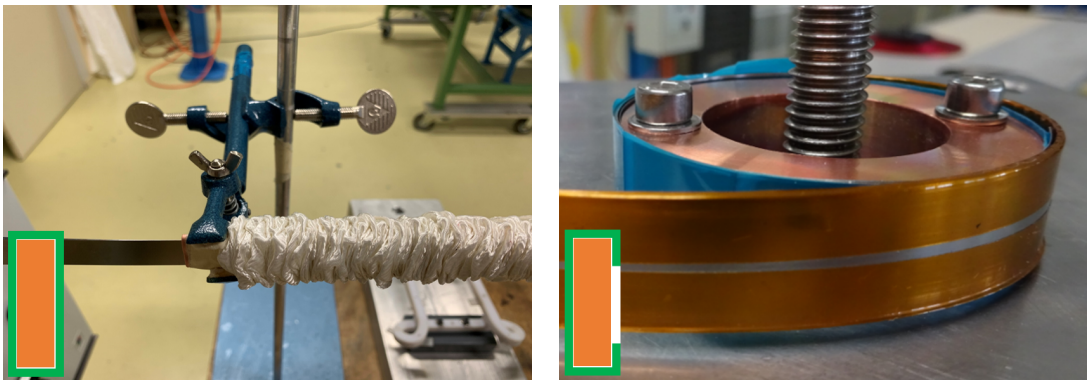

(a) **(b)**

Figure 6.24 *Pictures of the insulation schemes of GaToroid demonstrator, with a schematic representation: glass-fibre sleeve* ***(a)****, where the insulation complete surrounds the cable, and C-shape Kapton layer* ***(b)****, where the insulation leaves an aperture to the bare cable*

material can lead to delamination of the superconducting layer, degrading irreversibly the tape. To overcome this problem, it is possible to tune the CTE of the resin adding powders of low CTE materials. Quartz has a thermal expansion close to zero and it allows a significant reduction of resin CTE approaching the one of a ReBCO [125]. Even more effective results can be obtained with materials characterised by a negative CTE (they expand when cooled), such as diamond powder [126] and Zirconium Tungstate (ZrW_2O_8) [127]. Even carbon fibre can be used to modify the resin CTE, but the extremely high electrical conductivity does not make it a suitable candidate for an insulated configuration. Nevertheless, a carbon fibre reinforced resin could be an interesting solution for non-insulated coils.

However, the introduction of a high percentage of powders can strongly reduce the resin fluidity, leading a less uniform impregnation. At the same time, the different density between resin and additives can create deposits in the lower part of the coil and a consequent gradient of CTE along the thickness of the windings. The percentage of powders, the interaction with different resin and the effects on the coated conductors must be therefore validated through experimental tests. For this reason, an experimental setup for the impregnation of 4 cables stacks was installed at CERN TE-MSC-MDT section. The impregnation mould*, shown in *Fig.6.25*, would allow to test up to 3 stacks at the same time, varying the insulation scheme as well as the transversal pressure applied to the cables. The applied pressure can also provide insights on the winding tension required during the winding of the demonstrator. The impregnated stack will then undergo electric tests in liquid nitrogen, aiming to evaluate the effects of the resin on the superconductors (V-I curve, n-value) and on the electrical contact resistance

*the design and the machining of the mould was carried out by Lukas Henschel and Nicolas Bourcey

between the different tapes. The insulation and resin configuration that will exhibit a good resin adhesion, minimizing the effects of degradation on the cable, will be selected for the winding of the demonstrator.

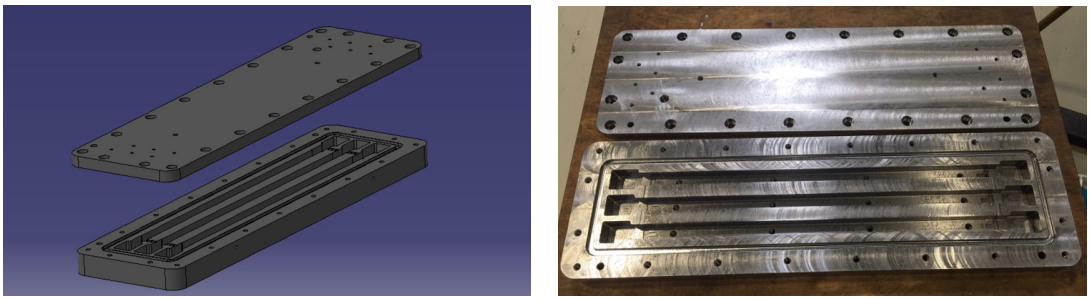

(a) **(b)**

Figure 6.25 *Design* ***(a)*** *and actual machined* ***(b)*** *impregnation mould used for the 4 cable stacks impregnation campaign.*

Samples of the impregnated cables stacks can be used to assess the mechanical properties of the impregnated coils, such as the coefficient of thermal expansion (CTE), Young's modulus and yield strength in the three dimensions. These parameters can then be used to refine the mechanical simulations presented in *Chap.6.2*.

To conclude, it is interesting to point out that the radial stresses and hence the degradation of impregnated coils generated during the cool-down are functions of the ratio between outer and inner diameter (OD/ID). It was observed that a coil radial subdivision can strongly reduce the degradation on impregnated coated conductors, and no effect on the magnet performances can be observed for a ratio (OD/ID) < 1.4 [128]. Thanks to the characteristic coil grading of GaToroid, the equivalent maximum (OD/ID) ratio is in the order of 1.1. With the proposed geometry, it should be therefore possible to achieve a degradation-free impregnated ReBCO coil.

6.3.2 Magnetic Measurements

The lack of a complete toroidal configuration prevents generating a representative field of the GaToroid concept. However, the measurement of the magnetic field is a fundamental validation of the demonstrator. The points of the equivalent beam trajectory were selected for the measurement on the middle plane in between the layers. The concept is better explained in *Fig.6.26*, where the normalised flux densities $B(s)/B_{peak}$ are plotted, along the equivalent s-coordinate, for a full-size single coil and the demonstrator. The s-coordinate represents the orbit of 250 MeV beam and the same orbit

scaled by a factor 3 (plotted with the normalised field on the demonstrator in the box *Fig.6.26*). The measurements can be performed in operating conditions of temperature and current with Hall probes, cross-calibrated *in situ* using induction-coil sensors [129]. Furthermore, to precisely align the sensors along the s-coordinate, an *ad hoc* printed circuit board (PCB) can be designed with specific traces to allocate the instrumentation and can be placed inside the intermediate plate. A similar approach was implemented for the Racetrack Model Coil (RMC) at CERN [130] [131].

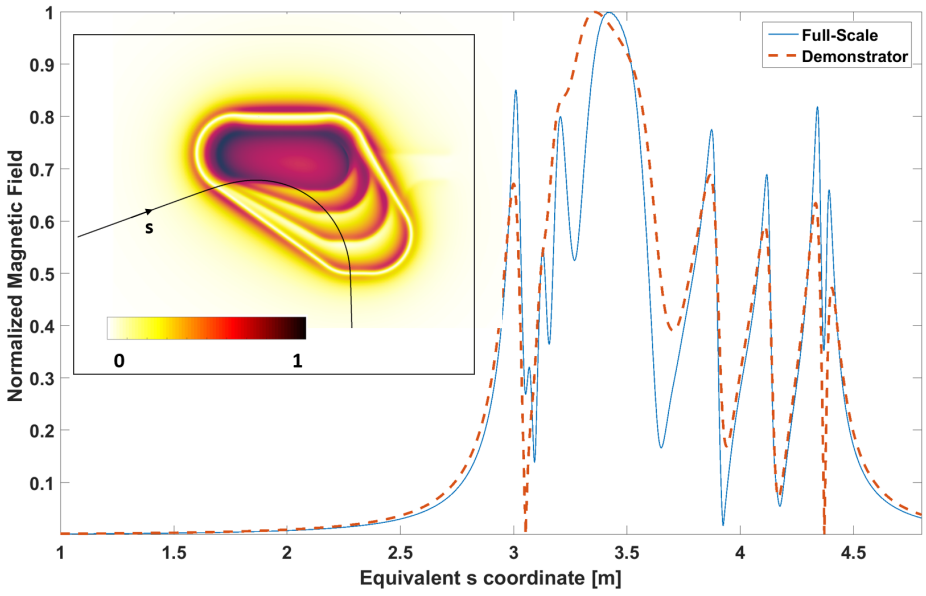

Figure 6.26 *Normalised magnetic flux density on the coil surface for the full-scale single coil (blue continue) and demonstrator (red dashed), as a function of the equivalent s coordinate of 250 MeV beam*

6.3.3 Electrical Measurements

Following the quench protection considerations presented in *Sec.6.1*, the voltage measurement in the coil is of uppermost importance for the effectiveness of the proposed quench protection system. During the cool-down and test of the demonstrator, it is important to have redundancy on the electrical measurements, *i.e.* doubling the number of voltage taps. Furthermore, the studied magnet is a composition of 4 sub-coils per layer. In this sense, it is interesting to measure the voltage for each of this coil, specifically at the grade jump position, where the mechanical deformations of the support

structure and the cable are more intense. Given the symmetry of the coils in respect with the two layers, it is also important to perform electrical measurement at a central point, the layer jump. This allows to differentiate the voltage signals and sensibly reduce the noise of the measurements. Finally, voltage taps at the current leads are also required, to have a global measurement of the voltage in the magnet. To sum up, the required voltage taps number for a reliable test is 22, as presented in the schematics of *Fig.6.27* (2 taps for each location).

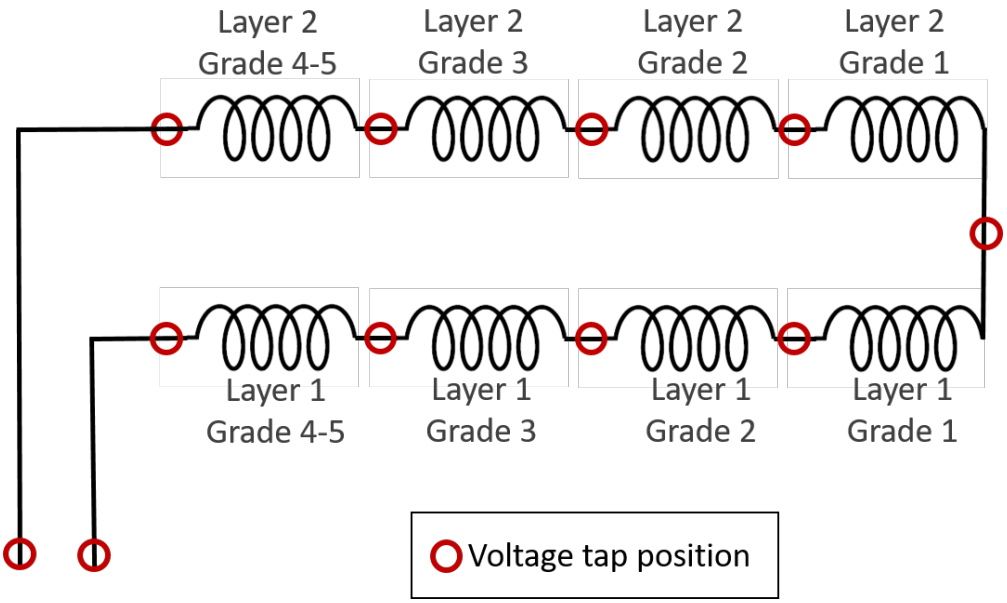

Figure 6.27 *Schematics for the electrical measurement concept. To provide more robust measurements, for each position (red circle) two voltage tapes need to be placed*

6.3.4 Assembly and Windings of Stainless Steel Demonstrator

As a step toward the HTS demonstrator construction, a first version of the demonstrator wound with stainless-steel tapes was built, in order to validate a first winding procedure and the design, as well as develop the required tooling for the magnet assembly. Starting from the precise conductor path of both layers, depicted in *Fig.6.28*, the spacers and the outer rims were defined. The spacers are open rings, with an aperture that follows the transition from one grade to another. The outer rims are open too and are extended to provide support to the cable up to the current leads. *Fig.6.29* shows the design of the demonstrator mechanical structure together with the 3D printed glass-filled nylon spacers used during the winding of the *dummy* coil.

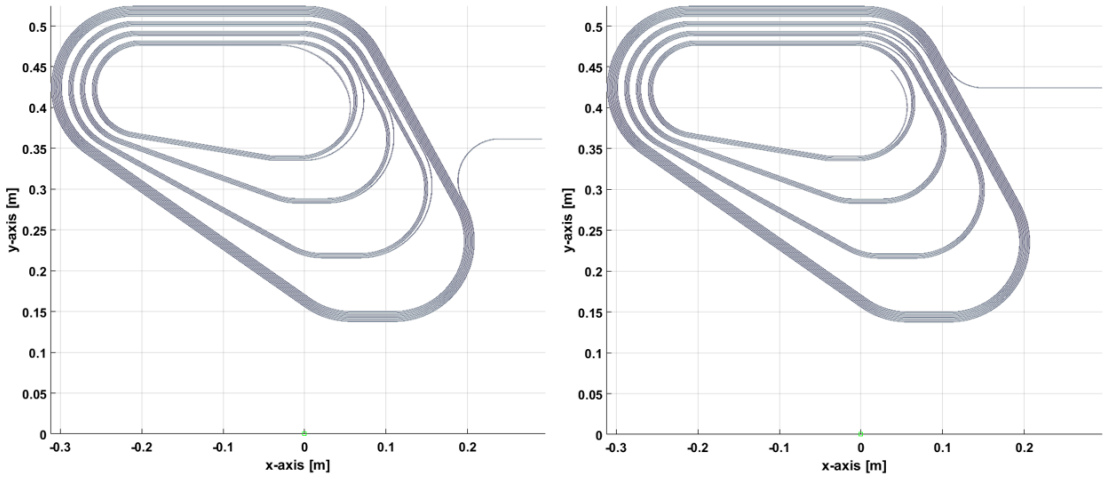

(a) **(b)**

Figure 6.28 *Lower* ***(a)*** *and upper* ***(b)*** *pancake layers of the GaToroid demonstrator, considering no-insulation between the windings*

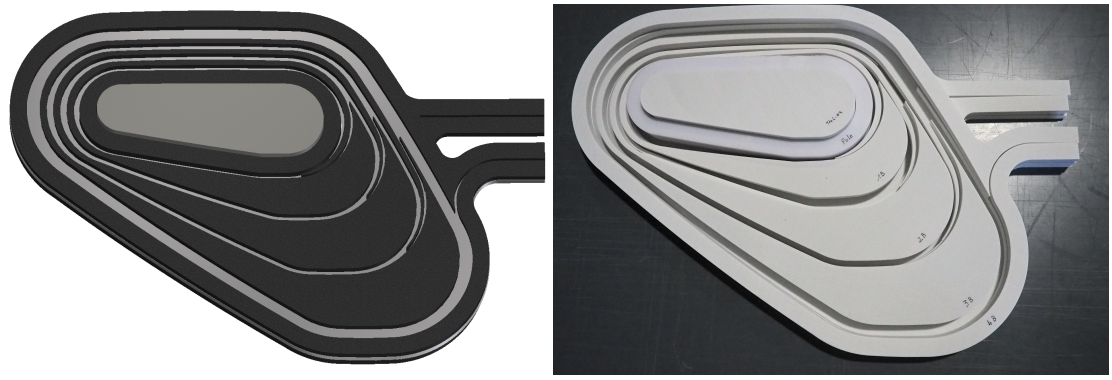

(a) **(b)**

Figure 6.29 *3D model* ***(a)*** *and 3D printed* ***(b)*** *spacers for GaToroid demonstrator.*

A picture of the first layer of the GaToroid demonstrator wound with stainless steel tape is presented in *Fig.6.30*, together with the *ad hoc* developed tooling and winding supports. The winding procedure was done with a single tape of the exact dimensions of a ReBCO conductor, *i.e.* 0.1 *mm* x 12 *mm*. Starting with the first layer, the tape was wound around the pole for the required number of turns. Once a grade was completed the relative spacer was added and the winding process continued around it, until reaching the last grade that was enclosed by the outer rim. The same process was done for the second layer and the assembled coil was finally blocked from the upper and lower cover plates. The red tooling of *Fig.6.30* was used to maintain the

pressure between the turns. For each grade, the winding tension was adjusted to limit misplacement (*waves*) on the conductors and to avoid piling up too much radial stress. The winding started with a tension of 5 Kg for the first 5 turns and was then reduced to 2 Kg for the remaining ones.

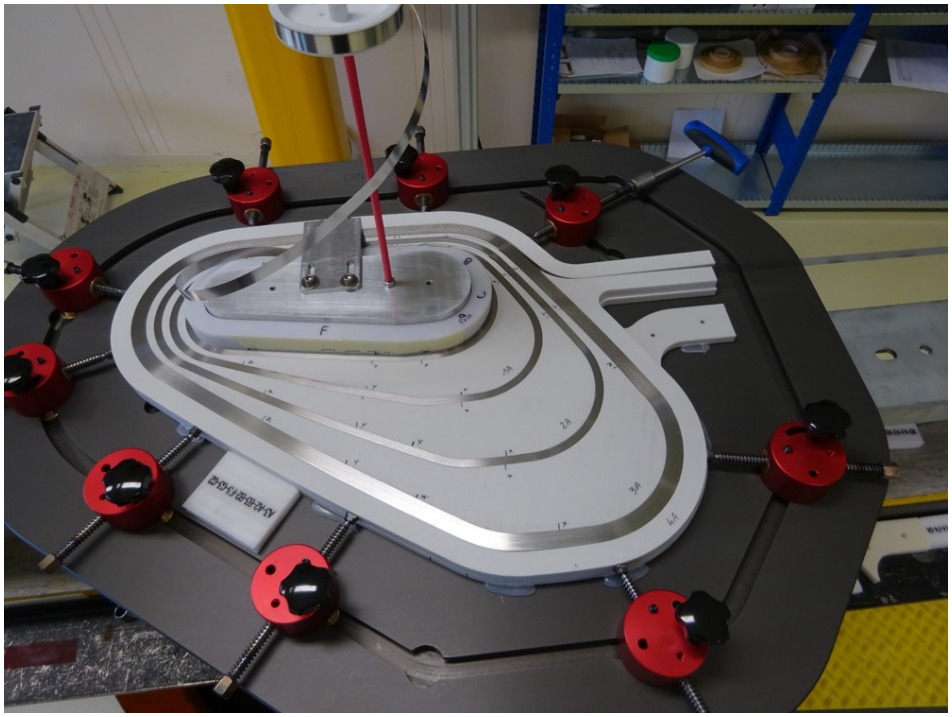

Figure 6.30 *First layer of GaToroid dummy prototype, wound in stainless steel tape on glass-filled nylon spacers (white), together with the winding plate (black) and the tooling (red)*

Furthermore, during the winding, it became evident how the transitions between the curved and the straight parts can generate *waves* in the conductor. The original GaToroid concept was conceived with a negative curvature (*Fig.3.1*), that was iteratively modified up to a slightly positive curvature to facilitate the winding procedure. Although the modification of the coil shape was in the correct direction, it was insufficient to guarantee a reliable positioning of the tapes. A new version is already under development, where a more evident curvature in the spacers will allow a simpler and more accurate winding.

Conclusions

7

"*And more, much more than this*
I did it my way"

Frank Sinatra, *My way*, 1968

The objective of the present work was to study the concept of a toroidal gantry configuration for hadron therapy, *GaToroid*, and proceed to a first layout design to identify potential and issue of such a system.

In the thesis I have first detailed the concept of GaToroid. The basic principle of this gantry is to use the toroidal axis-symmetric magnetic field to bend and focus accelerated particles down to the isocenter, delivering the radiation from discrete directions with neither rotation of the magnets nor the patient. The main benefits of the system are the symmetric configuration and steady state operation.

The focus here was the toroidal magnet, which should have large energy acceptance and good beam transmission properties. To create a magnet with a sufficiently large acceptance, I have developed a two-dimensional particle tracking, coupled with magnetic field calculations. This algorithm was used as the main optimization tool to find magnet geometries that satisfy the requirements of acceptance and precision at the isocenter. Specifically, I have applied the tool to the design of a proton gantry with minimal dimension to show the potential of the concept.

Two magnetic solutions were developed for the proton gantry (in the range 70-250 ßMeV), and presented in the thesis. Both solutions are composed of 16 coils arranged in a torus. The choice of 16 coils was derived from a compromise between the aperture available for the beam transport and the minimum (effective on the beam) and maximum (on the conductor) magnetic field ratio.

The first magnetic solution, characterized by a high engineering current density (500 A/mm^2) was conceived for the use on Non-Insulated High Temperature Superconductors. The second one, with a more modest value of engineering current density (100 A/mm^2), well suits the use of highly copper stabilized Nb-Ti and ReBCO cables. For both configurations the results show that the beam orbits can be directed to the isocenter within a precision of 1 mm over the whole treatment energy range for protons, confirming the working principle of GaToroid. Both solutions measure 3.3 m in

external diameter and 0.8 m in internal bore diameter, resulting in a reduction of at least a factor two if compared with traditional rotating gantries. The total length of the machines is about 4 meters, considering the punctual vector magnet location.

Based on the optimized magnetic design and resulting particle orbits, a linear beam optics formalism was developed and used to perform a three-dimensional particle tracking, able to determine focusing effects on the particles. This analysis identified the beam parameters at the isocenter and, despite a net defocusing effect of the torus, I have shown that a beam matching at the entrance of the gantry can be found so that they are coherent with clinical requirements.

Still, I have also shown that the long bending region inside the gantry strongly increases the beam divergence, affecting the beam size in the bending plane in case of a relevant momentum spread. A possible solution to this issue could be the use of a double achromatic torus or the propagation of a non-zero dispersion along the drift region. Further investigations are required to overcome this feature, moving to an adapted and better optimized magnetic configuration.

To simplify the future integration with traditional beam optics systems and accelerators, a fitting algorithm was used to identify the linear transfer matrix for each beam energy. These matrices precisely represent the global behaviour of the system and can be used to perform a proper matching between the accelerator and the vector magnet, avoiding more complex and time-consuming procedures as a complete three-dimensional tracking.

Moreover, I used the three-dimensional tracking to present the proof of principle of the beam spot scanning performed through the vector magnet. The results are promising, but with the present configuration the scanning field is limited to about 15x15 cm^2. To perform high-quality treatments it will necessary to enlarge the scanning field size, adapting the gantry geometry. At the same time, the Source-to-Axe Distance is in the order of 1 m, leading to a relevant increase of surface dose due to the finite angle of the incident beam. Further optimizations on the coil exit profile will be required to improve the efficiency of the scanning system. This study also pointed out that to obtain a satisfying beam positioning at the isocenter within 1 mm, the vector magnet should provide the required angles with an accuracy of few milliradians. This poses a non-trivial challenge to the design of the vector magnet.

In the thesis I finally produced a first engineering design of the proton gantry, focussing on the low current density solution for a detailed investigation. Two cable configurations were presented, one based on a conventional Nb-Ti Rutherford cable and the other composed of a non-twisted stack of ReBCO tapes. The cable designs were validated in terms of operating margin, and using thermo-electric models to evaluate hot-spot temperature in case of quench. Considering a quench protection system based on two external dump resistors and a peak voltage of ± 1 kV, the complete dis-

charge of the torus takes place about 8 seconds, and the peak temperature in adiabatic conditions is limited below 200 K in both cable configurations. Therefore, in the presented model approximations the cable topologies are suitable for a magnet protection system based on external dump, *i.e.* a relatively classical and simple scheme.

In the engineering design I also addressed the overall system mechanics. Integrating the electromagnetic forces generated by the intense magnetic field, it was possible to estimate the mass of the mechanical support of the structure. Analytical and numerical computations indicated that the mass of the complete torus structure is approximately 12 tons, *i.e.* one order of magnitude lighter than the state-of-the-art gantries for proton therapy.

Finally, a single-coil scaled-down demonstrator was designed to evaluate the practical feasibility of the coil and identify the main manufacturing and potential performance issues. The demonstrator is reduced in size by a factor three and the cable geometry, composed by non-twisted ReBCO tapes, was modified from the full-scale design to increase the generated magnetic field up to 3 Tesla. The demonstrator was designed to operate at the same current margin of the full scale torus, but with a higher current density and a lower magnetic field. Two operating regimes, at low (4.2 K) and high (20 K) temperature, will be useful to map the operating space.

Detailed quench protection analyses were performed on the demonstrator, indicating that the increase of the hot-spot temperature on the demonstrator is limited to 100 K, in both the high (20 K) and low (4.2 K) temperature operating regimes.

In addition, the mechanical studies on the demonstrator suggest the use of a selective impregnation strategy to limit the effects of the resin debonding and tape peeling. To maintain the contact pressure below the debonding limit, it is necessary that the coil pack and the spacers, impregnated together, were separated from the pole, the outer rim and the plates. Furthermore, the use of different materials (steel, aluminium and titanium) to generate pre-stress during cool-down was discarded due to the higher stresses induced on the conductors. These analyses are directly applicable to the final gantry concept, and provide directions towards the manufacturing of one such system.

At the same time, a number of small-scale experiments and tests were defined and designed, as described in the thesis, to assess the most appropriate combination of cable insulation and impregnation, considering all aspects from mechanics, to electrical insulation, including the compatibility of specific resins with the selected HTS material. The work on the design and development of technological solutions for the demonstrator included studies on suitable magnetic and electric measurements to guarantee an appropriate diagnostics and validation of the concept during a future demonstrator test.

In conclusion, I have shown that the GaToroid concept discussed in this thesis may offer an interesting alternative to the present state-of-the-art design of gantries for

hadron therapy. The magnet has a large acceptance and does not need to turn, eliminating the need for massive structures and high-precision mechanics. Furthermore, the static and axis-symmetric configuration is well suited to the use of a superconducting winding, with a considerable reduction in size and weight. Besides the issue and work in progress already mentioned, a detailed investigation on cryogenics and vacuum technologies, as well as studies on the vector magnet and beam diagnostic, are needed. Still, the work reported here can be used as a solid basis for the development of a new generation of gantries for proton and heavier ions.

Appendix I
GaToroid for Carbon Ions

The work presented in this appendix is the result of an intense and continuous collaboration with the experts of CNAO (IT), MedAustron (AT), INFN (IN) and CERN (CH).

Although the focus of the presented work is on the study of a GaToroid gantry for protons, relevant efforts have been dedicated to the investigation of a solution for carbon ions. The analysis of the proton configuration aimed at the realization of a machine as compact as possible, with inner and outer diameter of 0.8 m and 3.3 m respectively, maximizing the features of a superconducting toroidal magnet.
The carbon ions version hereafter presented was conceived, instead, to push the GaToroid concept toward the direction of classical rotating solutions.

As a result of the intense discussions with experts of hadron therapy centres such as CNAO (IT) and MedAustron (AT), three main clinical requirements were identified:

- large internal bore aperture ($\geq 3\ m$) to perform non-coplanar treatments, allowing the couch rotation around its vertical axis
- large number of treatment directions (≥ 20) to improve the treatment flexibility
- the beam path in air (after leaving the exit window(s) of the gantry) shall be energy independent, *i.e.* the beam orbits at different energies must be coincident at the exit of the gantry

The internal bore diameter was enlarged to 3.7 m (coil-to-coil) for a complete patient rotation on the plane, allowing the possibility for non-coplanar treatments, and to create enough room for auxiliary instrumentation. The concept of non-coplanar treatments is explained by *Fig.7.1*: without a relative movement between the toroidal gantry and the patient's couch it is possible to deliver the dose just on the plane $(\mathbb{X}, \mathbb{R})$ indicated in red. With a rotation of the couch around the $\mathbb{R}$, the space described by the whole sphere is available for treatment.

The number of treatment directions was increased up to 20, to maximize the flexibility of the treatment planning with the presented torus dimensions. Regarding the

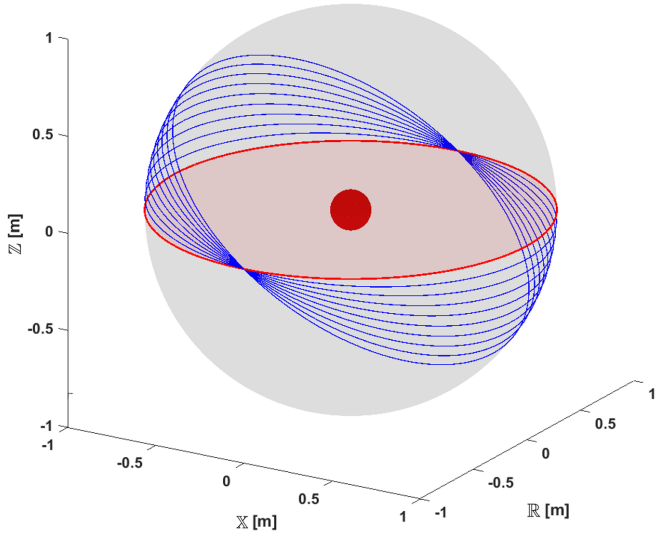

Figure 7.1 *Concept of non-coplanar treatment. Adding the possibility of couch rotation allows the delivery from a complete sphere instead of the single* $\mathbb{X}, \mathbb{R}$ *plane (in red). The red sphere in the centre represents the tumour*

number of irradiation direction, it is important to precise that 360 deg ions gantries are not validated and commissioned in the complete angular range. As reported by the Heidelberg Ion beam Therapy centre (HIT, DE) [132] a complete commissioning for 2 species (proton, carbon ion), at 10 steps in intensity, 255 steps in energy (every 1, 1.5 mm) and 4 steps in beam dimension requires the validation for 20'400 operating points for each angle. For 360 deg, with steps of 0.1 deg, this results in 73'440'000 of combinations. Furthermore, some angle of treatment must be avoided and cannot be certified due to steeps density changes in the material crossed by the beam. For these reasons, available treatment are, at this moment, limited in the order of 20 directions [132].

Finally, to remove the dependence of the beam path in air with the energy as imposed by the clinical requirements, a new optimization algorithm was developed and described in the following section.

The torus was assembled as a set of periodic but non-uniformly spaced coils, to maximize the magnetic efficiency of the machine. Each couple of coil creates a *parallel channel* for the beam transport.

Magnetic Optimization

To maximize the energy acceptance of the gantry in the carbon ions treatment range, *i.e.* 120 MeV/u to 430 MeV/u (3.3 Tm to 6.6 Tm), an optimization algorithm was developed. Similarly to the one described in *Sec.3.1*, this algorithm integrates two-dimensional tracking with magnetic field calculations. However, in this case, the beams of different energies were set coincident at the isocenter and perpendicular to the torus $\mathbb{Z}$-axis. A *reverse tracking* was then performed, from the isocentre to the vector magnet, aiming for a convergent point at the vector magnet, still considered punctual. The coil parametrization used for the optimization included the vector magnet position $\mathbb{Z} = z_v$, the internal bore radius R_{in} and the ideal magnetic flux density B_0, together with the grade positions and currents. Differently from the proton gantry optimizations presented in *Sec.3.1*, where a fixed value of current was set for each grade, in this optimization each grade is composed by a distinct number of cable turns, *i.e.* a different value of total current. While this method is more complex and requires a larger number of optimization parameters, it allows to reach higher level of precision if compared with the computations of *Sec.3.1*.

The results are presented in *Fig.7.2* together with the coil geometry. In the presented solution, coincident perpendicular beams at the isocenter converge at the vector magnet within 1 mm of precision over the whole spectrum of treatment energies. These results demonstrate once again the principle of a GaToroid system, showing its flexibility in terms of particle species, torus dimension, geometry of and number of coils.

A representation of the complete torus is depicted in *Fig.7.3* together with the magnetic flux density on the conductor surface. The peak field is 6.1 T and well suits the use of Nb-Ti cables, considered for this machine a more practical solution over the HTS conductor. The figure also shows a person for size comparison. If compared with the proton version discussed in the thesis, the dimensions of the torus are quite impressive and similar to the existing carbon ions gantries (see *Sec.1.2.2*). With an internal bore diameter of 3.7 m, the outer diameter results in 12.8 m and the total length, considering the vector magnet location (punctual) and the coil dimensions, is approximately 10 m. The mass of the machine, considering a preliminary mechanical structure, is estimated in the order of 270 tons.

The main coil and torus parameters are listed in *Tab.7.1* and *Tab.7.2*, respectively. Besides the overall dimensions, another impressive parameter is the 1.3 GJ of stored energy in the torus, comparable with the one of the ATLAS toroid at CERN (1.1 GJ for the barrel toroid, 1.6 GJ for the complete system) [133]. The cost and complexity of a magnetic system are related to its stored energy and the comparison with ATLAS, one of the largest superconducting systems in the worlds, can already provide a first glimpse of the challenges related to this version of GaToroid for carbon ions.

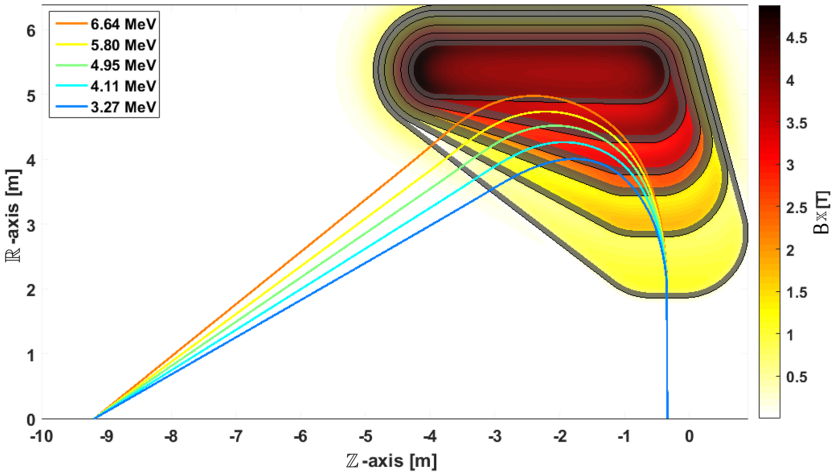

Figure 7.2 *Single particle trajectories in the whole range of carbon ions treatment energies with the optimised coil geometry for 20 treatment directions and 3.7 m of inner bore*

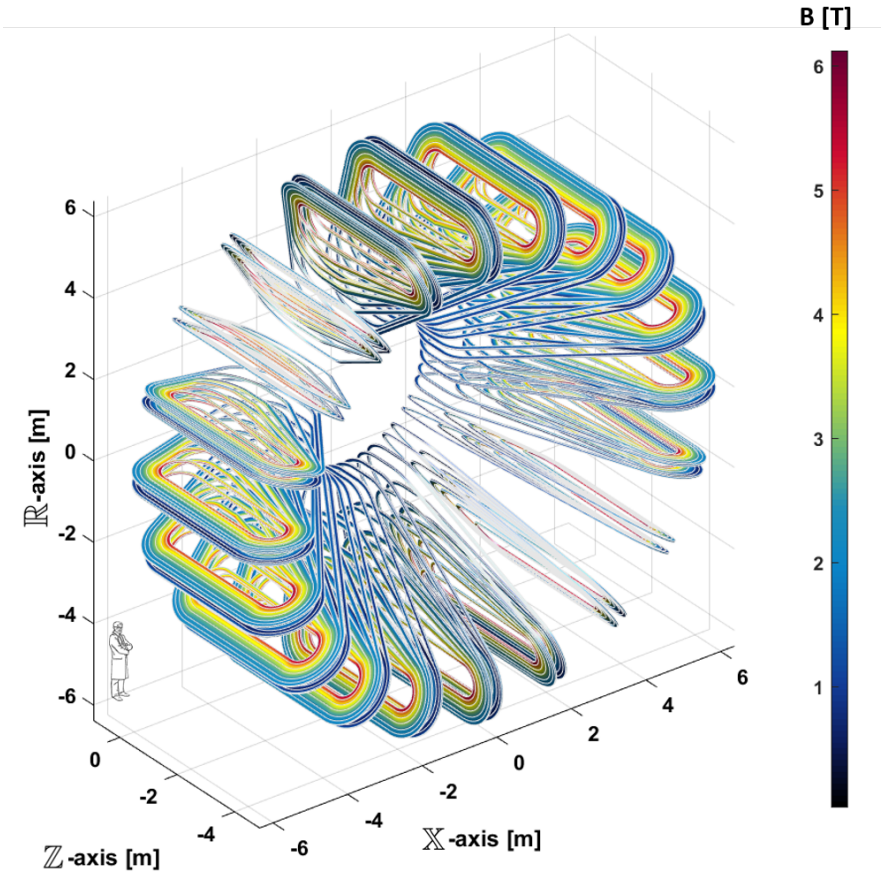

Figure 7.3 *Magnetic flux density map on the surface of the optimised GaToroid for carbon ions with 20 treatment directions and 3.7 m of inner bore. The schematic picture of a doctor is used for size comparison*

Carbon Ions GaToroid - Main Coil Parameters		
Parameter	Unit	Value
Number of Grades/Layer		6
Number of Layers		2
Length	[m]	5.8
Height	[m]	4.5
Thickness	[m]	0.036
Engineering Current Density | J_{en}	$[A/mm^2]$	100
Peak Magnetic Flux Density | B_p	[T]	6.1
Ampere-Turn	[MAt]	2.2

Table 7.1 *Main parameters of the optimised coils for carbon ions GaToroid with 20 treatment directions and 3.7 m of inner bore*

Carbon Ions GaToroid - Main Torus Parameters		
Parameter	Unit	Value
Engineering Current Density | J_{en}	$[A/mm^2]$	100
Peak Magnetic flux density | B_p	$[T]$	6.1
Number of Coils | N		40 (2 x 20)
Bore Radius | R_{in}	$[m]$	1.86
External Diameter	$[m]$	12.8
Torus Length	$[m]$	5.8
Vector Magnet Position | z_v	$[m]$	-9.2
Stored Energy	$[GJ]$	1.3
Total Ampere-Turn	$[MAt]$	89.6

Table 7.2 *Main parameters of the optimised torus for carbon ions GaToroid with 20 treatment directions and 3.7 m of inner bore*

Alternative Solution

It is clear that pushing the GaToroid gantry toward the operating functionalities of classical rotating solution risks to denature its original concept and main features.

Alternative solutions are clearly possible and hereafter a more modest configuration composed of 8 couples of coils (8 treatment directions), with an inner bore of 2.25 m is presented. The optimized coil geometry together with the two-dimensional particle tracking of the orbits in the complete treatment range are reported in *Fig.7.4*. The torus assembly, with the doctor for size comparison, is shown in *Fig.7.5*. As listed in *Tab.7.3* and *Tab.7.4* , the resulting torus, with a peak field on the conductor of 6.7 T, has an external diameter within 10 m and a total stored energy of 420 MJ. Once again, this solution demonstrated the working principle of GaToroid and the flexibility of the optimization algorithm.

The selection of the most appropriate configuration for carbon ion will result from the compromise between the complexity and cost of the machine, together with the quality and flexibility of treatments.

Carbon Ions GaToroid - Main Coil Parameters		
Parameter	Unit	Value
Number of Grades/Layer		6
Number of Layers		2
Length	[m]	5.6
Height	[m]	3.7
Thickness	[m]	0.036
Engineering Current Density | J_{en}	$[A/mm^2]$	100
Peak Magnetic Flux Density | B_p	[T]	6.7
Ampere-Turn	[MAt]	2.8

Table 7.3 *Main parameters of the optimised coils for carbon ions GaToroid with 8 treatment directions and 2.25 m of inner bore*

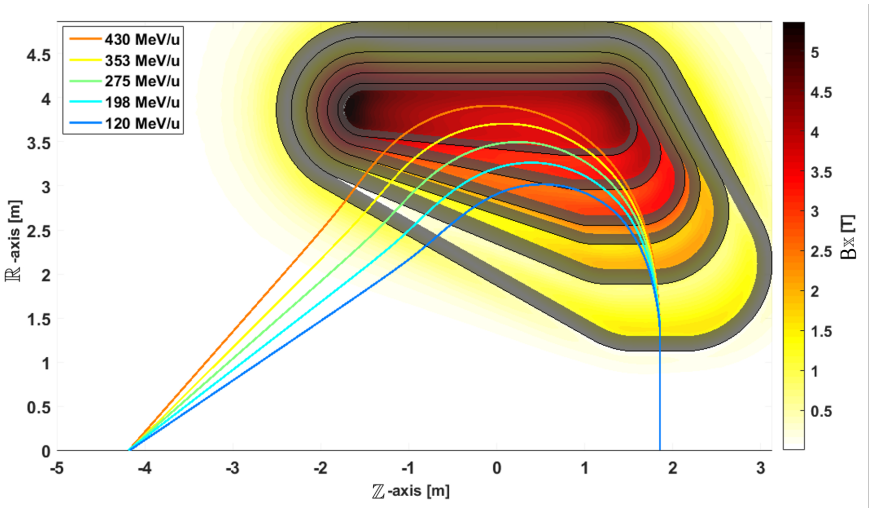

Figure 7.4 *Single particle trajectories in the whole range of carbon ions treatment energies with the optimised coil geometry for 8 treatment directions and 2.25 m of inner bore*

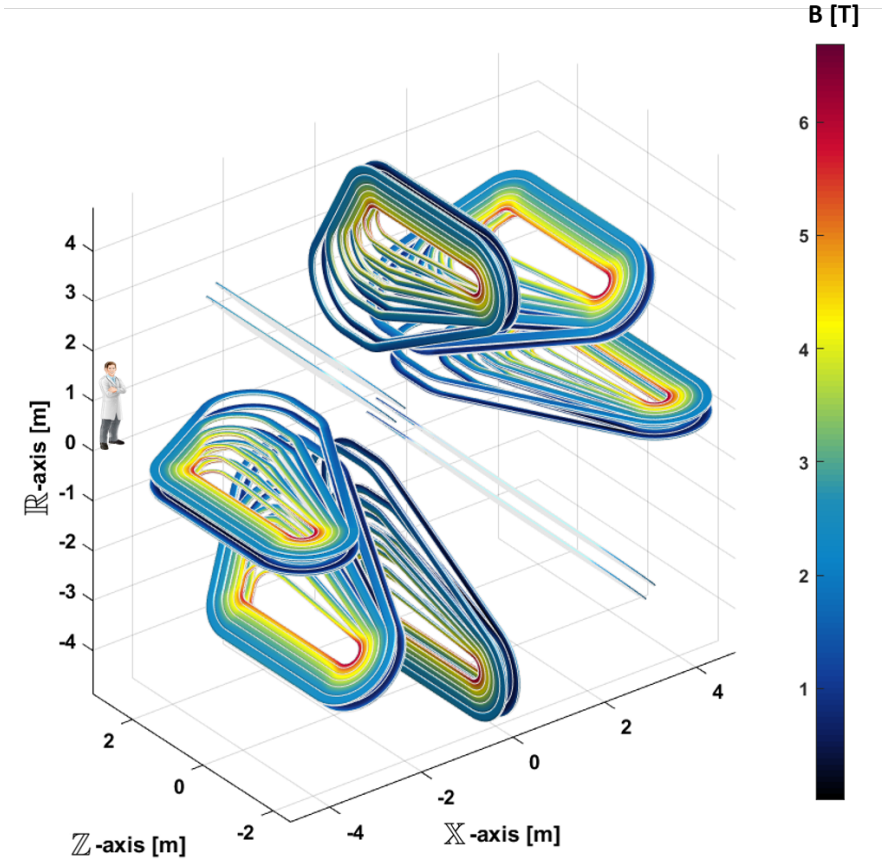

Figure 7.5 *Magnetic flux density map on the surface of the optimised GaToroid for carbon ions with 8 treatment directions and 2.25 m of inner bore. The schematic picture of a doctor is used for size comparison*

Carbon Ions GaToroid - Main Torus Parameters		
Parameter	Unit	Value
Engineering Current Density | J_{en}	$[A/mm^2]$	100
Peak Magnetic flux density | B_p	$[T]$	6.7
Number of Coils | N		16 (2 x 8)
Bore Radius | R_{in}	$[m]$	1.13
External Diameter	$[m]$	9.7
Torus Length	$[m]$	5.6
Vector Magnet Position | z_v	$[m]$	-4.2
Stored Energy	$[GJ]$	0.42
Total Ampere-Turn	$[MAt]$	44.9

Table 7.4 *Main parameters of the optimised torus for carbon ions GaToroid with 8 treatment directions and 2.25 m of inner bore*

Appendix II
Linear Beam Optics on Low J_{en} Configuration

Similarly to the work described in *Sec.4.3*, this appendix reports the beam optics analysis and three-dimensional particle tracking performed on the low J_{en} solution. This solution presents a similar defocusing effect as illustrated in *Fig.4.8*. Therefore, a convergent beam was used as input to obtain a beam of appropriate dimension at the isocenter. The same input beam parameters of *Sec.4.3* were used for the simulations over the whole energy range and they are reported in *Tab.7.5* for the sake of clarity.

Transverse beam optics parameters		
Parameter	Unit	Input
$N_{particles}$		10^5
$\Delta p/p$		0%
$\varepsilon_{x-1\sigma}$	[mm mrad]	1
$\varepsilon_{y-1\sigma}$	[mm mrad]	1
α_x		9.5
β_x	[m]	35.0
α_y		4.8
β_y	[m]	20.0

Table 7.5 *Input parameters used for the particle tracking over the whole spectrum of treatment energies (70-250 MeV)*

An overall view of the three-dimensional particle tracking for a 250 MeV beam, together with the geometry of the low engineering current coils, is reported in *Fig.7.6*. The tracking was done over the complete spectrum of treatment energies and the results are summarized in *Fig.7.7* in terms of Twiss parameters. Coherently with the results presented in *Sec.4.3*, the beam at the isocenter is round and symmetric for high energy, while became larger on the non-bending plane at lower energy. *Fig.7.8* shows the input and output beam dimensions for the 250 MeV case, while *Fig.7.9* illustrate the phase spaces in the horizontal and vertical planes at the isocenter for the 250 MeV beam. The difference between the 250 MeV and 70 MeV beams at isocenter can be also described by the particle distributions as shown in *Fig.7.10*. If

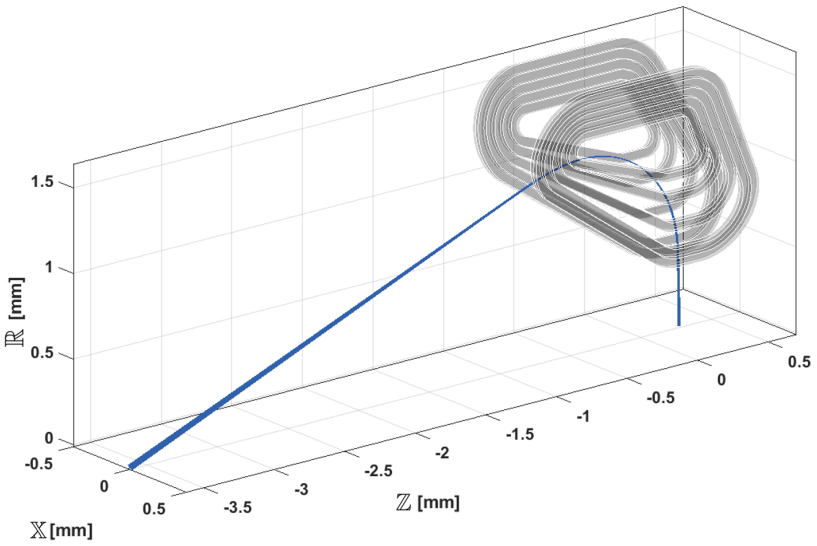

Figure 7.6 *Particle trajectories for a 250 MeV beam described in Tab.4.2 together with two coils of the low J_{en} torus*

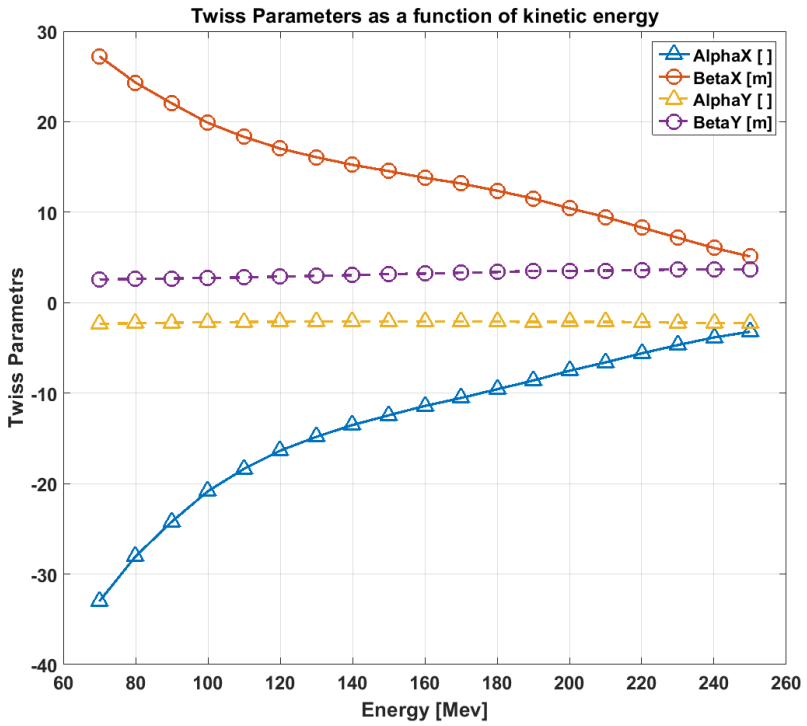

Figure 7.7 *Twiss parameters as a function of beam kinetic energy for the low J_{en} configuration*

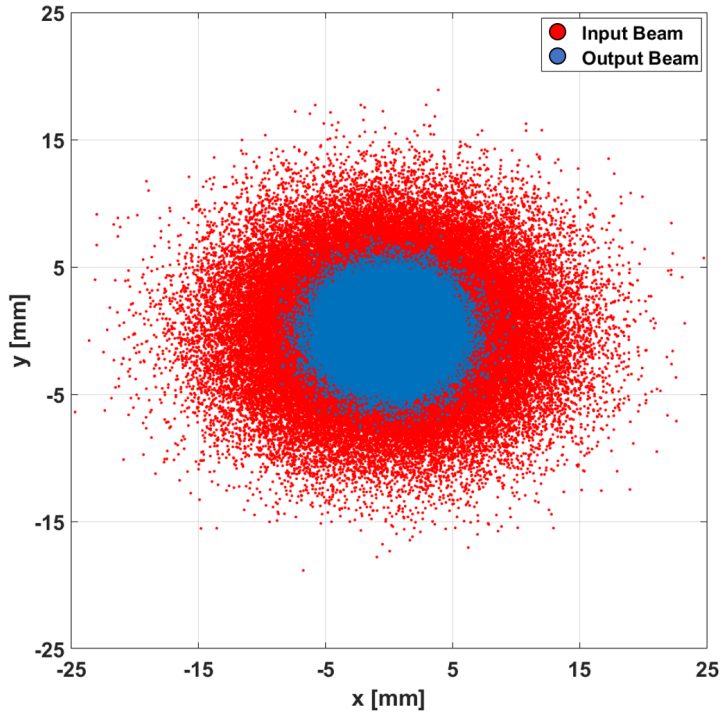

Figure 7.8 *Particle distributions at the exit of the vector magnet (red) and at the isocentre (blue) for the low J_{en} configuration, resulting from the tracking of 10^5 particles with Gaussian transverse distribution at 250 MeV*

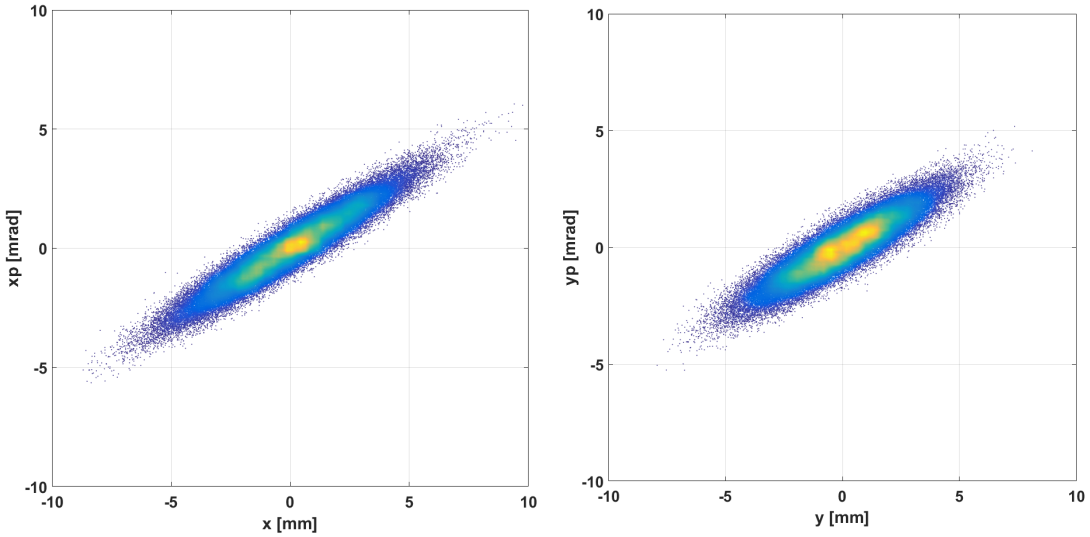

Figure 7.9 *$x - x'$ **(a)** and $y - y'$ **(b)** phase space at isocentre for the low J_{en} configuration, resulting from particle tracking at 250 MeV*

for the high energy beam, the x and y dimensions are equivalent, the low energy beam clearly presents an asymmetry between the planes.These difference can be reduced acting of the input beam parameters at the vector magnet. Furthermore, the equivalent

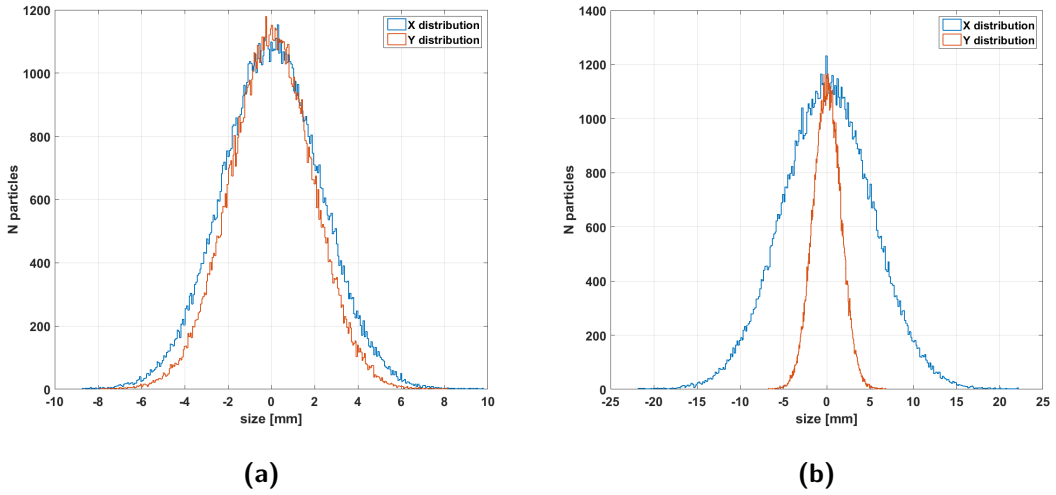

Figure 7.10 *x (blue) and y (red) beam profile at the isocentre for the low J_{en} configuration, resulting from particle tracking at 70 MeV* ***(a)*** *and 250 MeV* ***(b)***

linear transfer matrices were evaluated between the output and the input particle distributions. The relative error between the particle distributions simulated with the full three-dimensional tracking and those evaluated with the transfer matrices were then computed. *Fig.7.11* and *Fig.7.12* shows respectively the elements of the matrices and the relative errors as a function of the beam energy. The error is decreasing with the energy, with a maximum value of less than 0.1% at 70 MeV. The figures also report the value of the matrix determinant that for the Liouville's theorem must be equal to 1. A maximum value of 1.035 was calculated for the 70 MeV beam.

In conclusion, the beam optics properties of the low engineering current density solution are coherent with those described in *Sec.4.3* for the high J_{en} one. Both configurations present a net defocusing effect, but it is possible to tune the Twiss parameters at the vector magnet to obtain a suitable beam at the isocenter.

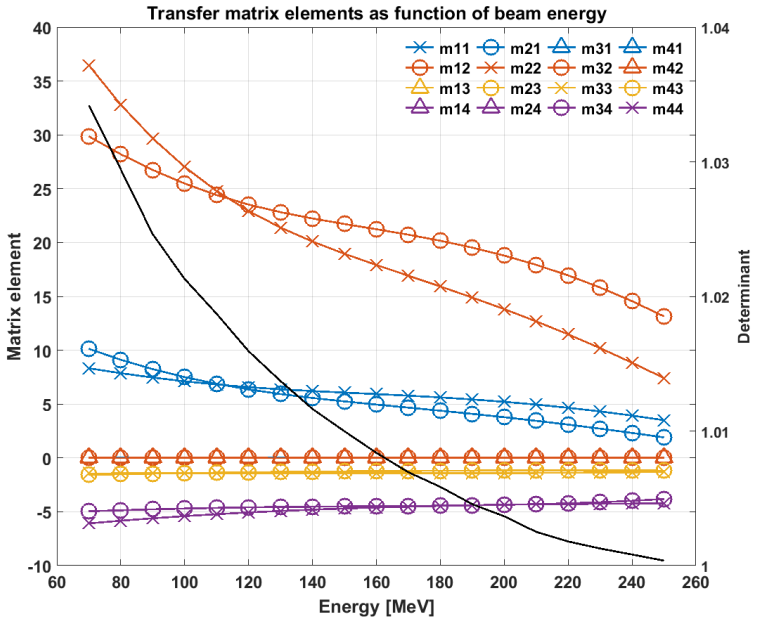

Figure 7.11 *Transfer matrix element values as a function of beam energy for the low J_{en} configuration, together with the matrix determinant (black line)*

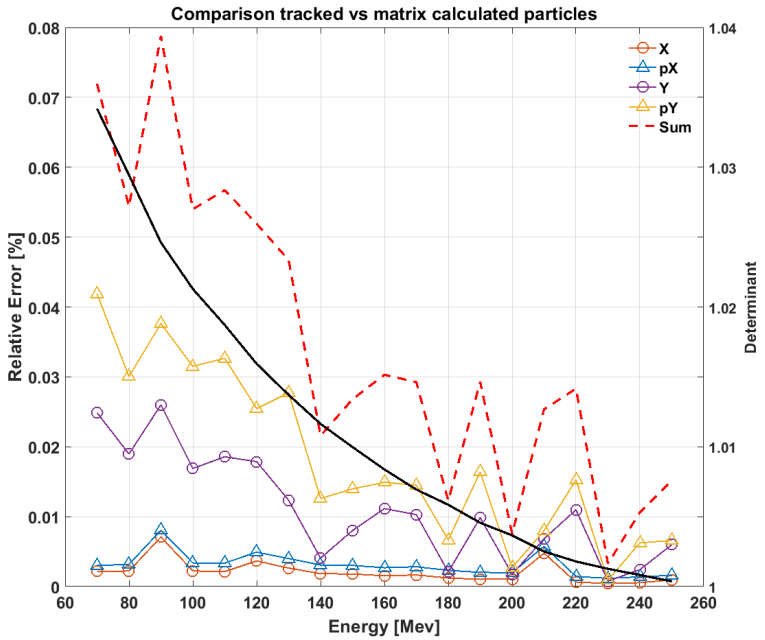

Figure 7.12 *Relative errors λ as a function of beam energy for the low J_{en} configuration. The sum of the errors is indicated in red dashed line, while the matrix determinant in black solid line (right axis)*

Appendix III
Quench Protection System with Quench Heaters

A possible alternative to the quench protection system based on external dump described in *Sec.5.1* is the use of quench heaters to dissipate the energy of the magnet inside the magnet itself. Given the operating conditions and margins listed in *Tab.3.3*, the LTS configuration requires 190 Joules to bring a whole coil from the operating temperature to the current sharing temperature.

Considering the coils powered in series, by-passed by diodes, and assuming 500 milliseconds of quench detection time, the temperature increase in the magnet is shown in *Fig.7.13*.

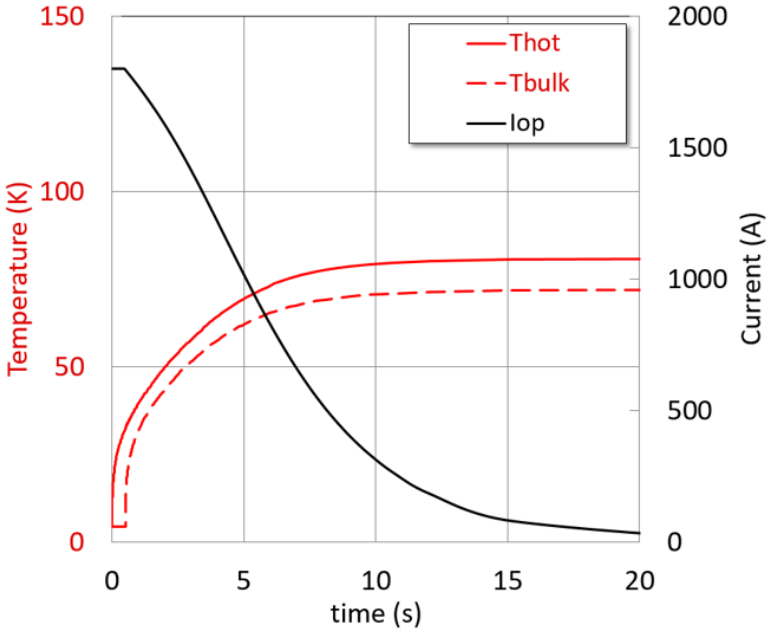

Figure 7.13 *Hot-spot (solid red line) and bulk (dashed red line) temperatures together with the current decay (black solid line) as a function of time for a quench protection system based on quench heaters*

As reported in the picture, the temperature of the hot-spot increases and after 500 ms the quench heater release the energy and the temperature of the whole coil start to raise (bulk temperature). The resistance of the winding increase with temperature and the current decays inside the magnet, with a time constant that ranges from 14 s

to 4 s. During the discharge, the hotspot temperature on the LTS cable reaches about 80 K, while the peak voltage on the coil is limited to 240 V. Therefore, the magnet can be considered safely protected.

Regarding the HTS cable in the operating conditions reported in *Tab.3.3*, due to the much larger energy margin, the energy required at the heaters would exceed one hundred kJ per coil (about 15 kJ per grade). Therefore, for the magnetic configuration in HTS, an internal protection system based on quench heaters was discarded. Nevertheless, given the steady-state configuration of GaToroid, HTS self-protected magnets, consisting of non or partially insulated windings [70][71], represent a further quench protection option to be evaluated in the future.

Bibliography

[1] U. Amaldi and G. Kraft, "Radiotherapy with beams of carbon ions," *Rep. Prog. Phys. 68 1861*, 2005.

[2] M. Durante and h. Paganetti, "Nuclear physics in particle therapy: a review," *Reports on Progress in Physics, Vol. 79, No. 9*, 2016.

[3] R. Wilson, "Radiological use of fast protons," *Radiology, 47:487-91*, 1946.

[4] J. Slater, J. Archambeau, D. Miller, *et al.*, "The proton treatment centerat Loma Linda University Medical Center: Rationale for and description ofits development," *Int J Radiat Oncol Biol Phys 22:383-389*, 1992.

[5] J. Castro, J. Quivey, J. Lyman, *et al.*, "Radiotherapy eith heavy charged particles at lawrence berkeley laboratory," *J Can Assoc Radiol., 31:30-4*, 1980.

[6] H. Tsujii, S. Minohara, and K. Noda, *Heavy-particle radiotherapy: system design and application*. Review of accelerator science and technology. Imperial College Press, 2009.

[7] H. Tsujii, T. Kamada, T. Shirai, K. Noda, H. Tsuji, and K. Karasawa, *Carbon-Ion Radiotherapy: Principles, Practices, and Treatment Planning*. Springer, 2013.

[8] PTCOG, "https://www.ptcog.ch/," *Particle Therapy Co-Operative Group*.

[9] G. Kraft, *The Physics of Multiply and Highly Charged IonsVolume 1: Sources, Applications and Fundamental*, ch. Radiobiological Effects of Highly Charged IonsPages, pp. 149–196. 2003.

[10] U. Amaldi, "History of Hadrontherapy," *Modern Physics Letters A 30(17):1540018*, May 2015.

[11] J. M. Schippers, A. Lomax, A. Garonna, and K. Parodi, "Can technological improvements reduce thecost of proton radiation therapy?," *Semin Radiat Oncol 28:150-159*, 2018.

[12] A. Degiovanni and U. Amaldi, *History of hadron therapy accelerators*. 2015.

[13] S. Yan, H.-M. Lu, J. Flanz, J. Adams, A. Trofimov, and T. Bortfeld, "Reassessment of the Necessity of the Proton Gantry: Analysis of Beam Orientations From

4332 Treatments at the Massachusetts General Hospital Proton Center Over the Past 10 Years," *International Journal of Radiation Oncology*Biology*Physics*, vol. 95, pp. 224–233, may 2016.

[14] J. Farr, J. Flanz, A. Gerbershagen, and M. Moyers, "New horizons in particle therapy systems," *Medical Physics (45) 11*, 2018.

[15] H. Kumada, *Proton Beam Radiotherapy Physics and Biology*, ch. Beam Delivery System for Proton Radiotherapy, pp. 96–112. Springer Nature Singapore, 2020.

[16] E. Pedroni, "Gantries," *PTCOG49 - Chiba, Japan*, 2010.

[17] Y. Jongen, "Review on cyclotrons for cancer therapy," *Proceedings of CYCLOTRONS 2010, Lanzhou, China*, 2010.

[18] VarianMedicalSystem, "Probeam 360°, next-generation proton therapy with a smaller footprint.," *https://www.varian.com/products/proton-therapy/treatment-delivery/probeam-360*.

[19] A. Godeke, "HTS for Commercial Proton Therapy," *WAMHTS-5 Workshop*, 2019.

[20] A. Koschik, C. Bula, J. Duppich, A. Gerbershagen, M. Grossmann, J. Schippers, and J. Welte, "Gantry 3: further development of the PSI Proscan proton therapy facility," *6th International Particle Accelerator Conference IPAC2015, Richmond, VA*, 2015.

[21] W. Kleeven, M. Abs, E. Forton, S. Henrotin, Y. Jongen, V. Nuttens, Y. Paradis, E. Pearson, S. Quets, J. V. D. Walle, P. Verbruggen, S. Zaremba, M. Conjat, J. Mandrillon, and P. Mandrillon, "The IBA Superconducting Synchrocyclotron Project S2C2," *Proceedings of Cyclotrons2013*, pp. 115–119, 2013.

[22] D. Bertrand, "Recent developments in proton accelerators," *Erice Workshop on Hadrontherapy*, May 2011.

[23] O. Legrain, "Capital market day," 2017.

[24] E. Pearson *et al.*, "Magnet developments and commissioning for the iba compact gantry," *IEEE, vol.24, No. 3*, June 2014.

[25] ProTom, "Accelerator, compact 330 mev synchrotron," *http://www.protominternational.com/about/about-radiance-330/accelerator-compact-330-mev-synchrotron/*.

[26] P. Symonds, J. A. Mills, and A. Duxbury, *Walter and Miller's Textbook of Radiotherapy: Radiation Physics, Therapy and Oncology.* Elsevier, 8th edition ed., 2019.

[27] M. M. System, "Mevion s250 proton therapy system," *https://www.mevion.com/products/mevion-s250-proton-therapy-system.*

[28] T. Zwart *et al.*, "Developing a modern, high-quality proton therapy medical device with a compact superconducting synchrocyclotron," *CIEMAT- Madrid*, Nov 2016.

[29] S. L. Civita, "Advances in integrated compactsingle-room proton therapysystems," *Caen, ENLIGHT*, 2019.

[30] V. Derenchuk, "The ProNova SC360 Gantry," *Cockcroft Institute, Daresbury UK*, January 2014.

[31] M. Umezawa, "Hitachi proton beam therapy system with various types of rotating gantries," *Modern Hadron Therapy Gantry Developments, Cockcroft Institute*, Jan 2014.

[32] Y. Kumata, "SUMITOMOParticle Therapy Technologies," *55th AAPM annual meetingParticle Beam Therapy Symposium*, 2013.

[33] M. Jermann and D. Baroke, "Proton therapy at the paul scherrer institute," *Paul Scherrer Institute*, 2011.

[34] E. Pedroni, "Gantry design and experience at psi," *Workshop on Hadron Beam Therapy of Cancer Erice, Italy*, Apr 2009.

[35] E. Pedroni, D. M. C. Bula, S. Safai, and S. Zenklusen, "Pencil beam characteristics of the next-generation proton scanning gantry of PSI: design issues and initial commissioning results," *Eur. Phys. J. Plus 126: 66*, 2011.

[36] K. P. Nesteruk, "Gantry design and experience at PSI," *Ions 2018, ESI, Archamps.*

[37] A. Koschik, U. Dorda, D. Meer, and E. Pedroni, "The medaustron proton gantry," *Proceedings of IPAC2012, New Orleans, Louisiana, USA*, 2012.

[38] HIT, "Heidelberg ion-beam therapy center," *https://www.klinikum.uni-heidelberg.de*, Jan 2014.

[39] R. Fuchs and U. Weinrich, "The heavy ion gantry of the hicat facility," *Proceedings of EPAC 2004, Lucerne, Switzerland.*

[40] M. Galonska *et al.*, "Heidelberg heavy ion gantry experience," *Cockcroft Institute, Daresbury UK*, Jan 2014.

[41] M. Galonska *et al.*, "The HIT gantry: from commissioning to operation," *Proceedings of IPAC2013, Shanghai, China*, 2013.

[42] Y. Iwata *et al.*, "Beam commissioning of a superconducting rotating-gantryfor carbon-ion radiotherapy," *Nuclear Instruments and Methods in Physics Research Section A, Vol. 834, Pages 71-80*, 2016.

[43] Y. Iwata *et al.*, "Design of a superconducting rotating gantry for heavy-ion therapy," *Physical Review Special Topics - Accelerators and Beam 15, 044701*, 2012.

[44] Y. Iwata, T. Shirai, , and K. Noda, "Design of superconducting magnetsfor a compact carbon gantry," *IEEE Trans. Appl. Supercond., Vol. 26, No. 4,*, 2016.

[45] Y. Iwata, T. Fujita, T.Fujimoto, *et al.*, "Development of Carbon-Ion RadiotherapyFacilities at NIRS," *IEEE Trans. Appl. Supercond., vol. 28, No. 3*, 2018.

[46] A. Garonna, "Delivery and Gantry Conceptsfrom TERA," *Ideas and Technologies for a next generation facility formedical research and therapy with ionsArchamps (ESI)*, 2018.

[47] E. Benedetto, "Sc synchrotron and gantry based oncanted cosine theta magnets," *deas and Technologies for a next generation facility for medical research andtherapy with ions, Archamps, FR (ESI)*, 2018.

[48] C. Cuccagna, V. Bencini, S. Benedetti, D. Bergesio, P. Carrio Perez, E. Felcini, A. Garonna, , W. S. Kozłowska, M. Varasteh Anvar, V. Vlachoudis, and U. Amaldi, "Beam parameters optimization and characterization for a TUrning LInac for Protontherapy," *Physica Medica*, vol. 54, no. September, pp. 152–165, 2018.

[49] S. Benedetti, A. Grudiev, and A. Latina, "High gradient linac for proton therapy," *Phys. Rev. Accel. Beam, 20, 040101*, 2017.

[50] A. Degiovanni, U. Amaldi, D. Bergesio, C. Cuccagna, A. L. Moro, P. Magagnin, P. Riboni, and V. Rizzoglio, "Design of a fast-cycling high-gradient rotating linacfor protontherapy," *Proceedings of IPAC2013, Shanghai, China*, 2013.

[51] R. Lopez and J. R. Anglada, "Development of a compact and fast trimmable FeCo magnetfor medical gantries," *Phys. Rev Accel. Beams, 23, 072401*, 2020.

[52] D. Trbojevic and W. River, "Gantry for medical particle therapy facility," *US 2010/0038552 A1*, 2010.

[53] D. Trbojevic, B. Parker, and M. Pullia, "Large momentum acceptance superconducting ns-ffag gantry for carbon cancer therapy," *Proceedings of PAC2013, Pasadena, CA USA*, 2013.

[54] M. M. Necchi, D. Bertrand, D. Bianculli, L. Berkeley, and M. Ferrarini, "Conceptual design for a carbon ion gantry - ULICE," Tech. Rep. October, 2012.

[55] M. Pullia, "The ULICE Gantry," *Modern Hadrontherapy Gantry Developments, Cockcroft Institute*, no. January, 2014.

[56] A. Gerbershagen, D. Meer, J. M. Schippers, and M. Seidel, "A novel beam optics concept in a particle therapy gantry utilizing the advantages of superconducting magnets," *Zeitschrift fur Medizinische Physik*, 2016.

[57] K. P. Nesteruk, C. Calzolaio, D. Meer, V. Rizzoglio, M. Seidel, and J. M. Schippers, "Large energy acceptance gantry for proton therapyutilizing superconducting technology," *Phys. Med. Biol. 64 175007*, 2019.

[58] C. Calzolaio, S. Sanfilippo, M. Calvi, A. Gerbershagen, M. Negrazus, M. Schippers, and M. Seidel, "Preliminary Magnetic Design of a Superconducting Dipole for Future Compact ScanningGantries for Proton Therapy," *IEEE Trans. Appl. Supercond., Vol. 26, No. 3*, 2016.

[59] M. Schippers, "New developments in acceleratorsand gantries for particle therapy," *ENLIGHT Meeting, Caen,*, 2019.

[60] W. Wan, L. Brouwer, S. Caspi, S. Prestemon, A. Gerbershagen, J. M. Schippers, and D. Robin, "Alternating-gradient canted cosine theta superconducting magnetsfor future compact proton gantries," *Physical Review Special Topics - Acceleraotrs and Beams 18, 103501*, 2015.

[61] Leslie Bromberg and P. C. Michael, "Toroidal Bending magnets for Hadron Therapy Gantries," *Patent US9711254B2*, 2017.

[62] I. Horvath, G. Vecsey, and J. Zellweger, "The piotron at sin - a large superconducting double torus spectrometer," *IEEE Transactions on Magnetics, Vol. Mag-17, No. 5*, 1981.

[63] D. Boyd, H. Schwettman, and J. Simpson, "Large acceptance pion channel for cancer therapy," *Nucl.Instrum.Meth. 111, 315-331*, 1973.

[64] C. F. Von Essen, H. Blattmann, J. F. Crawford, P. Fessenden, E. Pedroni, C. Perret, M. Salzmann, K. Shortt, and E. Walder, "The piotron: initial performance, preparation and experience with pion therapy," *International Journal of Radiation Oncology, Biology, Physics*, vol. 8, no. 9, pp. 1499–1509, 1982.

[65] L. Bottura, "A Gantry and apparatus for focussing beams of charged particles," *Patent, EP 18173426.0.*, May 2018.

[66] L. Bottura, E. Felcini, G. De Rijk, and B. Dutoit, "GaToroid: A Novel Toroidal Gantry for Hadron Therapy," *Submitted for Publication in Nuclear Instruments and Methods in Physics Research, Section A: Accelerators, Spectrometers, Detectors and Associated Equipment*, 2020.

[67] "Safety guidelines formagnetic resonance imaging equipmentin clinical use," tech. rep., Medicines and Healthcare Products Regulatory Agency, 2014.

[68] J. van Nugteren, "Software Development for the Science and Design behind Superconducting Magnet Systems," *CERN Internship Report*, September 2011.

[69] M. A. Green and B. P. Strauss, "The cost of superconducting magnets as a function of stored energy and design magnetic induction times the field volume," *IEEE Transactions on Applied Superconductivity*, vol. 18, no. 2, pp. 248–250, 2008.

[70] S. Hahn, D. K. Park, J. Bascuñán, and Y. Iwasa, "HTS pancake coils without turn-to-turn insulation," *IEEE Transactions on Applied Superconductivity*, vol. 21, no. 3 PART 2, pp. 1592–1595, 2011.

[71] S. Hahn *et al.*, "Current Status of and Challenge for No-Insulation HTS Winding Technique," *Journal of Cryogenics and Superconductivity Society of Japan, Vol.53 No.1 2018*, 30 November 2017.

[72] L. Bottura, E. Felcini, V. Ferrero, *et al.*, "Beam and range monitoring in Particle Therapy in a highly innovative integrated design," *Frontiers in Physics, Medical Physics and Imaging*, 2020.

[73] L. Rossi, "Superconducting cable and magnets for the large hadron collider," *LHC Project Report 694*, no. March 2004, pp. 14–18, 2003.

[74] A. Sykes, A. E. Costley, C. G. Windsor, O. Asunta, G. Brittles, P. Buxton, V. Chuyanov, J. W. Connor, M. P. Gryaznevich, B. Huang, J. Hugill, A. Kukushkin, D. Kingham, A. V. Langtry, S. McNamara, J. G. Morgan, P. Noonan, J. S. Ross, V. Shevchenko, R. Slade, and G. Smith, "Compact fusion energy based on the spherical tokamak," *Nuclear Fusion*, vol. 58, no. 1, 2018.

[75] D. G. Whyte, J. Minervini, B. LaBombard, E. Marmar, L. Bromberg, and M. Greenwald, "Smaller & Sooner: Exploiting High Magnetic Fields from New Superconductors for a More Attractive Fusion Energy Development Path," *Journal of Fusion Energy*, vol. 35, no. 1, pp. 41–53, 2016.

[76] G. A. Kirby, J. Van Nugteren, H. Bajas, V. Benda, A. Ballarino, M. Bajko, L. Bottura, K. Broekens, M. Canale, A. Chiuchiolo, L. Gentini, N. Peray, J. C. Perez, G. De Rijk, A. Rijllart, L. Rossi, J. Murtomaeki, J. Mazet, F. O. Pincot, G. Volpini, M. Durante, P. Fazilleau, C. Lorin, A. Stenvall, W. Goldacker, A. Kario, and A. Usoskin, "First Cold Powering Test of REBCO Roebel Wound Coil for the EuCARD2 Future Magnet Development Project," *IEEE Transactions on Applied Superconductivity*, vol. 27, no. 4, pp. 1–7, 2017.

[77] S. Takayama, K. Koyanagi, A. Yamaguchi, K. Tasaki, T. Kurusu, Y. Ishii, N. Amemiya, T. Ogitsu, and K. Noda, "Design of conduction-cooled HTS coils for a rotating gantry," *Physics Procedia*, vol. 67, pp. 879–884, 2015.

[78] J. Bascunan, Seungyong Hahn, Youngjae Kim, Jungbin Song, and Y. Iwasa, "90-mm/18.8-T All-HTS Insert Magnet for 1.3 GHz LTS/HTS NMR Application: Magnet Design and Double-Pancake Coil Fabrication," *IEEE Transactions on Applied Superconductivity*, vol. 24, no. 3, pp. 1–4, 2013.

[79] D. Uglietti, "A review of commercial high temperature superconducting materials for large magnets: From wires and tapes to cables and conductors," *Superconductor Science and Technology*, vol. 32, no. 5, 2019.

[80] L. Bottura, "Lhc project report 358," *A Practical Fit for the Critical Surface of NbTi*, 1999.

[81] M. Danial and J. van Nugteren, "Parametrization of the critical surface of REBCO conductors from Bruker," *CERN - Internal Report*, 20 July 2017.

[82] L. Gambini, M. Breschi, E. Felcini, A. Cristofolini, and L. Bottura, "An algorithm for toroidal field harmonics computa- tion in arbitrary magnetic configurations," *IEEE Transactions on Applied Superconductivity, vol. 30, no. 4, pp. 1-5, Art no. 4900705*, 2020.

[83] L. Gambini, "Expansion of the magnetic flux density field in toroidal harmonics," Master's thesis, University of Bologna, 2018.

[84] J. Boris and A. Kuckes, "Closed expression for the magnetic field in two-dimensional multipole configuration," *PPPL-MATT-473, Princeton Plasma Physics Laboratory*, 1966.

[85] R. J. Thome and J. Tarrh, *MHD and fusion magnets: field and force design concepts.* John Wiley & Sons Inc, 1982.

[86] N. Mitchell *et al.*, "The iter magnet system," *IEEE Transactions on Applied Superconductivity, vol. 18, no. 2, pp. 435-440*, 2008.

[87] E. F. Taylor and J. A. Wheeler, *Spacetime Physics, second edition.* 1992.

[88] ICRU, "Stopping powers for protons and alpha particles," tech. rep., ICRU Report 49 (ICRU, Bethesda, MD)., 1993.

[89] M. Ferrario, M. Migliorati, and L. Palumbo, "Space charge effects," *Proceedings of the CAS-CERN Accelerator School: Advanced Accelerator Physics*, vol. 009, no. August 2013, pp. 331–356, 2013.

[90] K. Wille, *The Physics of Particle Accelerator.* Oxford Univeristy Press Inc., 1996.

[91] D. Carey, *The Optics Of Charged Particle Beams.* Harwood academic, 1987.

[92] E. Felcini, L. Bottura, J. V. Nugteren, G. D. Rijk, G. Kirby, and B. Dutoit, "Magnetic Design of a Superconducting Toroidal Gantry for Hadron Therapy," *IEEE TRANSACTIONS ON APPLIED SUPERCONDUCTIVITY, VOL. 30, NO. 4*, pp. 1–5, June 2020.

[93] T. J. Kyng and O. Konstandatos, "Multivariate monte-carlo simulation and economic valuation of complex financial contracts: An excel based implementation," *Spreadsheets in education, 7(2), 1-38.*, 2014.

[94] G. Golub and C. F. V. Loan, *Matrix Computations.* JHU, 1996.

[95] R. Wicklin, "Use the cholesky transformation to correlate and uncorrelate variables," *Advanced Analytic Software - SAS*, Feb 2012.

[96] W. Y. Yang, W. Cao, T.-S. Chung, and J. Morris, *Applied Numerical Methods Using MATLAB®.*

[97] BE/ABP Accelerator Beam Physics Group, "Mad - methodical accelerator designcern," *https://mad.web.cern.ch/mad/.*

[98] F. M. Khan and J. P. Gibbons, *The Physics of Radiation Therapy.* 5 ed., 2014.

[99] M. Pullia, V. Lante, M. Necchi, S. Savazzi, and J. O. Moreno, "Deliverable report jra6.3 conceptual design of a carbon ion gantry ," *ULICE Union of Light Centres in Europe* , 2009.

[100] J. Osorio, C. Priano, and M. Pullia, "Electromagnetic characterization of a big aperture magnet used inparticle beam cancer – (ecbamupbc)," *Proceedings of the 2012 COMSOL Conference in Milan.*

[101] S. Hahn *et al.*, "No-Insulation Coil Under Time-Varying Condition: Magnetic Coupling With External Coil," *IEEE Trans. Appl. Supercond. 23*, June 2013.

[102] K. R. Bhattarai, K. Kim, K. Kim, K. Radcliff, X. Hu, C. Im, T. Painter, I. Dixon, D. Larbalestier, S. Lee, and S. Hahn, "Understanding quench in no-insulation (NI) REBCO magnets through experiments and simulations," *Superconductor Science and Technology*, vol. 33, p. 035002, jan 2020.

[103] J. Fleiter, A. Bonasia, B. Bordini, and A. Ballarino, "Rutherford cable design approach and experience at cern," in *US-EuroCirCol cable meeting*, January 2017.

[104] F. Borgnolutti, M. Durante, F. Debray, J. . Rifflet, G. De Rijk, P. Tixador, and J. . Tudela, "Status of the eucard 5.4-t rebco dipole magnet," *IEEE Transactions on Applied Superconductivity*, vol. 26, no. 4, pp. 1–5, 2016.

[105] M. Wilson, *Superconducting Magnets.* Oxford Science Publications, 1983.

[106] C. Barth, G. Mondonico, and C. Senatore, "Electro-mechanical properties of rebco coated conductors from various industrial manufacturers at 77 k, self-field and 4.2 k, 19 t," *Supercond. Sci. Technol. 28, 045011 (10pp)*, 2015.

[107] L. Bottura, M. Breschi, E. Felcini, and A. Lechner, "Stability modeling of the LHC Nb-Ti Rutherford cables subjected to beam losses," *Physical Review Accelerators and Beams*, vol. 22, no. 4, pp. 1–12, 2019.

[108] M. Breschi, E. Felcini, F. Breccia, *et al.*, "Modeling of beam loss induced quenches inthe lhc main dipole magnets," *IEEE Trans. Appl. Supercond., Vol. 29, No. 5*, 2019.

[109] M. Breschi, E. Felcini, and L. Bottura, "Quench Level of the HL-LHC Nb3Sn IR Quadrupoles," *IEEE Transactions on Applied Superconductivity*, vol. 27, no. 4, 2017.

[110] J. van Nugteren, M. Dhalle, S. Wessela, E. Krooshoopa, A. Nijhuisa, and H. ten Kate, "Measurement and analysis of normal zone propagation in a rebcocoated conductor at temperatures below 50 k," in *25th International Cryogenic Engineering Conference and the International Cryogenic MaterialsConference in 2014, ICEC 25–ICMC*, 2014.

[111] G. Kirby, "Private communication." https://www.researchgate.net/project/EuCARD2-HTS-Magnet.

[112] H. Bajas *et al.*, "Feather m2 3-4: Test results," in *HTS Program Meeting, Feather2-34 test results*, 2019.

[113] Y. Oga *et al.*, "Overturning Force Simulation of Chain of Quenches of Toroidal HTS-SMES," *IEEE Trans. Appl. Supercond. 2, no.3*, June 2012.

[114] A. Ballarino, "Current leads, links and buses," *Contribution to the CAS-CERN Accelerator School: Superconductivity for Accelerators, Erice, Italy,*, 2013.

[115] A. Ballarino, "Hts current leads for the lhc magnet powering system," *Physica C: SuperconductivityVolumes 372–376, Part 3*, 2002.

[116] V. Parma, "Cryostat design," *Contribution to the CAS-CERN Accelerator School: Superconductivity for Accelerators, Erice, Italy,*, 2013.

[117] J. Imazato, H. Tamura, T. I. Ishikawa, *et al.*, "A superconducting toroidal magnet for charged particle spectroscopy," *MT–11, pp. 368–371.*, (Japan, 1989).

[118] J. O. Meara, J. Alcorn, and e. o. P. Brindza, "A superconducting toroidal magnet for the cebaf large acceptance spectrometer," *IEEE Trans. Magn. 25 (2), 1902–1905*, 1989.

[119] C. Luongo *et al.*, "The clas12 torus detector magnet at jefferson laboratory," *IEEE Trans. Appl. Supercond., vol. 26, no. 4, pp. 1-5*, 2016.

[120] M. Bajko, "Test facility status for testing hts at cern," in *WP10, EUCARD 2, Task 4 - HTS Magnet Tests*, 2015.

[121] H. Maeda and Y. Yanagisawa, "Recent developments in high-temperature superconducting magnet technology (review)," *IEEE Trans. Appl. Supercond. Vol. 24, No. 3*, June, 2014.

[122] J. Harray, "Hts demonstrator mechanics gatoroid project," in *Novel toroidal configuration for hadron therapy gantry, TE-MSC / EN-MME Seminar*, 2020.

[123] J. Harray, E. Felcini, and T. Lehtinen, "Hts demonstrator mechanics - gatoroid project," tech. rep., CERN Internal Report, 2020.

[124] C. Senatore *et al.*, "Progresses and challenges in the development of high-field solenoidal magnets based on re123coated conductors," *Supercond. Sci. Technol. 27 103001*, 2014.

[125] C. Barth, *High Temperature Superconductor Cable Concepts for Fusion Magnets.* PhD thesis, Karlsruher Institut für Technologie (KIT), 2013.

[126] I. Kesgin, Q. Hasse, Y. Ivanyushenkov, and U. Welp, "Degradation free vacuum epoxy impregnated short rebcoundulator magnets," *IOP Conf. Series: Materials Science and Engineering 279, 012009*, 2017.

[127] L. A. Neely, V. Kochergin, E. M. See, and H. D. Robinson, "Negative thermal expansion in a zirconium tungstate/epoxy composite at low temperatures," *Journal of Materials Science volume 49, pages392–396*, 2014.

[128] H. Miyazaki, S. Iwai, T. Tosaka, K. Tasaki, and Y. Ishii, "Degradation-free impregnated ybco pancake coilsby decreasing radial stress in the windings andmethod for evaluating delamination strength ofybco-coated conductors," *IEEE Transaction on Applied Superconductivity, Vol. 24, No. 3, 4600905*, 2014.

[129] C. Petrone, J. vanNugteren, H. Bajas, L. Bottura, G. Kirby, L. Rossi, and S. Russenschuck, "Measurement and analysis of the dynamic effects in an hts dipole magnet," *IEEE Transactions on Applied Superconductivity*, vol. 28, no. 4, pp. 1–4, 2018.

[130] J. C. Perez, H. Bajas, M. Bajko, L. Bottura, B. Bordini, A. Chiuchiolo, G. De Rijk, P. Ferracin, J. Feuvrier, P. Grosclaude, M. Juchno, E. Rochepault, J. Rysti, and X. Sarasola, "16 t nb3sn racetrack model coil test result," *IEEE Transactions on Applied Superconductivity*, vol. 26, no. 4, pp. 1–6, 2016.

[131] C. Petrone, "Analysis of rmc test results, and proposal for rmm magnetic measurements instrumentation," in *RMM magnetic measurements*, 2017.

[132] T. Haberer, "The heidelberg ion beam therapy center, experience with the hit gantry," *Ideas and technologies for a next generation medical research and therapy facility with ions*, June 2018.

[133] H. H. J. ten Kate", "The superconducting magnet system fur the atlas detector at cern," *IEEE Trans. Appl. Supercond., Vo. 10, No. 1*, March 2000.